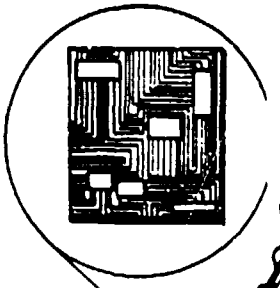

AD-A275 499

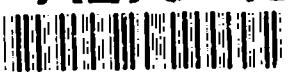

ESL-TR-92-40

(2)

RELIABILITY-BASED ANALYSIS AND DESIGN METHODS FOR REINFORCED CONCRETE PROTECTIVE STRUCTURES

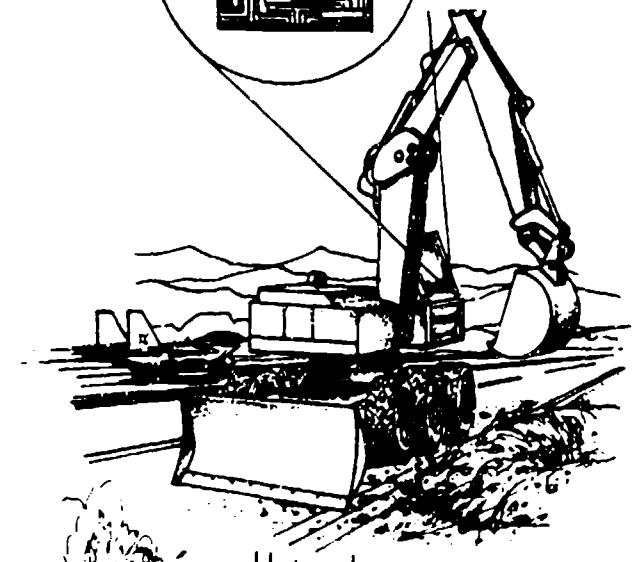

L.A. TWISDALE, R.H. SUES, F.M. LAVELLE

APPLIED RESEARCH ASSOCIATES, INC
4300 SAN MATEO BLVD., NE, SUITE A220
ALBUQUERQUE NM 87110

APRIL 1993

DTIC
ELECTE
FEB 14 1994
S A

FINAL REPORT

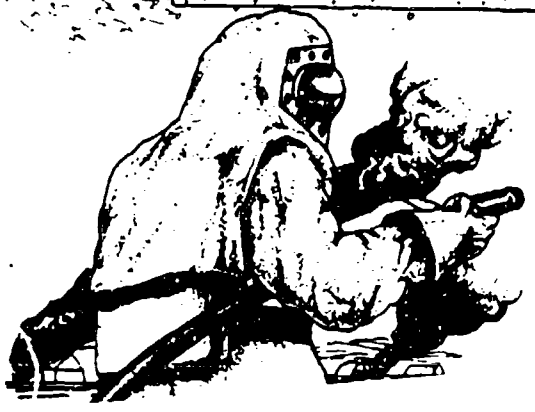

FEBRUARY 1989 - DECEMBER 1991

APPROVED FOR PUBLIC RELEASE:
DISTRIBUTION UNLIMITED

94-04591

ENGINEERING RESEARCH DIVISION
Air Force Civil Engineering Support Agency
Civil Engineering Laboratory
Tyndall Air Force Base, Florida 32403

NOTICE

PLEASE DO NOT REQUEST COPIES OF THIS REPORT FROM HQ AFCESA/RA (AIR FORCE CIVIL ENGINEERING SUPPORT AGENCY). ADDITIONAL COPIES MAY BE PURCHASED FROM:

NATIONAL TECHNICAL INFORMATION SERVICE
5285 PORT ROYAL ROAD
SPRINGFIELD, VIRGINIA 22161

FEDERAL GOVERNMENT AGENCIES AND THEIR CONTRACTORS REGISTERED WITH DEFENSE TECHNICAL INFORMATION CENTER SHOULD DIRECT REQUESTS FOR COPIES OF THIS REPORT TO:

DEFENSE TECHNICAL INFORMATION CENTER
CAMERON STATION
ALEXANDRIA, VIRGINIA 22314

REPORT DOCUMENTATION PAGE

Form Approved
OMB No. 0704-0188

1. AGENCY USE ONLY (Leave blank)	2. REPORT DATE	3. REPORT TYPE AND DATES COVERED
	April 1993	Final, 17 Feb 89-16 Dec 91

4. TITLE AND SUBTITLE
Reliability-Based Analysis and Design Methods for Reinforced Concrete Protective Structures

5. FUNDING NUMBERS
C: F08635-89-C-0121

6. AUTHORS
Twisdale, Lawrence A., Jr; Sues, Robert H.; and Lavelle, Francis M.

7. PERFORMING ORGANIZATION NAME(S) AND ADDRESS(ES)
Applied Research Associates, Inc.
4300 San Mateo Blvd., NE, Suite A220
Albuquerque, NM 87110

8. PERFORMING ORGANIZATION REPORT NUMBER
5555

9. SPONSORING/MONITORING AGENCY NAMES(S) AND ADDRESS(ES)
Air Force Civil Engineering Support Agency
Tyndall Air Force Base, Florida 32403

10. SPONSORING MONITORING AGENCY REPORT NUMBER
ESL-92-40

11. SUPPLEMENTARY NOTES

12a. DISTRIBUTION/AVAILABILITY STATEMENT
Approved for public release.
Distribution unlimited.

12b. DISTRIBUTION CODE

13. ABSTRACT *(Maximum 200 words)*

The objective of this research was to develop reliability-based design methods for reinforced protective concrete structures. The analysis and design methods in the Air Force *Protective Construction Design Manual (PCDM)* provided the nominal (deterministic) methods that were used to perform probabilistic response analyses and the reliability assessments. One of the key objectives of this effort was to develop simplified reliability-based design methods, in the form of reliability-based design factors (RBDFs), that can be used by designers who are unfamiliar with probabilistic methods.

Research was conducted in five fundamental areas: (1) airblast and aboveground structure response; (2) groundshock and belowground structure response; (3) fragmentation effects; (4) projectile penetration; and (5) protective structure systems reliability. In each of the areas, emphasis was on reinforced concrete structures; however, the load uncertainty analyses are applicable to structures of any materials. In some instances we found significant biases in the *PCDM* models. In those cases where we found significant biases that could not be corrected without changes to the fundamental approach, RBDFs were not developed. Over twenty tables of RBDFs were developed for use with the *PCDM* procedures.

14. SUBJECT TERMS
Conventional Weapon Effects
Airblast
Penetration
Fragmentation
Groundshock
Reliability

15. NUMBER OF PAGES

16. PRICE CODE

17. SECURITY CLASSIFICATION OF REPORT	18. SECURITY CLASSIFICATION OF THIS PAGE	19. SECURITY CLASSIFICATION OF ABSTRACT	20. LIMITATION OF ABSTRACT
UNCLASSIFIED	UNCLASSIFIED	UNCLASSIFIED	SAR

(The reverse of this page is blank.)

EXECUTIVE SUMMARY

The current state-of-the-art in protective construction design uses deterministic methods of analysis and does not provide systematic procedures for considering uncertainties in weapon effects, loads, or structure response. In addition, the current approach provides no guidance as to the degree of conservatism or unconservatism in the analysis methods (*e.g.*, free-field environments, penetration formulas, structure response models, etc.). Hence, the designer/analyst has very limited knowledge of the safety margins achieved when using these methods and there is no rational basis for performing cost-survivability tradeoffs.

The objective of this research was to develop reliability-based design methods for reinforced protective concrete structures. The analysis and design methods in the Air Force *Protective Construction Design Manual (PCDM)* provided the nominal (deterministic) methods that were used to perform probabilistic response analyses and the reliability assessments. One of the key objectives of this effort was to develop simplified reliability-based design methods, in the form of reliability-based design factors (RBDFs), that can be used by designers who are unfamiliar with probabilistic methods. The RBDFs account for the key design uncertainties and are used in conjunction with the *PCDM* methods. The RBDFs, which are in the form of load and resistance multipliers, are tabulated as a function of design reliability level. Generally, as higher reliability is required, load multipliers (factors that are typically less than 1.0) decrease. Using the reliability-based design procedures, the designer can evaluate the safety margin in the design and can perform cost-survivability tradeoffs.

Research was conducted in five fundamental areas: (1) airblast and aboveground structure response; (2) groundshock and belowground structure response; (3) fragmentation effects; (4) projectile penetration; and (5) protective structure systems reliability. In each of these areas, emphasis was on reinforced concrete structures; however, the load uncertainty analyses are applicable to structures of any materials. For all cases both model prediction errors and model parameter uncertainties were analyzed. To assess model prediction errors, we performed analysis using the *PCDM* methods and compared these results to experimental results. In some instances we found significant biases in the *PCDM* models. In most cases where we found significant biases that could not be corrected without changes to the fundamental approach, RBDFs were not developed. Rather, we identified the dominant sources of bias and uncertainty in the method and provided recommendations for improving the accuracy of the analysis methodology. When these models are improved and updated, it will be appropriate to develop the RBDFs.

RBDFs were developed for the following conventional weapons phenomena:

1. Free-field and reflected airblast pressures and impulses.
2. Breaching of aboveground reinforced concrete walls/slabs for closed-in cased bombs.
3. Spall of underground reinforced concrete walls/slabs due to standoff cased bombs.
4. Free-field groundshock (velocity and stress).
5. Breaching of buried reinforced concrete walls/slabs for close in buried burst.
6. Selection of design fragments for penetration, perforation, or spall effects.

7. Fragment impulse loading on aboveground walls/slabs for cased bombs.
8. Resistance factors for projectile penetration, perforation, and spall of reinforced concrete.
9. Velocity load factors for projectile penetration, perforation, and spall of reinforced concrete.
10. Residual velocity of projectiles that perforate reinforced concrete.

For the cases listed below we found significant biases in the analysis methods that could not be corrected without changes to the fundamental approach. RBDFs were not developed for these cases; however, either specific ways to improve the model prediction accuracy were recommended or improved models were provided and demonstrated.

1. Non-normally reflected airblast pressure and impulse.
2. Flexural response of aboveground reinforced concrete walls/slabs to airblast and fragment impulse.
3. Flexural response of belowground reinforced concrete walls/slabs to groundshock.
4. Resistance of reinforced concrete elements to fragment penetration, perforation, and spall.

Based on the ranking of dominant biases and uncertainties and the identification of the key methodological gaps, we summarized and prioritized the CWE research needed to improve the current *PCDM* methods.

PREFACE

This report was prepared by Applied Research Associates, Inc., (ARA) Southeast Division, 6404 Falls of Neuse Road, Suite 200, Raleigh, North Carolina 27615, under contract F08635-89-C-0121 for the Air Force Civil Engineering Services Agency, Tyndall AFB, Florida.

The principal Investigator was Dr. Lawrence A. Twisdale. Dr. Robert Sues was the senior analyst for many of the tasks. Dr. Frank Lavelle performed the analyses of the airblast loads and above ground structural response. Additional contributions to this report included: calculations of below-ground structural response by Mr. Tom Slawson of ARA's Southern Division; some of the initial work on fragment loading by Dr. Andy Hwang; and statistical analyses by Mr. Marsh Hardy. Mr. Jim Drake was ARA's internal technical reviewer.

The performance period for this contract was from 17 February 1989 to 17 December 1991. The AFCESA/RACS project officer was Captain Diane B. Miller.

This technical report has been reviewed and is approved for publication.

WILLIAM S. STRICKLAND, GM-14
Chief, Air Base Survivability Section

FELIX T. UHLIK III, Lt Col, USAF
Chief, Air Base Systems Branch (FIVC)

(The reverse of this page is blank.)

TABLE OF CONTENTS

TABLE OF CONTENTS
(continued)

TABLE OF CONTENTS
(continued)

TABLE OF CONTENTS
(continued)

LIST OF FIGURES

LIST OF FIGURES
(continued)

LIST OF FIGURES
(continued)

LIST OF FIGURES
(continued)

LIST OF TABLES

LIST OF TABLES
(continued)

LIST OF TABLES
(continued)

(The reverse of this page is blank.)

I. INTRODUCTION

A. OBJECTIVES

Recognizing the need for improved methods for protective structure design, the Air Force Civil Engineering Support Agency funded a Small Business Innovative Research (SBIR) project under the topic, "Stochastic Methods in Protective Structures." The initial SBIR Phase I feasibility study results of this project are reported in Twisdale, *et al.* [1988]. This document represents the final report of the Phase II research effort.

The overall goal of this effort was to develop reliability-based design methods for reinforced protective concrete structures. The analysis and design methods in the Air Force *Protective Construction Design Manual* [Drake, *et al.*, 1989] provided the nominal (deterministic) methods that were used to perform probabilistic response analyses and the reliability assessments. One of the key objectives of this effort was to develop simplified reliability-based design methods, in the form of reliability-based design factors (RBDFs), that can be used by designers who are unfamiliar with probabilistic methods. The RBDFs are a protective design analog to the load and resistance factor design format (LRFD) now commonly used for the design of conventional structures (*e.g.*, the AISC Specification for steel structures [AISC, 1986]).

The specific technical objectives of this Phase II Small Business Innovative Research (SBIR) effort were:

1. Review the Air Force *Protective Construction Design Manual* (herein referred to as the *PCDM* [Drake, *et al.*, 1989]) for the purposes of developing the nominal design parameters and procedures for aboveground and buried reinforced concrete protective structures.
2. Compile available experimental data relevant to the *PCDM* design methods identified under the first objective. Analyze the database to quantify model prediction errors associated with the deterministic methods in the *PCDM* and quantify the uncertainty typically encountered in specifying values for the parameters used in these methods.
3. Perform probabilistic response analyses and develop RBDFs, as appropriate, for individual failure modes, where the errors have acceptable prediction bias and random uncertainties. Use the probabilistic analysis results to identify and rank the importance of key uncertainties, biases, and methodology gaps in the *PCDM* methods.
4. Develop methods for facility-wide (systems) RBD, taking into account multiple failure modes across multiple structures. Develop generic fault trees for typical airbase structures.

B. BACKGROUND

1. Design Factors

The reliability of a structural system for a single failure mode is the probability that the load effect (*e.g.*, moment, deflection, etc) is less than the structure capacity. Because of uncertainties in the prediction of loads and structural response, the load effect E and structural

capacity C are uncertain, and are represented by probability density functions $f_E(e)$ and $f_C(c)$, respectively. The probability of unacceptable performance, P_f, is simply

$$P_f = P(C - E < 0) \tag{I-1}$$

which can be expressed as

$$P_f = \int_{-\infty}^{\infty} F_C(x)\, f_E(x)\, dx \tag{I-2}$$

where $F_C(x)$ is the cumulative distribution function. By conducting research to identify and analyze the uncertainties in load and structural response, Equation (I-2) can be solved and the uncertainties evaluated for nominal (deterministic) analysis/design procedures. In this manner, the safety margin in the nominal load, denoted E, and nominal capacity, C, can be quantified.

This approach logically leads to the concept of reliability-based design (RBD) for protective structures and the use of reliability-based design factors (RBDFs), or safety factors, as an integral part of the analysis/design process, just as for conventional structures. Once the research is completed, the analyst/designer does not perform "probabilistic" analysis, but simply uses the resulting probability-based safety factors. Hence, the design equation counterpart to Equation (I-1) for acceptable structural performance is

$$\psi \cdot C \geq \lambda \cdot E \tag{I-3}$$

where Ψ = RBDF on capacity and λ = RBDF on load effect. In some cases, a load factor of unity may be appropriate, whereas in others the load and capacity factors may be combined into a single factor. In general, a table of Ψ and λ values are provided corresponding to different levels of design survivability, P_S, where $P_S = 1 - P_f$, for each failure mode. A value of P_S is selected consistent with the design requirements, considering the consequences of failure and cost-survivability tradeoffs. Figure I-1 illustrates this process of developing RBDFs through the analysis of uncertainties in nominal (*PCDM*) design methods. A key advantage of the RBD approach is that optimized safety designs can be developed, whereas the traditional approach produces unknown safety margins. Reliability-based methods thus provide the designer with knowledge of the degree of conservatism or unconservatism in the design.

The benefits of reliability-based design have been recognized in the structural and geotechnical engineering community and several major design codes are now reliability-based (see Table I-1) Many additional codes, both in the United States and abroad, are being developed into RBD formats.

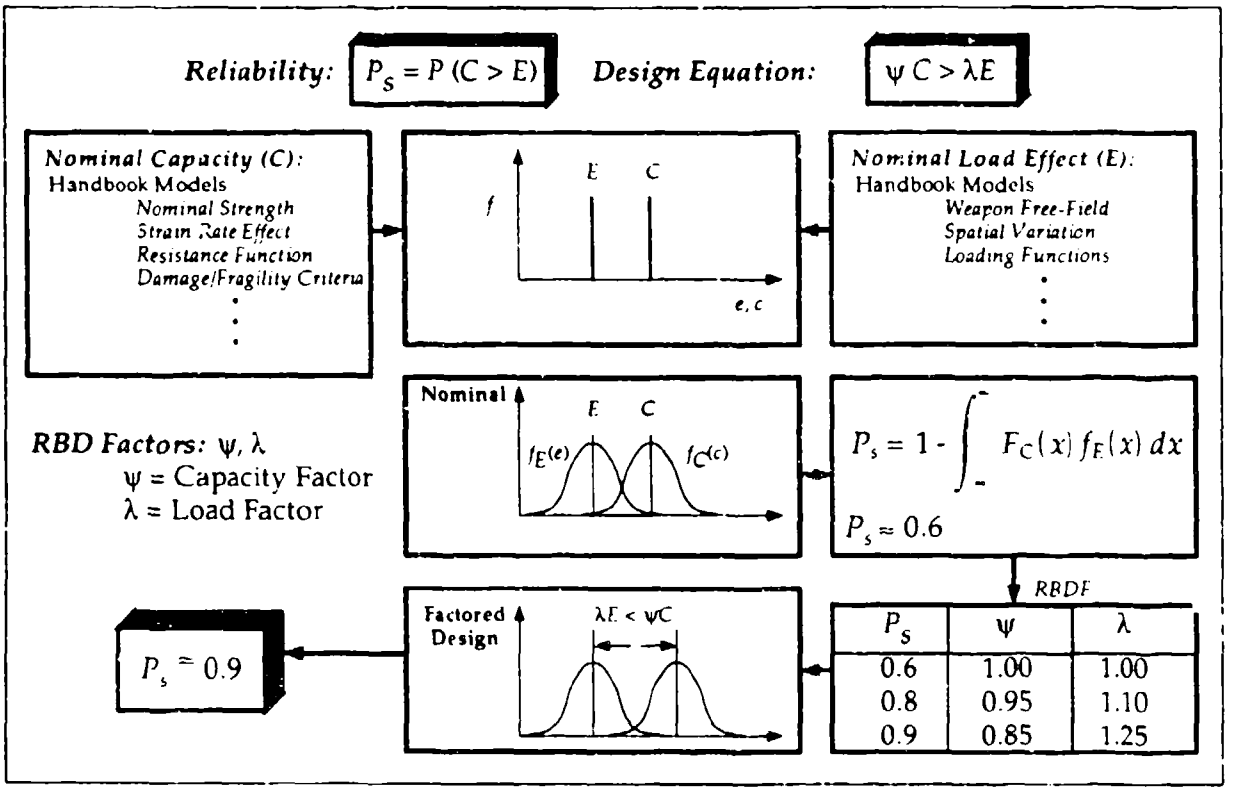

Figure I-1. Development of RBD Factors for Use with Nominal Design Methods.

TABLE I-1. SEVERAL RBD MANUALS AND DESIGN CODES.

Code[a]	Description
CSA, 1974	Canadian Standards Association - *Standards for the Design of Cold-Formed Steel Members in Buildings.*
ACI, 1977	American Concrete Institute - *Building Requirements for Reinforced Concrete.*
NKB, 1978	Nordic Committee on Building Regulations - *Recommendations for Loading and Safety Regulations for Structural Design.*
ANSI, 1982	American National Standards Institute - *Building Code Requirements for Minimum Design Loads for Buildings and Other Structures.*
OHBDC, 1983	Ontario Highway Bridge Design Code.
AASHTO, 1985	American Association of State Highway Transportation Organizations - *Guide for Design of Pavement Structures.*
AISC, 1986	American Institute of Steel Construction - *Manual of Steel Construction: Load and Resistance Factor Design.*

[a] Year shown = year that code first incorporated reliability-based design.

2. Application of RBD to Protective Structures

Table I-2 summarizes several RBD definitions and the three-step procedure for performing reliability-based design. This table emphasizes that reliability-based approaches are particularly relevant to protective construction where the accepted design philosophy has long

embraced the concept of limit states for both nuclear and nonnuclear weapon effects. Nonlinear response and local damage are acceptable to some degree, provided that structural integrity is maintained and critical assets are protected. Uncertainties are large due to the extreme load effects and the nonlinear dynamic response behavior of protective structures under these loads. Also, in protective construction it is important to have a quantifiable measure of the confidence that the protective structure will survive the weapon threat. In summary, the philosophy and approaches of protective design fit in ideally to the RBD concept. Concepts of structural reliability theory that pertain to protective construction are given in the Phase I research final report [Twisdale, *et al.*, 1988] and also in Section II of the *PCDM*.

TABLE I-2. DEFINITION OF RELIABILITY-BASED DESIGN.

Reliability = Probability that the system will perform to its intended function under specified conditions.

Reliability of a protective structure = Probability that the protective structure will perform to its intended function under specified conditions; *i.e.*, the probability of survival to specified weapon threat(s) where survival means that the structural response does not exceed specified design limit states.

Reliability-based design (RBD):

1. Integrally tied to limit states (functional and ultimate).
2. Three-step procedure:
   i. Identification of all modes of failure.
   ii. Analysis of uncertainties and determination of reliability for each limit state.
   iii. Analysis/design for the controlling limit states.
3. **RBD** = Structural analysis/design based on probability-based limit states using factored loads and capacities; permits a quantitative (reliability) measure of assurance of structural performance.

3. Uncertainties

In developing RBD methods, we use a systematic approach to characterize uncertainties so that significant uncertainties are not overlooked and the same uncertainty sources are not included more than once. Figure I-2 summarizes the sources of uncertainty considered in the RBD research phase. As shown, there are two main sources of uncertainty: (1) prediction error associated with the inability of an engineering model to perfectly predict the true or measured effects in each case; and (2) model parameter uncertainty associated with inability to deterministically specify values of the engineering model input parameters.

Model prediction error can have both a systematic component (error in the mean prediction) and a random component (variation about the mean prediction). Figure I-3 illustrates the concept of model prediction error ξ, defined as a ratio of measured (x_m) to calculated (x_c) response. This non-dimensional ratio is formed on a test-by-test basis, as illustrated in the table of hypothetical data in Figure I-3. The mean of ξ, $\hat{\mu}_\xi$, is a measure of the systematic bias and the standard deviation, $\hat{\sigma}_\xi$, is a measure of the random dispersion. Through detailed experiment-by-experiment analyses of the data and understanding of the model and its limitations, the sources of

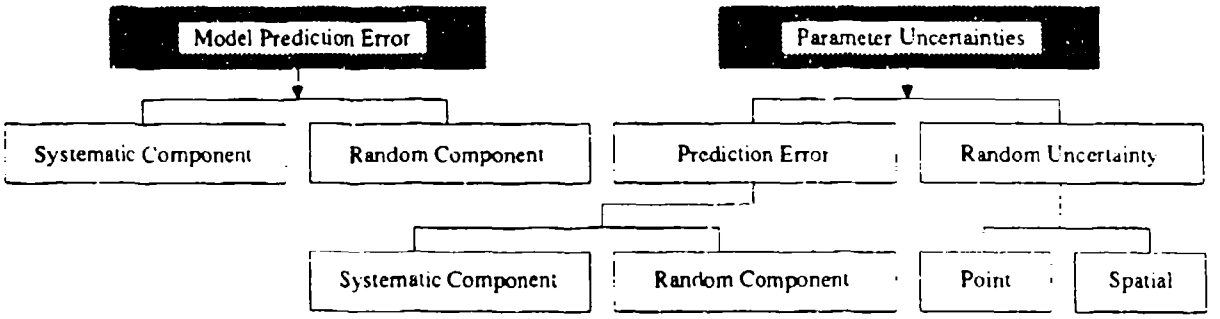

Figure I-2. Sources of Uncertainty in RBD Research.

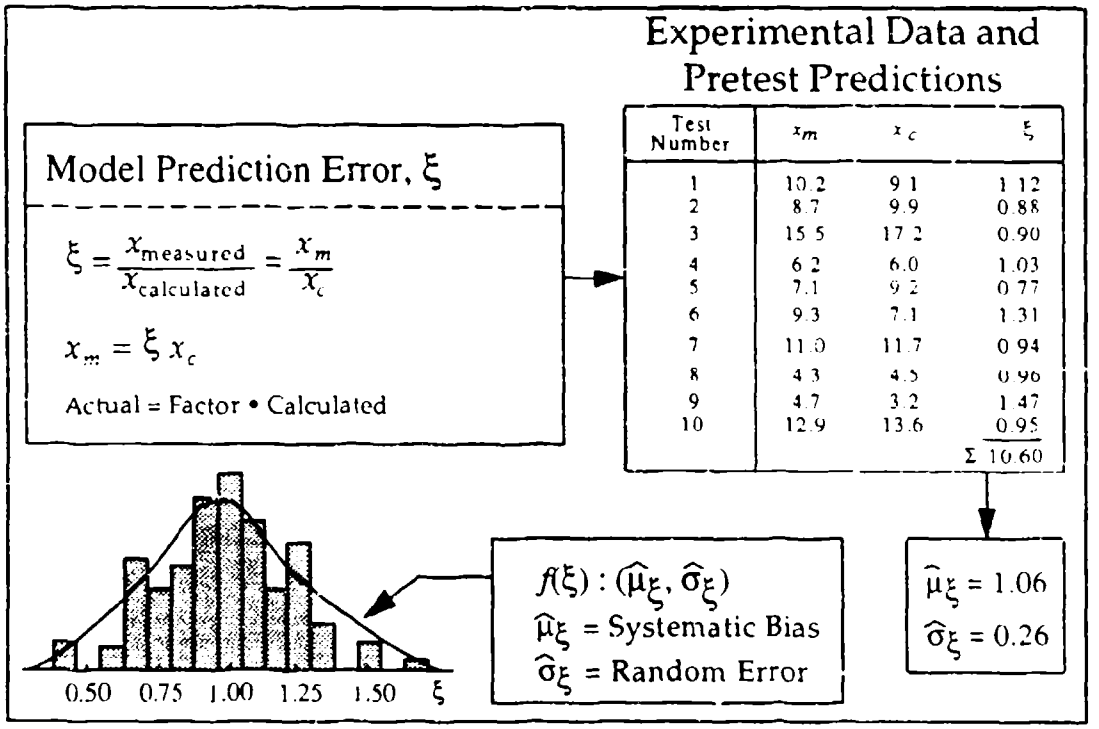

Figure I-3. Analysis of Model Prediction Error.

bias (if any) can be identified. If the model is essentially unbiased and the dispersion is adequately characterized as random prediction error, the analysis of ξ provides a quantitative basis to analyze model prediction error.

Model parameter uncertainty can also have both prediction error and random uncertainty, as noted in Figure I-2. Model parameter prediction error is generally due to limited data. For example, in a ground shock calculation some soil property parameters may need to be inferred from qualitative site descriptions or from a limited number of soil samples. Model parameter random uncertainty is due to what is often termed "inherent variability"; for example, the variability in concrete cylinder test results for samples taken from the same batch of concrete.

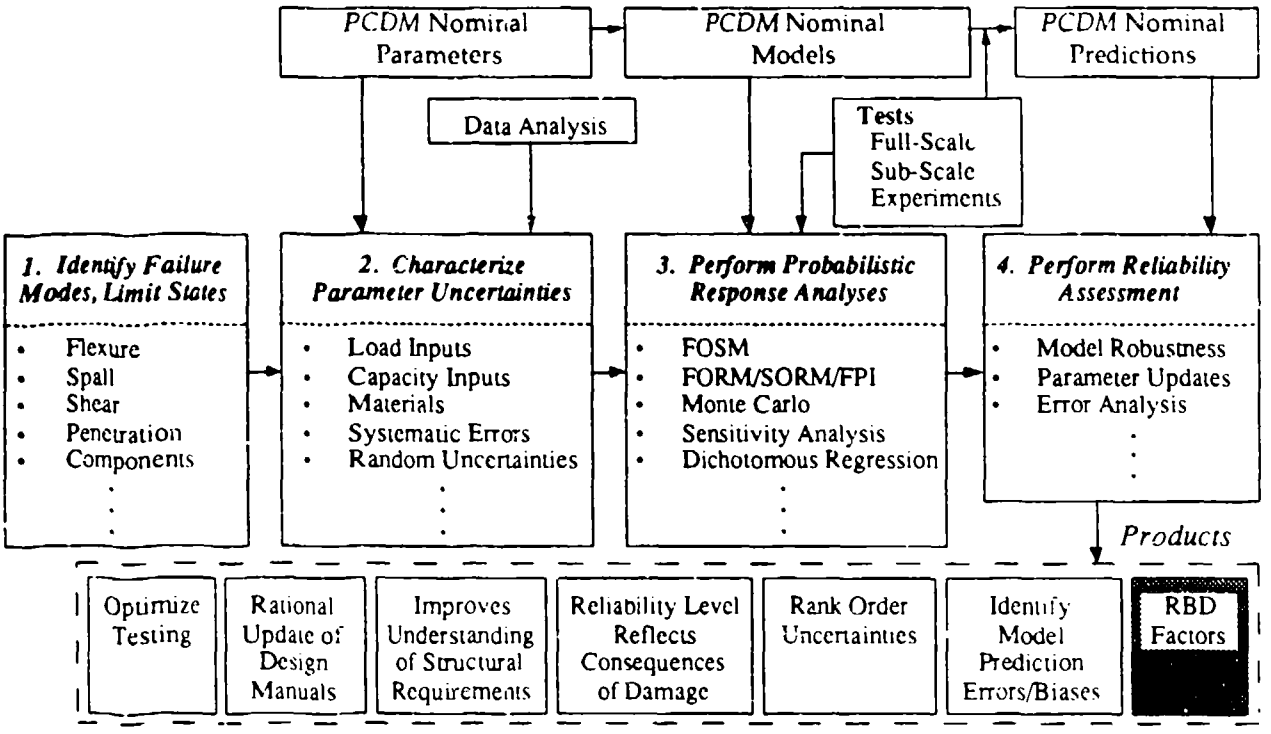

Figure I-4. The Four Steps of the RBD Process.

Examples of these sources of uncertainties are discussed in Section II of the *PCDM* and in the Phase I report [Twisdale, *et al.*, 1988]. These uncertainties are analyzed using statistical methods to estimate means, variances, model parameter significance, and probability distributions, and to reject data outliers. Multivariate parameter analysis methods are used to evaluate correlation, regression, and cluster relationships and to analyze sources of variance. The methods that are used herein are discussed individually for each load and response area considered.

C. APPROACH FOR DEVELOPING RBD FACTORS

For each design method that we analyzed from the *PCDM*, the approach for developing RBD procedures followed four basic steps. These steps are summarized in Figure I-4 as: (1) identify failure modes and limit states; (2) characterize parameter uncertainties; (3) perform the probabilistic response analyses; and (4) perform the reliability assessment. The nominal parameters and models are the prediction equation in the *PCDM* for each load/response failure mode considered. The experimental data provides the linkage between the nominal procedures and the RBD development process. Figure I-4 also illustrates that, in addition to RBDFs, there are many additional benefits of the RBD process.

This systematic step-by-step process may lead to one of several results in terms of how well the nominal procedures perform. Figure I-5 summarizes the approach used in this effort. If the systematic errors (biases) were acceptably small and the data were sufficient, RBDFs were developed for use with the nominal *PCDM* procedures. If we found marginally acceptable errors

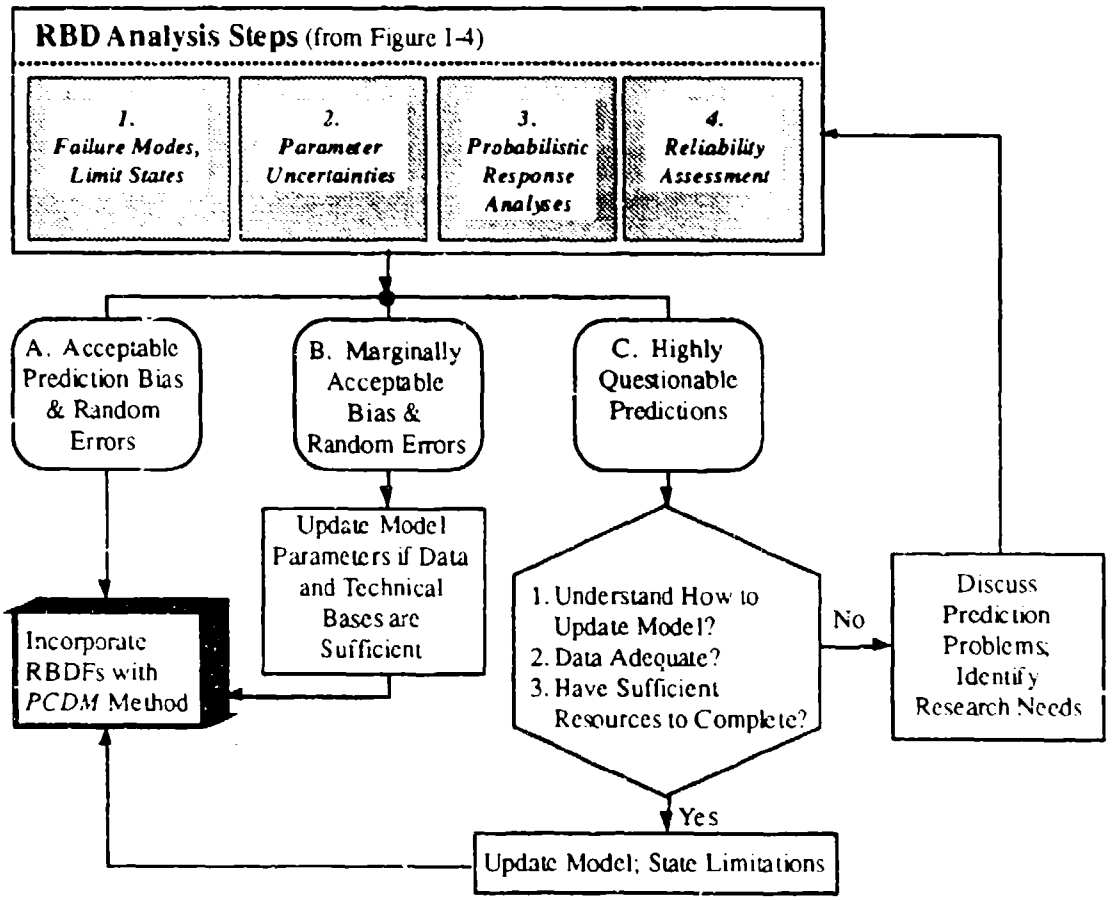

Figure I-5. RBD Guidance Provided as a Result of This Research Project.

and the data were sufficient to update the model parameters, we produced RBDFs for the *PCDM* procedures, using updated parameters. In most of these cases, we qualified the updates to the range of relevant data available. For cases in which the predictions did not agree with the experimental results, we determined if the data and our understanding of the issues and resources were sufficient to update the model. If so, we provided an updated or new model, stated necessary limitations, and gave factors for use with it. If not, and if the *PCDM* methods are conservative, we provide qualitative discussion and recommend that no additional factors be used.

An important final point regarding this research is that it has been done following the publication of the *PCDM*. Although in some cases we had access to new data or data not considered in the *PCDM*, the work would have proceeded more smoothly if it had been done in conjunction with *PCDM* development. We believe that Branch C in Figure I-5 could have been resolved by working directly with the *PCDM* technical experts for each failure mode investigated. When the *PCDM* models associated with Branch C are improved and updated, it will be appropriate to develop RBDFs. We recommend that future manuals be updated with a parallel RBD effort to evaluate the methods *vis a vis* the data and model parameter uncertainties. The ideal manner to resolve identified biases is through the feedback loop shown in Figure I-6.

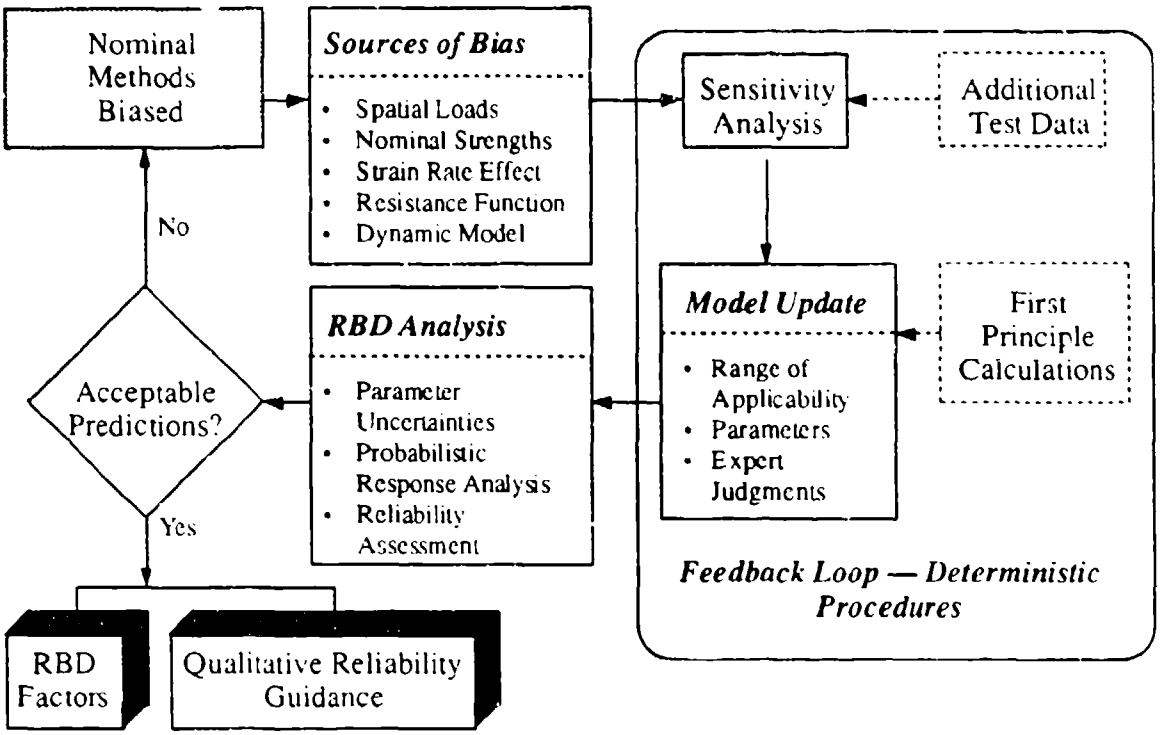

Figure I-6. Recommended Procedure to Resolve Systematic Prediction Biases for Reliability-Based Design.

D. SCOPE AND ADDENDUM REPORT

The Phase II research effort was conducted in five fundamental areas, as reported in Sections II through VI, respectively: (1) airblast and aboveground structure response; (2) groundshock and belowground structure response; (3) fragmentation effects; (4) projectile penetration; and (5) protective structure systems reliability. In each of the areas emphasis was on reinforced concrete structures; however, the load uncertainty analyses are applicable to structures of any materials. In the final section (Section VII) we summarize the significant biases and methodology gaps in the *PCDM* methods that were identified as a result of this research and prioritize protective design research needs. Section VII also provides a list of conclusions and recommendations with regard to the use of reliability-based design and analysis methods in protective construction. Appendices A and B present fragmentation information on the hypergeometric function and target solid angle intersection, respectively.

An RBD addendum to the *PCDM* will be published that will summarize the design factors and RBD procedures developed herein and include several RBD analysis/design problems.

II. AIRBLAST AND ABOVEGROUND STRUCTURE RESPONSE

A. INTRODUCTION

To develop reliability-based methods for the analysis and design of aboveground protective structures, we must characterize uncertainties associated with predicting both the airblast loads and the structural response. In this chapter, hemispherical surface burst prediction errors are quantified for peak pressures and impulses resulting from both incident airblast (Section II.B) and normally reflected airblast (Section II.C). Based on experimental databases that we were able to acquire and analyze, Reliability-Based Design Factors (RBDFs) are developed for airblast loads applied to aboveground structures subjected to stand-off surface bursts. In Section II.D, the procedures and requirements for developing RBDFs for the flexural resistance or load capacity of an aboveground structure wall are discussed. Large prediction biases were found in the *PCDM* flexural response prediction procedure, and meaningful RBDFs could not be developed within the scope of this task. However, we do identify several significant sources of bias and uncertainty in the *PCDM* prediction methodology. Quantitative estimates of the bias and uncertainties are given wherever possible. In Section II.E, RBDFs are developed for use with the *PCDM* method for design to resist breaching. Preliminary RBDFs for preventing spall are also derived in Section II.E.

B. PREDICTION ERRORS IN INCIDENT AIRBLAST PARAMETERS

The systematic and random errors associated with the deterministic incident airblast prediction methods recommended in the *PCDM* for hemispherical surface bursts are investigated in this section, and load factors for incident pressure and impulse applicable to Mk82 and Mk83 general-purpose bombs are derived. To derive the load factors, prediction error models for incident peak overpressure and positive impulse are developed by directly comparing experimentally obtained airblast data to *PCDM* predictions. The experimental observations are from the Conventional High-Explosive Blast and Shock (CHEBS) test series [Carson, *et al.*, 1984; Carson and Morrison, 1987]. The CHEBS test series involved sixteen general-purpose (Mk82 and Mk83) bomb tests with airblast data obtained over a range of standoffs applicable to protective structure design. Figure II-1 shows the CHEBS test bed layout.

1. Prediction Methodology

The prediction methodology in the *PCDM* is based on the airblast parameter polynomials for uncased TNT hemispherical surface bursts of Kingery and Bulmash [1984]. The Kingery and Bulmash polynomials are given in *PCDM* Appendix IV-1. These curve fits were implemented in a computer code and used to make all airblast predictions. The accuracy of the code was verified by comparing its output to *PCDM* Figure IV-5. The effective TNT weights used to predict the CHEBS observations are a function of the type of explosive and bomb depth-of-burial. Corrections for casing effects were not included in the effective weight computations in the final analysis since the CHEBS observations for Mk82 and Mk83 general-purpose bombs fit the

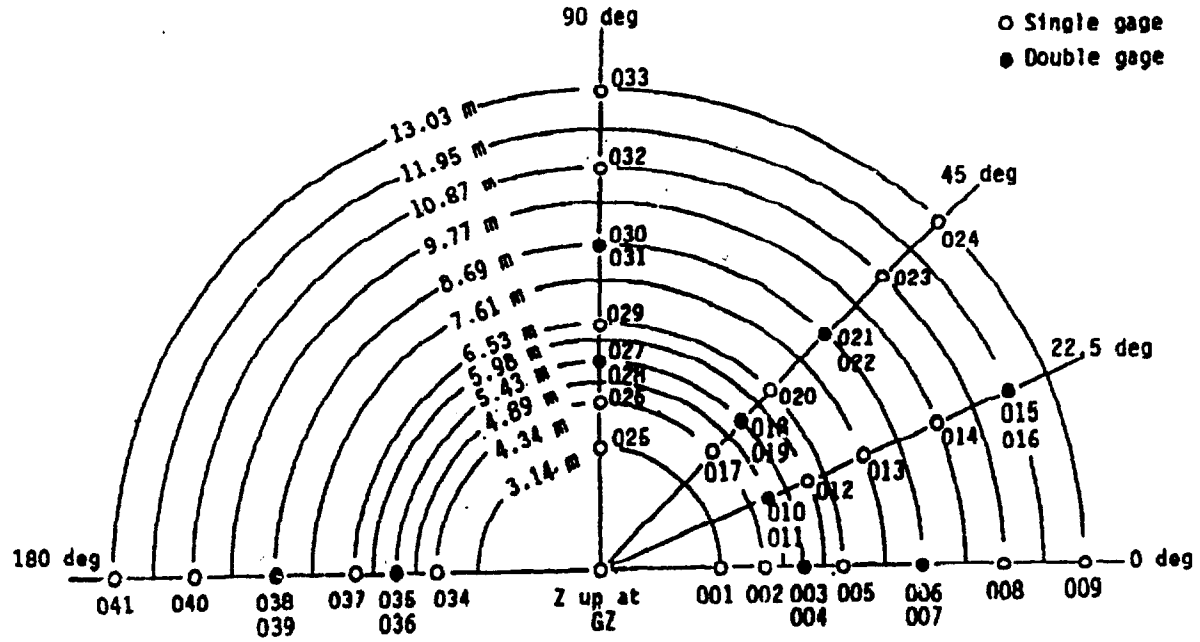

Figure II-1. CHEBS Test Bed Layout [Carson and Morrison, 1987].

predictions more closely when casing effects are not considered.[1] To include airblast data from CHEBS tests in which the bombs were half-buried rather than surface-tangent, the effective weights for the half-buried tests are divided by two. This approach is taken in the absence of *PCDM* guidance for airblast coupling factors for partially-buried conventional explosives. The resulting effective TNT weights are shown in Table II-1. Note that CHEBS test number 11 is not included because the bomb was fully buried.

TABLE II-1. EFFECTIVE TNT WEIGHTS USED TO PREDICT CHEBS AIRBLAST DATA.

Bomb Type	Explosive	TNT Factor		Bomb	CHEBS	Eff. Weight (*kg*)	
(Explosive)	Weight (*kg*)	Pressure	Impulse	Position	Tests	Pressure	Impulse
Mk82 (Tritonal)	86.6	1.07	0.96	Tangent	1	92.7	83.2
				Half-Buried	2-6	46.3	41.6
Mk83 (H6)	206.3	1.38	1.15	Tangent	9,10,16	284.8	237.3
				Half-Buried	7,8,12-15	142.4	118.7

2. Classification and Screening of CHEBS Data

The four groups of CHEBS tests considered for this study are described in Table II-2. The data groups have been formed by pooling together observations from tests having identical bomb orientations. Group II, for example, consists of pressure and impulse readings

[1]Casing effects are an important area for further study, particularly for penetrating weapons with heavy casings, for which there is little data.

TABLE II-2. CHEBS TEST GROUPS.

Group	Test Numbers	Bomb Orientation	Number of Observations	
			Pressure	Impulse
I	9,10,16	Vertical, Nose Tangent	85	83
II	5,6,14,15	Vertical, Half-Buried	146	143
III	1	Horizontal, Surface Tangent	5	7
IV	2-4,7,8,12,13	Horizontal, Half-Buried	89	87

from all of the tests in which the bomb was vertical and half-buried. Differences in the bomb sizes within each group (Mk82 *vs.* Mk83) are accounted for by scaling the standoffs and incident impulses according to the equivalent TNT weights given in Table II-1.[1]

Although the data presented in the CHEBS reports [Carson, *et al.*, 1984; Carson and Morrison, 1987] had already been screened to eliminate bad gage readings, further editing of the database was necessary. Changes to the pressure and impulse data sets are summarized in Table II-3. All of the changes to the summary data reported in Carson and Morrison [1987] were based on a detailed review of the individual pressure/impulse time history plots and were made for one of three reasons: (1) the peak values listed in the CHEBS tables did not coincide with the peak values shown in the pressure or impulse plot (in some cases the difference was a factor of ten, due to a change in the exponent); (2) the pressure curve did not completely return to zero and, as a result, the impulse was too large; or (3) noise in the pressure curve prior to the time of arrival caused an initial offset in the impulse. The readings marked by an "X" in Table II-3 were deleted from the database. Data was deleted if: (1) excessive noise was visible in the pressure plots, (2) the high pressure region of the signal was unusually wide or narrow compared to other similar gages, (3) the pressure curve was uncharacteristically smooth in comparison to other comparable signals, or (4) clipping occurred in the signal.

Additional screening of the CHEBS data set is required for the horizontal bomb tests (Groups III and IV). For these tests, only the gages oriented at 90 *degrees* to the bomb axis are retained. Gages oriented at other angles are excluded because peak pressures and impulses decrease significantly at angles closer to the nose or tail of cylindrically-cased explosives. Eliminating the non-normal gages in Groups III and IV also results in a more consistent set of data groups since all of the data in the vertical bomb tests (Groups I and II) are for gages at 90 *degrees* to the bomb axis.[2] Although a considerable number of data points are eliminated from Groups III and IV as a result of this analysis, a large data set still remains (see Table II-2). A total of 325 peak pressures and 320 positive impulses at scaled ranges varying from 0.5 to 2.6

[1] It will be demonstrated later, through statistical analysis of variance, that further grouping of the data by bomb size is unnecessary.

[2] This reasoning is verified through a statistical analysis of variance using the gage-to-bomb angle as the classification variable (Section II.B.3). The results of this procedure show that gage angle is a highly significant variable. Therefore, it is very unlikely that data acquired at different gage angles are representative samples from the same underlying population.

TABLE II-3. SUMMARY OF CHANGES TO CHEBS PRESSURE AND IMPULSE DATA.

Test	Gage	Pressure (*MPa*)	Impulse (*MPa-ms*)
2	637		X[a]
4	617		0.63 (0.703)[b]
5	601		0.80 (0.950)
	633	X	X
	637		X
7	727		X
9	701	X	X
	703	X	X
	704	X	X
	714		0.54 (5.40)
10	704		X
	709		0.80 (1.18)
	710		X
	727		X
	734		1.50 (2.83)
	737		X
13	707		0.88 (0.788)
	713		1.00 (1.21)
14	705		1.20 (1.65)
	712		X
16	720		2.54 (0.304)

[a]X denotes gage measurement deleted from database in the screening process.
[b]Value reported in Carson and Morrison [1987] summary tables is given in parentheses. Corrected value is based on the impulse time history plot shown in the test report.

meters/kilogram$^{1/3}$ (1.25 to 6.5 *feet/pound*$^{1/3}$) have been retained. Note that by retaining only the 90-*degree* gage data, we address the critical loading case for most above-ground structures subjected to stand-off bursts. The prediction errors are thus conservative for cases in which the bomb lands at an angle.

3. Statistical Analysis of Incident Airblast Prediction Error

Figures II-2 and II-3 are plots of the observed and predicted airblast parameters. The symbol for each observation is assigned according to the data groups described in Table II-2. The peak overpressures are plotted in Figure II-2, and the incident positive impulses are plotted in Figure II-3. The *PCDM* predictions described in Section II.B.1 (*i.e.*, the Kingery and Bulmash hemispherical surface burst polynomials given in *PCDM* Appendix IV-1) are shown as solid lines in each figure.

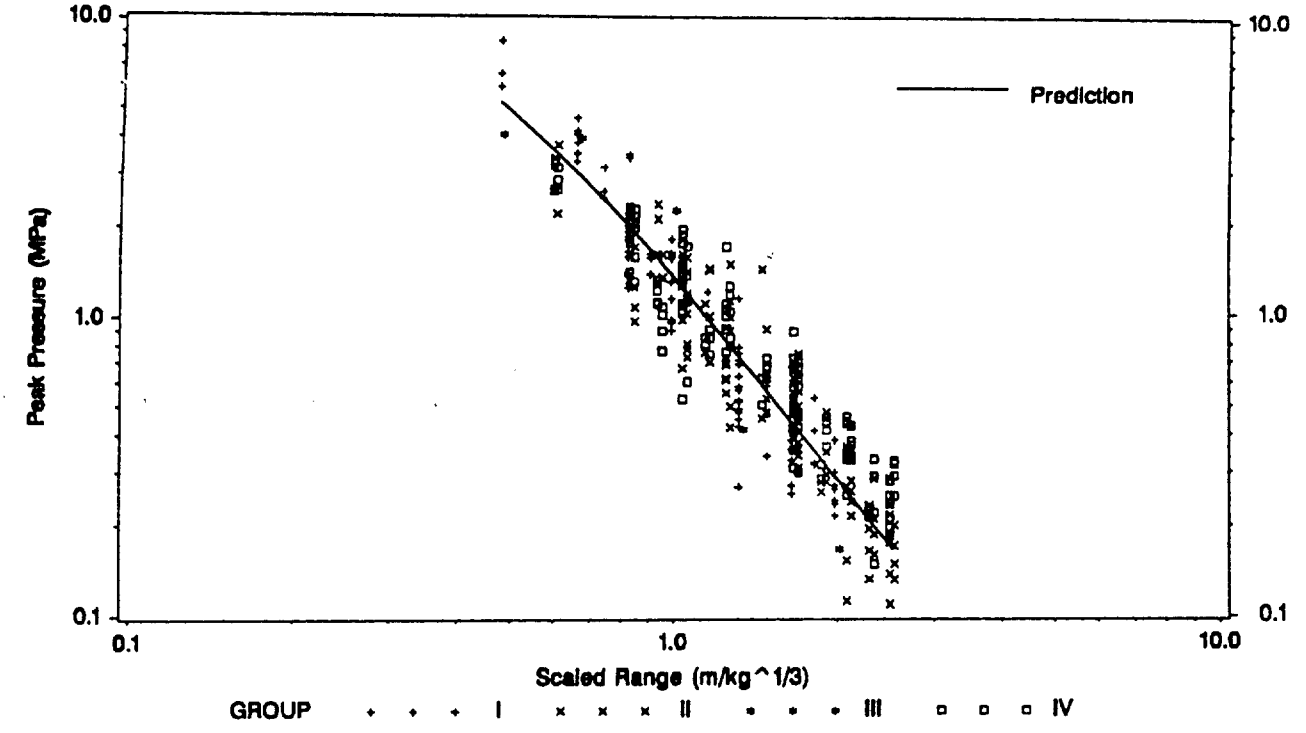

Figure II-2. CHEBS Peak Pressure Observations.

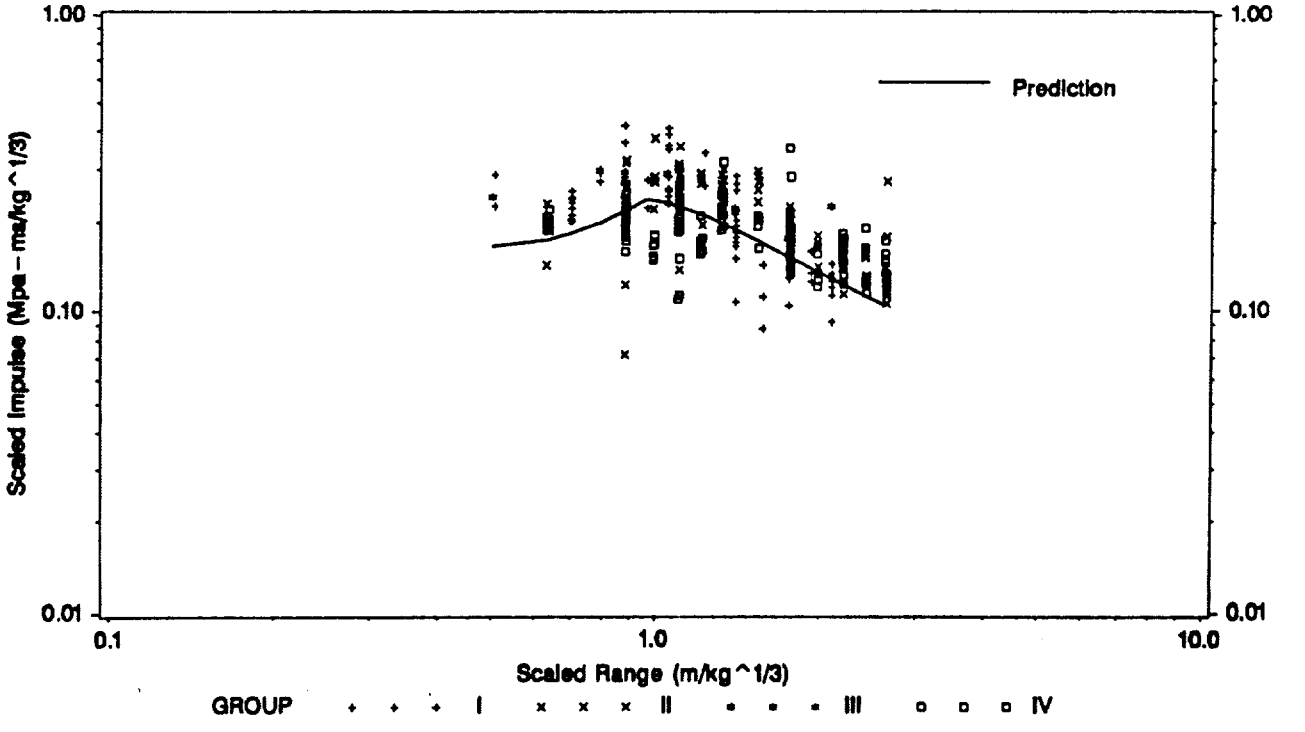

Figure II-3. CHEBS Positive Impulse Observations.

Denoting the j^{th} observation of pressure and impulse in each data group by P_{s_j} and i_{s_j} and the corresponding predictions by $\hat{P}_{s_j}$ and $\hat{i}_{s_j}$, the prediction error for the j^{th} observation can be expressed as

$$\xi_{P_{s_j}} = P_{s_j}/\hat{P}_{s_j} \tag{II-1}$$

$$\xi_{i_{s_j}} = i_{s_j}/\hat{i}_{s_j} \tag{II-2}$$

or in log space as

$$\ln\left(\xi_{P_{s_j}}\right) = \ln\left(P_{s_j}\right) - \ln\left(\hat{P}_{s_j}\right) \tag{II-3}$$

$$\ln\left(\xi_{i_{s_j}}\right) = \ln\left(i_{s_j}\right) - \ln\left(\hat{i}_{s_j}\right) \tag{II-4}$$

The statistics of $\xi_{P_{s_j}}$ and $\xi_{i_{s_j}}$ can be used to estimate the probability distributions of the underlying random variables ξ_{P_s} and ξ_{i_s}. These random variables provide a measure of the systematic and random components of the *PCDM* airblast parameter prediction errors.

Plots of the prediction error ratios for each data group are shown in Figures II-4 and II-5. Also shown on these plots are linear regression fits of the data in log-log space. Figures II-6 and II-7 show histograms of the prediction error ratios for all scaled ranges. Statistics of the observed prediction error ratios, as well as hypothesis tests for systematic bias and lognormality, are given in Table II-4. The tests for systematic bias are evaluated using the t-statistic for the hypothesis that the mean values of ξ_{P_s} and ξ_{i_s} are 1.0. A similar test is performed to see if the mean values of ln (ξ_{P_s}) and ln (ξ_{i_s}) are significantly different than zero. Because the prediction errors are bounded below by zero, the random variables ξ_{P_s} and ξ_{i_s} are hypothesized to be lognormally distributed (*i.e.*, ln (ξ_{P_s}) and ln (ξ_{i_s}) are tested against normal distributions). The tests for normality on ln (ξ_{P_s}) and ln (ξ_{i_s}) use the small-sample Wilks statistic. For each hypothesis test, the p-value is the probability of obtaining a more extreme value of the test statistic given that the hypothesis is true. Typically, a hypothesis is rejected if the p-value is less than 0.05. For example, the hypothesis that the mean impulse prediction error ratio is actually equal to one (H_0: Mean = 1) should be rejected for each of the impulse data groups as well as for the combined impulse data sets. As a result, it can be concluded that the *PCDM* prediction methodology is biased towards underpredicting the incident impulse produced by Mk82 and Mk83 bombs.

Statistics for the log-log regression fits shown in Figures II-4 and II-5 are summarized in Table II-5. The dependence of prediction error on range is tested by hypothesizing that the true slope of each regression line is zero. The low p-values indicate that, in most cases,

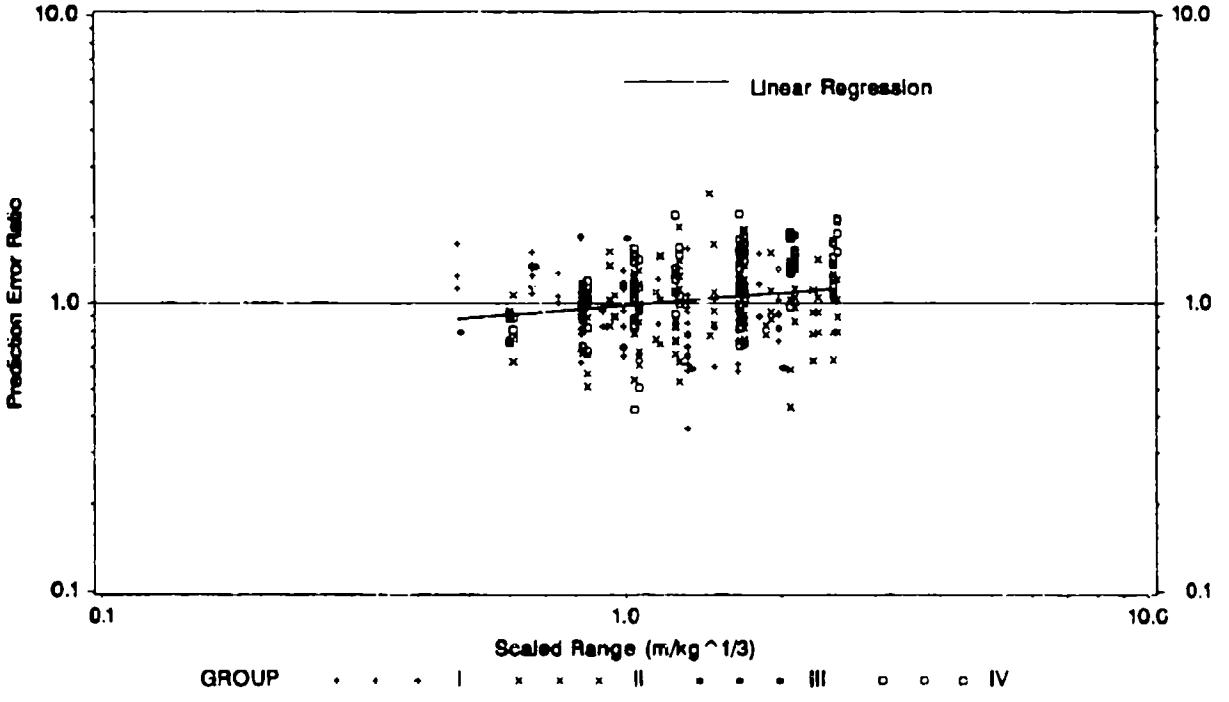

Figure II-4. CHEBS Peak Pressure Prediction Errors.

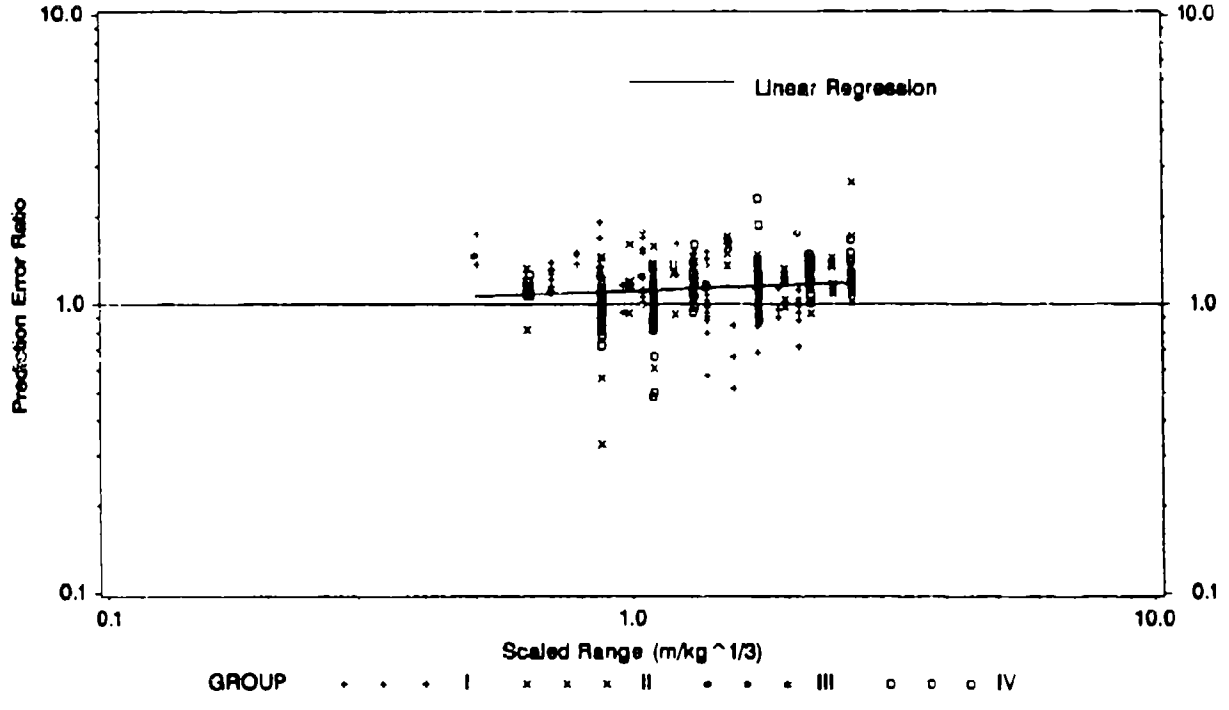

Figure II-5. CHEBS Positive Impulse Prediction Errors.

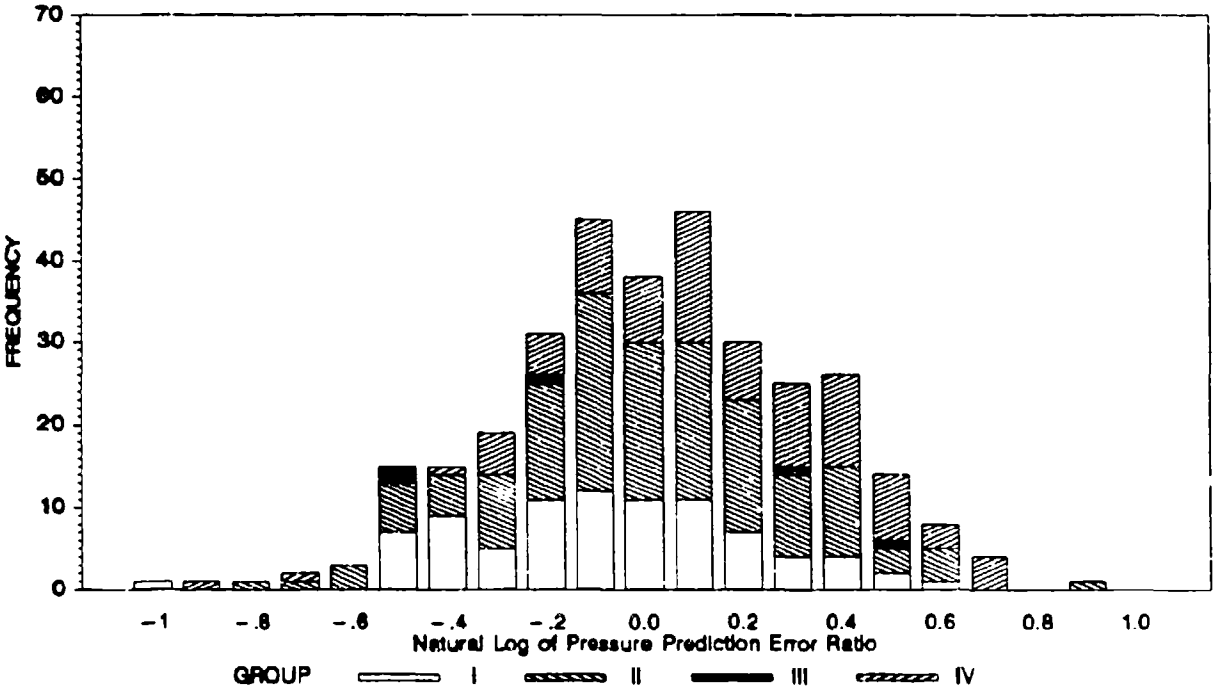

Figure II-6. Histogram of Peak Pressure Prediction Error Ratios.

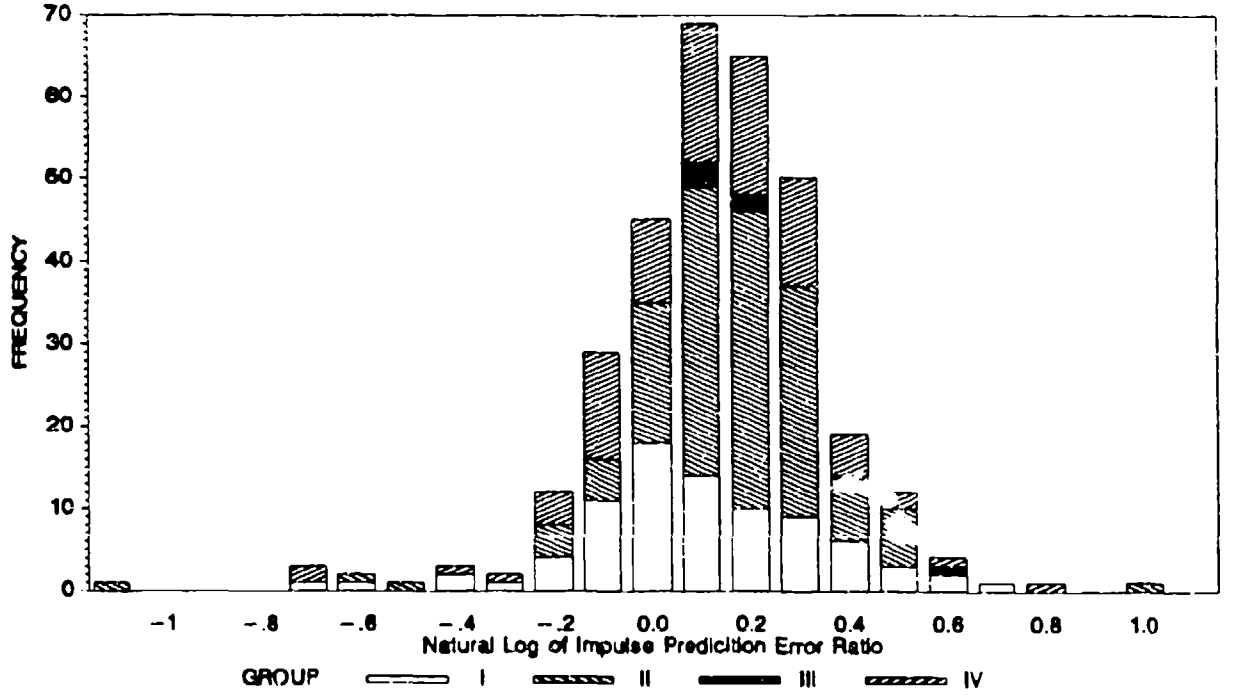

Figure II-7. Histogram of Incident Impulse Prediction Ratios.

TABLE II-4. STATISTICS OF THE INCIDENT AIRBLAST PREDICTION ERROR RATIOS.

Parameter	Group	Prediction Error Ratio, ξ			ln (ξ)			
		Mean	Coefficient of Variation	p-value for H_o: Mean = 1	Mean	$\sigma_{\ln(\xi)}$	p-values for H_o: Mean = 0	Lognormal
Pressure	I	0.973	0.289	0.372	-0.069	0.290	0.032	0.727
	II	1.049	0.298	0.058	0.006	0.294	0.820	0.989
	III	1.005	0.490	0.984	-0.089	0.479	0.700	0.261
	IV	1.220	0.288	0.0001	0.155	0.304	0.0001	0.192
	I, III	0.974	0.300	0.409	-0.070	0.300	0.030	0.554
	II, IV	1.114	0.303	0.0001	0.062	0.306	0.002	0.655
	I - IV	1.075	0.308	0.0001	0.026	0.310	0.135	0.781
Impulse	I	1.130	0.241	0.0001	0.093	0.243	0.0008	0.445
	II	1.199	0.198	0.0001	0.161	0.211	0.0001	0.0001
	III	1.291	0.184	0.018	0.242	0.170	0.009	0.068
	IV	1.142	0.236	0.0001	0.105	0.241	0.0001	0.063
	I, III	1.142	0.238	0.0001	0.105	0.241	0.0001	0.365
	II, IV	1.178	0.213	0.0001	0.140	0.224	0.0001	0.0001
	I - IV	1.168	0.220	0.0001	0.130	0.229	0.0001	0.0001

TABLE II-5. INCIDENT AIRBLAST PREDICTION ERROR REGRESSION STATISTICS.

Parameter	Group	Slope of Log-Log Fit	p-value for H_o: slope =0	R^2	$\sigma_{\ln(\xi)}$	$\sigma_{scatter}$
Pressure	I	-.268	.0012	.119	.290	.272
	II	+.167	.0068	.050	.294	.289
	III	-.375	.4579	.194	.479	.430
	IV	+.414	.0001	.321	.304	.251
	I, III	-.276	0.0007	.124	0.300	0.280
	II, IV	+.257	0.0001	.113	0.306	0.288
	I-IV	+.149	.0004	.039	.310	.304
Impulse	I	-.368	.0001	.304	.243	.203
	II	+.126	.0049	.055	.211	.205
	III	+.043	.7830	.017	.170	.168
	IV	+.275	.0001	.229	.241	.212
	I, III	-.319	0.0001	.245	.241	.209
	II, IV	+.190	0.0001	.116	.224	.210
	I-IV	+.068	.0327	.014	.229	.227

there is a significant range dependence (that is, the slope is not zero). However, the low R^2 values reveal that very little of the prediction error variability is "explained" by each regression line (although the slope is not zero, it is still relatively small). This point is further illustrated by the last two columns in Table II-5 The variability of the data about the regression line (denoted by $\sigma_{scatter}$) is only slightly smaller than the range-independent standard deviation, $\sigma_{\ln(\xi)}$. Hence, a range-independent model will be used in the reliability-based design method.

In order to have the largest database possible and to simplify the development and implementation of reliability-based design procedures, it is advantageous to pool together the Groups I through IV data into combined data sets — one for peak pressure and one for positive impulse. However, lumping the surface tangent and half-buried data groups together may not be justified. Therefore, separate statistics for the surface tangent (Groups I and III) and half-buried (Groups II and IV) must also be considered. The statistics of each of these combined data sets have already been given in Tables II-4 and II-5, and the plots shown in Figures II-2 through II-7 contain all of the observations in the combined data sets. The process of pooling the individual data sets can be justified if it is determined that the differences between the groups are not statistically significant. The statistical method for examining differences between data groups is Analysis of Variance (ANOVA). For example, ANOVA is used to determine whether the surface tangent and half-buried data groups can be pooled together.

A summary of ANOVA results for the CHEBS data groups is given in Table II-6. Results are shown for Groups I, II and IV (Group III was not studied because of its small number of observations) and for the combined data sets (Groups I-IV). Several classification variables have been tested for significance. With the exception of the tests comprising Group IV, tests having identical bomb orientations do not have significant statistical differences. Based on these results, we assume that test-to-test variations of the airblast statistics for a given weapon orientation are not significant and that grouping similar tests together is justified. In Section II.B.2 we intuitively argued that only those gages on a line perpendicular to the major axis of the bomb should be retained from the horizontal bomb tests. The statistical justification for this decision is the ANOVA results for Group IV (horizontal, half-buried) using gage angle as the classification variable. These results show that pressure and impulse observations from gages oriented at 67.5, 90, and 112.5 *degrees* are significantly different at the 1 *percent* confidence level. Carson and Morrison [1987] indicate that gage type (*i.e.*, "HKS" *vs.* "XT" gages) might be a significant classification variable. However, the gages are highly correlated with range since the type of gage selected depends on the anticipated overpressures. Therefore, an analysis of gage type significance is not possible since gage and range effects are intermingled.

The final ANOVA results given in Table II-6 concern the pooling of different bomb orientation groups into a single, combined data set, labeled Groups I-IV. When all of the data sets are pooled together, ANOVA reveals that the group number is a significant classification variable. Further investigation revealed that Group IV is highly different from Groups I, II, and III for peak pressure, while Group II differs from the other positive impulse data groups. The differences can

TABLE II-6. ANALYSIS OF VARIANCE RESULTS.

Group	Classification Variable	Probability of a Larger F-statistic	
		Pressure	Impulse
I (Vertical, Nose Tangent)	Test Number	0.8697	0.7182
II (Vertical, Half-Buried)	Test Number	0.1291	0.4102
IV (Horizontal, Half-Buried)	Test Number	0.0255[a]	0.4051
	Gage Angle (67.5°, 90°, 112.5°)	0.0006[b]	0.0013[b]
I-IV (All Orientations)	Group Number	0.0001[b]	0.0625
	Group IV *vs.* I, II, & III	0.0001[b]	–
	Group II *vs.* I, III, & IV	–	0.0297[a]
	Bomb Type (Mk82 *vs.* Mk83)	0.4406	0.1039

[a] Significant Variable (5 *percent* Confidence Level).
[b] Highly Significant Variable (1 *percent* Confidence Level).

most likely be attributed to the fact that Groups II and IV consist of data from the half-buried tests. As mentioned in Section II.B.1, the *PCDM* does not contain a procedure for scaling the explosive weight of partially buried bombs. For the purposes of this study, one-half of the equivalent TNT weight is used to predict the airblast produced in the half-buried CHEBS tests. Since the mean prediction errors for the half-buried data are significantly larger than the prediction errors for the surface tangent data, separate prediction error models shall be derived for these two cases.

4. Incident Airblast RBDFs

Based on this analysis of the CHEBS data, the following recommendations are made with respect to the development of incident airblast RBDFs:

1. ***Range-Independent Load Factors.*** Although significant regression models have been obtained for most of the data groups, it is recommended that a range-independent prediction error model be adopted for the development of reliability-based design methods. This recommendation can be justified for the following reasons: (1) range-dependent prediction error models do not substantially reduce the variance of the observed data, (2) there is no consistent trend in the slopes of the regression lines between the various data groups, and (3) a range-independent model will result in simpler design procedures.

2. ***Separate Load Factors for Surface Tangent and Half-Buried Bursts.*** Separate prediction error models for surface tangent (Groups I and III) and half-buried (Groups II and IV) bombs are recommended. Although the prediction error variabilities for these two bomb classifications are quite similar, significant differences have been detected in the mean prediction errors. The larger mean prediction errors for the half-buried data indicates that the 50 *percent* reduction in effective explosive weight for these predictions is unconservative. Therefore, larger reliability-based load factors for incident airblast from half-buried bombs are required to provide reliability levels that are equivalent to the surface tangent airblast reliabilities.

3. ***Lognormal Model of Prediction Errors.*** The statistics for both peak pressure and positive impulse support the use of lognormal prediction error models. For pressure, the computed p-values shown in Table II-4 give no indication that the lognormal hypothesis should be rejected. For incident impulse, the p-values for Group II and the combined data sets that include Group II suggest that the lognormal distribution should not be accepted. However, incident impulse Groups I, III, and IV do not fail the test for lognormality when taken individually or in combination. Based on the results for Groups I, III, and IV, the lognormal model for incident impulse is used to develop the RBDFs.

From the statistics of the surface tangent and half-buried bomb data sets, separate model parameters for pressure and impulse prediction error are given in Table II-7. The models are completely defined by the mean and cov statistics, along with the assumption of lognormality (see Recommendation 3, above). Using these inputs, derived logarithmic means and standard deviations are also given in Table II-7. Using the lognormal model parameters, incident airblast load factors can be computed by

$$\xi(R) = \exp[\mu_{\ln} + \Phi^{-1}(R)\sigma_{\ln}] \qquad \text{(II-5)}$$

where R is the desired reliability level, Φ is the standard unit normal function, and $\mu_{\ln}$ and $\sigma_{\ln}$ are the logarithmic mean and standard deviation, respectively. Airblast load factors computed using Equation (II-5) appear in Table II-8 for several commonly used reliability levels. The load factors are applied directly to the *PCDM* predictions for a given range and explosive weight. For example, multiplying the *PCDM* prediction for positive pressure by 1.55 produces a factored incident pressure that is exceeded by approximately 5 *percent* of the surface tangent CHEBS observations.

TABLE II-7. INCIDENT AIRBLAST UNCERTAINTY MODEL.

Model Parameters	Surface Tangent		Half-Buried	
	Pressure, ξ_P,	Impulse, ξ_i,	Pressure, ξ_P,	Impulse, ξ_i,
Mean, μ	1.00	1.15	1.15	1.20
cov, $\delta = \sigma/\mu$	0.30	0.25	0.30	0.25
Logarithmic Mean, $\mu_{\ln}$	-0.0431	0.1094	0.0967	0.1520
Logarithmic Standard Deviation, $\sigma_{\ln}$	0.2936	0.2462	0.2936	0.2462

5. Incident Airblast Comparison

The incident airblast prediction model is compared to an independent set of incident pressure and impulse data in Figure II-8. The box plots shown in Figure II-8 illustrate the spread of the experimental data in terms of minimum, maximum, and quartile values. The experimental data were obtained in half-scale tests of vertical, surface tangent, cylindrically cased explosives [Coltharp, *et al.*, 1985]. The data consist of 12 pressure observations and 10 impulse observations. The box plots of the observed data agree reasonably well with the factored airblast

TABLE II-8. INCIDENT AIRBLAST RELIABILITY-BASED LOAD FACTORS.

Reliability	Load Factor			
	Surface Tangent		Half-Buried	
	Pressure	Impulse	Pressure	Impulse
0.05	0.59	0.74	0.68	0.78
0.10	0.66	0.81	0.76	0.85
0.25	0.79	0.94	0.90	0.99
0.50	0.96	1.12	1.10	1.16
0.75	1.17	1.32	1.34	1.37
0.90	1.40	1.53	1.60	1.60
0.95	1.55	1.67	1.79	1.75
0.99	1.90	1.98	2.18	2.06

predictions. The unfactored predictions given by Coltharp, *et al.* [1985] were an incident pressure of 5.62 *MPa* and an incident impulse of 0.56 *MPa-ms*.[1] The load factors in Table II-8 for incident airblast due to surface tangent, cased explosives are used to factor the predicted airblast loads. For example, the 75 *percent* reliability prediction for incident impulse is 1.32 × 0.56 *MPa-ms*, or 0.74 *MPa-ms*.

C. PREDICTION ERRORS IN REFLECTED AIRBLAST PARAMETERS

The prediction error models generated from the statistical analysis of the CHEBS test data provide a rational basis for estimating the uncertainties in predicting peak overpressures and incident impulses for cased, general-purpose bombs. However, the loading parameters that directly impact the analysis of aboveground structures are reflected pressure and impulse. To our knowledge, there are no comprehensive data sets of normally reflected pressure and impulse observations for full-scale, non-idealized bomb threats. However, it is still possible to develop preliminary estimates of reflected airblast uncertainties for realistic bomb threats based on the uncertainties observed in idealized, bare charge bomb tests. By comparing the variability in incident and reflected airblast data obtained in controlled experiments and combining this information with the additional uncertainties observed in the CHEBS incident airblast data, we are able to make inferences on the uncertainties associated with the *PCDM* reflected airblast predictions when designing for realistic bomb threats.

[1]These predictions were made using the hemispherical surface burst polynomials recommended in the *PCDM*. However, casing corrections were made by Coltharp, *et al.* in determining the effective explosive weight. Since the actual explosive weight is not reported, we were unable to make our own *PCDM* predictions omitting the casing correction factors. Based on the small casing correction factors and the airblast predictions given in the report, we estimate that the casing corrections used by Coltharp, *et al.*, reduced the pressure and impulse predictions by 2 *percent* and 9 *percent*, respectively. Thus, the airblast prediction box plots could be shifted upward by these amounts to account for the differences in the prediction techniques.

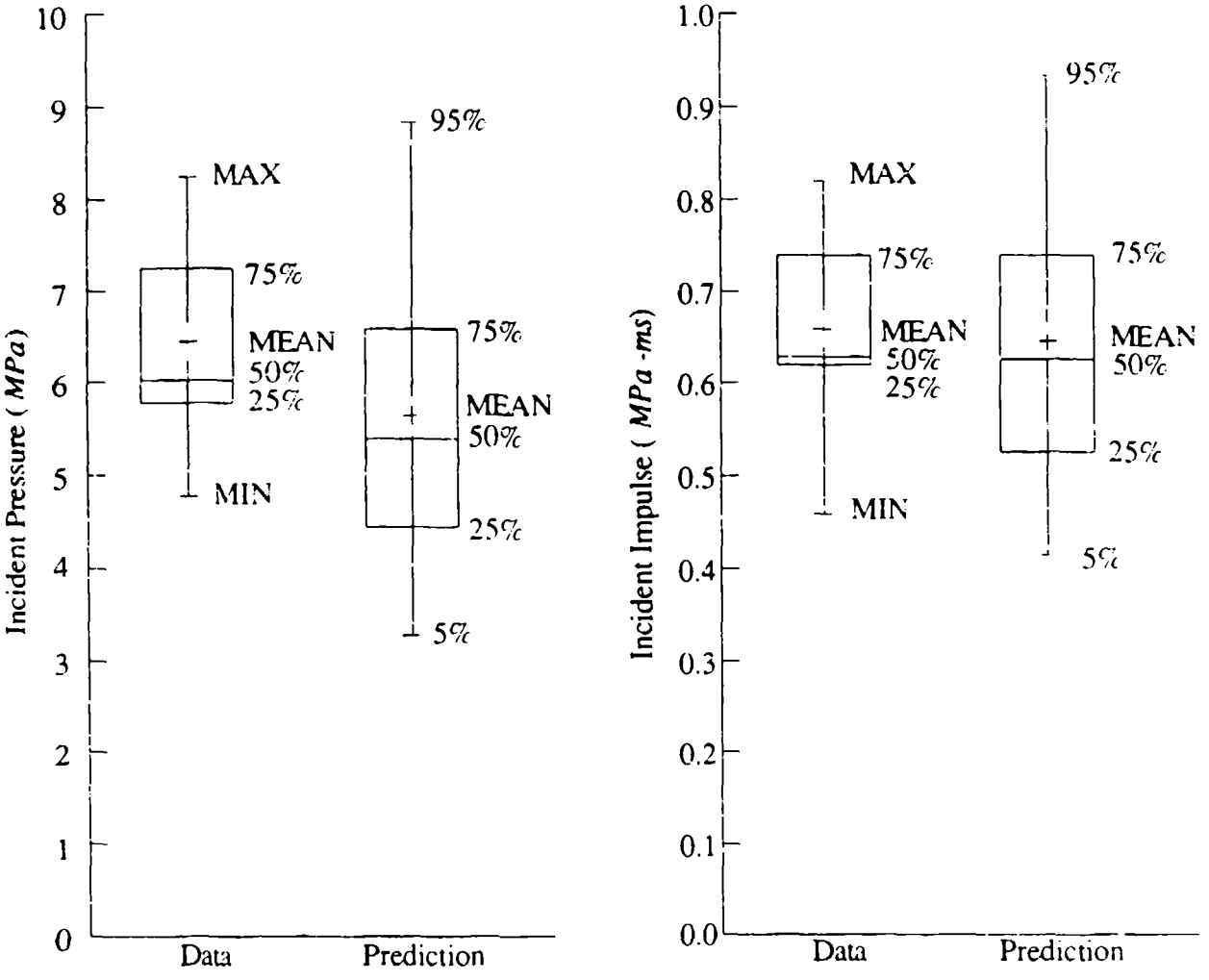

Figure II-8. Incident Airblast Observations from Coltharp, *et al.* [1985] *vs.* Predictions for Various Reliability Levels.

1. Normally Reflected Airblast Prediction Error Model

A large database of observations compiled by Goodman [1960] is available for comparing the uncertainties in incident and normally reflected airblast due to idealized bomb threats. All of the data is for bare pentolite spheres exploded in air. The data compiled by Goodman consists of means and standard deviations for groups of tests performed at different scaled ranges. Prediction error ratio statistics for each data group have been computed using the free airburst parameter prediction equations given in *PCDM* Appendix IV-1. To be consistent with the incident airblast models developed in Section II.B, a range independent prediction error model is assumed. Range-independent prediction error statistics are given in Table II-9. The basic variabilities (*i.e.*, standard deviations or coefficients of variation) represent a combination of the scatter observed within each data group and the group-to-group scatter of the individual mean prediction error ratios. The covs for both incident and reflected airblast are in the 10 *percent* to

TABLE II-9. AIRBLAST PREDICTION ERROR STATISTICS FOR FREE-AIR, BARE, SPHERICAL PENTOLITE.[a]

	Peak Pressures		Positive Impulse	
	Incident	Reflected[b]	Incident	Reflected
Pentolite to TNT factor	1.38	1.38	1.14	1.14
Scaled Ranges ($ft/lb^{1/3}$)	0.48-7.88	1.42-9.30	0.18-22.8	0.42-21.4
Number of Data	1153	169	715	997
Mean Prediction Error	0.929	0.847	0.914	0.981
Prediction Error Std. Dev.	0.098	0.133	0.131	0.142
Prediction Error COV (*percent*)	10.6	15.6	14.3	14.5

[a] Based on airblast data compiled by Goodman [1960].

[b] The 87 reflected pressure data points reported in [Goodman, 1960] have been supplemented with 82 scaled observations from bare spherical pentolite tests conducted at ambient pressures of 0.3 and 0.1 atmospheres [Jack and Armendt, 1965].

15 *percent* range for the bare spherical pentolite data. Recall that the covs selected in Section II.B for incident pressure and impulse due to realistic bomb threats were 30 *percent* and 25 *percent*, respectively. Therefore, the variability observed in tests using idealized explosives is approximately one-half of the variability observed in the realistic general-purpose bomb tests.

For the design of aboveground structures subjected to stand-off surface bursts, the hemispherical surface burst airblast curves of Kingery and Bulmash [1984] are recommended in the *PCDM* for predicting reflected pressures and impulses. One might expect that the basic variability in hemispherical surface burst prediction errors is similar to that observed in free-air spherical bursts. To verify this expectation, the prediction error ratios for a set of hemispherical surface burst incident and reflected airblast data [Hamilton, *et al.*, 1989] is compared to the free-air spherical burst prediction errors. Prediction error ratio statistics for the idealized hemispherical surface burst explosives are summarized in Table II-10.

TABLE II-10. INCIDENT AND REFLECTED AIRBLAST DATA FOR SURFACE BURSTS OF BARE C-4 HEMISPHERES.[a]

	Peak Pressures		Positive Impulse	
	Incident	Reflected	Incident	Reflected
C-4 to TNT factor[b]	1.28	1.28	1.28	1.28
Scaled Ranges ($feet/pound^{1/3}$)	4.0-21.0	4.0-30.0	4.0-21.0	4.0-30.0
Number of Data	21	57	21	57
Mean Prediction Error	0.974	0.902	0.776	0.915
Prediction Error Std. Dev.	0.196	0.150	0.089	0.109
Prediction Error COV (*percent*)	20.2	16.6	11.5	11.9

[a] Based on data reported in [Hamilton, *et al.*, 1989]

[b] *PCDM* equivalent TNT factors for C-4 are 1.37 for pressure and 1.19 for impulse. The factor used here (1.28) is "an average factor which is widely accepted" [Hamilton, *et al.*, 1989].

In spite of a considerable difference in the ranges of standoffs covered in the two data sets, the reflected airblast prediction error standard deviations for the hemispherical C-4 surface bursts (Table II-10) are, in fact, similar to those of the free-air spherical pentolite tests (Table II-9). Therefore, based on the experimental data analyzed in this effort, we conclude that the basic uncertainties in the reflected airblast predictions for hemispherical surface bursts are similar to those of spherical free-air bursts. In addition, the similarity between incident airblast covs and normally reflected airblast covs within both the free-air spherical pentolite tests and the surface tangent hemispherical C-4 test indicates that the process of reflecting the blast wave does not significantly affect airblast prediction uncertainties.

To assess the uncertainties in the *PCDM* predictions for reflected airblast resulting from realistic bombs, it is useful to compare the incident airblast prediction error ratio statistics for idealized and realistic bombs. The "idealized" and "CHEBS" statistics given in Table II-11 have been extracted from Tables II-9 and II-4 respectively. Again, the substantial increase in variability between idealized bomb tests and realistic bomb tests is noted.

TABLE II-11. COMPARISON OF IDEALIZED INCIDENT AIRBLAST STATISTICS AND THE SURFACE TANGENT CHEBS STATISTICS.

	Incident Pressure		Incident Impulse	
	Idealized[a]	CHEBS[b]	Idealized[a]	CHEBS[b]
Mean Prediction Error	0.929	0.974	0.914	1.142
Prediction Error Std. Dev.	0.098	0.292	0.131	0.272
Prediction Error cov (*percent*)	10.6	30.0	14.3	23.8

[a] Free-air, bare, spherical pentolite data.
[b] Surface tangent CHEBS data (*i.e.*, Groups I and III).

Although it is possible to eliminate the prediction error biases by improving the accuracy of the *PCDM* prediction curves, corrections to the prediction curves would not change the scatter of prediction errors about their mean. Therefore, the standard deviations listed above are equal to the covs which would be obtained if the prediction curves were unbiased (*i.e.*, if $\bar{\xi} = 1$). Thus, for the following calculations, the covs are taken to be the standard deviations given in Table II-11.

In an attempt to estimate the overall prediction error uncertainty for reflected airblast, we assume that the uncertainties in the *PCDM* prediction can be divided into two independent components: (1) the basic variability in predicting airblast for idealized bombs, and (2) the additional variability due to non-ideal bomb configurations (*i.e.*, casing, geometry, etc.). If we also assume that the reflected airblast prediction errors are lognormally distributed (which is consistent with the incident airblast model) then the total cov for reflected airblast of realistic bombs, δ_t, can be approximated as

$$\delta_t^2 \equiv \delta_i^2 + \delta_n^2 \qquad \text{(II-6)}$$

where δ_i is the idealized bomb airblast cov (*i.e.*, bare pentolite sphere) and δ_n is the cov associated with nonideal bomb effects (*i.e.*, casing, bomb geometry, etc.). Using Equation (II-6) and the incident airblast data in Table II-11, δ_n for incident pressure and impulse can be directly computed. If we further assume that the effects of nonideal bombs on reflected airblast uncertainty are the same as the effects of nonideal bombs on incident airblast uncertainty, δ_n can be combined with the δ_i for reflected airblast (see Table II-9) to give an estimate of the overall uncertainty in predicting reflected airblast. The resulting covs are summarized in Table II-12.

TABLE II-12. OBSERVED AND DERIVED COVS FOR INCIDENT AND REFLECTED AIRBLAST.

	Peak Pressures		Positive Impulse	
	Incident[a]	Reflected[b]	Incident[a]	Reflected[b]
δ_t	0.292	0.305	0.272	0.277
δ_i	0.098	0.133	0.131	0.142
δ_n	0.275	0.275	0.238	0.238

[a] For incident airblast, δ_n is computed using Equation (II-6).

[b] For reflected airblast, δ_n is assumed to be the same as the incident δ_n , and δ_i is computed using Equation (II-6).

The empirical derivation of the reflected airblast variabilities reveals that the overall airblast uncertainty is dominated by the uncertainty associated with nonideal bomb effects. The basic reflected airblast uncertainties contribute very little to the overall uncertainty. Several factors contribute to the substantial increase in airblast uncertainty when comparing realistic weapons to idealized explosives. The majority of additional variability observed in the realistic bomb tests can be attributed to casing effects and the effects of cylindrical bomb geometry. Another contributing factor is the uncertainty associated with the equivalent TNT weights used in the prediction methodology.

Although estimates of the variability in reflected airblast have been made in this section, the lack of reflected airblast data for realistic bombs prevents the evaluation of biases that may be present in the *PCDM* reflected airblast prediction methodology. The data in Tables II-9 and II-10 indicate that the *PCDM* method is moderately biased towards overpredicting incident and reflected airblast produced by spherical or hemispherical uncased explosives. However, the incident airblast data for realistic bombs analyzed in Section II.B demonstrate that the mean prediction error, like the prediction error variability, is sensitive to casing effects, bomb geometry effects, and other non-ideal bomb factors. In fact, the incident airblast mean prediction error ratios for realistic bombs are all greater than or equal to one (*i.e.*, the *PCDM* methods are not conservative for incident airblast due to realistic bombs). Therefore, the *PCDM* may also be somewhat unconservative for predicting reflected airblast from realistic bombs. The possibility of such a bias should be investigated in future conventional weapon tests.

2. Normally Reflected Airblast Summary and RBDFs

Accurate estimates of both the mean prediction error and the prediction error variability are required to develop RBDFs for normally reflected airblast. Since we were unable to identify any definitive data for the mean normally reflected airblast prediction error for realistic bombs within the scope of this effort, we assumed that the *PCDM* methodology is unbiased. With this major assumption in mind, our conclusions for reflected airblast RBDFs are stated below:

1. ***Uncertainties in Bare Charge Incident and Reflected Airblast.*** For the idealized free-air spherical pentolite explosives, the basic uncertainty in reflected airblast is similar to the uncertainty in incident airblast.

2. ***Nonideal Bomb Effects Dominate Incident Airblast Uncertainty.*** The uncertainty in incident airblast predictions for realistic bombs is dominated by non-ideal bomb effects such as casing and bomb geometry. The basic uncertainty observed in the idealized explosives due to factors such as random fluctuations in the explosive yield contributes very little to the overall uncertainty in predicting incident airblast for realistic bombs.

3. ***Assumption for Reflected Airblast.*** Based on the similarities between incident and reflected airblast uncertainties for idealized bomb tests, it is assumed that the uncertainties related to non-ideal bomb effects for reflected airblast are also similar in magnitude to those observed in incident airblast. Thus, the overall uncertainties in reflected airblast are dominated by the same nonideal bomb effects that dominate the incident airblast uncertainties.

4. ***Preliminary RBDFs Assume Unbiased PCDM.*** Assuming that the idealized airblast prediction uncertainty and the uncertainty due to nonideal bomb effects are independent and lognormally distributed, Equation (II-6) can be used to combine these uncertainties to obtain estimates of the overall reflected airblast variability. The overall covs are approximately 0.30 for both reflected pressure and impulse. A set of preliminary RBDFs for reflected airblast based on these covs, the lognormal distribution assumption, and the assumption that the *PCDM* method is median-centered is given in Table II-13.

5. ***Additional Work Needed.*** The difficulties encountered in developing prediction error models for reflected airblast emphasize the need for realistic bomb reflected airblast data that is similar in quality and quantity to the CHEBS incident airblast data. The first task is to identify any existing data not considered in this effort. A centralized conventional weapons effects database would significantly reduce the possibility of overlooking existing data sources. If, in fact, there is not adequate existing data, additional work is needed to improve the database. In order to cost effectively build an experimental database of normally reflected airblast observations for nonideal weapons, it is important to obtain multiple data points from each shot. For example, several rigid stagnating walls, each fit with several pressure transducers, could be laid out along different radials to maximize data collection, similar to the CHEBS side-on transducers (see Figure II-1). Another alternative is to propagate uncertainties through a first principles airblast diffraction model. However, the ability to model nonideal bomb effects (*i.e.*, casing

TABLE II-13. PRELIMINARY NORMALLY REFLECTED AIRBLAST RELIABILITY-BASED LOAD FACTORS.

Reliability	Preliminary Load Factors for Normally Reflected Pressure and Impulse
0.05	0.61
0.10	0.68
0.25	0.81
0.50	1.00
0.75	1.22
0.90	1.47
0.95	1.64

corrections, geometry corrections, etc.) may govern the accuracy of an analytical approach.

3. Comparison to Independent Data

The preliminary normally reflected airblast prediction model is compared to an independent set of reflected pressure and impulse data in Figure II-9. The data consist of 12 reflected pressure observations and 7 reflected impulse observations reported by Coltharp, *et al.* [1985]. The incident airblast data from these experiments were compared to the incident airblast model in Section II.B.5. The reflected airblast measurements from these tests were recorded by gages mounted on a half-scale aboveground structure subjected to a cylindrically cased explosive. Only data from the gage at the bottom centerline of the wall and from the gages immediately adjacent to the bottom centerline gage are included in the data shown in Figure II-9. The agreement between the factored *PCDM* airblast predictions and the observed data is acceptable; however, the predictions tend to underestimate the data scatter. The increased scatter in the observed data may be attributable to experimental error. Acquiring accurate reflected airblast measurements at the bottom of a wall is typically very difficult. In six Series I tests, only 8 of 24 potential reflected pressure data points were considered valid, and only 3 of 24 possible reflected impulse data points were obtained. Given the high failure rate of the gages at or adjacent to the bottom centerline of the wall, it is probable that experimental error was a significant factor in the scatter of the observed data. Further research is needed to assess experimental error and to increase the pool of reflected airblast observations.

4. Non-Normally Reflected Airblast

Section IV.B.3 of the *PCDM* provides some guidance on predicting non-normally reflected pressures and impulses; however, *PCDM* Section VIII ("Loads on Structures") does not give a specific methodology for computing other than normally reflected airblast loads. To simplify the design process, the *PCDM* permits designers to conservatively assume that the incident overpressure is fully reflected at every point on the wall that is directly exposed to the blast. This assumption can be overly conservative for close-in blasts because the blast wave angle

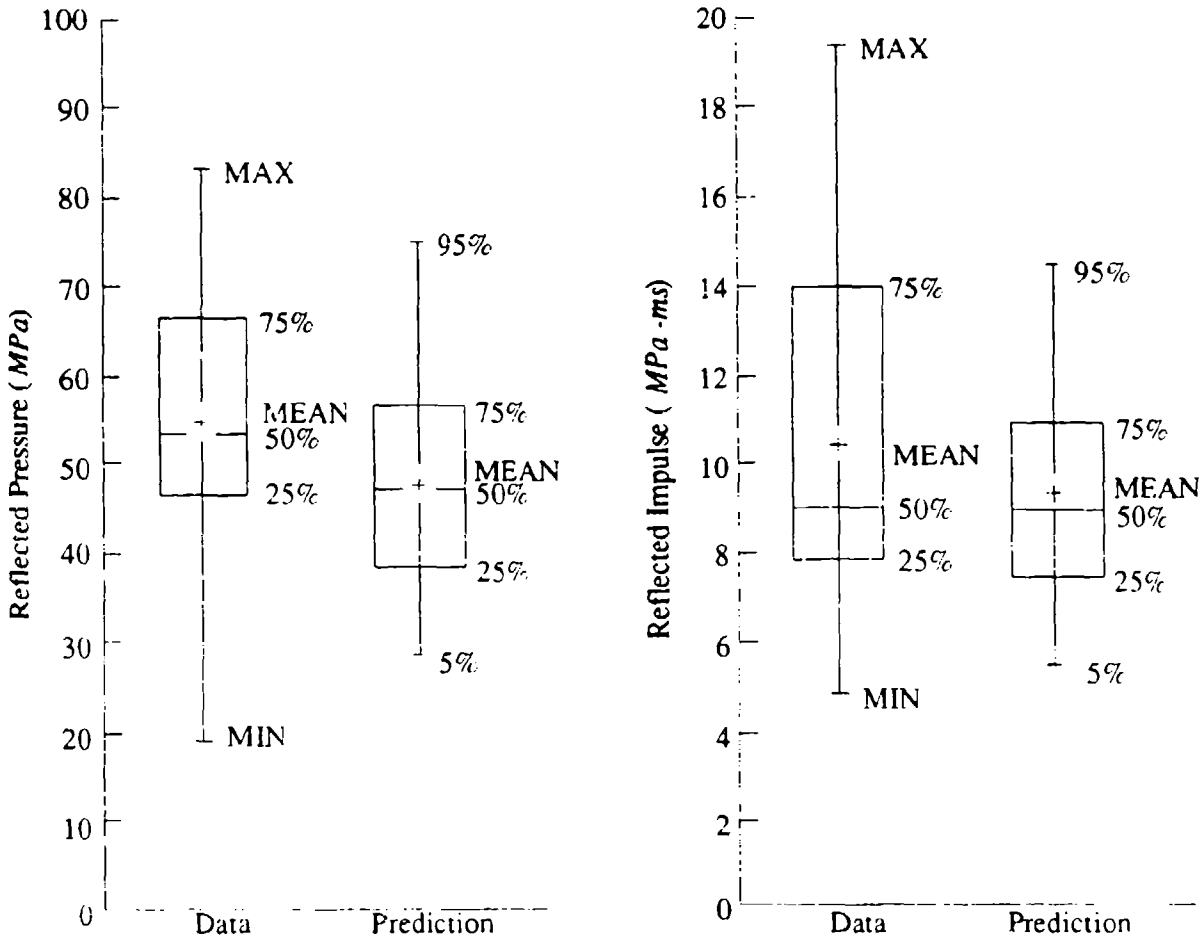

Figure II-9. Reflected Airblast Observations from Coltharp, *et al.* [1985] vs. Predictions for Various Reliability Levels.

of incidence is significantly less than 90 *degrees* over large portions of the wall surface. In addition to nonnormal reflection of the incident airblast, the actual loads may be further reduced near the free edges of the wall where the clearing time is short enough to prevent complete reflection of the airblast.

To illustrate these effects, data from the half-scale aboveground structure tests [Coltharp, *et al.*, 1985] are again considered. Figure II-10 shows the mean reflected airblast *PCDM* prediction error ratios (assuming normal reflection) for the Series I tests. Except at the gage on the bottom centerline of the wall and at the gages immediately adjacent to it, the *PCDM* methodology significantly overpredicts the reflected airblast at all of the remaining locations (*i.e.*, $\xi < 1$) even though the increased range to these gages has been taken into consideration. Note that the gages highest up on the wall have the greatest overpredictions. In addition to nonnormal reflection and clearing time effects, these gages also experience less reflected airblast loads because they are located nearest to the "tail" region of the cylindrically shaped, cased explosives.

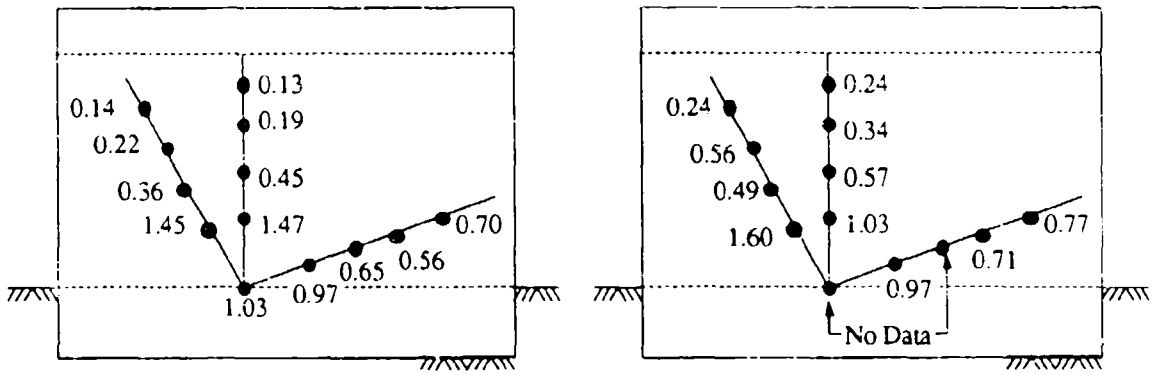

a. Peak Pressure

b. Impulse

Figure II-10. Mean Reflected Airblast Prediction Error Ratios.

Given the large bias towards overpredicting non-normally reflected airblast loads from realistic bombs close to aboveground walls, the development of a prediction error model for the *PCDM* methodology is not justified. Additional research is needed to accurately quantify the multiple sources of reflected airblast load prediction bias for arbitrary points on an aboveground structure wall. This research can be done in coordination with the development of PC-based CWE loading and response models and in coordination with the planning of experiments designed to assess 2-D and 3-D loading effects. Prediction error models can then be derived that are appropriate to the level of loading detail considered in future design manuals.

D. ABOVEGROUND WALL FLEXURAL RESPONSE

In this section, we investigate the prediction errors associated with the *PCDM* methodology for estimating peak flexural response of an aboveground structure wall subjected to a standoff surface burst from a fragmenting weapon. We do not derive RBDFs for aboveground structural response because: (1) significant conservative biases appear to be present in the *PCDM* methodology; (2) fundamental changes to the *PCDM* procedure were not practical and were beyond the scope of this effort; and (3) given the scale of these biases, the database of well-instrumented aboveground structure tests that we were able to identify within the scope of this task was not sufficient to work around the *PCDM* method in order to accurately quantify each potential source of error and uncertainty. However, we do examine experimental data from a recent series of aboveground tests and perform a preliminary sensitivity analysis of the sources of prediction or bias and uncertainty. The sensitivity studies are intended to identify research areas that can be expected to provide the best payoffs in terms of reducing prediction error bias and uncertainty. The results of these studies provide guidance for the future development and improvement of both deterministic and reliability-based structural response models.

1. Experimental Data

Prediction error ratios for the peak response of several half-scale aboveground reinforced concrete structure tests are given in Table II-14. In these tests [Coltharp, *et al.*, 1985], the front walls of the structures were subjected to identical, cylindrically cased, half-scale explosives. The response of each wall to the combined airblast and fragmentation loads was primarily a one-way slab inelastic bending mode. SDOF impulsive response prediction error ratios based on *PCDM* Equation (X-34) are tabulated for three different loading conditions: (1) observed reflected impulses obtained from the vertical center strip of the wall (directly opposite the bomb); (2) impulsive loads (derived according to *PCDM* Example VIII-1) applied vertically along the center strip of the wall; and (3) two-way *PCDM*-type loads that include reductions in the airblast intensity for load variations in the horizontal direction (due to increased range) and for non-normal reflection (based on *PCDM* Figure IV-11). For each loading condition, wall deflections are computed for the combined impulse due to airblast and fragmentation. Because fragmentation impulse data is not available for these tests, the fragmentation impulse has been estimated using the procedure given in the *PCDM* Section VI.C. In all cases, the loads have been transformed into equivalent uniform loads in accordance with the simplified SDOF analysis procedure given in *PCDM* Section X.B.

TABLE II-14. ABOVEGROUND WALL DEFLECTION PREDICTION ERROR.

Test	Reinforced Steel (*percent*)	Observed Deflection (*in*)	Prediction Error Ratios[a]		
			Observed Airblast Loads[c]	*PCDM* Airblast Loads[c]	2-D Airblast and Fragment Loads[b,c]
I6	0.25	1.46	0.39	0.25	0.36
II5	0.25	1.75	0.52	0.29	0.43
II9	0.25[d]	0.95	0.45	0.16	0.23
I2	0.50	0.91	0.54	0.30	0.44
II4	0.50	0.79	0.19	0.26	0.38
I1	1.00	0.61	0.82	0.37	0.55
Prediction Error Statistics		Mean	0.49	0.27	0.40
		COV (*percent*)	43	26	26

[a] Observed/Predicted Deflection.
[b] Includes reductions in airblast intensity due to increased range away from the center-strip and a reduction for non-normal angles of incidence.
[c] All fragmentation loads are estimated using *PCDM* procedures.
[d] Closed stirrups, all other walls have open stirrups for shear reinforcing.

For each of the three loading cases, the *PCDM* SDOF impulsive response model significantly overpredicts the observed wall deflections (*i.e.*, $\xi << 1$). The mean overpredictions range from a factor of approximately two when the observed airblast loads are used to a factor of about four when the one-way *PCDM* airblast loads are used. The increase in mean prediction error from a factor of two to a factor of four implies that a significant portion of the prediction error bias

can be attributed to the conservatisms of the *PCDM* airblast loads model (see Section II.C.4). This result emphasizes the need for actual loads data to separate the structural response uncertainties from the load prediction uncertainties. However, even with the use of observed airblast loads, the *PCDM* predictions are still conservative by a factor of two, and the prediction error ratio covs increase from 26 *percent* to 43 *percent* when the observed loads are used to predict the response. Random fluctuations in the limited number of airblast gage readings have a significant impact on the prediction error variability because the peak wall deflection depends on the square of the applied impulse.

The prediction error ratio statistics from the half-scale aboveground structure tests provide some insight into the sources of bias and uncertainty for aboveground structural response. However, due to the large prediction biases, it is not practical to develop RBDFs for aboveground wall flexural response. The following subsections discuss these sources of bias and uncertainty and present a preliminary sensitivity study to rank their relative importance.

2. Sources of Uncertainty

For an equivalent elasto-plastic SDOF system, the maximum deflection due to an impulsive load is given by *PCDM* Equation (X-34):

$$u_{max} = \frac{1}{2}\left(\frac{I^2}{MR_m} + \frac{R_m}{k}\right) \tag{II-7}$$

where I is the applied impulsive load, k is the equivalent initial stiffness, M is the mass of the equivalent SDOF oscillator, and R_m is the equivalent maximum resistance. For the large ductilities commonly required of protective structures, the second term in Equation (II-7) is small compared to the first term (*i.e.*, the maximum response is much greater than the yield displacement). Therefore, the maximum displacement of the equivalent SDOF system is well approximated by

$$u_{max} \approx \frac{I^2}{2MR_m} \tag{II-8}$$

Neglecting the variability in mass, the SDOF response uncertainty depends primarily on the loads uncertainties (see Sections II.B and II.C) and the uncertainty in the maximum resistance. In addition, there are also fundamental uncertainties associated with the equivalent SDOF model. Therefore, for the development of aboveground structure response RBDFs, the major uncertainties can be classified into four groups: (1) airblast impulse, (2) fragmentation impulse, (3) resistance capacities of structural elements, and (4) SDOF dynamic response modeling. A brief summary of the factors that contribute to each of these major sources of bias and uncertainty is presented in the following paragraphs.

Airblast Impulse. Several factors contribute to the bias and uncertainty in the applied airblast impulse: (1) the basic uncertainty in estimating normally reflected airblast from nonidealized bombs (as discussed in Sections II.B and II.C); (2) the variation in reflected airblast

due to phenomena such as non-normal reflections, angle from the main bomb axis (*i.e.*, airblast reductions in the nose and tail regions), and edge effects (*i.e.*, clearing time); and (3) the effective width of the loaded area of the wall.

Fragmentation Impulse. Two basic components of the fragmentation impulse uncertainty are the fragment striking velocity and the assumed fragment spray pattern (*e.g.*, expanding cylinder or expanding sphere, which determines the mass of fragments per unit wall area). Additional sources of uncertainty in the fragmentation impulse are the effects of non-normal impacts, ricochets, fragment perforation, front face scabbing, and rear face spall. These sources of uncertainty are discussed in Section IV.C.

Structural Resistance. Bias and uncertainty in estimating the SDOF resistance function of an aboveground wall can be broken down into several components. Two sources of bias and uncertainty that are reasonably well understood are the use of nominal rather than actual (*i.e.*, "as built") material properties and the use of conservative dynamic increase factors when modeling the effects of high strain rates. Corrections for these sources of bias can be easily introduced into the SDOF impulsive response model. In addition, static load-displacement functions for protective structure walls are complicated by effects such as membrane action and partially restrained boundary conditions [Guice, 1986]. Membrane action can significantly enhance the maximum load capacity of deep beams that have fixed or nearly fixed supports. Because it is difficult to accurately estimate the increase in resistance, membrane action is conservatively neglected in the *PCDM*. Thus, biases in predicting the static strength of deep members could be corrected by developing design procedures that account for membrane action. However, any uncertainties in these procedures must also be reflected in the development of compatible reliability-based capacity reduction factors.

SDOF Response Model. The uncertainties related to the equivalent SDOF impulsive response model recommended in the *PCDM* arise from the dynamic response assumptions that are inherent to the simplified model — that is: (1) using a single displacement mode to characterize the wall response; (2) assuming that airblast and fragmentation loads are applied to the structure simultaneously and impulsively; and (3) approximating the best-estimate structural resistance function with a simple elasto-plastic resistance function and neglecting damping to permit the use of a simple energy-based solution.

3. Preliminary Sensitivity Study

In an effort to understand the relative importance of the sources of bias and uncertainty discussed in Section II.D.2, we perform a preliminary sensitivity study based on the first three half-scale tests listed in Table II-14 (*i.e.*, the three half-scale structures having 0.25 *percent* flexural reinforcing). The sensitivity of peak flexural response to uncertainties in airblast impulse and structural resistance is evaluated via Monte Carlo simulation. For this preliminary study, the *PCDM* fragmentation impulse and SDOF response models are assumed to be deterministic and unbiased.

Fragmentation impulse bias and uncertainty are not considered in the sensitivity study because a full fragmentation impulse uncertainty model is not available. Although we do develop an uncertainty model for fragment striking velocity in Section IV.C, there are several additional factors that may contribute significantly to the overall prediction error for fragmentation impulse: fragment spray pattern, non-normal impacts, ricochets, perforation, scabbing, and spall. Since we have not yet quantified these potential sources of bias and uncertainty, we proceed with the interim assumption that the *PCDM* fragment impulse model is unbiased and deterministic.

Bias and uncertainty in the *PCDM* SDOF response model are also not included in the preliminary sensitivity study since we have not developed a prediction error model for the SDOF approximation. The most promising approach for assessing SDOF model uncertainties is to compute detailed structural response predictions based on finite element computations and compare the results to the simple SDOF model. However, the detailed finite element computations required to assess SDOF model error are beyond the scope of this effort. Therefore, for the sensitivity study, we assume that the *PCDM* SDOF response model is deterministic and unbiased for a given set of input parameters.

Table II-15 summarizes the assumed distributions for the airblast and resistance uncertainties used in the sensitivity study. Each of the factors that contributes to airblast and resistance prediction error is assumed to be lognormally distributed. Errors in the *PCDM* airblast impulse model are modeled with three factors: (1) uncertainty in predicting normally reflected airblast impulse for real, cased weapons (Section II.C.2); (2) additional uncertainties due to non-normal reflection, clearing time effects, and polar angle effects (*i.e.*, reduced airblast in the nose and tail sectors of elongated, cylindrical explosives) (Section II.C.4); and (3) *PCDM* conservatism resulting from the use of center-strip loads rather than loads that vary along the length of the wall (Section II.C.4). The three sources of airblast prediction error are assumed to be multiplicative. The structural resistance prediction error model is also assumed to be composed of three multiplicative factors: (1) a correction factor for actual material strengths as compared to nominally specified strengths [*PCDM* Appendix IX-1]; (2) corrections in material properties for high strain rate effects (*i.e.*, dynamic increase factors) [*PCDM* Appendix IX-1]; and (3) increased resistance due to compressive and tensile membrane actions in deep flexural members [TM 5-855-1, 1984; Guice, 1986].

TABLE II-15. ASSUMED AIRBLAST AND RESISTANCE CORRECTION FACTOR PARAMETERS USED IN THE PRELIMINARY SENSITIVITY STUDY.

Error Source	Contributing Factors	Mean	Coefficient of Variation
Airblast Impulse	Cased Weapon, Normal Reflection	1.00	0.30
	Nonnormal Refl., Edge Effects, and Nose/Tail Sector Reductions	0.70	0.20
	Center Strip Loading Conservatism	0.95	0.10
Str. Resistance	Nominal *vs.* Actual Material Strength	1.18	0.08
	Dynamic Increase Factor (Strain Rate = 1 *inch/second/second*)	1.40	0.10
	Membrane Action (l/d=5.2)	1.50	0.30

The parameter estimates given in Table II-15 for the model correction factors are specific to the half-scale tests presently under consideration. Biases and uncertainties in the airblast loads and structural resistance function depend directly on the structure and standoff geometries. Therefore, the error models used in this sensitivity study are not universally applicable to arbitrary aboveground wall flexural response problems. Our purpose is to develop an understanding of the relative importance of airblast and resistance uncertainties and to lay the groundwork for more general reliability-based design procedures.

Using the estimated parameters given in Table II-15 and the *PCDM* SDOF impulsive response model, we have performed a series of Monte Carlo simulations to generate a cumulative distribution function (CDF) for peak flexural response of the half-scale walls. The CDF gives the probability that the peak response will be less than a given deflection. The CDF derived from the simulations and the observed peak deflections from the three half-scale tests are shown in Figure II-11. The observed peak deflections (0.95 *inch*, 1.46 *inches*, and 1.75 *inches*) fall at approximately the 20^{th}, 47^{th}, and 58^{th} percentiles of the simulated data. Thus, the experimental data tends to support our preliminary estimates of the *PCDM* airblast and resistance errors. The nominal *PCDM* peak deflection (5.95 *inches*) falls above the 98^{th} percentile of the simulated responses, demonstrating the conservatism of the *PCDM* model for this particular example.

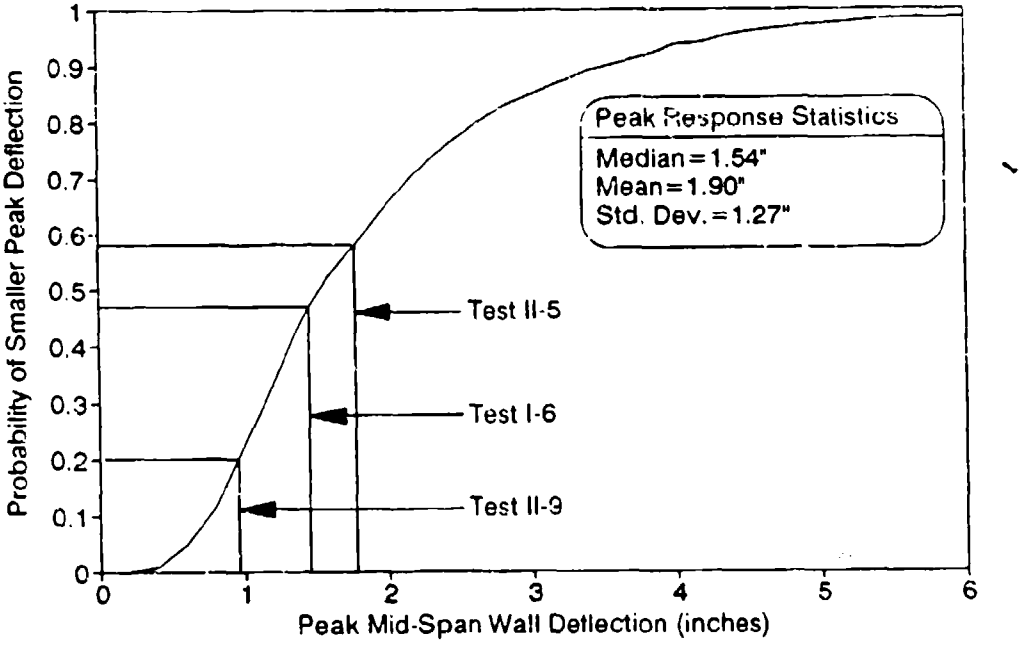

Figure II-11. Cumulative Distribution Function of Peak Flexural Response for Sensitivity Study Example Problem.

The parameters used in the simulations essentially eliminate all bias in the median peak response prediction. Recall that the overpredictions of the half-scale structure response given in Table II-14 ranged from factors of approximately two to four, depending on the assumed loading model. Based on this data and data reported by Guice [1986], a preliminary ranking of the

sources of bias and their possible influences on the peak response bias is given in Table II-16. As described in the "comments" column of the table, the *PCDM* airblast impulse methodology is more conservative as scaled range decreases, and the degree to which *PCDM* maximum resistance biases the peak response depends on the *l/d* ratio, the degree of fixity at the supports, and the flexural reinforcement ratio. Currently, response biases resulting from the *PCDM* fragmentation impulse model or the *PCDM* SDOF impulsive response model are thought to be secondary to the biases resulting from the airblast impulse and the maximum resistance. Although reliability-based analysis is useful for identifying these major sources of bias, the issue of improving the accuracy of the nominal *PCDM* response prediction is primarily a deterministic modeling problem that should be addressed in future updates to the *PCDM* structural response methodology.

TABLE II-16. PRELIMINARY PEAK RESPONSE BIAS RANKING.

Source of Bias	Possible Range of Bias	Comments
Airblast Impulse	1.0-2.5	Increases as scaled range decreases.
Maximum Resistance	1.0-2.5	Increases as *l/d* decreases. Also depends on support fixity and flexural reinforcement ratio.

To assess the relative importance of the airblast and resistance uncertainties, we also propagated the uncertainties for airblast and resistance through the Monte Carlo simulation model separately. The peak response uncertainties (*i.e.*, coefficients of variation) resulting from the combined and individual uncertainty simulations are summarized in Table II-17. The results indicate that airblast uncertainty has the more significant influence on the overall response uncertainty. The factors that contribute to airblast impulse uncertainty produce 82 *percent* of the total peak response uncertainty. The peak response uncertainty is very sensitive to the airblast uncertainty because peak response depends on the square of the airblast impulse and because there are substantial uncertainties involved in estimating the equivalent uniform airblast impulse. The dependence of the peak response uncertainty on the equivalent resistance function prediction uncertainties are also significant. The factors contributing to structural resistance uncertainty account for 51 *percent* of the peak response uncertainty. Thus, the preliminary sensitivity analysis indicates that additional data on airblast impulse loads for close-in, non-ideal bursts and the dynamic resistance of deep flexural members are needed to establish reliable prediction error models and to reduce response prediction uncertainty.

TABLE II-17. PRELIMINARY PEAK RESPONSE UNCERTAINTY RANKING.

Uncertainties Considered	Peak Response COV ($\delta_{u_{max}}$)	$\delta_{u_{max}}/\delta_{u_{max}}^{tota}$
Airblast and Resistance	0.67	1.00
Airblast Impulse Only	0.55	0.82
Resistance Only	0.34	0.51

We emphasize again that the fragmentation impulse and SDOF model error uncertainties have not been modeled in the preliminary sensitivity study. Uncertainties in fragmentation impulse prediction could have a particularly significant affect on the peak response uncertainty since peak response depends on the square of fragment impulse load and since the magnitudes of fragment impulses can be comparable to airblast impulses in many cases of interest. We also emphasize that additional research is required to substantiate the prediction error model parameter estimates given in Table II-15. Therefore, the bias and uncertainty rankings given in Tables II-16 and II-17 are only intended to suggest areas of research that may provide the best payoffs in reducing bias and uncertainty in flexural response predictions for aboveground structures.

4. Summary and Recommendations

The current *PCDM* methodology is overly conservative. The two largest sources of prediction error bias appear to be: (1) reflected impulse predictions (particularly for small standoffs), and (2) flexural load capacity predictions (particularly if significant membrane action is likely). More accurate prediction methods must be developed to eliminate excessive *PCDM* conservatisms before meaningful RBDFs can be developed. To maximize future research efforts, sensitivity studies (see Section II.D.3) should be periodically updated and refined to help identify and prioritize experimental and analytical research needs.

PCDM predictions should also be compared to sophisticated structural response model predictions (*e.g.*, finite element computations). This approach would permit the exclusion of all loading uncertainties from the analysis. Detailed structural resistance models generated with random material properties can be used to develop structural resistance prediction error models and reliability-based capacity factors. Prediction error models for simplified SDOF dynamic response modeling can also be developed via comparison to detailed response models.

Cost-effective development of RBDFs for aboveground structural response will ultimately require a combination of experimentally and computationally derived prediction error models. Therefore, future reliability-based design research on aboveground structural response should be closely coordinated with experimental planning and future improvements to the *PCDM* deterministic design and analysis procedures.

E. BREACH AND SPALL DAMAGE FROM CASED CHARGES — ABOVEGROUND STRUCTURES

For detonation close to an aboveground structure, a localized breaching failure mode can occur that differs from the flexural response mode considered in Section II.D. Spall, which is the ejection of concrete fragments from the inside face of the structure due to exterior blast and fragment effects, can also produce damage to interior equipment. Hence, as illustrated in the fault trees in Section VI, both breaching and spall are potential failure modes, in addition to overall structural response.

Breaching and spall failure modes are analyzed in the *PCDM* using empirical techniques developed by McVay [1988]. Since the empirical formulas (*PCDM* Equation (IX-2)) are derived using related data sets, we will develop the reliability-based design methodology for both failure modes concurrently. The analysis herein is for cased charges only.

Figure II-12 (*PCDM* Figure IX-2) shows the basis of McVay's empirical analysis procedures used in the *PCDM*. McVay reviews empirical spall prediction methods, noting disagreements among the prediction curves in TM5-855-1 and a set of curves by Basler [1982] and Hader [1983]. McVay conducted 40 new tests to augment the existing breaching/spall database. The No Damage - Spall - Breach areas in Figure II-12 were then drawn by eye. Based on the range of the data, McVay [1988] developed Table II-18 to show the range over which the procedures are valid. Most of these data are for scaled model tests and, as pointed out by McVay, model tests may suffer slightly less damage than full-scale tests due to strain rate effects.

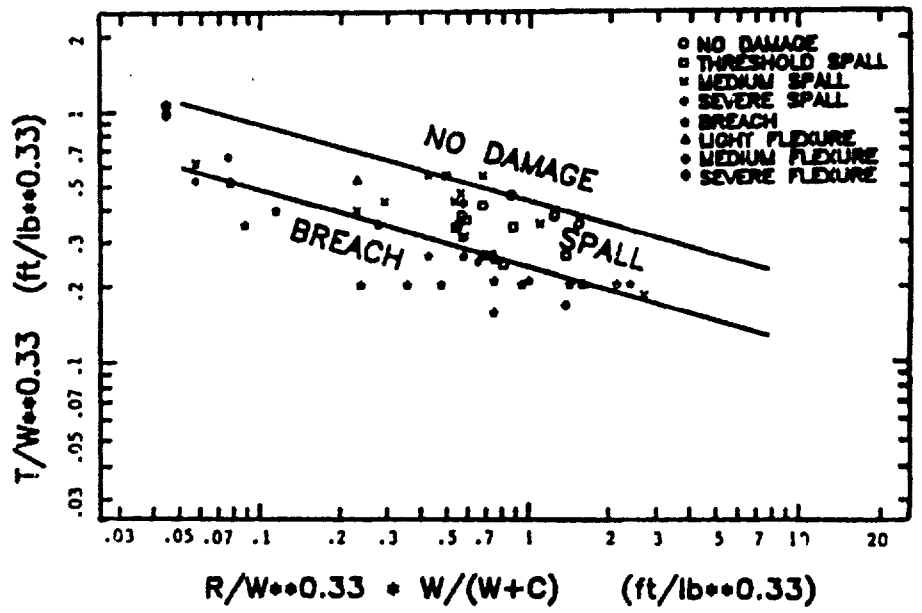

Figure II-12. Damage to Aboveground Walls Due to Standoff Cased Bombs [after McVay, 1988].

Using the *PCDM* approach, the designer can determine the wall thickness required to defeat breach and spall for a given weapon and standoff. The breach and spall thickness prediction equations (*PCDM* Equation (IX-2)) developed by McVay are:

$$\frac{t_b}{W^{1/3}} = 0.23 \left(\frac{R}{W^{1/3}}\right)^{-0.3} \left(\frac{W}{W+C}\right)^{-0.3} \qquad \text{(II-9)}$$

$$\frac{t_s}{W^{1/3}} = 0.43 \left(\frac{R}{W^{1/3}}\right)^{-0.3} \left(\frac{W}{W+C}\right)^{-0.3} \qquad \text{(II-10)}$$

TABLE II-18. RANGES OF PARAMETERS FOR DATA IN FIGURE II-12.

Parameter	Range	Recommended Use Range
Standoff distance	Contact to 30.0 *ft*	Contact to 7.5 *ft*
Equivalent TNT charge weight	0.824 to 2,299 *lbs*	0.824 to 220 *lbs*
Charge weight to charge plus casing weight	0.172 to 0.978	0.172 to 0.978
Scaled Standoff	0.077 to 12.06 $ft/lb^{1/3}$	0.077 to 5.00 $ft/lb^{1/3}$
Wall thickness	3.94 to 84.0 *in*	3.94 to 84.0 *in*
Scaled wall thickness	0.155 to 1.08 $ft/lb^{1/3}$	0.155 to 1.08 $ft/lb^{1/3}$
Static compressive strength of concrete	2,500 to 7,110 *psi*	2,500 to 7,110 *psi*
Principal steel ratio	0.11 to 1.34 *percent*	0.11 to 1.34 *percent*

where, t_b is the wall thickness to prevent breach (*feet*), t_s is the wall thickness to prevent spall (*feet*), W is the explosive weight (*pounds* TNT), C is the casing weight (*pounds*), and R is the bomb standoff (*feet*).

There are both systematic and random uncertainties associated with the *PCDM* empirical equations. The random uncertainty is visible in Figure II-12 as the data scatter about the prediction model (*i.e.*, the solid damage lines in the figure). Systematic uncertainty is a bias in the prediction method. For example, we note that in Figure II-12 spall damage is generally overpredicted (that is, design conservative) since there are many instances of no damage that fall below the no damage line. The reliability-based design method presented here quantifies and accounts for the systematic and random uncertainty associated with the test data shown in Figure II-12 and provides factors to be applied to the nominal wall thicknesses obtained using the *PCDM* empirically-based equations.[1]

1. Dichotomous Regression Formulation

The dichotomous regression technique [Cox and Snell, 1989; Hosmer and Lemeshow, 1989; Veneziano and Liao, 1984] is used to develop the reliability-based design method for spall and breach. Dichotomous regression fits a probability distribution to the data set using the method of maximum likelihood. Often, the logistic form is used as the probability distribution since it allows for a mathematically tractable treatment. The logistic form used here is

$$P_d(\underline{x}) = \frac{exp\,[G\,(\underline{x})]}{1 + exp\,[G\,(\underline{x})]} \qquad \text{(II-11)}$$

where P_d is the probability of damage; $\underline{x}$ is the set of problem parameters (*i.e.*, bomb and target descriptors); and the function $G\,(\underline{x})$ is a linear combination of given functions of the problem parameters, $\underline{x}$, *i.e.*,

[1]There is another source of systematic uncertainty due to the use of scale model test data that is not included. This additional systematic uncertainty can be quantified by theoretical analysis and comparison of scale model test results with other full-scale test data. Quantifying this source of systematic uncertainty is an important area of further research.

$$G(\underline{x}) = A_o + \sum_{i=1}^{n} A_i\, g_i(\underline{x}). \qquad \text{(II-12)}$$

Different logistic models correspond to different choices of the functions $g_1, g_2, \ldots g_n$, whereas the coefficients, $A_1, A_2, \ldots A_n$, are determined from the data. Two choices of G functions are discussed in the following paragraphs.

a. Generalized G Function

For breach and spall, the model parameters can be any physical or mechanical properties of the bomb and structure, *e.g.*, slab thickness, bomb weight, etc. To select a general form for the G function, we consider the empirical models given in the *PCDM* (Equations (II-9) and (II-10) herein). Based on these models the following G function is formulated

$$G = A_0 + A_1 \ln\left(\frac{t}{W^{1/3}}\right) + A_2 \ln\left(\frac{R}{W^{1/3}}\right) + A_3 \ln\left(\frac{W}{W+C}\right) \qquad \text{(II-13)}$$

where t is the wall thickness (*feet*), W is the explosive weight (*pounds TNT*), C is the casing weight (*pounds*), and R is the bomb standoff (*feet*). This G function will be called the general model, and it is applicable for both breach and spall (only the constants to be determined in Equation (II-13) change).

b. *PCDM* G Function

Simplified G functions, which directly use the empirical formulas given in the *PCDM*, were also postulated for breach and spall. The simplified G functions can be written as

$$G(t/t_b) = A_0 + A_1 \ln(t/t_b) \qquad \text{(II-14)}$$

$$G(t/t_s) = A_0 + A_1 \ln(t/t_s) \qquad \text{(II-15)}$$

where t_b and t_s are given by Equations (II-9) and (II-10), respectively. These functions allow a nondimensional prediction ratio of t/t_b or t/t_s to be formed similar to the prediction error models used in the airblast RBDF analysis. For these simplified models, the dichotomous regression procedure is not free to select independent coefficients for all of the parameters in the prediction equation. Hence, the simplified models will only work well if the *PCDM* method can accurately discriminate between survival and failure (breach or spall). The general model (Equation (II-13)) and the *PCDM* models (Equations (II-14) and (II-15) provide a starting point for the development of RBDFs for both breach and spall of aboveground structures using McVay's database (Figure II-12).

2. Parameter Estimation

The data in Figure II-12 were analyzed by assigning the eight damage states into dichotomous states for breach and spall analysis, *i.e.*, breach *vs.* no-breach and spall *vs.* no-spall.

In the analysis of spall *vs.* no-spall, the no-spall data include no damage and threshold spall; the spall data include medium spall, severe spall, and breach. In the analysis of breach *vs.* no-breach, the no-breach data include no damage, threshold spall, medium spall, severe spall, light flexure, medium flexure, and severe flexure; the breach data include only those cases where damage is reported as breach.

The SAS procedure LOGISTIC [SAS, 1990] is used to perform the maximum likelihood estimation of the G function parameters (*i.e.*, the dichotomous regression). Once the parameters are estimated, statistical measures are presented to quantify goodness of fit and compare the different models. Several measures can be used to quantify goodness-of-fit and to compare different models. The measures used in this study are defined below:

Percent Correctly Predicted (PCP). A data point $(\underline{x}_i, K_i)$ is said to be correctly predicted if failure occurs ($K_i = 1$) and $\hat{P}_d(\underline{x}_i) > 0.5$. Here, $\hat{P}_d(\underline{x})$ is given by Equation (II-11), with the parameters A_i estimated from dichotomous regression. The PCP statistic has an intuitive meaning; but it is not discriminating in model comparison because it depends only on the 0.5 contour line of $\hat{P}_d(\underline{x})$, not the entire $\hat{P}_d(\underline{x})$ function.

Likelihood Ratio Statistic (LR). The likelihood ratio statistic used here is the log ratio between the likelihood function of the model, $\hat{P}_d(\underline{x})$, obtained from dichotomous regression, and that of the model $\hat{P}_d(\underline{x}) = \exp(\hat{A}_0)/\{1 + \exp(\hat{A}_0)\}$, where $\hat{A}_0$ is the only parameter that is estimated from dichotomous regression. This statistic is given by

$$LR = 2[\ln L\ (\hat{A}_0,\ \hat{A}_1,\ldots,\ \hat{A}_k) - n_1 \ln n_1 - n_0 \ln n_0 + n \ln n] \tag{II-16}$$

in which n_1 and n_0 are the number of data records in the catalog that respectively have and have not failed, and $n = n_0 + n_1$. The function $L(\cdots)$ is the likelihood function

$$L\ (\hat{A}_0,\ \hat{A}_1,\ldots,\ \hat{A}_k) = \prod_{i=1}^{n} P_d(\underline{x}_i)^{K_i}(1 - P_d(\underline{x}_i))^{1-K_i} \tag{II-17}$$

and $\hat{A}_i$ are the estimated values of A_i. The larger *LR* is, the more "significant" the model is.

Akaike Information Criterion (AIC). This statistic is used for comparing different models for the same data. A lower *AIC* value indicates a better model. It is based on the likelihood functions of the different models but also accounts for the number of variables included in the predictive model. The *AIC* value is given as

$$AIC = -2 \ln L + 2(k + s) \tag{II-18}$$

where L is the likelihood function (defined above), k is the number of ordered values minus 1 for the response ($k = 1$ for binary response data as herein), and s is the number of model variables.

Schwartz Criterion (SC). This statistic is also used for comparing different models; a lower *SC* value indicates a better model. It is similar to the *AIC* measure but also accounts for the number of observations. The *SC* value is given as

$$SC = -2 \ln L + (k + s) \ln (n) \tag{II-19}$$

where L is the likelihood function (defined above), k is the number of ordered values minus 1 for the response ($k = 1$ for binary response data as herein), s is the number of model variables, and n is the number of observations.

Chi-Square Test for Covariates. This test is used to determine whether the model is statistically significant. It can be shown that -2 ln L (where L is the likelihood function) has a chi-square distribution under the hypothesis that all the model variables are zero (*i.e.*, the null hypothesis), with s degrees of freedom (where s is the number of model parameters). The chi-square statistic is computed as $2 \ln\left[L(\hat{A}_0, \hat{A}_1, \ldots, \hat{A}_k)/L(\hat{A}_0)\right]$. Thus, the chi-square statistic is the same as the likelihood ratio statistic when the model includes an intercept term (A_0). When the model does not include an intercept (*i.e.*, $A_0 = 0$) then the chi-square statistic differs from the likelihood ratio statistic in that the denominator of the chi-square statistic is taken as $L(0)$ (which is the same as Equation (II-16) with $n_0 = n_1 = n/2$).

Tables II-19 and II-20 show the estimated G functions for modeling breach and spall and the goodness-of-fit measures for each model. The first model (Generalized A) uses the functional form given by Equation (II-13), the second model (Generalized B) is the same as the first, but with A_0 fixed to equal 0.0; the third model (*PCDM* A) uses the simplified prediction G function (Equations (II-14) and (II-9) for breach, Equations (II-15) and (II-10) for spall), and the fourth model (*PCDM* B) is the same as the third but with A_0 fixed to equal 0.0.

3. Reliability-Based Design for Breaching

a. Breaching Model

From Table II-19, Model 4 (*PCDM* B) has the best goodness-of-fit statistics to the data set. Only the likelihood ratio statistic is better for Model 1. The Chi-Square test shows that Models 1, 3, and 4 are statistically significant. Based on the goodness-of-fit measures and a desire to develop a reliability-based model that is easy to apply and consistent with the *PCDM* deterministic models, we select Model 4 (the no-intercept, simplified model). Figure II-13 shows the logistic probability plot for this model. The data are plotted such that occurrence of breach is plotted as 1.0 and no occurrence is plotted as 0.0.

The ability of the Model 4 G function (and, therefore, the *PCDM* formula on which it is based) to discriminate breach and no-breach is evident from Figure II-13 since high G values almost always indicate breach and low G values almost always indicate no-breach. Furthermore, if Model 4 is algebraically expanded by substituting in the equation for t_b (*i.e.*,

TABLE II-19. G FUNCTIONS FOR MODELING BREACH DUE TO STANDOFF CASED BOMB AND ASSOCIATED GOODNESS-OF-FIT STATISTICS.[a]

Candidate Breach G Function Models				
Model 1 - Generalized A. $G(\underline{x}) = -1.68 - 11.2 \ln\left(\frac{t}{W^{1/3}}\right) - 3.24 \ln\left(\frac{R}{W^{1/3}}\right) - 4.00 \ln\left(\frac{W}{W+C}\right)$				
Model 2 - Generalized B. $G(\underline{x}) = +0.222 \ln\left(\frac{t}{W^{1/3}}\right) + 0.328 \ln\left(\frac{R}{W^{1/3}}\right) + 0.0191 \ln\left(\frac{W}{W+C}\right)$				
Model 3 - *PCDM* A. $G(\underline{x}) = +0.0234 - 11.6 \ln(t/t_b)$				
Model 4 - *PCDM* B. $G(\underline{x}) = -11.6 \ln(t/t_b)$				
Model	1	2	3	4
Intercept	Yes	No	Yes	No
Percent Correctly Predicted	83.3	61.7	85.0	86.7
Likelihood Ratio Statistic	41.0	-3.61	39.7	39.7
Akaike Information Criterion	43.1	86.0	40.6	38.6
Schwartz Criterion	51.8	92.3	44.8	40.7
Chi-Square	41.0	3.19	39.7	46.5
Pr > Chi-Square	0.0001	0.36	0.0001	0.0001

[a] Shading indicates best fit.

TABLE II-20. G FUNCTIONS FOR MODELING SPALL DUE TO STANDOFF CASED BOMB AND ASSOCIATED GOODNESS-OF-FIT STATISTICS.[a]

Candidate Spall G Function Models				
Model 1 - Generalized A. $G(\underline{x}) = -5.43 - 3.41 \ln\left(\frac{t}{W^{1/3}}\right) - 2.40 \ln\left(\frac{R}{W^{1/3}}\right) - 4.48 \ln\left(\frac{W}{W+C}\right)$				
Model 2 - Generalized B. $G(\underline{x}) = +0.266 \ln\left(\frac{t}{W^{1/3}}\right) - 0.995 \ln\left(\frac{R}{W^{1/3}}\right) - 2.13 \ln\left(\frac{W}{W+C}\right)$				
Model 3 - *PCDM* A. $G(\underline{x}) = -0.529 - 3.41 \ln(t/t_s)$				
Model 4 - *PCDM* B. $G(\underline{x}) = -2.47 \ln(t/t_s)$				
Model	1	2	3	4
Intercept	Yes	No	Yes	No
Percent Correctly Predicted	72.4	70.7	70.7	72.4
Likelihood Ratio Statistic	24.2	14.2	10.4	9.41
Akaike Information Criterion	53.9	61.9	63.8	62.8
Schwartz Criterion	62.2	68.1	67.9	64.8
Chi-Square	24.2	24.5	10.4	19.6
Pr > Chi-Square	0.0001	0.0001	0.0013	0.0001

[a] Shading indicates best fit.

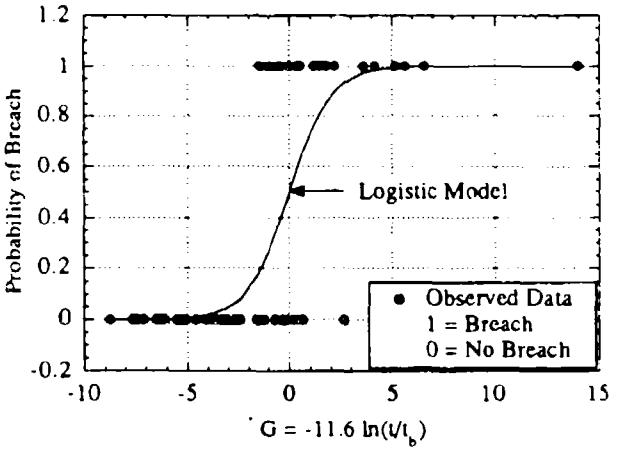

Figure II-13. Logistic Probability Model for Breach for Standoff Cased Bomb.

Equation (II-9)), it can be shown that the Model 4 G function and the Model 1 G function (the generalized model) are actually quite similar — that is, the generalized dichotomous regression gives a model that is similar to that given in the *PCDM*.

Because of the simplified analytical form of the logistic function and the use of the *PCDM* formulas as the basis for the RBD model, it is possible to derive a closed form expression for the design reliability that is a function of the wall thickness, t, and the *PCDM* design thickness, t_b. Given that all problem inputs are known (*i.e.*, R, W, C), the reliability of a wall of thickness t to resist breach from an aboveground standoff burst can be determined from:

$$R\,(t/t_b) = 1 - P_d\,(t/t_b) = 1 - \frac{exp\,[G\,(x)]}{1 + exp\,[G\,(x)]} = \frac{1}{1 + exp\,[G\,(x)]} \qquad \text{(II-20)}$$

$$= \frac{1}{1 + exp\,[\,-11.6\,ln\,(t/t_b)]}$$

$$= \frac{1}{1 + (t/t_b)^{-11.6}}$$

Using Equation (II-20), Table II-21 lists the reliability-based design factors, t/t_b and their associated reliabilities that account for the breach model error. We assume here that all of the model inputs (*i.e.*, R, W, C) will be specified for protective design with a specified threat. Thus, these variables are deterministic and only model error is considered in the reliability-based design at the *PCDM* level. Note that it is still possible to compute reliabilities for variable values of the weapon threat parameters in the event that a probabilistic threat criteria is considered.

b. Reliability-Based Design Breaching Example

The procedure for reliability-based design to prevent breach involves three simple steps:

TABLE II-21. RELIABILITY OF WALL THICKNESS TO PREVENT BREACH FROM A STANDOFF CASED BOMB.[a, b]

Reliability[c]	$P_d(x)$	G(x)	RBDF t/t_b
0.05	0.95	2.94	0.78
0.10	0.90	2.20	0.83
0.25	0.75	1.10	0.91
0.50	0.50	0.00	1.00
0.75	0.25	-1.10	1.10
0.90	0.10	-2.20	1.21
0.95	0.05	-2.94	1.29

[a] t_b as defined by Equation (II-9) (*PCDM* deterministic prediction method, *PCDM* Equation (IX-2)).

[b] *PCDM* deterministic method and RBDFs are based principally on data from scale model tests. Additional research is required to assess the systematic bias and additional uncertainty due to the use of scale model data.

[c] Assumes all inputs to Equation (II-9) are deterministic.

1. Compute the nominal thickness to prevent breaching using the *PCDM* formula, given as Equation (II-9), herein;
2. Select the desired reliability level for the design and the corresponding reliability-based design factor from Table II-21, or alternatively, use Equation (II-20);
3. Multiply the thickness computed in step 1 by the RBDF from step 2 to obtain the final design thickness.

This procedure is valid only for the ranges of applicability of the *PCDM* formula (see Table II-18). As an example, suppose that a wall is to be designed to resist breaching by a general purpose bomb burst at a scaled standoff of 1 *feet/pound*$^{1/3}$, that the charge weight is 175 *pounds* TNT, and the charge-to-weight ratio is 0.35. Based on the mission of the structure, the required design reliability for this threat is 90 *percent*. First, from Equation (II-9), the nominal thickness to prevent breaching is found to be approximately 21 *inches*. Next, from Table II-21 (or Equation (II-20)) we find that the RBDF for 90 *percent* reliability is 1.21. Thus, the nominal thickness of 21 *inches* is multiplied by 1.21 to obtain a design thickness for P_s = 0.90 of 25.4 *inches*.

4. Reliability-Based Design for Spall

For spall, Model 1 (generalized model with intercept) is the best considering the goodness-of-fit statistics in Table II-20; however, the candidate models are not as good as for breach.

Figures II-14, II-15, and II-16 show the logistic probability models and the spall data, for Models 1, 3, and 4, respectively. Comparing Model 1 with Model 4 (by substituting in the equation for t_s, *i.e.*, Equation (II-10)), we find that the exponents on scaled range and casing factor in the *PCDM* formula may be too small, and also that they should not be the same.

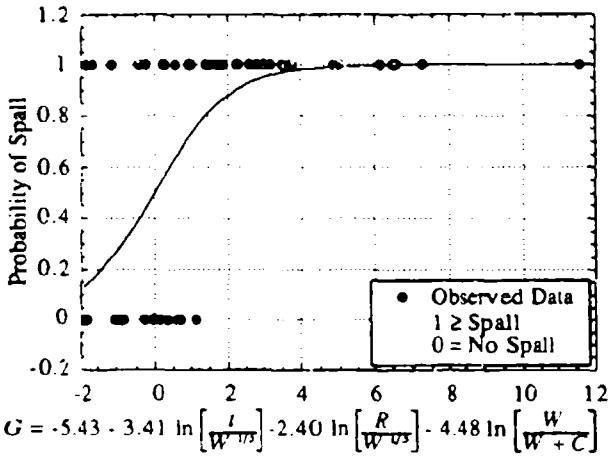

Figure II-14. Logistic Probability Model for Spall — Model 1 Generalized Dichotomous Regression.

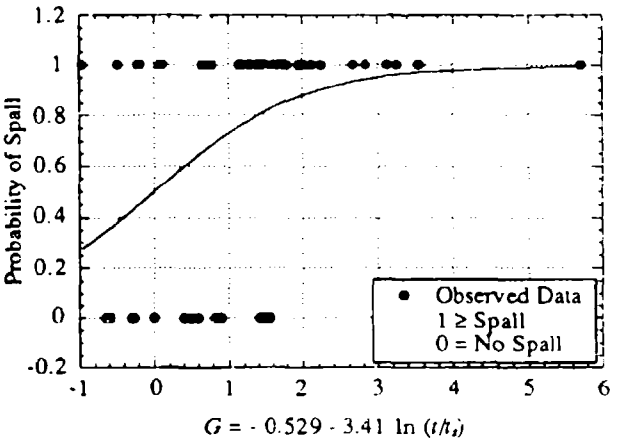

Figure II-15. Logistic Probability Model for Spall — Model 3 *PCDM*-based Model with Intercept.

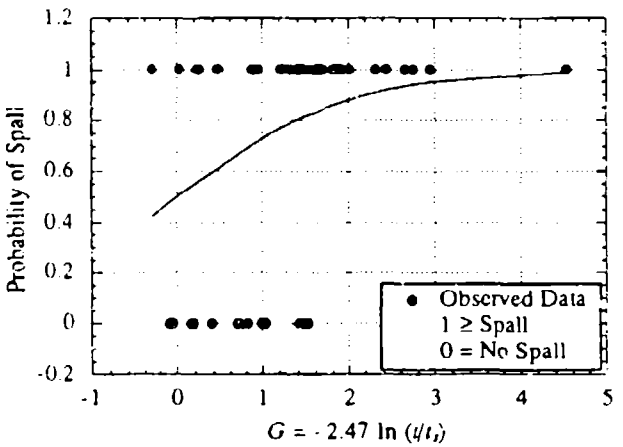

Figure II-16. Logistic Probability Model for Spall — Model 4 *PCDM*-based Model with Zero Intercept.

The conservatism of the *PCDM* formula can be seen in Figure II-16 where, without an intercept, spall probabilities of 0.50 to 0.80 are predicted for many tests that exhibited threshold spall or did not spall (note that threshold spall is considered here as no-spall). The poor ability of the *PCDM* formula to discriminate the spall data is also evident in Figure II-12. It is clear that the *PCDM* formula is a conservative upper bound and does not discriminate between the no-spall and spall cases.

a. A New Empirically Derived Spall Model

From the dichotomous regression analysis an improved deterministic formula for thickness required to defeat spall can be derived. The new deterministic equation is obtained by setting G = 0, in Model 1, and solving for t. This gives the wall thickness corresponding to a 50 *percent* probability of spall:

$$\frac{t_s'}{W^{1/3}} = 0.20 \left(\frac{R}{W^{1/3}}\right)^{-0.70} \left(\frac{W}{W+C}\right)^{-1.31} \qquad \text{(II-21)}$$

where t_s' is the wall thickness required to defeat spall in *feet*. This equation differs from the *PCDM* equation (*PCDM* Equation (IX-2), Equation (II-10) here) in the exponents and the multiplying coefficient. Note that in the *PCDM* formula the exponents on scaled range and casing factor are the same; whereas, in Equation (II-21) they differ by roughly a factor of two. Thus, based on McVay's data, spall thickness is not uniformly sensitive to these two variables.

Figure II-17 shows the data from Figure II-12 replotted with the abscissa redefined to use the square root of scaled range. With a slight adjustment to the exponent of the scaled range term ($R/W^{1/3}$) in Equation (II-21) (-0.70 to -0.655), it plots as a straight line in Figure II-17. Only the spall data are plotted (the breach data are omitted for clarity). The approximate form of Equation (II-21) shown in the figure is an improvement over the *PCDM* formula for discriminating between spall and no-spall, although there are still several discrepant points (*i.e.*, occurrences of spall above the line and occurrences of no-spall below the line) that reflect the uncertainties in the prediction method. Observe that data for no spall in Figure II-19 are only present between values of 0.4 to 1.0 on the abscissa. Therefore, the square root of scaled standoff times the charge-to-weight ratio should be between 0.4 and 1.0 to use the preliminary spall design thickness formula. This restriction is in addition to those given in Table II-18. The proposed empirical model, given by Equation (II-21), will give smaller thicknesses than the *PCDM* equation in the range of interest. For example, for a charge to total weight ratio of 0.5 (*i.e.*, $W/(W+C) = 0.5$), the new model gives smaller thicknesses when scaled range is greater than 0.85 $feet/pound^{1/3}$.

Because of the bias in the *PCDM* spall equation, the reliability-based design procedure is developed using the proposed new empirical spall model given by Equation (II-21). If the wall thickness is selected to be t_s' from Equation (II-21), then the Model 1 G function is

$$G = -3.41 \ln\left(t/t_s'\right) \qquad \text{(II-22)}$$

where t is the actual wall thickness and t_s' is the wall thickness given by Equation (II-21). Thus, following the derivation procedure used for Equation (II-20), the reliability of the wall against spall is given as

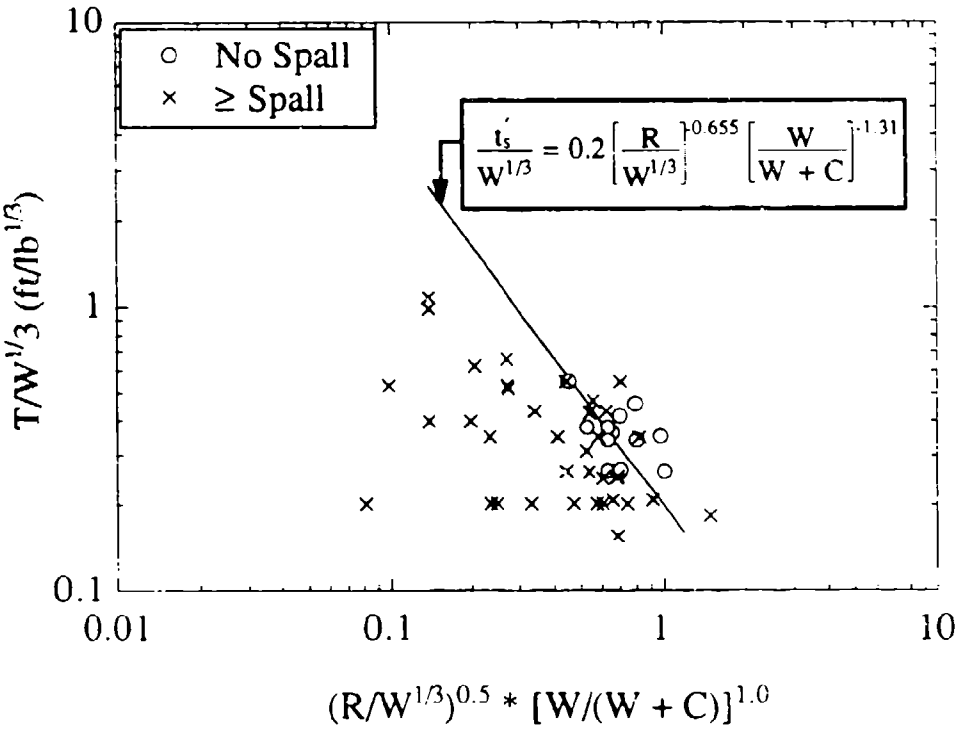

Figure II-17. Spall Data with Preliminary Spall Design Thickness.

$$R(t/t_s') = \frac{1}{1 + (t/t_s')^{3.41}} \qquad \text{(II-23)}$$

With the Model 1 G function written as in Equation (II-22), it can be directly compared with the Model 4 G function which uses the *PCDM* formula to select wall thickness. Since the multiplying coefficient is smaller for the Model 4 G function (2.47 *vs.* 3.41), larger RBDFs would be required when using the *PCDM* formula. Thus, the *PCDM* model requires larger nominal wall thicknesses than the new model and larger design factors to achieve the same level of reliability because predictions using the *PCDM* model are more uncertain.

Using Equation (II-23), Table II-22 lists the reliability-based design factors, t/t_s', and their associated reliabilities that account for the error in the new spall model. As for breach, we assume here that all of the model inputs will be specified for protective design with a specified threat. Notice that the RBDFs are larger than for breach because of greater model uncertainty.

The new spall model is a significant improvement over the current *PCDM* model. Both systematic and random uncertainties are reduced, which will lead to more efficient design. However, we strongly recommend that additional research be conducted to develop improved prediction models. Because of the limited scope of this task it was not possible to

TABLE II-22. RELIABILITY OF WALL THICKNESS TO PREVENT SPALL FROM A STANDOFF CASED BOMB.[a,b]

Reliability[c]	$P_d(x)$	G(x)	RBDF t/t_S'
0.05	0.95	2.94	0.42
0.10	0.90	2.20	0 52
0.25	0.75	1.10	0.72
0.50	0.50	0.00	1.00
0.75	0.25	-1.10	1.38
0.90	0.10	-2.20	1.91
0.95	0.05	-2.94	2.37

[a] t_S' as defined by Equation (II-21) (new spall model).
[b] RBDFs are based principally on data from scale model tests. Additional research is required to assess the systematic bias and additional uncertainty due to the use of scale model data.
[c] Assumes all inputs to Equation (II-21) are deterministic.

investigate additional G function forms that might better discriminate between cases of spall and no-spall. Equation (II-21) defines some of the important prediction parameters and provides a starting point for developing improved empirical and theoretical spall models. With improved models it may be possible to further reduce the design factors for high reliability.

b. Reliability-Based Design Spall Example

The procedure for reliability-based design to prevent spall is identical to the breach design procedure given in Section II.E.3.b except that the nominal thickness to prevent spall is computed using the new spall model (Equation (II-21)), rather than using the *PCDM* formula. The RBDFs for spall are selected from Table II-22. The procedure is valid only for the ranges of applicability given in Table II-18 and only if the square root of the scaled standoff times the charge-to-weight ratio is between 0.4 and 1.0 (see Figure II-17).

As an example, consider a 250-*pound* general purpose bomb at scaled standoffs of 1.0 and 1.5 *feet/pound*$^{1/3}$. We wish to compute the wall thickness required to prevent spall. For this threat, the charge weight is assumed to be 125 *pounds* TNT, and the ratio of charge weight to total weight is 0.48 (see *PCDM* Table III-4). Based on the mission of the structure, the required design reliability for this threat is 90 *percent*. The nominal thicknesses to prevent spall at the two standoffs (5.0 *feet* and 7.5 *feet*) are given by Equation (II-21) as approximately 31 *inches* and 24 *inches*, respectively. From Table II-22 (or Equation (II-23)), we find that the RBDF for 90 *percent* reliability is 1.91. Observe that the spall RBDF for 90 *percent* reliability is much larger than the corresponding breach RBDF (1.21) due to the greater uncertainty in predicting spall. Thus, the design thicknesses for $P_S = 0.90$ are 1.91 × 31 *inches* = 59 *inches* at a 5.0-*foot* standoff and 1.91 × 24 *inches* = 46 *inches* at a 7.5-*foot* standoff. Therefore, to prevent spall damage with 90 *percent* reliability at these standoffs, spall plates will be required in order to maintain a reasonable wall thickness.

The reliability-based spall design can also be compared to the current *PCDM* design obtained using Equation (II-10). At standoffs of 5.0 and 7.5 *feet*, the *PCDM* nominal thicknesses to prevent spall are approximately 32 *inches* and 28 *inches*, respectively. Thus, for the 5.0-*foot* standoff, the *PCDM* spall design provides approximately 50 *percent* design reliability since the *PCDM* design and the nominal design given by the proposed spall formula (Equation (II-21)) are nearly identical. At the 7.5-*foot* standoff, however, the *PCDM* design is 21 *percent* larger than the nominal design given by Equation (II-21). Using Equation (II-23), the reliability of the *PCDM* design at the 7.5-*foot* standoff is estimated as 66 *percent*. Therefore, for the charge-to-weight ratio considered in this example ($W/(W + C) = 0.48$), the *PCDM* spall design becomes progressively more conservative at scaled ranges beyond 1.0 *feet/pound*$^{1/3}$. A comparison of the *PCDM* design and the reliability-based designs over standoffs ranging from 4.5 to 7.5 *feet* (*i.e.*, within the range of spall/no-spall data) is shown in Figure II-18.

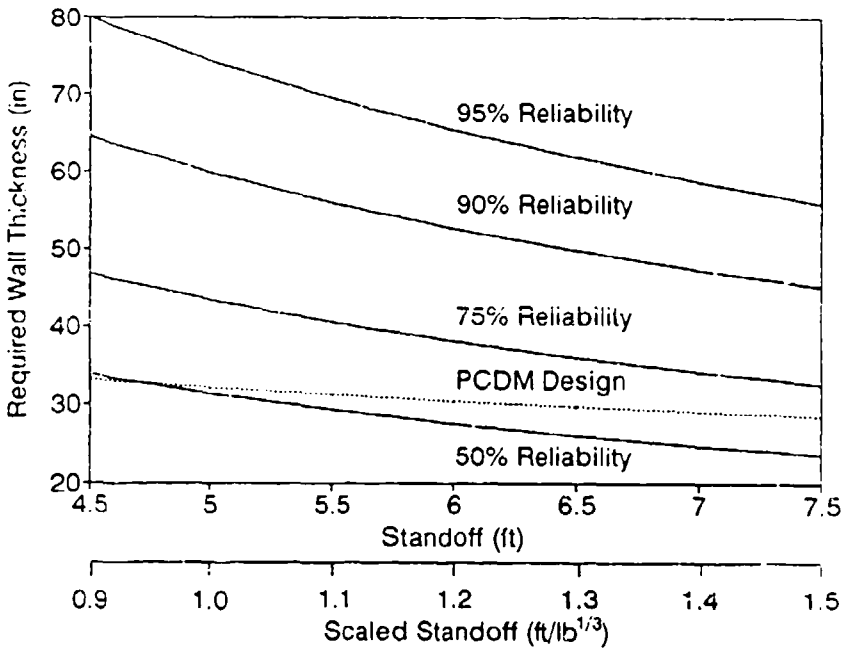

Figure II-18. Comparison of *PCDM* and Reliability-Based Spall Designs for 250-*pound* GP Bomb Example.

(The reverse of this page is blank.)

III. GROUND SHOCK AND BELOWGROUND STRUCTURE RESPONSE

A. INTRODUCTION

This section considers reliability-based design of buried structures subjected to a standoff buried burst. We analyze uncertainty in the *PCDM* methods for predicting free-field ground shock and two failure modes: breaching of concrete walls and flexural failure. Free-field ground shock is covered in Section V of the *PCDM*, breaching in Section IX, and flexural response in Sections III and X. The *PCDM* methods for groundshock and breaching analysis are based on semiempirical formulas, and the flexural failure analysis is based on a dynamic single-degree-of-freedom (SDOF) model that incorporates structure-media interaction (SMI). RBDFs are given for ground shock prediction and for wall thickness to prevent breaching. RBDFs are not given for the flexural response failure mode because our analysis revealed that there can be significant systematic errors with the *PCDM* methodology; for this case we provide recommendations for improving the accuracy of the methodology and for prioritizing research.

B. FREE-FIELD GROUND SHOCK

1. Introduction

Ground shock loading is a highly variable conventional weapons effect. This variability is due to the complex multiphase composition of geologic materials and their inherent spatial variability. To develop survivable buried structure designs, we must first characterize the uncertainty in predicting free-field ground shock. The emphasis of this section is on characterizing the uncertainty in predicting peak free-field velocity and stress.

To characterize ground shock prediction uncertainty, it is important to consider and quantify both the model prediction error and the model parameter (*i.e.*, geologic descriptors) uncertainties. Model prediction error has both a systematic component and a random component. Model parameter uncertainties have both prediction error and random components. Uncertainties are quantified by analysis of ground shock data. However, to prevent model prediction error uncertainty from confounding with model parameter uncertainty, the approach taken herein is to first group the data by geologic and hydrologic conditions. The individual groups are then separately analyzed for model prediction error.

Since the uncertainty in predicting ground shock is site-specific and range-dependent, reliability-based load factors for ground shock are both site-specific and range-specific. Hence, we provide a reliability-based model for computing case-specific reliability-based load factors. However, since most cases for protective design fall within a limited range of parameter values, we are also able to present generic load factors that can be selected from a table.

2. *PCDM* Model

The *PCDM* prediction model for peak free-field velocity and stress from bombs detonating on or within the soil near a structure is given as (*PCDM* Equations (V-11) and (V-10)):

$$V_o = f \cdot 160 \cdot \left(\frac{R}{W^{1/3}}\right)^{-n} \tag{III-1}$$

$$P_o = \frac{\rho_o C_1 V_o}{144} = f \cdot \rho_o C_1 \cdot \frac{160}{144} \cdot \left(\frac{R}{W^{1/3}}\right)^{-n} \tag{III-2}$$

where P_o = peak pressure, *psi*; f = coupling factor for near-surface detonations, C_1 = loading wave velocity, *feet/second*, R = distance to the explosion, *feet*, W = charge weight, *pounds*, V_o = peak particle velocity, *feet/second*, ρ_o = mass density, *pound-seconds*^{2}*/feet*^{4}, n = attenuation coefficient; and

$$C_1 = max \begin{cases} kc \\ c \end{cases} + SV_o \tag{III-3}$$

where k = 0.06 for clay; k = 1.0 for sand; c is the seismic velocity; $S \approx 1/\varepsilon_0$ for partially saturated soils; and S = 0.0 for fully saturated soils (ε_o = irreversible volumetric compaction behind the wave front).

3. Ground Shock Database

The database used for quantifying the model prediction error is a collection of both published and unpublished free-field velocity and stress measurements as discussed in Section V.A.3 of the *PCDM*. The data are shown in the plots of Figures III-1 and III-2. The geologic conditions and shot names are shown on each plot. A best-fit log-log regression line, which will be used for the uncertainty analysis, is also shown.

4. Model Prediction Error

The model prediction error can have both a systematic and a random component. The systematic component is the bias in the model (*i.e.*, a systematic under or over prediction at some range) and the random component is the unexplained variation of measured ground shock about the prediction model (*i.e.*, the scatter of the data). Since the prediction model is linear with scaled range in the log-log space, the random component of the model prediction error is the variability (or scatter) of the data about the linear regression in the log-log space. This is pure error that cannot be accounted for by systematic adjustment to the model. The systematic error is the difference in the prediction and the linear regression.

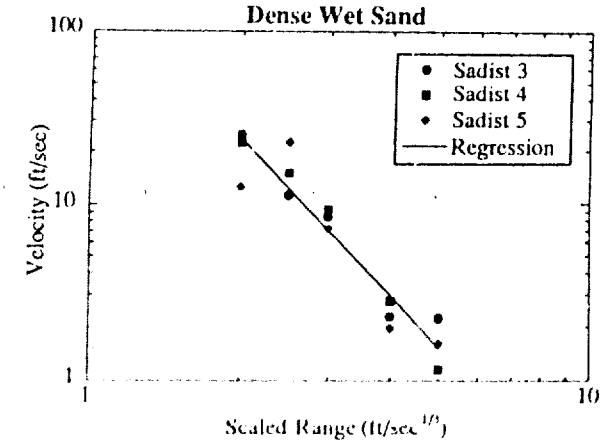

a. Dense Wet Sand - Sadist 3, 4, 5.

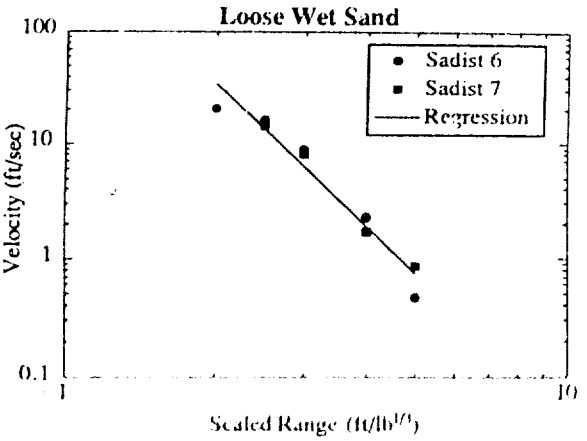

b. Loose Wet Sand - Sadist 6, 7.

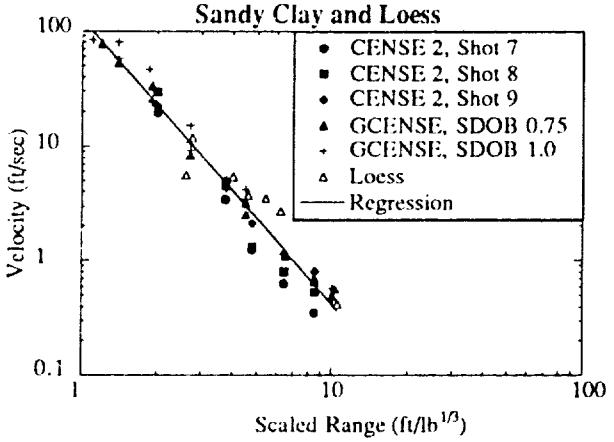

c. Sandy Clay & Loess - Cense 2, Shots 7, 8, 9; Gcense SDOB 0.75, SDOB 1.0; Loess.

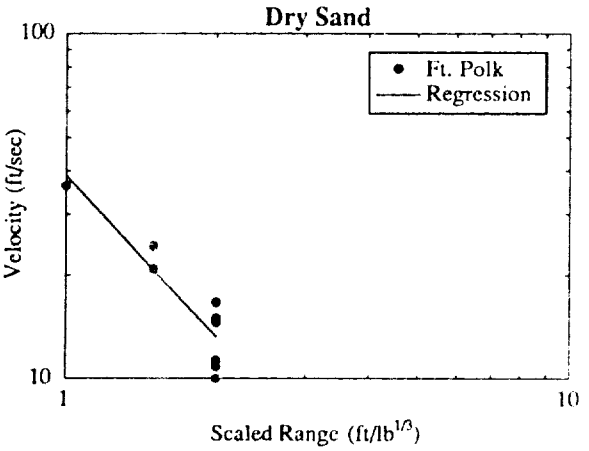

d. Dry Sand - Fort Polk.

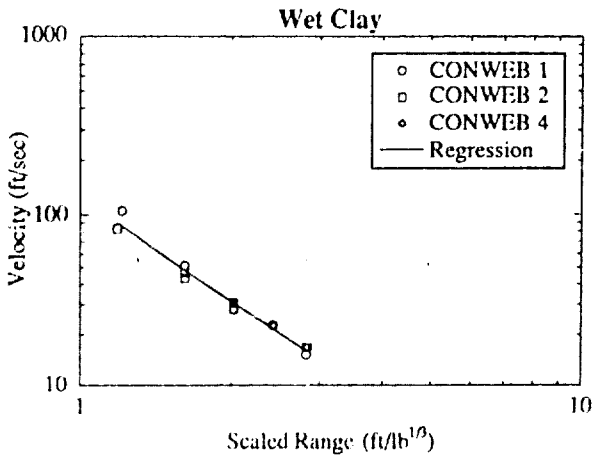

e. Wet Clay - Conweb 1, 2, 4.

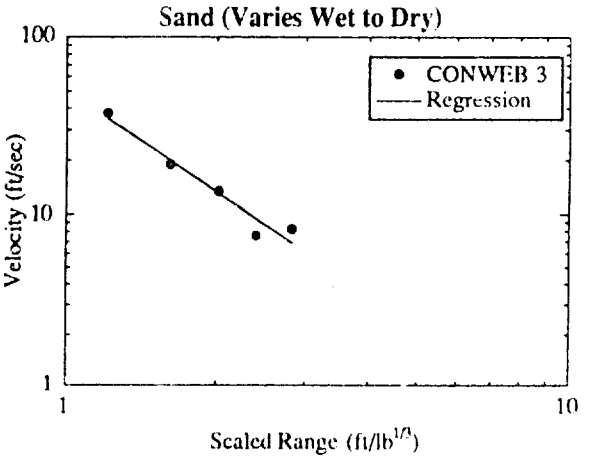

f. Sand (Varies Wet to Dry) - Conweb 3.

Figure III-1. Free-Field Velocity *vs.* Scaled Range.

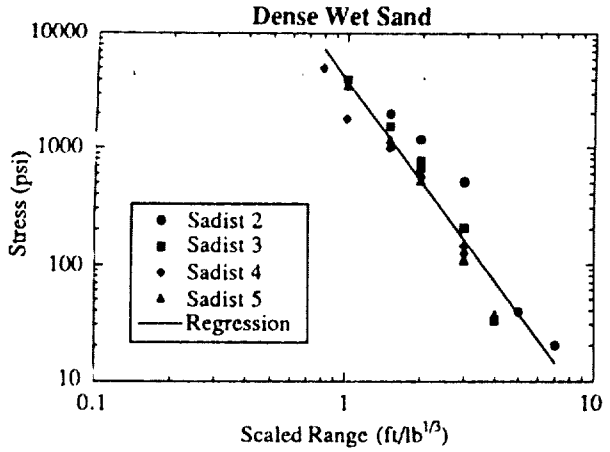

a. Dense Wet Sand - Sadist 2, 3, 4, 5.

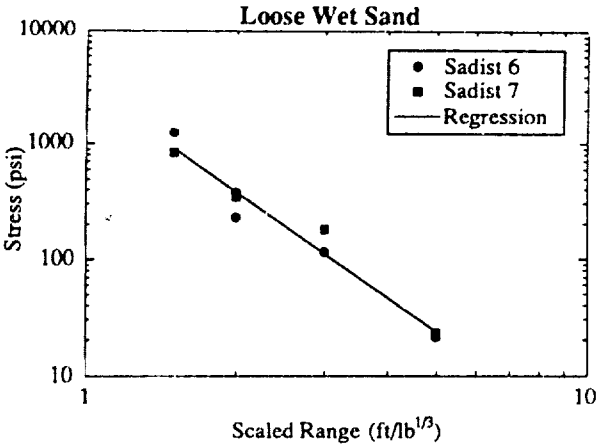

b. Loose Wet Sand - Sadist 6, 7.

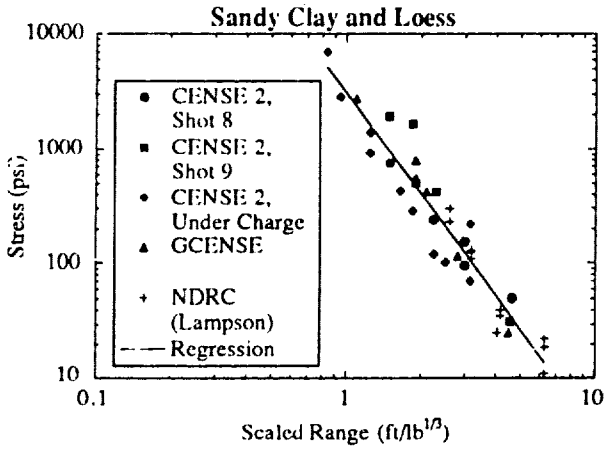

c. Sandy Clay & Loess - Cense 2, Shots 8, 9, Under Charge; Gcense; NDRC (Lampson).

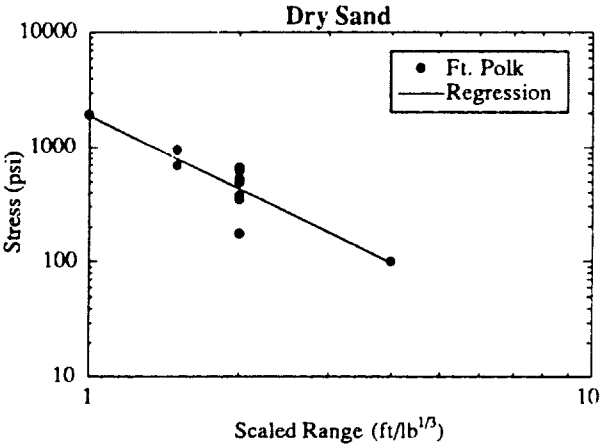

d. Dry Sand - Fort Polk.

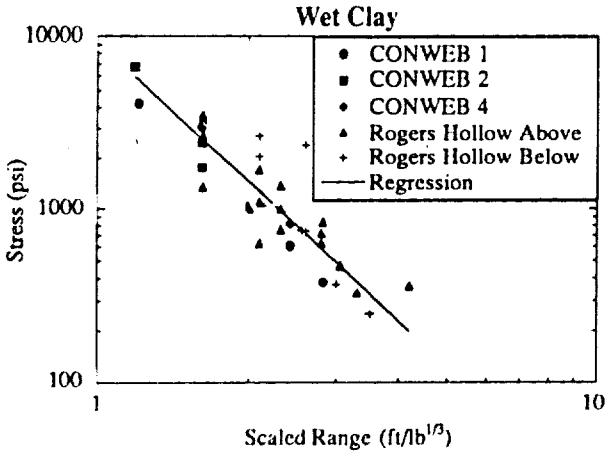

e. Wet Clay - Conweb 1, 2, 4; Rogers Hollow Above Water, Below Water.

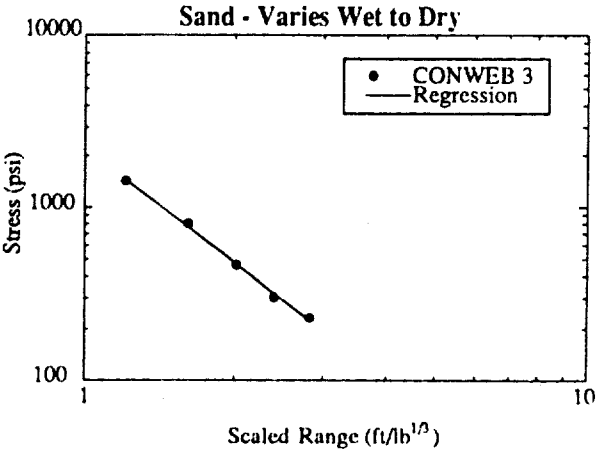

f. Sand (Varies Wet to Dry) - Conweb 3.

Figure III-2. Free-Field Stress *vs.* Scaled Range.

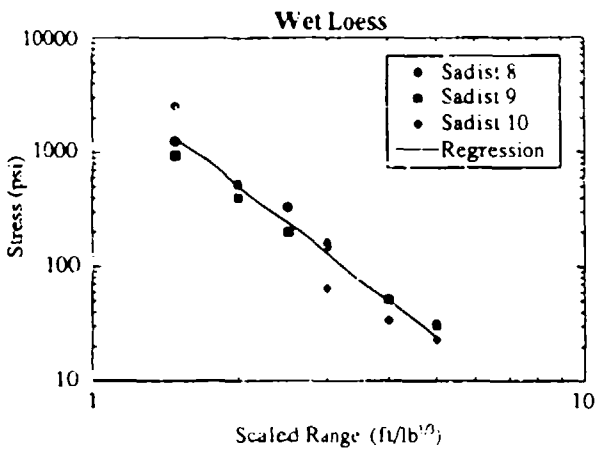

g. Wet Loess - Sadist 8, 9, 10.

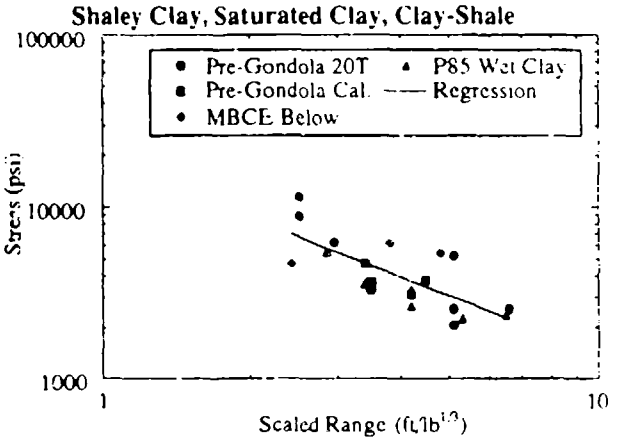

h. Shaley Clay, Saturated Clay, Clay-Shale - P85; Rogers Hollow Below Water; Pre-Gondola Cal; Pre-Gondola 20T, MBCE Below.

Figure III-2. Free-Field Stress *vs.* Scaled Range (Continued).

a. Random Component

To quantify the random component of the model prediction error, the data are grouped by soil type (*i.e.*, groups for which the same model parameters are used) and analyzed by linear regression in log-log space. The data and the regression lines are shown in Figures III-1 and III-2 for free-field velocity and free-field stress, respectively. The random component of the model prediction error is now characterized by the distribution of the natural log of the prediction error ratio. The prediction error ratio, ξ, is evaluated for each data point as the ratio of the observed ground shock (velocity or stress) to the value given by the regression line. For linear regression in the log-log space this is proportional to the regression residual. Table III-1 shows the standard deviation of the natural log of ξ for each soil type, for both the velocity and stress data. The expected value of the natural log of ξ (not shown) is 0 for all cases because the regression line is an unbiased model. The table also shows the results of the hypothesis test for lognormality of ξ.

Since peak free-field stress is simply $\rho_o \times C_1$ times free-field velocity, we use the free-field velocity data to quantify the random component of the model prediction error. The larger data scatter for free-field stress is due to greater sensitivity of free-field stress to spatial variation of the geologic parameters ρ_o and C_1. Since this additional uncertainty is highly site specific, we will treat it as a parameter uncertainty.

There are three main contributors to the free-field velocity model random prediction error (*i.e.*, factors that are not accounted for in the model): (1) bomb-to-bomb

TABLE III-1. VARIABILITY OF LOG-PREDICTION ERROR RATIO (ln [ξ]).[a]

Soil Type	Free-Field Velocity		Free-Field Stress	
	Standard Deviation $\sigma_{ln\xi}$	Hypothesis: Reject Lognormal ?	Standard Deviation $\sigma_{ln\xi}$	Hypothesis: Reject Lognormal?
a. Dense Wet Sand	0.32	No	0.48	No
b. Loose Wet Sand	0.31	Marg.	0.28	No
c. Sandy Clay & Loess	0.33	No	0.45	No
d. Dry Sand	0.17	No	0.36	No
e. Wet Clay	0.08	No	0.39	No
f. Sand (Varied Wet to Dry)	0.15	No	0.04	No
g. Wet Loess	-	-	0.32	No
h. Shaley-Clay, Clay-Shale	-	-	0.31	No

[a] ln(ξ) = Natural logarithm of prediction error ratio, $\xi = \frac{\text{Observed Ground Shock}}{\text{Regression Model Prediction}}$.

variability (*i.e.*, repeatability of experiments at a single site; (2) site-to-site differences for sites that fall into a single category (*e.g.*, all dry sand sites are not the same); and (3) spatial variability of velocity attenuation within a single soil type.[1] Not all sources of uncertainty are adequately represented for each of the soil types. For example, for case f in Table III-1 (sand varied wet to dry, Figure III-1f) we have only one shot, so that bomb-to-bomb and site-to-site variability is not represented. Hence, we estimate the random component of the model prediction using only those cases wherein we have multiple shots -- that is: case a (dense wet sand, Figure III-1a); case b (loose wet sand, Figure III-1b); and case c (sandy clay & loess, Figure III-1c). We do not include case e (wet clay, Figure III-1e), even though there were multiple shots, because these shots used an atypical, highly controlled clay material that is not representative of backfill used in protective design.[2]

From Table III-1, the logarithmic standard deviations of ξ, for the three selected soil cases (a, b, c), vary over a small range from 0.31 to 0.33 and for all three cases we do not reject the lognormal model. Hence, we model the random component of the model prediction error as lognormal with a unit median and conservatively select the logarithmic standard deviation to be 0.35 (slightly larger than the observed 0.31 to 0.33 range). Figure III-3 shows a histogram of ξ for the three cases combined and Figure III-4 shows ξ plotted on log-normal

[1] Random measurement error can also add to the data scatter, however, we have not attempted to remove the measurement error component in this analysis.

[2] An alternative approach would be to use analysis of variance techniques to separately quantify each uncertainty source. This method would allow us to use all of the data and would be more accurate. It would also allow us to determine the percent contribution of each source of uncertainty and to determine if each source of uncertainty is sufficiently represented in the database to reliably estimate the prediction error statistics. This more detailed approach was not, however, pursued, since the data from the selected cases gave consistent results for the prediction error statistics and resources to perform this task were limited. We strongly recommend, however, that future research investigate each of the uncertainty sources. Although the prediction error modeling might not change significantly, such research could have a high payoff in pointing out ways to improve the *PCDM* prediction method.

probability paper along with the lognormal model (the straight solid line). As can be seen, the model is a good fit.

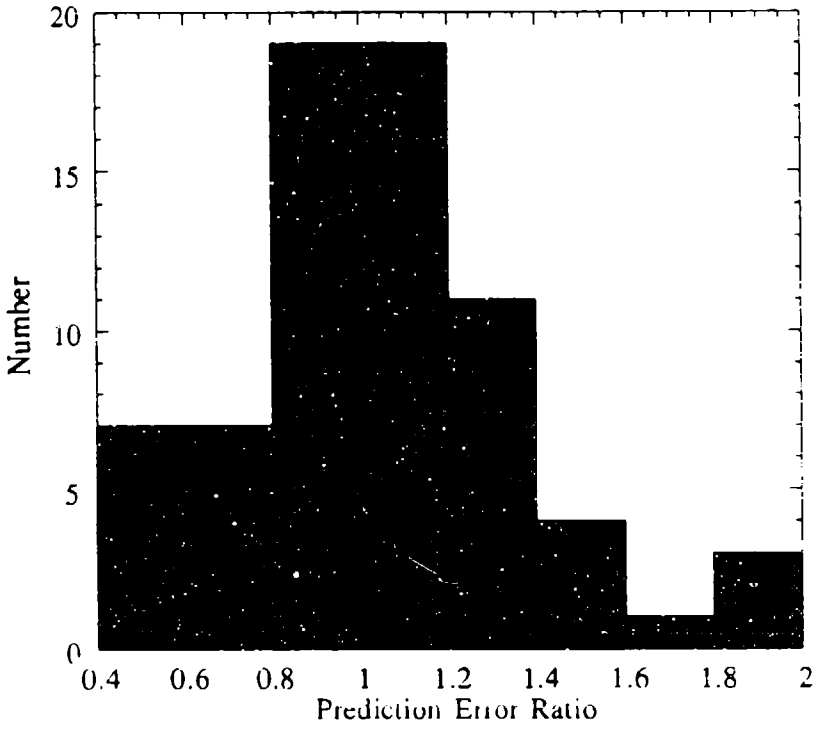

Figure III-3. Histogram of Free-Field Velocity Prediction Error Ratio (cases a, b, and c from Table III-1).

The model presented above does not attempt to represent any change in the mean and standard deviation of ξ with range. For example, it is possible that at close range the logarithmic standard deviation may be less than 35 *percent* while at far range it is possible that it may be greater than 35 *percent*. To investigate range variability, the log of the prediction error ratio is plotted as a function of scaled range in Figure III-5, and we regress ξ on range and $(\xi - 1)^2$ on range. In both cases the R^2 value is very small, indicating that the mean and standard deviation can be modeled as range-independent. Hence, the range-independent model is used herein.

b. Systematic Component

The systematic component of the model prediction error is the difference between the model prediction and the mean of the data. From the analyses performed in the previous section we observe that the mean ground shock is a linear function of scaled range in the log-log space (if it were not then prediction error would show a significant trend with range). Therefore, the systematic component of the model prediction error is simply the error in selecting the attenuation exponent, n (slope of the model in the log-log space) and the multiplying coefficient

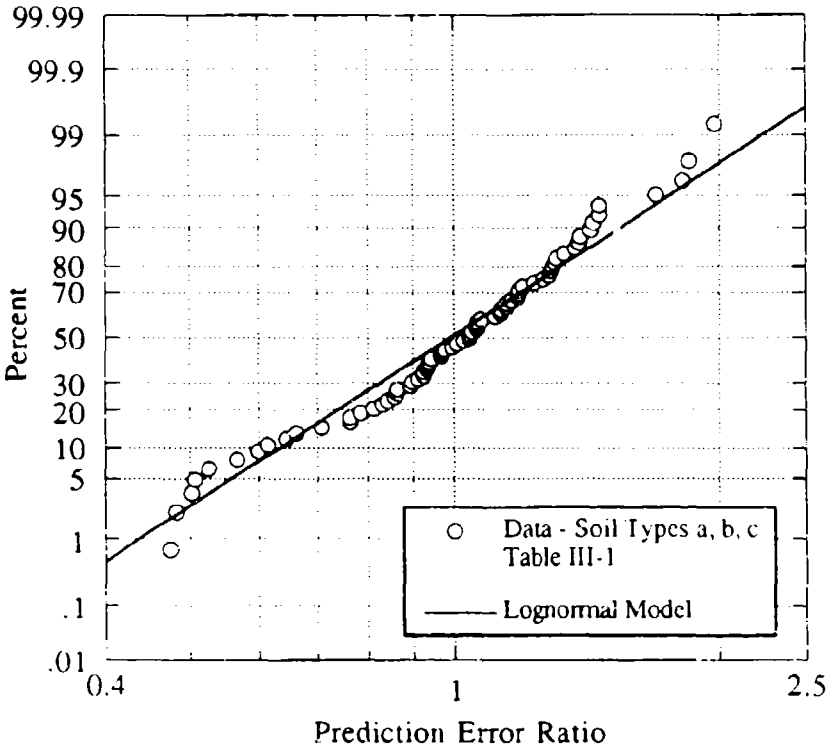

Figure III-4. Lognormal Modeling of Free-Field Velocity Prediction Error Ratio.

of the model. For purposes of the following discussion we will refer to the multiplying coefficient as v_1. For the *PCDM* free-field velocity model, $v_1 = 160$, as given by Equation (III-1) (v_1 is the free-field velocity at a scaled range of 1 *feet/pound*$^{1/3}$, and is constant for all soil types in the *PCDM* model).

The systematic model error that is due to error in selecting the attenuation exponent is in addition to the basic parameter uncertainty which is the subject of Section III.B.5 to follow. Basic parameter uncertainty is due to variability in the soil properties at the site and uncertainty in predicting the soil properties due to limited testing and site characterization. The systematic model error is in specifying the proper attenuation exponent given that the soil properties are known or well understood. These two sources of error are difficult to separate since we don't have precise soil characterization data for all of the tests. Hence, we will present a procedure for quantifying attenuation exponent uncertainty in Section III.B.5 that combines both sources of uncertainty.

It remains to quantify the systematic component of the model prediction error that is due to the use of a fixed value for v_1 for all soil types. The *PCDM* model is a simplified procedure wherein v_1 is independent of material properties. In actuality, v_1 is a function of the size of the expanded cavity and the expansion velocity, and, therefore, depends on the material density, strength, and compressibility. The dependence on density is relatively weak since

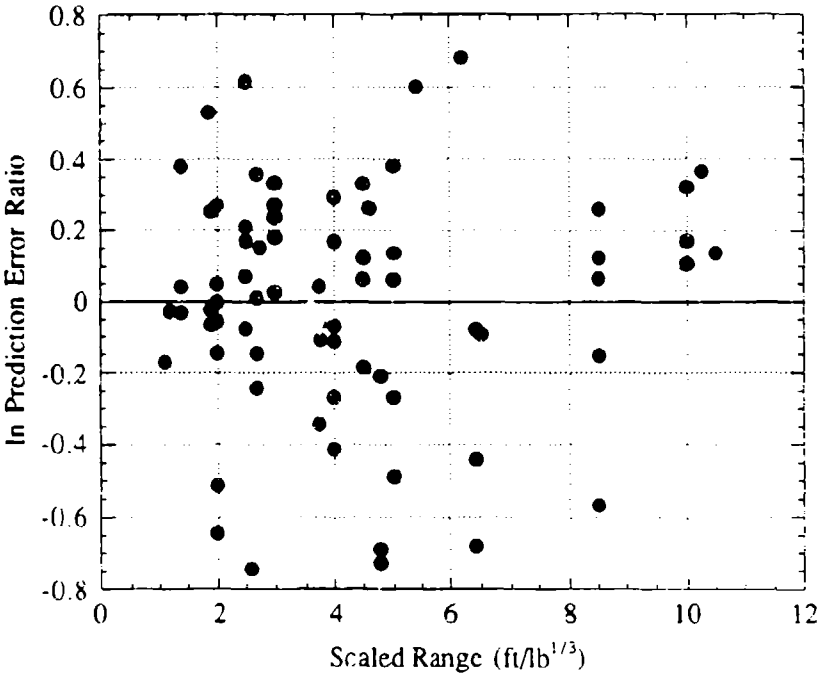

Figure III-5. LN of Free-Field Velocity Prediction Error as a Function of Scaled Range (Soil Types a, b, and c from Table III-1).

the coefficient is functionally dependent on the square root of the density. For the range of soil densities that are encountered in protective design, the effect on v_1 is approximately ±5 *percent* and can be neglected. The dependence on material strength and compressibility, however, can be significant. Material strength and compressibility can affect the size of the expanded cavity and the expansion velocity. The simplified *PCDM* procedure addresses this model deficiency by recommending attenuation exponents that compensate for this source of error. Because the compensating affect is range dependent, and was developed to match the ground shock data in the range of interest in protective design (*i.e.*, scaled range of 1.0 *feet/pound*$^{1/3}$ to 3 *feet/pound*$^{1/3}$), the *PCDM* model should only be used in this range. For most soil types the *PCDM* model tends to overpredict the ground shock loading and is, therefore, design-conservative in the range of interest.

At this time we do not believe that it is appropriate to correct the bias that may be present in the *PCDM* model via a systematic adjustment, without a more thorough investigation of the physical sources of the variation. We strongly recommend that the data be reanalyzed, in light of the above discussions, and compared with improved prediction models that take into account material strength and compressibility. Because of the simplified nature of the prediction model, however, we recommend that additional uncertainty be included to account for the potential systematic error. To quantify this uncertainty, we use a bounding procedure and estimate that conservative 90 *percent* bounds on the systematic error, in the scaled range of interest,

is from 1/2 the predicted value to 1 1/2 times the predicted value. These bounds are approximately fit by a lognormal distribution with unit median and a logarithmic standard deviation of 0.30.

5. Model Parameter Uncertainty

The parameters used in the free-field stress prediction for a fully coupled burst are:

- Charge Weight, W
- Slant Range, R
- Peak Velocity Attenuation Exponent, n
- Mass Density, ρ_o
- Seismic Wave Speed, c

The following paragraphs discuss how the uncertainties (both prediction error and random uncertainty components) in each of these parameters should be modeled in the analysis of the predicted free-field velocity and stress.

a. Charge Weight

Assuming that the weapon threat is specified in protective design, it is only necessary to consider the additional uncertainty in predicting actual explosive energy-yield for a specified explosive weight. The analysis presented in Section III.B.4 is based on explosive weights of actual bombs, hence the data scatter already reflects randomness in yield prediction. In addition, since the exponent on weapon yield in the prediction model will usually be less than one (approximately two-thirds), and since the uncertainty in weapon yield is expected to be small with respect to other uncertainties, this random uncertainty will be a small contributor to free-field velocity and stress uncertainty, and can be taken as deterministic.

b. Slant Range

For design to a specified threat, slant range is treated as a deterministic quantity. When the weapon standoff is variable, the procedures described herein should be used to compute design reliability for the range of possible standoffs and then convolved with the weapon standoff probability distribution to obtain the overall structural reliability — that is $P_S = \Sigma P_S(r_i) \times P_R(r_i)$, where $P_S(r_i)$ is the probability of survival when standoff = r_i and $P_R(r_i)$ is the probability that standoff = r_i.

c. Attenuation Exponent

For purposes of predicting ground shock, the *PCDM* provides recommendations for the attenuation exponents as shown in Table III-2. These recommended values are based on fits of the prediction equations to observed ground shock data and expert judgment.

TABLE III-2. *PCDM*-RECOMMENDED SOIL PROPERTIES FOR EQUATIONS (III-1) AND (III-2) (*PCDM*, TABLE V-1).

	Dry Unit Weight γ_d (*pcf*)	Total Unit Weight γ (*pcf*)	Air-Filled Voids (*percent*)	Seismic Velocity c (*feet/second*)	Attenuation Coefficient (n)	S
Dry desert alluvium and playa, partially cemented	87	93-100	>25	2,000-4,200[a]	3.0-3.25	4
Loose, dry, poorly graded sand	80	90	>30	600	3.0-3.5	3
Loose, wet, poorly graded sand with free-standing water	97	116	10	500-600	3.0	10
Dense, dry sand, poorly graded	90	104	32	900-1,300	2.5-2.75	3
Dense, wet sand, poorly graded with free-standing water	108	124	9	1,000	2.75	11
Very dense dry sand, high relative density	105	109	30	1,600	2.5	3
Silty-clay wet	95-100	120-125	9	700-900	2.75-3.0	11
Moist, loose, clayey sand	100	122	5-10	1,000	2.75-3.0	10
Wet sandy clay, above water table	95	120-125	4	1,000-1,800	2.25	25
Nearly saturated sand, below water table	–	–	1-4[b]	1,800-4,900	2.0-2.25	50
Saturated sandy clay, below water table	100	125	<1	5,000-6,600	1.5	0
Saturated stiff clay, saturated clay-shale	–	120-130	0	>5,000	1.5	0

[a] High because of cementation, use c = 600 *feet/second* for design purposes.
[b] Estimated.

There are two types of uncertainty in the attenuation exponent. First, basic model parameter uncertainty results from variability in the soil properties at the site and uncertainty in predicting the soil properties due to limited testing and site characterization. Second, there is uncertainty in selecting the proper attenuation coefficient once the soil properties have been characterized. As discussed in Section III.B.4, this latter uncertainty models part of the systematic component of the model prediction error.

To simplify the process for quantifying the attenuation exponent uncertainty, both types of uncertainty are combined in the following procedure:

1. Categorize the soil according to Table III-2.[1]

2. Select the mean value of the attenuation coefficient to be the value recommended in the table. If a range of values is given in the table, select the midpoint of the range.[2]

[1] If the soil does not fall precisely into one of the categories, select the two that best describe the site. Assign each category a weighting factor representing the degree of belief for each category. The weighting factors must sum to 1.0. If each category is equally likely, assign each category a weighting factor of 0.5.
[2] If more than one soil category was selected in Step 1, use a weighted average of the tabulated values.

3. Quantify the uncertainty in the attenuation exponent as follows: (a) if a range of values is given in the table, assume that this range represents ± 1 standard deviation; (b) if the standard deviation obtained from the above procedure is less than 5 *percent* of the mean value, set the standard deviations to 5 *percent* of the mean attenuation exponent.[1]

The above approach considers uncertainty in soil properties by allowing selection of different soil categories. It also considers uncertainty in selecting the attenuation exponent once the soil has been categorized, based on the ranges recommended in the design manual. This range is a reflection of the uncertainty in selecting an attenuation exponent and was estimated from observed systematic variations in ground shock measurements. The assumption that the design manual range is ± 1 standard deviation is equivalent to assuming that the two values given are equally likely point estimates and is consistent with the intent of the table.[2] The minimum standard deviation value of 5 *percent* of the mean attenuation exponent is provided as a lower bound and is based on experience with ground shock predictions.

d. Mass Density and Seismic Wave Speed

Mass density and seismic wave speed are the basic physical and mechanical descriptors of the geology used in the ground shock prediction model. The basic model parameter uncertainty results from variability in the soil properties at the site (random component) and uncertainty in predicting the soil properties due to limited testing and site characterization (prediction error component). Both uncertainties will be case specific. For example, for design of a new buried structure located in a well controlled and well characterized backfill, the model parameter uncertainty will be small. However, for survivability assessment of an existing structure wherein the soil properties are not well characterized the uncertainty could be large. As a general rule, even for a well characterized and well controlled site, mass density and seismic velocity can be expected to have coefficients of variation of at least 5 *percent*.

6. Reliability Model

The objective of the reliability-based ground shock prediction model is to systematically consider all of the important uncertainties that influence the confidence levels associated with the peak free-field velocity and stress predictions. The reliability model for free-field velocity can be formulated as

$$V_o = \xi \cdot 160 \cdot \left(\frac{R}{W^{1/3}}\right)^{-n} \qquad \text{(III-4)}$$

where the random variables are the attenuation exponent, n, and the model prediction error variable, ξ. The scaled range, $R/W^{1/3}$, is typically taken to be deterministic (for a specified threat) as discussed in Section III.B.5.

---

[1] If more than one soil category was selected in Step 1 evaluate the total standard deviation using the weighting factors assigned to each attenuation exponent and the standard deviations evaluated in Step 3a.

[2] Alternatively the range could be interpreted as the extremes or bounds of a range of possible values.

The reliability evaluation can be simplified by taking the natural logarithm of both sides of Equation (III-4) — that is,

$$\ln V_o = \ln \xi + \ln 160 - n \ln (R/W^{1/3}) \quad \text{(III-5)}$$

The mean and standard deviation of the natural log of the free-field velocity can now be obtained as

$$E [\ln V_o] = E [\ln \xi] + \ln 160 - E [n] \ln (R/W^{1/3}) \quad \text{(III-6)}$$

$$\sigma^2_{\ln V_o} = \sigma^2_{\ln \xi} + [\ln (R/W^{1/3})]^2 \sigma^2_n \quad \text{(III-7)}$$

assuming that $R/W^{1/3}$ is deterministic. Also, for calculation of $\sigma^2_{\ln V_o}$, we assume that ξ, and n are independent. Thus, the statistics of V_o are obtained directly from the statistics presented in Sections III.B.4 and III.B.5.

The prediction error random variable, ξ, is used here to model both the random component of the model prediction error and the systematic error due to the use of the fixed multiplying coefficient ($v_1 = 160$) for all soil types. As presented above, both the random and systematic components are modeled as lognormally distributed random variables with unit median and logarithmic standard deviations of 0.35 (which is approximately a coefficient of variation of 35 *percent*) for the random component, and 0.30 for the systematic component. Since the total prediction error is the product of these two components, ξ is also a lognormal random variable with unit median and logarithmic standard deviation of $\sqrt{0.35^2 + 0.3^2} = 0.46$.

Assuming that n is normally distributed, the free-field velocity is lognormally distributed. Even if n is not normally distributed, we can still use the lognormal distribution for free-field velocity since its distribution will be dominated by the distribution of ξ, which is lognormal (ξ will be the dominant uncertainty contributor for ranges of interest in protective design).

For free-field stress, the process is similar except that additional uncertainty is included to account for uncertainty in specifying the material mass density and loading wave velocity at the location of interest. Taking the natural logarithm of Equation (III-2) gives

$$\ln P_o = \ln \rho_o + \ln C_1 + \ln V_o - \ln 144 \quad \text{(III-8)}$$

Thus, the statistics of free-field stress are obtained as

$$E [\ln P_o] = E [\ln \rho_o] + E [\ln C_1] + E [\ln V_o] - \ln 144 \quad \text{(III-9)}$$

$$\sigma^2_{\ln P_o} = \sigma^2_{\ln \rho_o} + \sigma^2_{\ln C_1} + \sigma^2_{\ln V_o} + 2\, COV (\ln \rho_o, \ln C_1) \quad \text{(III-10)}$$

where, for calculation of $\sigma^2_{\ln P_o}$ we assumed that the uncertainty in free-field velocity is independent of both mass density and loading wave velocity C_l. Although, these variable are correlated, the contribution to uncertainty in predicted free-field stress will be small, and can be neglected. Correlation of ρ_o and C_l is however included by the covariance (COV) term.

The free-field stress statistics are, therefore, dependent on the free-field velocity statistics and the statistics of the mass density and loading wave velocity. The statistics and distribution of the mass density and loading wave velocity will, of course, be site-dependent. If these two material property variables are lognormally distributed, the free-field stress will also be lognormally distributed (assuming free-field velocity is lognormal). The correlation coefficient (covariance divided by standard deviation of each variable) of ρ_o and C_l is taken as 0.9, based on work of Sues and Twisdale [1990].

To summarize, the statistics of a free-field velocity or stress prediction can be obtained using Equations (III-6) and (III-7), and (III-9) and (III-10), respectively and the uncertainty characterizations presented in Sections III.B.4 and III.B.5. The prediction corresponding to a particular reliability or confidence level is then obtained using a tabulation of the lognormal probability function. Thus, the free-field velocity that corresponds to reliability level R is

$$V_{oR} = \exp\left[E(\ln V_o) + \Phi^{-1}(R) \times \sigma_{\ln V_o}\right] \qquad \text{(III-11)}$$

Similarly the free-field stress that corresponds to reliability level R is

$$P_{oR} = \exp\left[E(\ln P_o) + \Phi^{-1}(R) \times \sigma_{\ln P_o}\right] \qquad \text{(III-12)}$$

Table III-3 is a tabulation of a several discrete values of the Φ function.

TABLE III-3. STANDARD NORMAL FUNCTION FOR USE IN FREE-FIELD GROUND SHOCK RELIABILITY CALCULATION.

R	$\Phi^{-1}(R)$
0.05	-1.65
0.10	-1.28
0.25	-0.67
0.50	0.00
0.75	0.67
0.90	1.28
0.95	1.65

7. Reliability-Based Design Factors

For many protective design situations, ground shock predictions are necessary for only a limited range from 1.0 to 3.0 *feet/pound*$^{1/3}$. Since model prediction errors will dominate the prediction uncertainty, it is possible to tabulate generic RBDFs for ground shock prediction. We have tabulated reliability-based load factors for two cases (A and B) that represent two different degrees of uncertainty in the site geologic properties. For Case A, we use $\sigma_n = 0.15$, $\sigma_{\ln\rho_o} = \sigma_{\ln c_1} = 0.10$, and $\mathrm{COV}(\ln\rho_o, \ln c_1) = 0.9 \times 0.1 \times 0.1$; and for Case B, we use $\sigma_n = 0.25$, $\sigma_{\ln\rho_o} = \sigma_{\ln c_1} = 0.25$, and $\mathrm{COV}(\ln\rho_o, \ln c_1) = 0.9 \times 0.25 \times 0.25$. Case A corresponds to a controlled backfill material typical of protective construction, and Case B corresponds to a site where only limited material property information is available.

The reliability-based load factors are derived using the equations given in Section III.B.6 and are tabulated in Table III-4. When specific site information is available, and for final designs of mission critical structures (*e.g.*, buried command center) we recommend that site-specific load factors be derived using the equations given in Section III.B.6. with soil property data from the site or backfill material.

8. Reliability-Based Ground Shock Prediction Procedure and Example

Reliability-based analysis for ground shock prediction consists of three simple steps:

1. Evaluate the nominal ground shock values (velocity and/or stress — Equations (III-1) and (III-2)).
2. Select the desired reliability level based on the mission criteria and the corresponding load factor from Table III-4.
3. Multiply the nominal ground shock value by the load factor obtained in Step 2. Note that for free-field stress, the load factor is applied to the nominal free-field stress value; do not use the factored velocity to compute the free-field stress.

For example, suppose that we wish to compute a 90 *percent* reliability level for free-field stress at a scaled range of 2 *feet/pound*$^{1/3}$. The soil is a dense dry sand whose properties will be controlled during construction to have a target density of 104 *feet/pound*^{3}, a seismic wave speed of 1000 *feet/second*, and 32 *percent* air voids.

The first step is to use Equation (III-1) to get the nominal PCDM prediction of peak free-field velocity. We select a value for the attenuation exponent, n, from Table II-2. For a dense dry sand, a range of values is given in the table, *i.e.*, 2.5 - 2.75, and we select the midpoint, or 2.63. The nominal value of the peak free-field velocity is obtained from Equation (III-1) as:

$$v_0 = 160 \times (2.0)^{-2.63} = 25.8 \text{ feet/second} \qquad \text{(III-13)}$$

The next step is to evaluate the nominal peak free-field stress. To evaluate peak free stress we multiply the nominal peak free-field velocity by the soil mass density and loading wave

velocity. Thus (after converting to proper units), the mass density, loading wave velocity, and free-field stress are obtained using Equations (III-2) and (III-3) as

$$\rho_o = 104/32.2 = 3.23 \; pound\text{-}seconds^2/feet^4 \qquad \text{(III-14)}$$
$$C_1 = 1000 + (1/.32)(25.8) = 1081 \; feet/second$$
$$P_o = 3.23 \times 1081 \; feet/pound^{1/3} \; 25.8/144 = 626 \; pounds/inch^2$$

Table III-4 shows that $\lambda = 1.97$ for 90 *percent* reliability and the 90 *percent* reliability-based peak free-field stress prediction is 1.97 $feet/pound^{1/3}$ 626 = 1233 $pounds/inch^2$. Thus, to achieve 90 *percent* reliability the free-field stress prediction is increased roughly by a factor of 2. Note, that a more exact analysis using the equations given in Section III.B.6, yields a slightly smaller $\lambda = 1.9$.

TABLE III-4. FREE-FIELD GROUND SHOCK LOAD FACTORS, λ.

	Free-Field Velocity		Free-Field Stress	
Reliability	Case A[a] $\sigma_{\ln v_o} = 0.49$	Case B[b] $\sigma_{\ln v_o} = 0.54$	Case A $\sigma_{\ln \rho_o} = 0.53$	Case B $\sigma_{\ln \rho_o} = 0.73$
0.05	0.45	0.41	0.41	0.30
0.10	0.53	0.50	0.51	0.39
0.25	0.72	0.70	0.70	0.61
0.50	1.00	1.00	1.00	1.00
0.75	1.39	1.44	1.43	1.63
0.90	1.87	2.00	1.97	2.55
0.95	2.24	2.44	2.40	3.34

[a]Case A: Typical Backfills: $\sigma_n = 0.15$, $\sigma_{\ln \rho_o} = \sigma_{\ln c_1} = 0.10$
$\mathrm{COV}[\ln \rho_o, \ln c_1] = (0.9)\,(0.10)\,(0.10)$, $R/W^{1/3} = 3.0$
$\rightarrow \sigma_{\ln v_o} = 0.49$, $\sigma_{\ln \rho_o} = 0.53$

[b]Case B: High Site Uncertainty: $\sigma_n = 0.25$, $\sigma_{\ln \rho_o} = \sigma_{\ln c_1} = 0.25$
$\mathrm{COV}[\ln \rho_o, \ln c_1] = (0.9)\,(0.25)\,(0.25)$, $R/W^{1/3} = 3.0$
$\rightarrow \sigma_{\ln v_o} = 0.54$, $\sigma_{\ln \rho_o} = 0.73$

C. FLEXURAL FAILURE

1. Introduction

In the *PCDM*, flexural response is evaluated via a dynamic equivalent single-degree-of-freedom (SDOF) model that incorporates structure-media interaction. Computed wall deflections are then compared with empirically-based damage criteria.

There are three main sources of uncertainty in analyzing a structural slab for flexural failure. The first is the uncertainty in predicting the free-field ground shock loading; the second is

the uncertainty in predicting the structure response given the ground shock loading; and the third is the uncertainty in predicting the state of damage given the structural response. Analysis of free-field ground shock uncertainty was presented in Section III.B. Uncertainty in predicting structure response is discussed in this section. The structure response uncertainty has both model prediction error and model parameter uncertainty components. Final RBDFs are not given for flexural response and damage prediction because of systematic errors in the response analysis and limited resources for this multitask project. Recommendations are included for improving the accuracy of the response prediction methodology.

2. Structure Response Model Prediction Error

The structural response model for the flexural mode given in the *PCDM* models the wall as an equivalent lumped mass-spring system and accounts for the effects of structure-medium interaction. The basic equation of motion for the wall is given by:

$$\rho_c L\ddot{u} + \rho_s c_s \dot{u} + R(u) = P_{ff} + \rho_s c_s V_{ff} \qquad \text{(III-13)}$$

where ρ_c = concrete wall density, L = wall thickness, $\ddot{u}$ = wall acceleration, ρ_s = soil density, c_s = soil seismic wave speed, $\dot{u}$ = wall velocity, $R(u)$ = wall resistance as a function of displacement, u, and P_{ff} and V_{ff} = free-field stress and velocity, respectively, at a range equal to the distance between the bomb and the wall. Any consistent set of units can be used in Equation (III-13).

Each term in the equation of motion is multiplied by a single-degree-of-freedom transformation factor in the *PCDM*. This approach ensures that the equivalent system does the same work and dissipates the same energy as the real system (for an assumed deformed shape). Also, the peak free-field stress is multiplied by an equivalent uniform load factor. This factor accounts for the nonuniform nature of loads due to conventional explosives and is a function of the wall aspect ratio (width to height) and the distance between the bomb and the wall. The solution of the equation of motion is the displacement of the center of the wall.

Two approaches are possible for analyzing the model prediction error. The first is to assess the uncertainty and conservatisms in each of the assumptions, idealizations and prediction equations used in the SMI model; these are listed in Table III-5. The second approach is to analyze the model prediction error by comparing overall predicted and observed response. While the former approach would provide results that are more general, the latter approach is used herein because of the difficulties of separately analyzing each of the uncertainties in the model. The former approach would require analysis of variance of controlled test data to separately analyze each source of uncertainty. Also, the latter approach provides results that are more directly usable, as long as the structures of interest exhibit behavior that is similar to the test structures.

To analyze the SMI model prediction error we compared test results and predictions for fourteen test cases. The prediction calculations were made using the *PCDM* model presented above, and also with two modifications on the procedure given in the *PCDM*. The first modification involves the use of an additional degree-of-freedom to account for motion of the

reaction structure during the test; and the second modification involves the use of an improved structural restoring force function (resistance function) [Drake, *et al.*, 1989; Slawson, *et al.*, 1989]. Figure III-6 compares the improved resistance function with the standard design resistance function. The improved resistance function includes compressive membrane action and tensile membrane action. Both of these phenomena increase the ultimate capacity of the slab beyond the yield line capacity used in the *PCDM* method.

TABLE III-5. IDEALIZATIONS AND PREDICTION EQUATIONS USED IN SMI MODEL.

Model Idealizations	Prediction Equations
1. One-way slab behavior	1. Moment of Inertia
2. Single-degree-of-freedom	2. Stiffness
3. Fixed Supports	3. Structure restoring force
4. Location and pattern of flexural hinge formation	

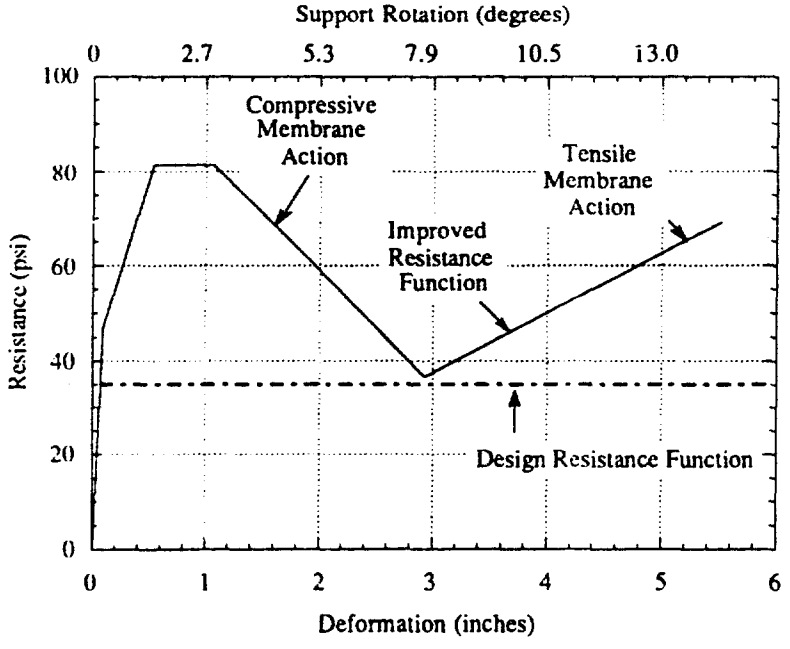

Figure III-6. Example Comparison of Improved Resistance Function with Standard Design Resistance Function.

Four sets of calculations were performed: (1) a base case with one DOF and the *PCDM* resistance function; (2) one DOF with the improved resistance function; (3) two DOFs with the *PCDM* resistance function; and (4) two DOFs with the improved resistance function. Table III-6 compares the four predictions and the observed wall rotations for the 14 test cases in the data base. The column headings denote the use of the one or two DOF model, and the design or improved resistance function. The table also shows the *L/t* ratio (clear span-to-thickness) for the test slabs.

TABLE III-6. COMPARISON OF OBSERVED AND PREDICTED ROTATIONS FOR BURIED SLABS SUBJECTED TO BURIED BURST.

Test[d]	L/t	Observed Rotation (Degrees)	Single Degree-of-Freedom				Two Degree-of-Freedom			
			PCDM R		Improved *R*		*PCDM R*		Improved *R*	
			Rotation (Degrees)	Prediction Error Ratio[c]	Rotation (Degrees)	Prediction Error Ratio[c]	Rotation (Degrees)	Prediction Error Ratio[c]	Rotation (Degrees)	Prediction Error Ratio[c]
A4	10	0.99	4.28	0.23	1.94	0.51	1.55	0.64	0.95	1.04
A5	10	5.62	10.29	0.55	9.60	0.59	6.11	0.92	4.94	1.14
A5A	10	Breach	10.60	–	9.51	–	7.29	–	5.78	–
A6	10	4.13	13.38	0.31	12.09	0.34	7.92	0.52	7.11	0.58
A6A[a]	10	9.53	15.96	0.60	13.63	0.70	11.41	0.84	9.64	0.99
A7	5	1.66	6.59	0.25	2.74	0.61	3.72	0.51	1.65	1.01
A7A[a]	5	9.2	13.32	0.69	8.26	1.11	10.58	0.87	5.90	1.56
A8[b]	10	2.65	7.46	0.36	6.45	0.41	4.32	0.61	3.27	0.81
A8A[a]	10	2.49	6.74	0.37	5.58	0.45	3.88	0.64	2.87	0.87
A9	10	7.75	13.72	0.56	12.59	0.62	8.42	0.92	7.35	1.06
B1	10	Breach	25.68	–	22.90	–	14.61	–	12.76	–
B2	5	4.1	20.32	0.20	15.79	0.26	9.87	0.42	5.09	0.81
B3	10	3.8	7.05	0.54	6.12	0.62	3.94	0.96	3.06	1.24
B4	10	30	24.68	–	21.74	–	11.26	–	9.97	–

Notes:

[a] Retest of preceding test element.

[b] Retest of Test 4 test element.

[c] Prediction Error Ratio = Observed Rotation/Predicted Rotation.

[d] Test Series A = Tests performed at Fort Polk [Baylot, *et al.*, 1985].
Test Series B = CONWEB test series performed at Fort Knox [Hayes, 1989].

The results shown in Table III-6 were computed using measured peak free-field ground shock data, in an attempt to remove ground shock prediction uncertainty. However, complete removal of loading uncertainty is not possible since computation of structural response requires the complete time histories for both free-field stress and free-field velocity. While some complete load history data were available for some of the test articles, the data were not of consistent high-fidelity. Hence, the waveforms given in the *PCDM* were used. Also, the peak free-field velocity was computed from the peak stress using Equation (III-2).

Figure III-7 (*PCDM* Figure V-6) illustrates the free-field stress and velocity waveforms, as used in the computations to obtain Table III-6. As can be seen, the free-field stress decays more rapidly than the free-field velocity. Although the *PCDM* provides these waveforms, the use of different waveforms for stress and velocity in computing structural response is a departure from the basic *PCDM* approach, since the *PCDM* permits the designer to use a single waveform (the stress waveform) for computation of structural response, to simplify the design process. That is, the designer is permitted to estimate the free-field velocity from the free-field

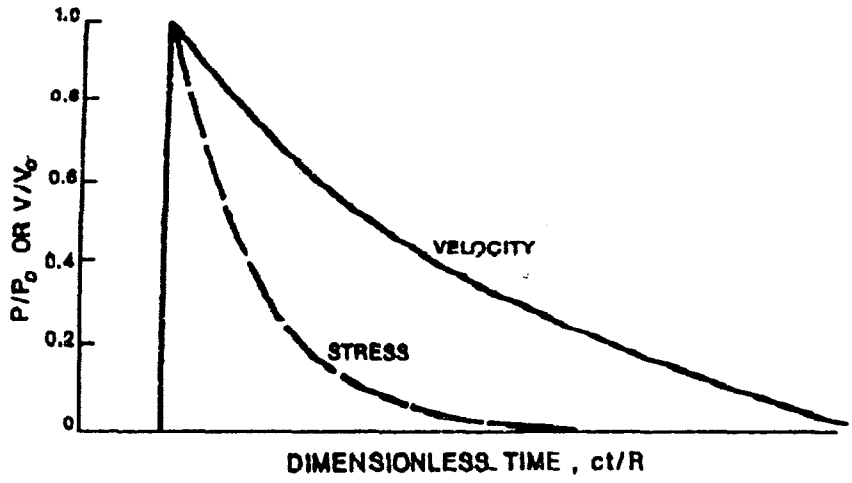

Figure III-7. Typical Free-Field Stress and Particle Velocity Waveforms.

stress using Equation (III-2), at all times. Estimating the free-field velocity waveform using the stress waveform underestimates the free-field velocity, after the peak has occurred, and can result in underestimates of structural displacement. Underestimates are likely for stiffer structures that stay in contact with the soil longer and are, therefore, more sensitive to the entire loading history. This effect is also amplified in weaker and/or compressible soils that exhibit slowly decaying velocity histories and large free-field displacement.

Different waveforms for stress and velocity were used in the computations for Table III-6 so as not to confound the prediction error introduced by using a single waveform with the basic structural response prediction uncertainty. The prediction error introduced by using a single waveform will be a function of the structural stiffness (related to the *L/t* ratio) and the soil properties. The waveforms used were those given in the *PCDM*, except for the structures labeled B1, B2, and B4 in Table III-6. For these structures, the basic waveform shape given in the *PCDM* was used, but the rate of velocity decay was reduced to match actual measurement records obtained during the test. These structures were situated in clay backfill and the *PCDM* tends to overestimate the rate of decay for such soils.

Table III-7 presents the summary statistics (for each of the four computational cases) of the prediction error ratios given in Table III-6. Also, statistics are provided considering all of the data together and separately for the two *L/t* ratios. A distinction between the *L/t* ratios is made since the flexural response mode may not be valid for very short stiff spans. The results show that the model appears to perform better for the larger *L/t* ratio (mean prediction error ratio generally closer to 1.0 and smaller coefficient of variation), although the sample size for *L/t*=5 is quite small.

Table III-7 indicates that as improvements to the model are made (*i.e.*, SDOF to 2DOF; and *PCDM R* to improved *R*), the mean prediction errors tend to 1.0 and the coefficient of variation reduces. The fact that the coefficient of variation improves indicates that the model

TABLE III-7. STATISTICS OF PREDICTION ERROR RATIOS REPORTED IN TABLE II-5.

		Single-Degree-of-Freedom		Two Degree-of-Freedom	
		PCDM R	Improved *R*	*PCDM R*	Improved *R*
All Data $n = 11$	Mean	0.42	0.57	0.71	1.01
	σ	0.17	0.23	0.19	0.26
	δ	0.40	0.40	0.27	0.25
$L/t = 10$ $n = 8$	Mean	0.44	0.53	0.76	0.97
	σ	0.14	0.12	0.17	0.21
	δ	0.31	0.23	0.23	0.22
$L/t = 5$ $n = 3$	Mean	0.38	0.66	0.60	1.13
	σ	0.27	0.43	0.24	0.39
	δ	0.71	0.65	0.40	0.34

Notes:
σ = Standard Deviation
δ = Coefficient of Variation = Standard Deviation/Mean
n = Number of Data Points

improvements are not simply systematic adjustments, but are theoretical improvements that account for behavioral differences of different structures.

As mentioned above, the 2DOF model accounts for possible motion of the reaction structure and is necessary because of the small size of the test articles. Actual full-scale protective structures are not likely to be displaced significantly (relative to the wall deflection); hence, the SDOF prediction error statistics in Table III-7 overstate the prediction error associated with using the SDOF model for a full scale structure. Thus, the 2DOF prediction error statistics are more indicative of the prediction error for full scale structures (*i.e.*, even when the SDOF model is used).

The effect of using the improved resistance function will depend on the response level. A review of Table III-6 shows that the ratio of the predicted rotations using the design and improved resistance function varies from about 1.1 to 1.6. Thus, it is not possible to develop a simple systematic correction factor for the response obtained using the design resistance function. Hence, for reliability-based design, the improved resistance function should be used.

Based on the above analyses, the results in Table III-7 under the 2DOF, Improved *R*, column heading, for L/t=10 indicate that the improved resistance function should be used in place of the design *R*, when performing reliability-based design. This RBD model is, however, valid only for structures that exhibit behavior similar to the test structure (*i.e.*, similar flexibility and predicted rotations in the range of the test data).

3. Model Parameter Uncertainty

The parameters used in the flexural response model are the soil parameters used in the free-field velocity and ground shock model, the slab thickness, and the reinforced concrete material parameters used in the structural restoring force function. Uncertainty in the soil parameters was discussed previously in Section III.B.5. For protective design, the importance of uncertainties in the wall thickness and the reinforced concrete material parameters is small compared with model prediction error uncertainties and soil property variability. Hence, these parameters can be assumed deterministic for protective design.

4. Reliability Model

To develop RBDFs for flexural mode analysis of buried structures, the ground motion uncertainty is propagated through the structural response analysis procedure, incorporating the structural response prediction and parameter uncertainties as described and characterized above. At this time, we have not, however, developed simplified RBDFs for use with the *PCDM* deterministic methodology because of the previously noted systematic errors. The following paragraphs discuss the factors that will influence the RBDFs.

The reliability-based design factors for flexural response of a buried slab depend on the flexibility of the slab and the soil properties. For stiff slabs that stay in contact with the soil throughout all, or most of the loading (*i.e.*, do not cavitate), the peak deflection is approximately the free-field ground displacement (less any rigid-body structural motion). Thus, the uncertainty in predicting the peak slab deflection will be equivalent to the uncertainty in the peak free-field displacement (which is dependent on soil strength and compressibility). For very flexible slabs, the slab will separate from the soil very early in the load history, so that the peak deflection will be that required to dissipate the impulse imparted to the structure. Thus, the structural response will be most sensitive to the peak free-field velocity (rather than displacement) and the structural restoring force function. Therefore, the response prediction uncertainty will depend on the uncertainty in the peak free-field velocity, the structural restoring force uncertainty, and the response prediction uncertainty.

In practice, structural slabs will fall in between the two extreme cases described above. The RBDFs will need to be developed for several cases, considering stiff to flexible walls (over the range for which the structure-media interaction model is applicable), for soils of poor to excellent competence, and for different levels of soil property uncertainty. Developing the RBDFs for stiff slabs will require a comprehensive review of peak free-field displacement data.

Based on the review of flexural response analysis of buried structures, we summarize the further research needs as follows:

1. Perform bounding probabilistic analyses for SMI cases of interest in protective design. These analyses would permit the prioritization of the research requirements.

2. Develop improved peak free-field displacement prediction methods and perform uncertainty quantification, noting that free-field displacement is a lower bound to the structural deflection.
3. Improve characterization of the decay portions of the free-field stress and velocity waveforms and quantification of the uncertainty.
4. Develop improved resistance functions for structural slabs under large displacement and quantification of the uncertainty.
5. Develop improved models of the state of damage based on the structural response computation and quantification of the uncertainty.

D. BREACHING

For detonation close to a buried structure failure tends to be due to localized breaching. A methodology for determining wall thickness required to prevent breaching is given in the *PCDM* (*PCDM* Equation (IX-1)). Figure III-8 shows the breaching curve and an equation for the curve developed from regression analysis [Fuehrer and Keeser, 1977]. The data points in Figure III-8 are approximately the scaled range of incipient breach.[1] The breaching equation is given as:

$$\frac{R}{W^{1/3}} = 0.038\left(\frac{t^2}{LW^{1/3}}\right)^{-0.88} \qquad \text{(III-14)}$$

where R is the standoff distance (*feet*) at which breaching occurs, W is the charge weight (*pounds* of C-4), t is the slab thickness (*feet*), and L is the free span length (short span) (*feet*).

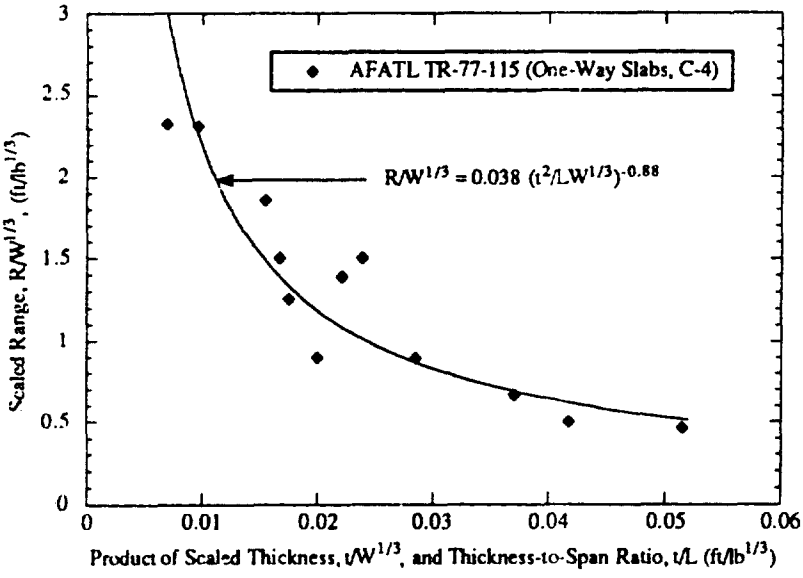

Figure III-8. Scaled Breach Range *vs.* Product of Scaled Thickness and Thickness-to-Span Ratio.

[1]Each data point represents the results of a test series wherein the bomb was moved closer and closer to the structure in order to define the range of incipient breach.

The structures tested were all one-way slabs, and the explosive used in the tests was C-4. Hence, for other explosive types, W should be adjusted by the appropriate equivalence factors given in the *PCDM*. Also, Equation (III-14) should not be used for values of $(t/L) \times (t/W^{1/3})$ greater than approximately $0.05\ feet/pound^{1/3}$. For very deep walls the breaching equation may be significantly in error [Kiger and Albritton, 1980].

The data shown in Figure III-8 were used to develop reliability-based design factors for breaching. Equation (III-14) is first rewritten in terms of the wall thickness required to prevent breach, t_b — that is,

$$t_b = \left[0.0243 \left(\frac{R}{W^{1/3}}\right)^{-1.136} L\, W^{1/3}\right]^{1/2} \qquad \text{(III-15)}$$

The prediction error associated with this equation can be characterized by the prediction error ratio:

$$\xi = \frac{t_{obs}}{t_{pred}} \qquad \text{(III-16)}$$

where t_{obs} = experimentally observed thickness required to prevent breaching, and t_{pred} = predicted thickness required to prevent breaching (Equation (III-15)).

Figure III-9 shows a plot of the prediction error ratio as a function of scaled range. There is a significant range bias in the data. This response was noted by Fuehrer and Keeser [1977], as scaled range decreases through $1.3\ feet/pound^{1/3}$, there is an apparent change in response behavior from flexural failure to massive concrete failure (crushing of the front face). This systematic bias in the breaching model is also demonstrated by the box plots of Figure III-10. The figure shows the prediction error ratios for scaled range less than $1.3\ feet/pound^{1/3}$ plotted alongside the prediction error ratios for scaled range greater than $1.3\ feet/pound^{1/3}$. The bottom line of the box is the 25^{th} percentile value, the middle line is the 50^{th} percentile value, and the top line is the 75^{th} percentile value. The vertical lines extending from the box show the range of the data. The dot inside the box is the mean value. A statistical t-test (mean separation test) verifies that the difference in mean prediction error ratio for the two range sets is significant.

From these results we conclude that the breaching model should only be used for scaled ranges less than $1.3\ feet/pound^{1/3}$. Beyond this range, the flexural response model (described in Section III.C) should be used. Thus, reliability-based design factors are developed here for designing wall thicknesses for scaled ranges less than $1.3\ feet/pound^{1/3}$.

To develop the reliability-based design factors, the dependence of the prediction error on range (for scaled range less than $1.3\ feet/pound^{1/3}$) is first investigated. A regression analysis was performed for this investigation. The results of the regression analysis show that there is a positive slope for prediction error ratio *vs.* range, (that is, the prediction error ratio increases with scaled range); however, the slope is not statistically significant due to the wide scatter in the data and the relatively small amount of data.

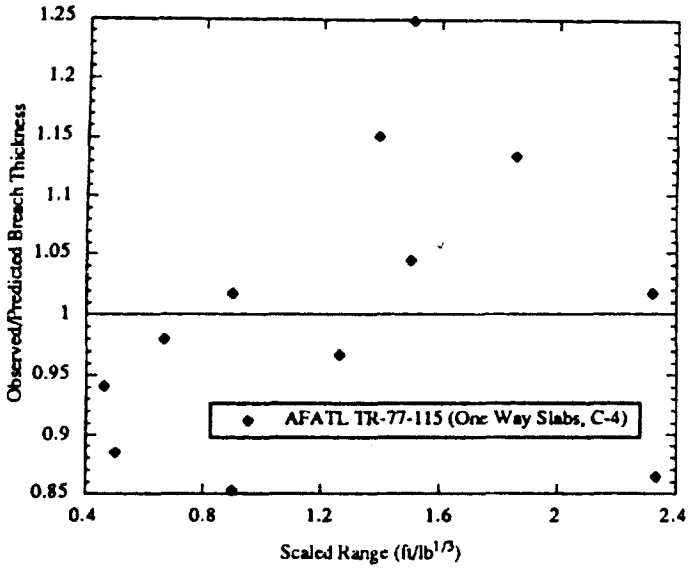

Figure III-9. Prediction Error Ratio *vs.* Scaled Range.

Based on the above results, the reliability-based design model is taken to be range-independent. For scaled range less than or equal to 1.3 *feet/pound*$^{1/3}$, the mean prediction error ratio is 0.94 and the coefficient of variation is 6.5 *percent*. Both normal and lognormal models fit the limited data. Rounded reliability-based factors are given for only the three reliability levels shown in Table III-8. At this time it is not possible to substantiate factors at higher or lower reliability levels.

The design factors in Table III-8 are used as follows:

1. Evaluate nominal thickness required to defeat breaching using Equation (III-15).
2. Select the desired design reliability based on the structure mission and then select the corresponding design factor from Table III-8.
3. Multiply the nominal thickness obtained in Step 1 by the design factor obtained in Step 2 to obtain the RBD thickness.

Note that the RBDFs assume that, for protective design, the scaled range is specified and the wall dimensions are well-controlled so that all parameters in Equation (III-15) are deterministic.

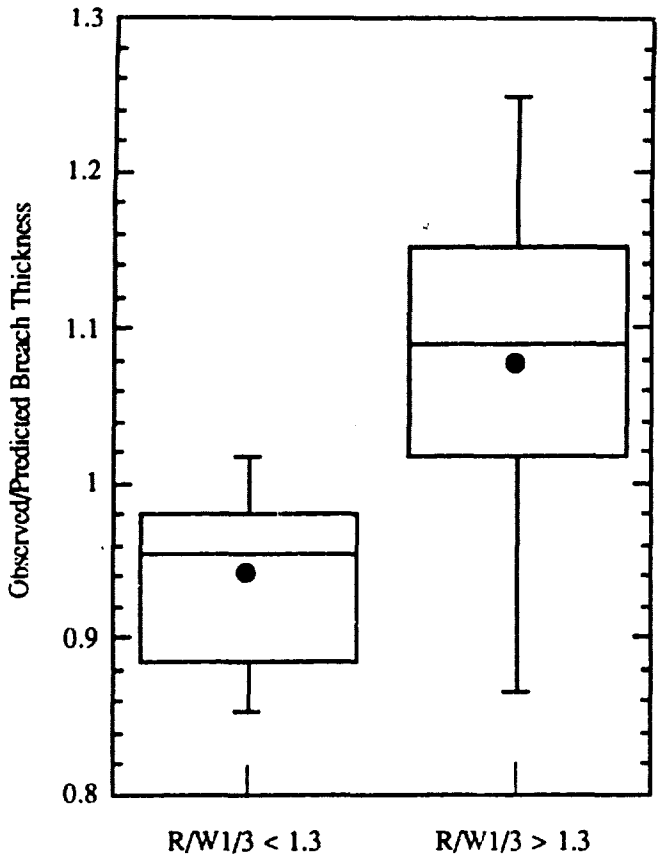

Figure III-10. Comparison of Prediction Error Ratio, Scaled Range < 1.3 *vs.* Scaled Range > 1.3.

TABLE III-8. RELIABILITY-BASED DESIGN FACTORS FOR BURIED REINFORCED CONCRETE STRUCTURES TO RESIST BREACHING (SCALED RANGE LESS THAN 1.3 *feet/pound*$^{1/3}$).

Reliability	RBDF (t/t_b)
0.25	0.90
0.50	0.95
0.75	1.00

IV. FRAGMENTATION EFFECTS

A. INTRODUCTION

Fragments from a standoff burst of a cased weapon produce damage to protective structures by their ability to penetrate structural elements and because of the loads they impart to structural elements. Both of these effects are inherently random since the physical parameters describing fragments and their trajectories are random variables (*e.g.*, weight, velocity, shape, impact angle, impact orientation, and number of impacting fragments). In this section, we develop preliminary reliability-based design procedures for both design fragment selection and fragment impulse.

The current procedures for design fragment selection and fragment penetration are given in *PCDM* Sections VI.B and VI.D.2, respectively. Although the *PCDM* design fragment selection procedure recognizes variability in fragment mass (via Mott's distribution), *PCDM* Section VI.B.2.c specifically states that there is no direct relationship between confidence levels selected using Mott's distribution and survival probability. The level of safety provided by protecting against a design fragment of a given Mott distribution confidence level varies significantly with changes in the weapon/target geometry (*i.e.*, standoff and presented area of the target). The dependence of reliability on weapon/target geometry is illustrated in *PCDM* Section II.F.2, *PCDM* Example VI-7, and in a paper by Dass and Twisdale [1987]. Therefore, reliability-based design fragments must incorporate parameters beyond those currently considered in the *PCDM* methodology. A preliminary RBD framework for selecting a design fragment is developed in Section IV.B. The methodology is illustrated for a Mk82 500-*pound* GP bomb using the *PCDM* fragment penetration formula for concrete (*i.e.*, *PCDM* Equation (VI-39)). The design fragment selection procedure summarized in Section IV.B.3 is based only on the distributions of the fragment parameters, the weapon/target geometry, and a lethality function that specifies the relative importance of the random fragment parameters. Uncertainty in target resistance to fragment penetration, perforation, or spall is not considered in the reliability-based selection of a design fragment.

Because a suitable design fragment selection model was not available at the outset of this task, efforts were focused on developing and illustrating the RBD framework mentioned above. Additional research will be required to tabulate results for use in selecting design fragments. In addition, further research is required to develop validated fragment penetration formulas, since the current formulas tend to significantly overpredict penetration depth for high-speed fragments, generated by modern weapons.

A preliminary RBD procedure for estimating fragment impulse is given in Section IV.C. The procedure is consistent with the current *PCDM* deterministic approach (Sections VI.C.3 and VI.C.4 of the *PCDM*), and assumes that the fragment spray pattern is a uniformly expanding cylinder. The primary random variable considered in the fragment impulse procedure, therefore, is the mean fragment striking velocity. RBDFs for fragment velocity are provided for use with the *PCDM* fragment impulse methodology. Current research efforts are developing improved

fragment dispersion and fragment-structure interaction models that will allow for more detailed treatment of fragment load uncertainties.

B. RELIABILITY-BASED FRAMEWORK FOR SELECTION OF A DESIGN FRAGMENT

In traditional, deterministic protective construction, the structure is designed to withstand the penetration, perforation, and/or spall effects of a "design" fragment. The *PCDM* procedure for specifying the weight, initial velocity, and nose shape of a design fragment is given in *PCDM* Section VI.B. Specifying appropriate design values for these parameters is complicated by the uncertainties in predicting them. Although *PCDM* Section II.F.2 presents the exploratory research by Dass and Twisdale [1987] that demonstrated the dependence of design reliability on weapon/target geometry, and *PCDM* Section VI.B.2.c alerts the designer to this fact, simplified reliability-based procedures for design fragment selection were not available at the time the *PCDM* was published. The *PCDM* procedure is therefore a traditional one (similar to that given in the Army manual, TM5-855) and only recognizes uncertainty in fragment weight using the Mott distribution and probabilistic confidence levels. However, since this traditional procedure assumes that confidence levels represent the probability that the design fragment will be the heaviest fragment produced, and since it does not take into account the number of fragments that strike the target, there is no general relationship between confidence level and survivability, as demonstrated by Dass and Twisdale [1987].

The design fragment should be specified so that the structure designed to resist this fragment will protect its contents with some known level of confidence. Thus, specification of the design fragment must consider uncertainty in each of the fragment variables, how these variables combine to produce a load-effect (*i.e.*, the synergism of the fragmentation variables), and the number of fragments that will strike the target. We shall refer to the load-effect produced by a design fragment as its lethality. For example, lethality can be quantified in terms of the design fragment's ability to penetrate, perforate, or cause back face spalling of a protective structure element. Since lethality represents a load-effect (as opposed to a measure of structural capacity), lethality is a function of the fragment variables only.

1. Review of *PCDM* Procedure for Selection of Design Fragment

The parameters used in the current *PCDM* approach for characterizing the design fragment are the fragment weight, striking velocity, and nose shape. The design fragment is assumed to be on a trajectory that is normal to the target, to impact with an orientation that is collinear with the target normal, and is assumed to have zero rotational velocity. Selection of the design fragment parameters is briefly summarized in the following paragraphs.

a. Shape

In the current design approach the standard fragment shape illustrated in Figure IV-1 is assumed. As seen, the standard fragment shape has an axisymmetric blunt-nosed geometry. For penetration analysis, the nose shape factor is given by *PCDM* Equation (VI-19):

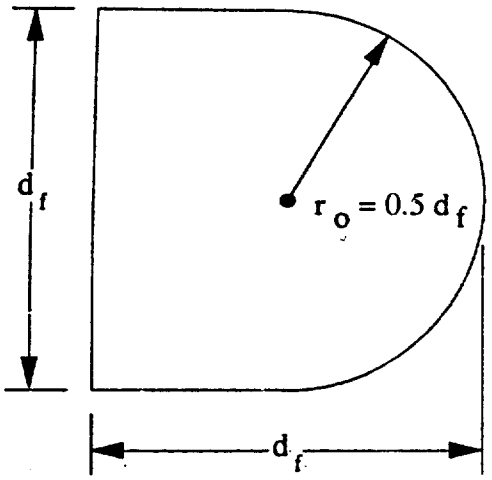

Figure IV-1. The Standard Fragment Shape.

$$N = 0.72 + 0.25\sqrt{n_c - 0.25} \tag{IV-1}$$

where n_c is the caliber radius of the fragment nose,

$$n_c = r_o/d_f, \tag{IV-2}$$

r_o is the tangent ogive radius, and d_f is the fragment diameter. For the standard fragment shape, n_c = 0.5 and N = 0.845.

b. Velocity

Both the *PCDM* and TM5-855-1 [Department of the Army, 1984] assume that all fragments have the same initial velocity as given by Gurney's formula (*PCDM* Equation (VI-20) [Gurney, 1947]):

$$v_0 = \frac{G}{\left(\frac{W_c}{W} + \frac{n_G}{n_G + 2}\right)^{1/2}} \tag{IV-3}$$

where v_0 is initial fragment velocity, G is the Gurney characteristic velocity (a constant for a given explosive), W_c is casing weight, W is explosive weight, and n_G = 1, 2, or 3 for plane, cylindrical, or spherical geometry, respectively. Assuming the standard fragment shape, the striking velocity (velocity of the fragment at the target) of the design fragment is given by *PCDM* Equation (VI-24):

$$v_s = v_0 \exp\left(-7.70 \times 10^{-4} \frac{R}{W_f^{1/3}}\right) \tag{IV-4}$$

where v_s is the striking velocity (*feet/second*), R is the distance from the bomb to the target (*feet*), and W_f is the weight of the design fragment (*pounds*).

c. Weight

The weight of the design fragment is selected using Mott's distribution and is given by *PCDM* Equation (VI-11):

$$W_f^* = M_A^2 \ln^2 (1 - CL) \qquad (CL \leq 0.9999) \qquad \text{(IV-5)}$$

where W_f^* is the weight of the design fragment (*pounds*), M_A is the fragment weight probability distribution parameter ($\sqrt{lbs}$), and CL is the confidence level. The confidence level specifies the fraction of the fragments that will have weight less than the design fragment.

It is important to comment here that the term "confidence level" is actually a misnomer since the Mott distribution does not give the confidence that the design fragment will be the largest fragment produced or the largest fragment to strike the target. In fact, even for high confidence levels (*e.g.*, exceeding 90 *percent*), there could still be very high probability (*e.g.*, exceeding 99 *percent*) that fragments larger than the design fragment will strike the target. For example, general purpose bombs can generate tens of thousands of fragments. For a 90 *percent* confidence level design fragment, 10 *percent* of the fragments will have weight greater than the design fragment. Thus, there could be more than 1,000 fragments larger than the design fragment that could potentially perforate the structure. Clearly, if a sufficient number of fragments impact the target structure, the probability of failure will be very high and thäöëe probability of survival will be much lower than the 90 *percent* confidence level.

The importance of considering the number of fragment hits is illustrated in Figure IV-2 for target impacts by fragments from a 500-*pound* GP bomb. The actual probability function of the largest fragment that will strike the target is shown, assuming 1, 10, 100, or 1000 fragments hit the target. For one hit, the 90^{th} percentile fragment has a weight of about 170 *grains*. For 10, 100, and 1000 hits, however, the 90^{th} percentile weights of the largest fragment are approximately 650, 1500, and 2700 *grains*, respectively. To obtain a design fragment with a 90 *percent* probability that no heavier fragments will strike the target when n = 100, a Mott distribution confidence level of 0.999 is required.

2. Reliability-Based Procedure for Selection of Design Fragment

Since the protective structure will be dimensioned to defeat the design fragment, the design fragment should be selected so that it is associated with a true confidence level. The true confidence level is the confidence (or probability) that the structure will not be struck by a fragment that is more lethal (*e.g.*, penetrates deeper, is more likely to perforate, or is more likely to cause spall) than the design fragment. A simplified reliability-based procedure is developed in the following paragraphs, including design charts and tables for some specific cases and concluding with an example problem.

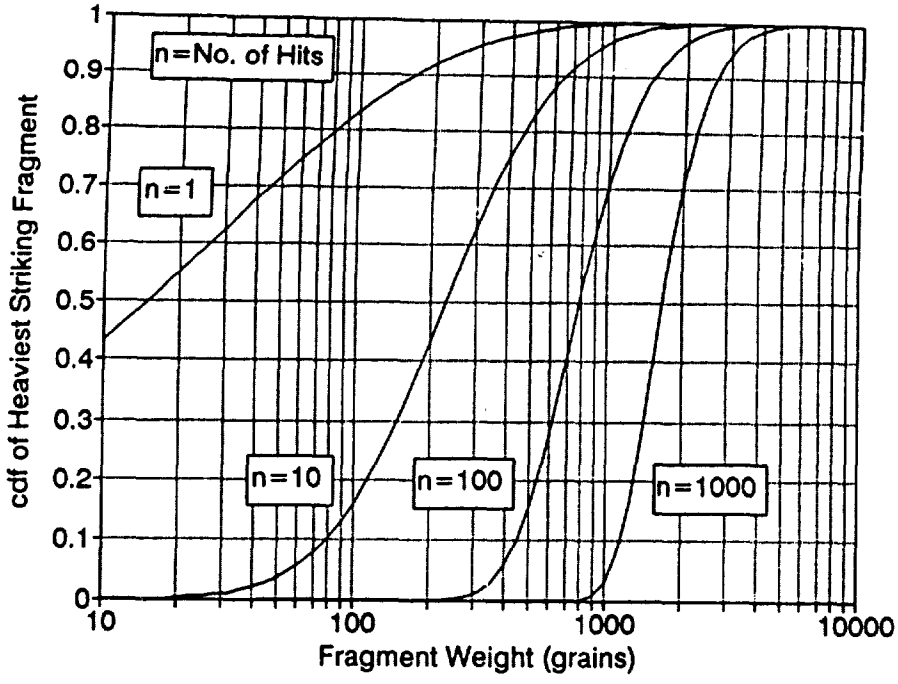

Figure IV-2. 500-*pound* GP Bomb Cumulative Distribution Function for the Heaviest Fragment to Strike a Target (Number of Hits = 1, 10, 100, or 1000).

a. Overview of RBD Framework

A number of variables affect the lethality of a fragment, such as the fragment weight, striking velocity (translational and rotational), shape and dimensions, impact angle, impact orientation, and hardness. The values of the fragmentation variables for individual fragments generated by a single bomb can vary widely. Thus, selection of a design fragment is not simply a matter of specifying the fragment weight as in the current design approach. In addition, the probability that the protective structure will fail will be a function of the number of fragments that impact the structure. The greater the number of impacting fragments, the greater the chance that fragments more lethal than the design fragment will hit the structure.

The reliability-based design approach developed herein encompasses the important fragmentation variables as well as the number of fragments that strike the target. The RBD approach is depicted in Figure IV-3. The method accounts for the multivariate nature of penetration by transforming the problem variables into a single load effect called the fragment lethality variable. Using this transformation and the distributions of the underlying fragment variables, the probability distribution for the lethality variable is computed. Finally, the expected number of fragment hits on the structure is evaluated and the extreme value distribution for the lethality variable is derived. The extreme value distribution is the appropriate distribution for use in designing the structure since it gives the probability that no fragments more lethal than the design fragment will hit the structure. Thus, the design fragment is selected from the extreme value

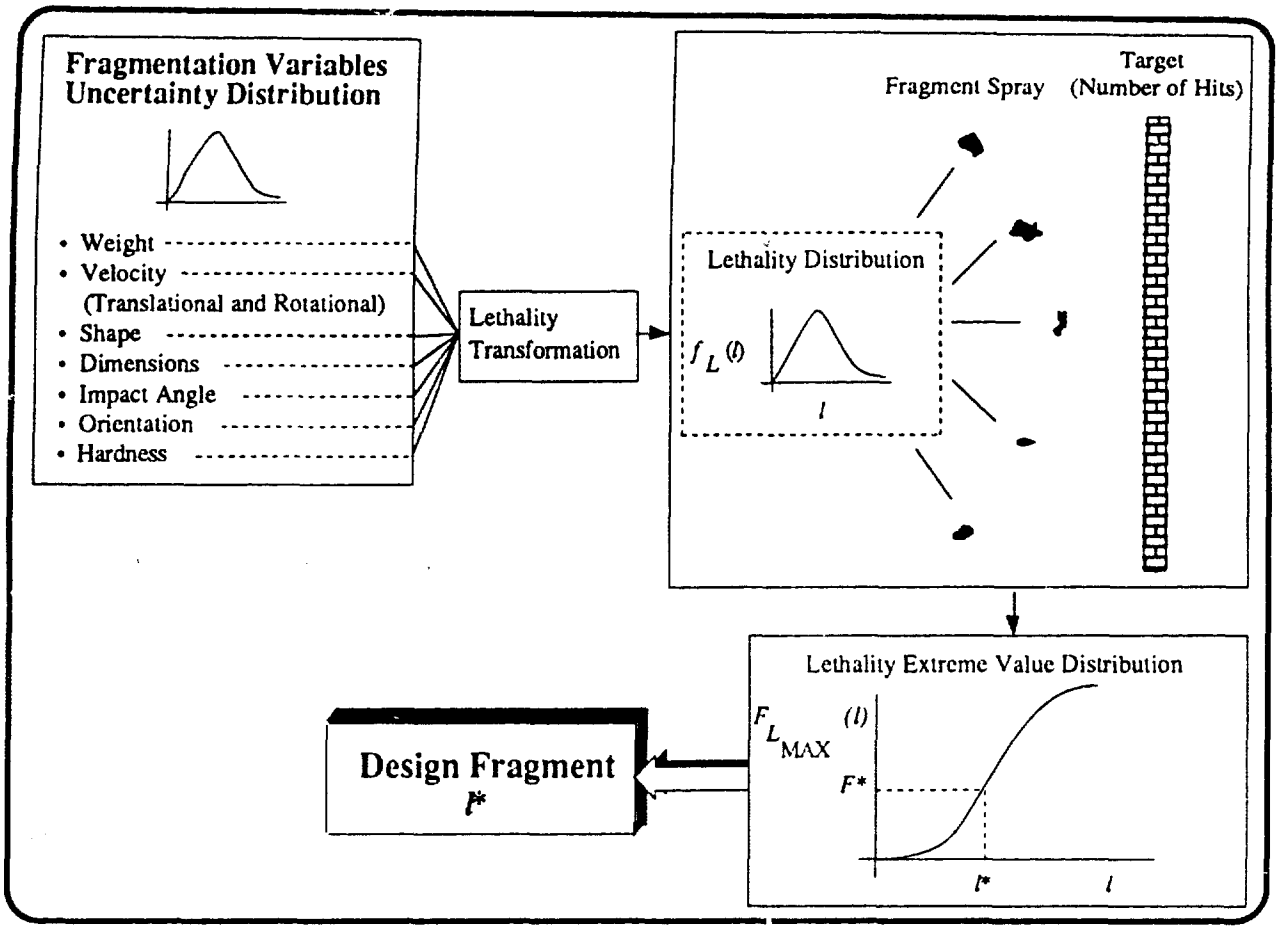

Figure IV-3. Developmental Framework for Reliability-Based Selection of a Design Fragment.

distribution for the lethality variable. Design charts and tables can be developed for a range of cases to aid in the selection of the design fragment so that the designer need not perform any probabilistic computations. Also, the probability that one or more fragments that are more lethal than the design fragment will hit the target (*i.e.*, in addition to the probability that no fragments more lethal than the design fragment impact the structure) can be obtained in closed form.

b. Lethality Variable Transformation

The first step in deriving the simplified reliability-based procedure is to transform the fragment descriptor variables into a single measure called the lethality variable. To do this, a transformation function is developed that accounts for the relative importance of each variable as it affects the ability of an individual fragment to penetrate, perforate, or spall the target (lethality). The transformation function used here is derived from existing penetration formulas.

The lethality of general purpose bomb fragments is a function of the fragment variables. Therefore, lethality can be generalized as

$$L = f(W_f, v_s, d_f, N, \theta, \phi, \phi, H) \qquad \text{(IV-6)}$$

where W_f is the fragment weight, v_s is the striking velocity, d_f is the fragment diameter, N is the nose shape factor, θ is the impact angle (*i.e.*, the angle between the fragment velocity vector and the target normal), ϕ is the angular orientation of the fragment on impact, $\dot{\phi}$ is the angular velocity of the fragment on impact, and H is a measure of the fragment hardness (*e.g.*, Brinnell hardness number).

To clarify Equation (IV-6), consider the *PCDM* fragment penetration equation for massive (*i.e.*, semi-infinite) concrete (*PCDM* Equation (VI-39)):

$$x_f = \frac{3.75\, W_f^{0.37}\, v_s^{0.9}}{(f_c')^{0.25}} \qquad x_f \le 3.5 W_f^{1/3}$$

$$x_f = \frac{2.01\, W_f^{0.40}\, v_s^{1.8}}{(f_c')^{0.50}} + 1.75 W_f^{0.33} \qquad x_f > 3.5 W_f^{1/3} \tag{IV-7}$$

In Equation (IV-7), x_f is the penetration depth (*inches*), W_f is the fragment weight (*pounds*), v_s is the striking velocity (*kilo-feet/second*), and f_c' is the concrete compressive strength (*ksi*). Equation (IV-7) assumes the standard fragment shape ($N = 0.845$), normal impact ($\theta = 0$), collinear impact ($\phi = 0$), and no tumbling ($\dot{\phi} = 0$). Fragment diameter (d_f) has been eliminated from Equation (IV-7) by assuming a density of 0.186 *pounds/inch*^{3} and expressing diameter in terms of weight for the standard fragment shape. Fragment hardness (*e.g.*, Brinell hardness number) is not a factor in the penetration equation because armor-piercing steel fragments are assumed (a correction factor for fragment hardness for other types of casing material is given by *PCDM* Equation (VI-41)). Thus, the only remaining fragment variables are W_f and v_s (f'_c is a structural resistance parameter).

If we restrict our attention to wall thicknesses typically used in concrete protective construction (*i.e.*, at least 12 *inches*), the second form of Equation (IV-7) will usually control the design. Furthermore, the contribution of the second term in the equation ($1.75\, W_f^{0.33}$) will usually be small compared to the first term for the striking velocities of interest (*i.e.*, 10 *percent* or less). Therefore, we select the following simplified lethality function to illustrate the reliability-based selection of design fragments:

$$L = W_f^{0.4}\, v_s^{1.8} \tag{IV-8}$$

The lethality function provides a relative measure of the ability of different fragments to penetrate concrete. However, since the *PCDM* fragment spall and perforation equations (*PCDM* Equations (VI-43) and (VI-45)) depend directly on the fragment penetration depth, x_f, the lethality function given in Equation (IV-8) is also a measure of a fragment's ability to cause spall or perforate a concrete element.

c. Lethality Variable Probability Density Function

The next step in deriving the reliability-based procedure is to compute the cumulative distribution function (cdf) for the lethality variable. The cdf gives the fraction of the fragments that will have lethality less than specified values. The cdf for the lethality variable will be a function of the transformation equation (Equation (IV-6)) and the probability distribution functions of the variables in Equation (IV-6). Standard probabilistic methods can be used here; however, closed form expressions for the lethality variable cdf will not be possible for most cases. Since the transformation equation is computationally simple to evaluate, it is straightforward to tabulate Monte-Carlo solutions for the lethality cdf for the weapons of interest, given a lethality transformation function and the required probability distributions for the fragment variables. Further, if we neglect drag effects and assume that striking velocity, v_s, is approximately equal to initial velocity, the tabulations are range-independent. Although neglecting drag effects is conservative, the assumption is most accurate for large fragments (*i.e.*, the fragments most likely to cause damage). Also, for small standoffs associated with modern weapons, drag effects are not expected to be significant.

To illustrate the process of tabulating a lethality cdf, we consider a Mk82 (500-*pound* general purpose bomb) and define the fragment lethality variable using Equation (IV-8). Based on this definition, and assuming that striking velocity, v_s, is approximately equal to initial velocity, preliminary results for the Mk-82 bomb are given in Table IV-1. The results must be taken as preliminary because (1) the use of *PCDM* Equation (IV-7) for high velocity fragment penetrators, (2) an assumed distribution is used for fragment velocity, and (3) the distributions of fragment weight and velocity are taken as independent.

As mentioned above, the cdf values shown in Table IV-1 are evaluated by Monte-Carlo simulation. For this analysis, Mott's distribution is used for fragment weight, with the parameter value given in *PCDM* Table VI-2 (*i.e.*, $M_A = 0.067$ *pounds*$^{1/2}$). *PCDM* Table VI-2 also provides estimates of the average initial velocity, and *PCDM* Section VI.B.4 provides limited information on the distribution of fragment velocity. For this illustration, a truncated lognormal probability distribution is assumed for fragment velocity. To account for an unconservative bias in *PCDM* Equation (VI-20), the mean fragment velocity is taken to be 5 *percent* greater than that given by the *PCDM* (see Section IV.C). The coefficient of variation (cov) is estimated using the following bounding procedure. Based on observations presented in *PCDM* Section VI.B.4, it is assumed that the 5th percentile fragment velocity is 1/2 of the mean velocity. This results in a cov for fragment velocity of approximately 40 *percent* (for a lognormal distribution). An upper bound velocity of 12,000 *feet/second* is assumed.[1] Finally, because paired data on the weights and velocities of individual fragments are not available, it is assumed that fragment weight and velocity

[1]The use of an upper bound in the fragment velocity distributions results in more realistic distributions. It also decreases the mean values and coefficients of variation slightly; however, this effect is small for the problem of interest.

TABLE IV-1. PRELIMINARY LETHALITY VARIABLE CUMULATIVE DISTRIBUTION FUNCTION FOR Mk-82 500-*pound* GP BOMBS BASED ON THE *PCDM* PENETRATION EQUATION.

Fraction of Fragments with Lethality < l, $F_L(l)$	Lethality, l ($pounds^{0.4}kilo\text{-}feet/second^{1.8}$)
0.01	0.05
0.1	0.33
0.2	0.64
0.3	0.98
0.4	1.4
0.5	1.9
0.6	2.4
0.7	3.2
0.8	4.6
0.9	7.2
0.95	9.6
0.975	13.1
0.99	16.3
0.995	19.9
0.999	26.0
0.9995	29.0
0.9999	37.0

are independent. This assumption is likely to be conservative since it is expected that these two variables may be negatively correlated (*i.e.*, fragments with larger weights probably tend to have lower velocities).

The above assumptions are conservative and are consistent with the currently available data. Since improvements are already being made in reporting the results of arena test data, more accurate characterization of the fragment variable distributions will be possible in the near future. As these data become available, revised tables of fragment lethality cdfs can be developed.

d. Probability Density Function for Selection of the Design Fragment - Lethality Extreme Value Distribution

For reliability-based design we need a simple procedure to completely specify the design fragment variables (*i.e.*, weight, velocity, etc.) so that the structure designed to defeat this fragment will have a known survivability level. Thus, we need to estimate the probability that the structure will not be impacted by a fragment that is more lethal than the design fragment. This probability is given in closed form by the Hypergeometric distribution

$$P(X=x) = \frac{\binom{m}{x}\binom{N_t - m}{n - x}}{\binom{N_t}{n}} \qquad \text{(IV-9)}$$

where the notation $\binom{m}{x}$ is the binomial coefficient

$$\binom{m}{x} = \frac{m!}{x!\,(m-x)!} \qquad \text{(IV-10)}$$

! is the factorial symbol,[1] N_t is the total number of fragments generated by the bomb, m is the number of these fragments with lethality greater than the design fragment, n is the number of fragments that actually impact the structure and do not ricochet, and x is the number of fragments that impact the structure with lethality greater than the design fragment.

The probability that no fragments with lethality greater than the design fragment will impact the structure is given by Equation (IV-9) with $x = 0$. For $x = 0$, Equation (IV-9) is also the extreme value distribution for the lethality random variable, $F_{L_{max}}(l)$. Extreme value distributions give the probability distribution of the largest (or smallest) value of a random variable that is sampled a known number of times. As the number of times the random variable is sampled increases, the probability of obtaining a larger maximum value increases. Here, the number of samples corresponds to the number of fragments that strike the target, n. As more fragments hit (*i.e.*, smaller standoffs, larger weapons, or larger targets), the probability of being hit by a fragment that is more lethal than the design fragment increases. This probability is precisely the probability given by Equation (IV-9) when $x = 0$. Thus, the extreme value distribution for the most lethal fragment to strike the target is

$$F_{L_{max}}(l) = P(L_{max} < l) = \frac{\binom{m}{0}\binom{N_t - m}{n - o}}{\binom{N_t}{n}} = \frac{\binom{N_t - m}{n}}{\binom{N_t}{n}} \qquad \text{(IV-11)}$$

$$= \frac{(N_t - m)!\,(N_t - n)!}{N_t!\,(N_t - m - n)!}$$

The design fragment is selected so that the probability given by Equation (IV-11) is the desired confidence level.[2] To evaluate Equation (IV-11), we need the total number of fragments generated, N_t; the fraction of these fragments with lethality greater than the design fragment, m; and the total number of non-ricochet fragment hits, n. Each of these variables is a random variable and cannot be deterministically predicted from bomb to bomb. However, a first order

---

[1] $m! = (m)\,(m-1)\,(m-2)\ldots(1)$.

[2] Because a general purpose bomb can generate tens of thousands of fragments, some numerical difficulty may be encountered in evaluating the factorials in Equation IV-11. To avoid the problem, two simple approaches for evaluating $F_{L_{max}}(l)$ are given in Appendix A.

approximation to the extreme value distribution can be obtained using the expected values of these variables. Procedures for estimating N_t, m, and n are given in the following subsections.

e. Total Number of Fragments

The expected total number of fragments generated by specific general purpose bombs can be obtained from the published results of arena testing. Alternatively, the number of fragments can be estimated by combining *PCDM* Equations (VI-4) and (VI-5):

$$N_t = \frac{W_c}{2 M_A^2} \tag{IV-12}$$

where W_c is the bomb casing weight, and M_A is the fragment weight probability distribution parameter. Values of M_A for several different weapons are provided in *PCDM* Table VI-2.

f. Number of Lethal Fragments

Once the total number of fragments is obtained, the expected number of these fragments with lethality greater than the design fragment, m, is obtained using the tabulated values of the cumulative distribution function of the lethality variable, $F_L(l)$ (*e.g.*, Table IV-1). That is,

$$m = N_t [1 - F_L(l)] \tag{IV-13}$$

where l is the lethality of the selected design fragment. Thus, the dependence of the extreme value distribution (Equation (IV-11)) on the number of fragments with lethality greater than the design fragment, m, is actually a dependence on the lethality of the design fragment, l, and the total number of fragments, N_t.

g. Number of Nonricochet Hits

The fraction of the bomb fragments that will hit the structure without ricocheting depends on the bomb standoff and orientation, the spatial distribution of the fragments (*i.e.*, spray pattern), the target size, and the angle at which ricochet occurs. Simple models are presented in *PCDM* Section VI.C.3 for both cylindrical and spherical fragment spray patterns. The procedures for estimating the number of non-ricochet hits for these two models are summarized in the following subsections. The *PCDM* also discusses the use of nonuniform fragment distributions that are based on polar zone data from arena tests. As PC-based CWE design tools come into use, more detailed fragment spray models should be incorporated into protective construction analysis and design. For the present, however, we shall restrict our attention to the more tractable cylindrical and spherical spray models.

(1) Cylindrical Pattern

The cylindrical spray pattern is most appropriate when c/R_o (*i.e.*, bomb length to standoff ratio) is relatively large and for weapons having significant beam sprays. Figure IV-4 illustrates the problem of computing the number of nonricochet hits when the fragment spatial distribution is assumed to be cylindrical (with all fragments having sufficient initial velocity to travel the distance to the target), and the bomb is assumed parallel to the target plane and nose tangent. For most cases this will be the most conservative situation. The number of non-ricochet hits is simply computed as the fraction of the expanding surface area that intersects the target within the ricochet angle. Thus,

$$n = N_t \frac{\left(\theta^+_{max} + \theta^-_{max}\right)}{2\pi} \frac{y}{c} \tag{IV-14}$$

where the two angles θ^+_{max} and θ^-_{max}, and the vertical dimension y are given by

$$\theta^+_{max} = min\left[\alpha, \tan^{-1}\frac{w - x}{R_o}\right] \qquad \textit{(radians)} \tag{IV-15}$$

$$\theta^-_{max} = min\left[\alpha, \tan^{-1}\frac{x}{R_o}\right] \qquad \textit{(radians)} \tag{IV-16}$$

$$y = min\ [c, h] \tag{IV-17}$$

As illustrated in Figure IV-4, w is the width of the target, x is the distance from the edge of the target to the point on the target directly opposite the bomb, h is the height of the wall, and c is the length of the bomb. The angle, α, is the ricochet angle measured from the target normal vector in *radians*. The fragments that have impact angles, θ (the angle between the normal to the target and the fragment velocity vector), less than α do not ricochet.

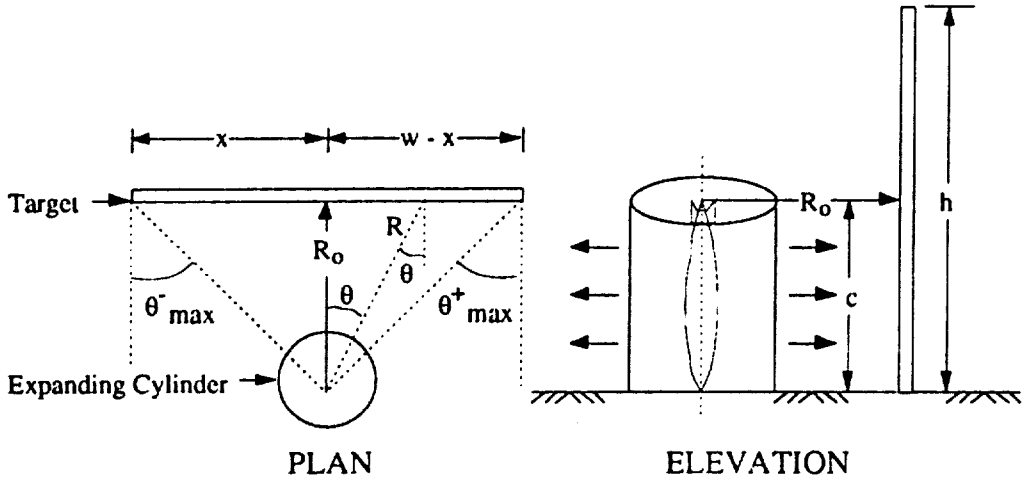

Figure IV-4. Fragment Non-Ricochet Hit Analysis Assuming a Cylindrical Dispersion Pattern.

(2) Spherical Pattern

The spherical spray pattern is most appropriate for small values of c/R_O and for weapons that have less distinct beam sprays. The spatial distribution is an expanding sphere centered at the weapon center of gravity, and all fragments are distributed uniformly over the surface of the sphere. The fraction of the fragments that will impact the structure is equal to percentage of the surface area of the expanding sphere intersected by the structure. Using the same definition as for the cylindrical case above, the fragments that do not ricochet are those that impact at an angle, θ, less than the ricochet angle, α; where θ and α are measured from the normal to the structure. The percentage of the expanding sphere surface area for non-ricochet is given by $\Omega/4\pi$. In which Ω is the intersected solid angle for nonricochet and 4 π is the total number of steradians in a sphere.

When the target structure is very large and the detonation is very close to and centered on the target, up to one-half of the fragments can impact the target. In this limiting case, the intersected solid angle of the fragment-spray sphere for fragments striking at angles less than the ricochet angle is

$$\Omega = 2\pi (1 - \cos \alpha) \qquad \text{(IV-18)}$$

Thus, the fraction of the fragments which strike the structure and do not ricochet is, $\Omega/4\pi = (1 - \cos \alpha)/2$. Note that for $\alpha = 45$ *degrees*, less than 15 *percent* of the total number of fragments will impact the structure and not ricochet in this most limiting case.

There is no simple equation that can be used to directly calculate the fraction of nonricochet fragments for all possible combinations of standoff, ricochet angle, etc. Assuming a planar target surface, Appendix B derives the equations needed to compute the fraction of nonricochet fragments for five cases that cover the range of possibilities. Using the formulation given in Appendix B, design charts have been developed, and a simple method is presented below to evaluate the fraction of fragments which strike the target structure and do not ricochet.

A typical weapon-structure geometry is sketched in Figure IV-5. The problem geometry is defined such that the structure is located in the X-Y plane and the weapon CG is located on the Z-axis. The Z-axis meets the X-Y plane in a point, O, which is also the orthogonal projection of the weapon CG on the structure plane. Typically the structure is divided into four separate sections with a common corner, O, and the total number of fragments hitting the target is obtained by summing over the four subsections. However, the point O need not lie within ABCD. The number of fragments hitting the target when O is outside ABCD must be obtained through proper addition and subtraction of the fragments hitting a larger rectangle that contains the point O.

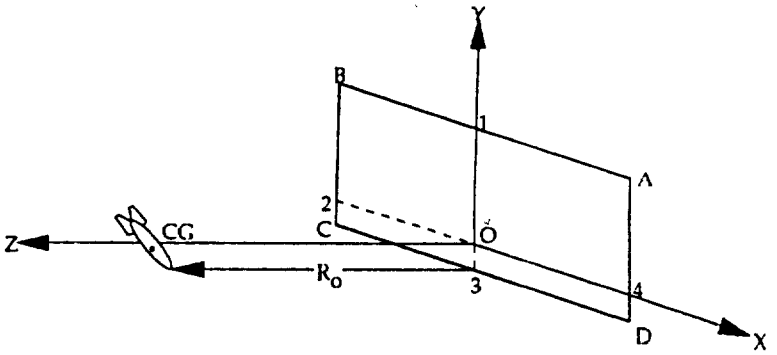

Figure IV-5. Typical Weapon Structure Geometry.

The fraction of nonricochet fragments impacting each section of the structure under the threat at a standoff, R_o, is calculated as follows:

1. Calculate the values of s ($= R_o/a$) and t ($= R_o/b$) where R_o is the standoff distance, a is section length, and b is the section height.
2. From the design charts (Figure IV-6 or IV-7) or the formulas in Table B-1 of Appendix B, obtain the fraction of nonricochet fragments, $\Omega/4\pi$, for the section. The design charts of Figures IV-6 and IV-7 have been developed for ricochet angles of 30 and 45 *degrees*, respectively.
3. The total number of nonricochet fragments impacting the section is now obtained by multiplying the fraction $\Omega/4\pi$ by the total number of fragments N_t (Equation (IV-12)).
4. This procedure is repeated for each section and the total number of nonricochet fragments impacting the structure is obtained by summing over each section.

3. Summary of Reliability-Based Procedure for Selection of Design Fragment

The preliminary reliability-based procedure for selection of the design fragment can be summarized as follows:

1. Select a reliability level based on the mission of the protective structure and an assessment of the threat.
2. Compute the expected number of total fragments generated by the specified threat, N_t (Equation (IV-12)).
3. Select a ricochet angle and fragment spray pattern, and compute the expected number of nonricochet hits. For a spherical spray pattern, use the design charts (Figures IV-6 and IV-7) or Table B-1 in Appendix B. For a cylindrical spray pattern, use Equation (IV-14).
4. Select a trial design fragment and compute its lethality (Equation (IV-8)).
5. Get the estimated nonexceedance probability for the design fragment lethality (computed in Step 4) from a design table (*e.g.*, Table IV-1 for a Mk-82 bomb; for other weapons, new lethality cdfs must be developed via Monte Carlo simulation).
6. Compute the expected number of lethal fragments in the total fragment population (Equation (IV-13)).

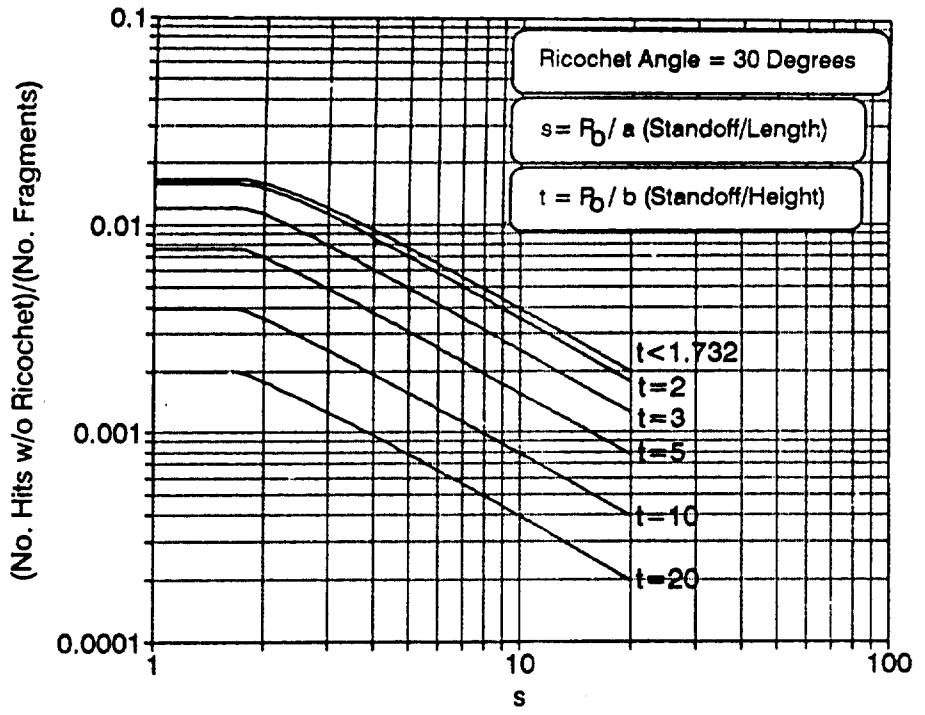

Figure IV-6. Fraction of Nonricochet Fragments Impacting Section (Ricochet Angle = 30 *Degrees*).

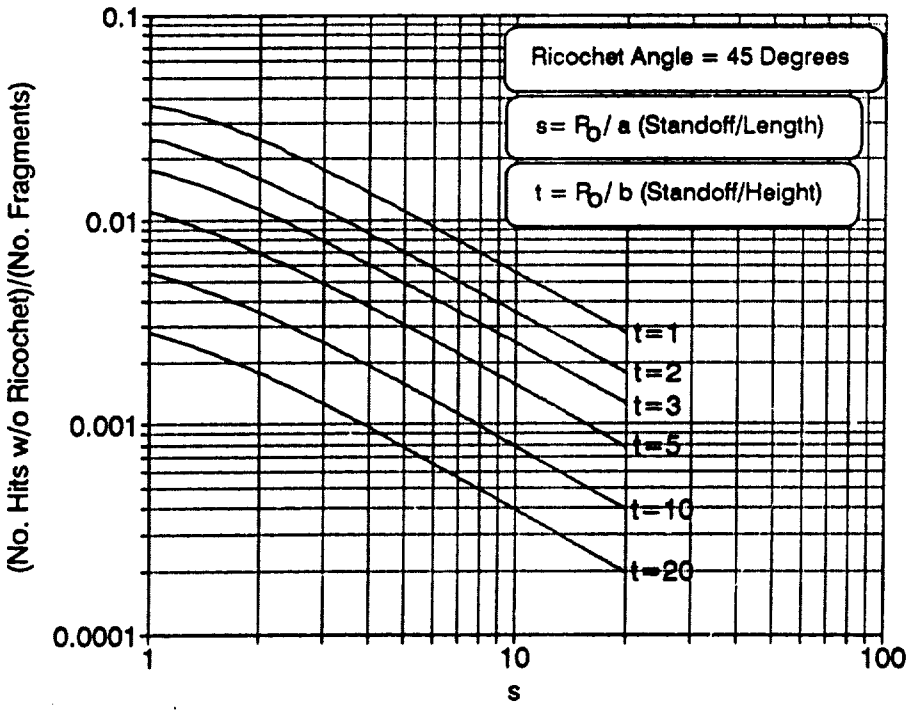

Figure IV-7. Fraction of Nonricochet Fragments Impacting Section (Ricochet Angle = 45 *Degrees*).

7. Compute the probability of no lethal hits from the Hypergeometric distribution (Equation (IV-11)).
8. If the probability in Step 7 is acceptable, go to Step 9; otherwise, revise the design fragment lethality up if the probability in Step 7 is too small, revise the design fragment lethality down if the probability in Step 7 is too large and go back to Step 4.
9. Design the wall to resist the design fragment using procedures given in *PCDM* Section VI.D.2. Note that Steps 1-8 only address fragment load-effect uncertainties. Reliability-based capacity reduction factors to account for penetration equation prediction errors and material property uncertainties should also be included in the final design.

The above steps are illustrated in the flowchart of Figure IV-8. Several assumptions and limitations of the procedure in its current state of development should be restated: (1) only cylindrical or spherical spray patterns are considered; (2) $F_L(l)$ has been tabulated only for a Mk82 GP bomb; (3) the tabulation for $F_L(l)$ assumes Motts distribution for weight, a lognormal distribution for velocity, and no correlation between weight and velocity; (4) the distribution for $F_{L_{max}}(l)$ is based on the expected values of N_t, m, and N (even though each of these variables is random); and (5) the lethality function is a simplified version of the *PCDM* fragment penetration formula for concrete that assumes normal collinear impact, no tumbling, standard shape, and standard armor-piercing steel hardness. As additional data become available and new deterministic procedures are developed, each of these assumptions and limitations can be relaxed within the general RBD framework presented in this section.

4. Reliability-Based Design Fragment Selection Example

As an example, we consider the selection of design fragments for a 12 *feet* by 12 *feet* door panel on a protective shelter that must resist penetration of fragments from a 500-*pound* Mk82 GP bomb at standoffs of 10, 20, 50, and 100 *feet*. Both spherical and cylindrical spray patterns are to be considered and a ricochet angle of 45 *degrees* is assumed. Pertinent parameters for the Mk82 threat are: $W_c = 311$ *pounds*, $M_A = 0.067$ *pounds*$^{1/2}$, and $c = 7.5$ *feet*.

To illustrate the design steps, we focus on selecting the design fragment for 90 *percent* reliability at a standoff of 50 *feet* for a spherical spray pattern.

First, we compute the expected total number of fragments generated by the bomb. The number of fragments is given by Equation (IV-12) as

$$N_t = \frac{311}{2(0.067)^2} = 34640 \qquad \text{(IV-19)}$$

where we have rounded to the nearest integer.

The second step is to compute the expected number of nonricochet hits on the panel. Given the 45-*degree* ricochet angle, we can either use the design chart given in Figure IV-7

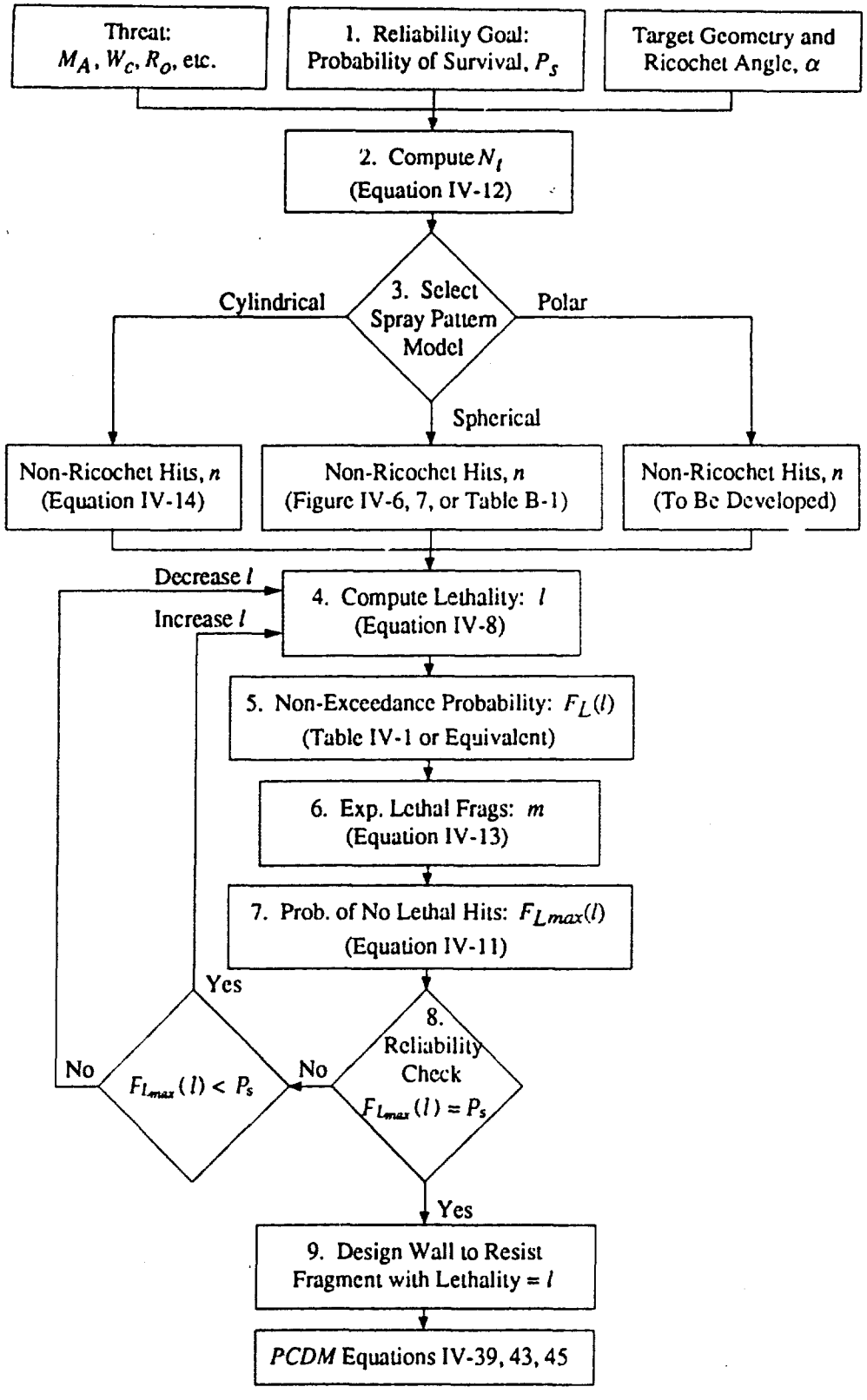

Figure IV-8. Preliminary Flowchart for Reliability-Based Selection of a Design Fragment

or use the formulas given in Appendix B. Assuming that the bomb is centered horizontally along the wall and that the center of the bomb is at a height of 3.75 *feet* (*i.e.*, half of the bomb length), the wall can be broken up into for sections — two that are 6 *feet* wide by 8.25 *feet* high and two that are 6 *feet* wide by 3.75 *feet* high. The calculations for the fraction of fragments hitting the panel are summarized in Figure IV-9. The expected number of nonricochet hits for a 50-*foot* standoff and spherical spray pattern is 156.

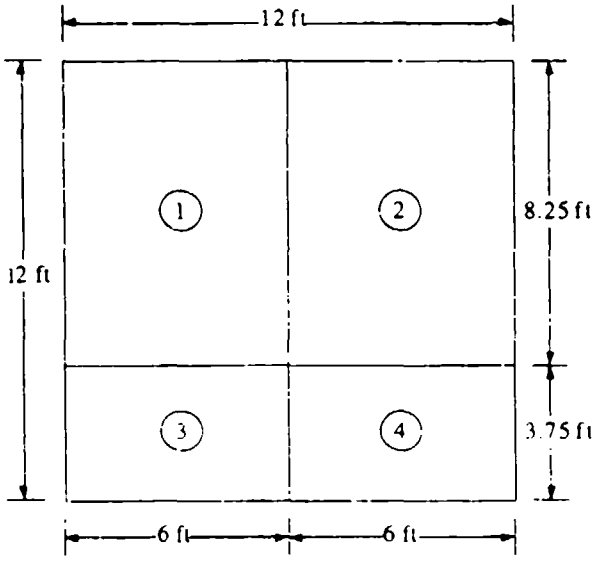

Section 1 or 2:

$R_O = 50ft$
$a = 6ft$, b = $8.25ft$
$s = 50/6 = 8.33$, $t = 50/8.25 = 6.07$
$\Omega/4\pi = 0.00154$ (see Figure IV-7 or Appendix B)

Section 3 or 4:

$R_O = 50ft$
$a = 6ft$, b = $3.75ft$
$s = 50/6 = 8.33$, $t = 50/3.75 = 13.33$
$\Omega/4\pi = 0.000710$ (see Figure IV-7 or Appendix B)

$n = [(2) \times (0.00154) + (2) \times (0.000710)] \times (34{,}640)$
$= 156$

Figure IV-9. Expected Number of Nonricochet Hits Computation for a 50-*foot* Standoff and Spherical Spray Pattern.

The next two steps are to select a trial design fragment and determine its non-exceedance probability using the preliminary lethality probabilities for Mk-82 bombs given in Table IV-1. To begin the iterative design process, we select a fragment with lethality greater than 99.9 *percent* of the fragments (*i.e.*, the 0.999 fragment with a lethality of 26.0 $pound^{0.4}$ $kilo\text{-}feet/second^{1.8}$).

The expected number of fragments with lethality greater than 26.0 $pound^{0.4}$ $kilo\text{-}feet/second^{1.8}$ is given by Equation (IV-13) as

$$m = 34640(1\text{-}0.999) \qquad \text{(IV-20)}$$

or 35 fragments, rounding to the nearest integer.

We now have all of the inputs needed to compute the reliability of the selected design fragment. The probability that no fragments more lethal than 26.0 $pound^{0.4}$ $kilo\text{-}feet/second^{1.8}$ will strike the panel is evaluated using Equation (IV-11) along with one of the two computational procedures given in Appendix A. The resulting probability is

$$P(L_{max} < l) = \frac{(34640 - 35)!\,(34640 - 156)!}{(34640)!\,(34640 - 35 - 156)!} = 0.854 \qquad \text{(IV-21)}$$

Thus, the 0.999 fragment almost provides the required reliability of 90 *percent*. If we increase the design fragment to 29.0 *pounds*$^{0.4}$ *kilo-feet/second*$^{1.8}$ (*i.e.*, the 0.9995 fragment) and repeat the above steps, the resulting reliability is 92.7 *percent*. Simple linear interpolation between these points yields a design fragment of approximately 27.9 *pounds*$^{0.4}$ *kilo-feet/second*$^{1.8}$ to achieve 90 *percent* reliability.

With a cylindrical spray pattern, the expected number of fragments striking the panel increases significantly. Using Equation (IV-14), the number of hits is

$$n = 34640 \frac{\left(2\tan^{-1}(6/50)\right)}{2\pi} \frac{7.5}{7.5} = 1317 \qquad \text{(IV-22)}$$

Since many more fragments strike the panel when the cylindrical spray pattern is used, the design fragment must be larger than in the spherical case. A design fragment at the 0.9999 lethality level (*i.e.*, 37.0 *pounds*$^{0.4}$ *kilo-feet/second*$^{1.8}$) produces a reliability of 89.0 *percent* which for all practical purposes meets the 90 *percent* reliability requirement. The 90 *percent* reliability design fragment obtained using the cylindrical spray pattern is approximately one-third more lethal than the corresponding fragment obtained using the spherical spray model due to the difference in the expected number of hits.

Table IV-2 gives the expected number of hits for each spray pattern model at standoffs of 10, 20, 50, and 100 *feet*. For the spherical spray pattern, the number of hits decays approximately as the square of the standoff. For the cylindrical spray pattern, the number of hits decays only linearly with range.

TABLE IV-2. NUMBER OF Mk82 BOMB FRAGMENTS STRIKING A 12-*FOOT* BY 12-*FOOT* PANEL (RICOCHET ANGLE = 45 *DEGREES*).

	Standoff (*feet*)			
Spray Pattern	10	20	50	100
Spherical	2834	898	156	40
Cylindrical	5958	3215	1316	662

The design reliabilities provided by the five largest entries given in Table IV-1 (*i.e.*, the 0.99, 0.995, 0.999, 0.9995, and 0.9999 fragments) are evaluated at the four standoffs ranging from 10 *feet* to 100 *feet* and are plotted in Figure IV-10 for both spherical and cylindrical spray patterns. The significant differences between the two plots emphasize the need for refined spray pattern models. For the cylindrical model, the 0.99 and 0.995 fragments are virtually certain to underpredict the most lethal fragment to strike the panel for any of the standoffs considered. The spherical model, on the other hand, leads to reliabilities of 67 *percent* and 82 *percent*, respectively, for these fragments at a 100-*foot* standoff.

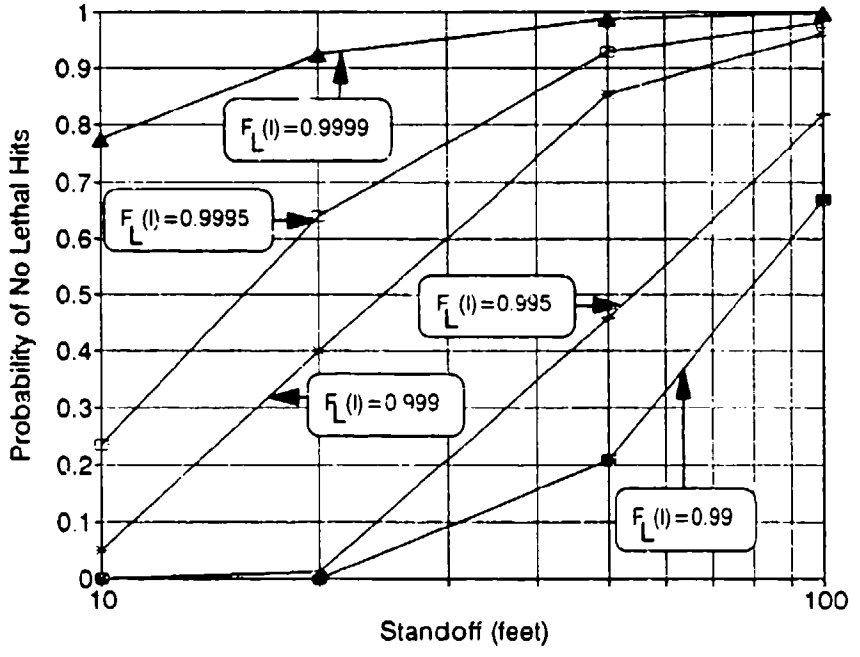

a. Spherical Spray Pattern

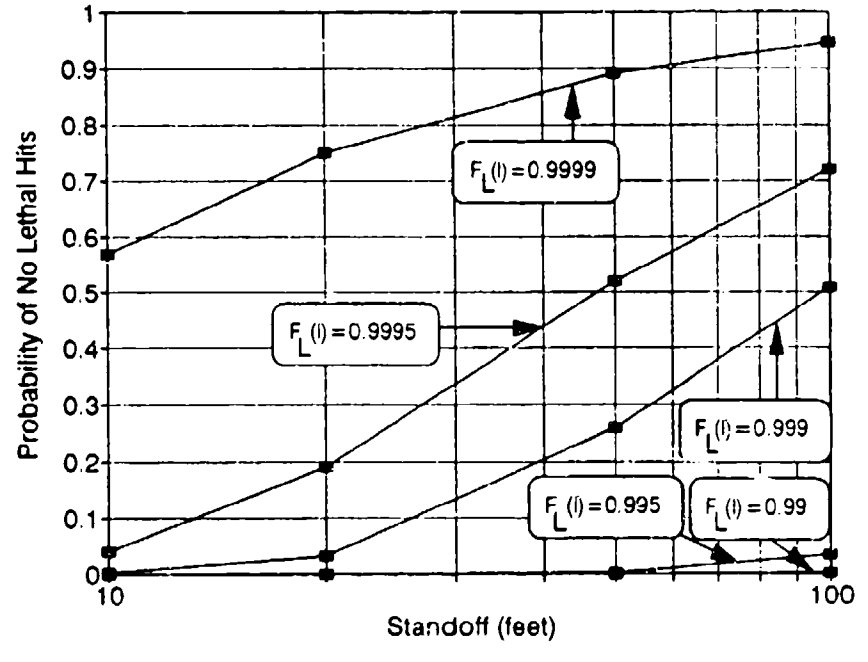

b. Cylindrical Spray Pattern

Figure IV-10. Reliability of Several Design Fragments for a 12-*foot* by 12-*foot* Panel Subjected to a Mk-82 GP Bomb.

Although the cylindrical model may be closer to actual fragment spray patterns, the cylindrical model is increasingly conservative as standoff increases and may lead to significant overdesigns. Thus, the potential payoff for developing improved spray pattern models for the selection of design fragments is significant.

5. Discussion and Need for Further Research

The foregoing is a systematic framework for reliability-based selection of design fragments. A validated, robust procedure can be implemented for PC-based design that is significantly better than the outdated CL approach. Final RBDFs can be developed within this framework as new bomb arena test data become available. New sophisticated data acquisition systems are making it possible to do a much better job of characterizing the fragmentation environment for protective design. In particular, better characterizations of the upper tail of the fragment weight distribution and of the entire fragment velocity distribution are needed, and the correlation between weight and velocity should be studied.

We emphasize that it is necessary to use the raw arena test data, before it is reduced, as presented in manuals such as the JMEM [1990]. The reduced data tables only provide averages and are insufficient for characterizing the distributions, in particular the upper tails required for protective design. In addition, the current JMEM tables are erroneous for the large weight fragments. The error arises because the new tabular format includes a finer discretization of the large fragment weights than was used in the old format. Finer discretization of fragment weight classes is a needed improvement; however, in fitting the old data into the new format, the JMEM authors have "created data." All of the fragments from the heaviest fragment group in the old table have been lumped in the new table assuming that they all have a weight equal to the average weight of the group. Thus, the new table implies that there is a large number of fragments at this average weight and that no fragments heavier than this were generated. Clearly this is unconservative for protective design.

Finally, we mention that the reliability framework, as presented here, makes it probable that the structure will not be hit by a fragment more lethal than the design fragment. However, the methodology can also be used to compute the probability that the structure will not be hit by any number of fragments more lethal than the design fragment. Thus, for cases wherein more than one fragment penetration would be required to cause damage, selecting the design fragment can be tailored to the specific damage criteria (*e.g.*, allowing one hit more lethal than the design fragment per 100 $feet^2$ of target area).

C. FRAGMENT IMPULSE

1. Overview and Assumptions

As a fragment impacts and penetrates a protective structure, it decelerates rapidly and its momentum is transferred to the structure. Due to the time scales involved, it is reasonable to assume that the fragment impact momentum is converted to an impulsive load on the structure.

The total impulsive load from the fragment spray of a standoff general-purpose bomb can be a significant part of the total load effect on a protective structure. This impulse must be combined with the airblast impulse for calculation of structural response as discussed in Section II.D.

The fragment impulsive load imparted to the structure depends on the mass of the fragments that impact the structure, their impact velocity, and whether the fragments perforate, penetrate and stick, or ricochet. Also, the spatial distribution of the impulse over the surface of the target can be important. As described above these quantities are random variables. However, a simplified reliability-based design approach can be derived.

Several assumptions are used to simplify the design approach. These assumptions are consistent with current deterministic analysis methodology and are as follows:

1. The fragment loadings are impulsive.
2. The individual fragment impulses can be added.
3. For perforating fragments, all of the fragment momentum is dissipated during transit through the target (wall, roof, etc.).
4. The added impulse that results from ricochet can be neglected.
5. Front-face cratering is neglected.
6. The fragment mass and velocity distributions are independent.

The first two assumptions deal with the impulsive nature of the fragment loading. These assumptions are reasonable since the time scale during which the fragment load acts (*i.e.*, the time during which the fragment momentum is reduced to zero) and the difference in the fragment arrival times are both small compared to the structure response time (particularly for inelastic response of interest in protective design).

The third assumption is slightly conservative since fragments that pass through the structural barrier exit with some residual velocity. Thus, not all of the fragment's momentum is converted to structural load. However, the protective structures of interest here are designed to resist perforation so that the number of perforating fragments will be zero or a very small percentage of the total number of impacting fragments. Also, the exit velocities of any fragments that do actually perforate will likely be a small percentage of the striking velocity.

The fourth and fifth assumptions are slightly unconservative. Fragments that ricochet actually impart a momentum that can be up to twice the normal component of the striking momentum. Similarly, front-face cratering causes additional impulse to be imparted on the wall. These assumptions are unconservative, but the contribution of these effects may be small compared with the total impulse imparted.

The assumption of independence of mass and velocity is necessary due to the way arena test data are currently collected. The assumption can be conservative if large fragments contribute significantly to the total impulse imparted to the structure and velocity is actually negatively correlated with fragment mass. Assumptions 4, 5, and 6 need to be investigated further.

2. Reliability-Based Design

The fragment impulse loading uncertainties can be analyzed by considering the impulse imparted on a finite cell on the target surface. Based on Assumptions 1-5 given above, the normal component of the momentum imparted on a finite-sized cell on the target surface is

$$M_N = \sum_{i=1}^{n} m_i v_i \cos\theta \qquad \text{(IV-23)}$$

where m_i and v_i are the respective mass and velocity of each fragment impacting within the cell, and n is the total number of fragments that impact within the cell. All three variables, m, v, and n are random quantities; thus, the total impulse imparted to an individual cell is random. However, as the size of the cell increases, the variability decreases for a given bomb standoff, orientation, etc. The decrease in impulse variability occurs because, as the number of impacting fragments increases, differences between the individual fragments are averaged out and the uncertainty in the total momentum (sum of all fragments) reduces. Conversely, for very small cells, the variability can be large. The impulse variability for a cell will also be affected by bomb standoff since bomb standoff affects the number of fragments within a cell.

Based on the above factors, we can identify four different sources of uncertainty. The first is the variability of the total impulse in a cell for a given fragment spray pattern and a given mean fragment velocity (where mean fragment velocity is defined as the average velocity over all fragments from the bomb). The second is uncertainty in the fragment spray pattern. The third is the variability of the total impulse in a cell due to bomb-to-bomb variation of the mean fragment velocity. Finally, there is prediction error bias and uncertainty in the mean fragment velocity, *PCDM* Equation (VI-20) (Gurney's formula).

a. Mean Impulse Spatial Variability

The importance of the first source of uncertainty is coupled to the structural response. If the structural response is affected by fluctuations in impulse over short distances on the structure surface then it will be important to consider this variability. In this case we would need to analyze the structure using small cell sizes which would have large total impulse variability. However, these small-scale fluctuations will usually not be important except in special circumstances (*e.g.*, at structural discontinuities). Analysis of these effects requires a finite element analysis of the structure. When using the equivalent SDOF response models given in *PCDM* Section X.B, the fragment impulse loads are transformed into an equivalent uniform load. The equivalent uniform load does not account for small-scale fluctuations in the loading and implicitly assumes that these fluctuations will not affect the structure response. Therefore, given the current state of practice and based on the assumption that small-scale variations will not be important in predicting structure response, we neglect the mean impulse spatial variability.

b. Fragment Spray Pattern

Fragment spray pattern is probably the most important source of uncertainty for predicting fragment impulse. As discussed in Section IV.C.B.2.g, the current state of practice for modeling fragment spray patterns in the design of protective structures is to use either the cylindrical or spherical spray models. Since the most important cases for fragment impulse are close-in bursts of large-cased weapons, the cylindrical model is more appropriate for this application. Although there are uncertainties and conservatisms associated with the cylindrical spray pattern, the development of more sophisticated spray patterns is beyond the scope of this effort. Therefore, we proceed with the interim assumption that the cylindrical spray pattern is deterministic and unbiased. However, we note the need for characterizing fragment spray uncertainty and incorporating this uncertainty in future improvements to the RBD procedures for predicting fragment impulse (or selecting design fragments).

c. Bomb-to-Bomb Variability of Mean Fragment Velocity

Because of bomb-to-bomb variation, the average fragment velocity is a random variable. Uncertainty in fragment velocity within a single bomb has been addressed in the discussion of mean impulse spatial variability in Section IV.C.2.a. Bomb-to-bomb uncertainty in mean fragment velocity can be quantified by compiling statistics from independent explosions of the same type of bomb. Kidd [1968] presents the raw data from arena tests of five detonations of Tritonal-filled Mk84 general purpose bombs. Kidd also gives the average fragment velocity for each of the five bombs. Table IV-3 shows these results and the mean, standard deviation, and coefficient of variation of the data. The data show that the bomb-to-bomb variation is relatively small; the mean fragment velocity has a coefficient of variation of approximately 2.5 *percent*.

TABLE IV-3. MEAN UNCORRECTED FRAGMENT VELOCITIES FROM FIVE TRITONAL-FILLED Mk84 GENERAL PURPOSE BOMBS [Kidd, 1968].[a]

Detonation Number	Mean Velocity *(feet/second)*
1	5350
2	5713
3	5576
4	5549
5	5425
Mean	5523
Standard Deviation	140
Coefficient of Variation	2.5 *percent*

[a] For each detonation, the data in this table are raw averages of the fragments that impacted flash panels. The data are not corrected to initial velocity, and the averages are not weighted by appropriate polar zone multipliers. Therefore, the data are valid only for estimation of variability and should not be used to estimate fragment velocity.

d. Mean Fragment Velocity Prediction Error Bias and Uncertainty

To assess prediction errors in the *PCDM* formula (Gurney's formula) for fragment initial velocity (see Equation (IV-3) or *PCDM* Equation (VI-20)), we can use the data given in the Joint Munitions Effectiveness Manual [JMEM, 1990].[1] Table IV-4 gives the average fragment velocities (unclassified) for several different configurations of Mk-82, 83, and 84 general-purpose bombs taken from the JMEM and the initial velocity computed using the *PCDM* formula.[2] The bomb description column contains the key descriptive information that was available in the reference, including explosive type and whether the detonation was tail or nose initiated. The final column gives the prediction error ratio — that is, the observed mean velocity divided by the *PCDM* prediction.

TABLE IV-4. AVERAGE FRAGMENT VELOCITIES (UNCLASSIFIED) FOR GENERAL-PURPOSE BOMBS [JMEM, 1990].

Bomb Description	Number of Rounds Tested	Mean Fragment Velocity	*PCDM* Prediction	Prediction Error Ratio
Mk82 Mods 1, 2; H-6	3	6198	5910	1.05
Mk82; Tritonal; Nose-Initiated	6	5054	5220	0.97
Mk82; BLU-111/B; PBX-109; Tail-Initiated	4	5492	N/A	
Mk83 Mods 3 & above; H-6; Nose-Initiated	3	7137	6520	1.09
Mk83; H-6; Tail-Initiated	3	6197	6520	0.95
Mk83; PBX-109; Tail-Initiated	3	6200	N/A[a]	
Mk84; Mods 1, 2; Tritonal	8	7068	6250	1.13
Mk84; Mods 1, 2; H-6	6	7873	7077	1.11
Mean	-	-	-	1.05
Coefficient of Variation	-	-	-	0.07

[a]N/A - *PCDM* does not provide a Gurney constant value for PBX-109.

The mean prediction error ratio is 1.05 and the median is approximately 1.07, with a coefficient of variation of about 7 *percent*. This indicates that the formula given in the *PCDM* is 5 *percent* unconservative, on average. This is contrary to expectation. The *PCDM* formula is intended to give the initial velocity of the fragments emanating from the central portion of the bomb, which typically have velocities higher than the overall average. Thus, we would expect the *PCDM* formula to be conservative. This was true only for two of the JMEM data sets. Clearly, further research is required since the predicted average fragment velocity directly affects the predicted fragment impulse.[3] Further, in many cases, the structure response will be

[1] The JMEM data could not be used to assess bomb-to-bomb variability since the data presented are summaries over several detonations of the same type of bomb. Kidd's data (corrected for initial velocity and weighted by polar zone multiplier) was likely included in these summaries; hence we do not include these now as an independent data set.

[2]For the *PCDM* formula, explosive weight and case weight are obtained from the JMEM. Case weight does not include the weight of the fins.

[3]Review of recent arena test data indicates that the JMEM data may be conservatively biased. Older test data on which the JMEM is based may only have included velocities of the earliest arriving and, therefore, fastest fragments.

predominantly influenced by fragments emanating from the central portion of the bomb. Hence, in these cases, it would be necessary to further increase the *PCDM* prediction.

The data in the table also show that explosive type significantly affects average fragment velocity, with H-6 loaded bombs being greater than Tritonal loaded bombs, as expected. Thus, for design it will be important to know the type of explosive used in the threat weapon. If explosives other than H-6 or Tritonal are of interest it may be possible to extrapolate the results here based on the similarity of the explosive compositions; however, if this is not possible, additional testing would be needed.

At this time, we recommend that the mean fragment velocity be treated as a lognormally distributed random variable with a median of 7 *percent* greater than that given by the design manual and a coefficient of variation of 10 *percent*. The 10 *percent* cov is a conservative combination of the bomb-to-bomb variability and the mean velocity prediction error uncertainty. Table IV-5 gives the design factors to be applied to the velocity obtained using the *PCDM* formula. That is, the nominal mean fragment velocity is obtained using *PCDM* Equation (VI-20) and then multiplied by the factor given in Table IV-5 for the desired reliability level.

TABLE IV-5. VELOCITY LOAD FACTORS FOR CALCULATION OF FRAGMENT IMPULSE.

Reliability	Velocity Factor
0.05	0.91
0.10	0.94
0.20	0.98
0.30	1.02
0.40	1.04
0.50	1.07
0.60	1.10
0.70	1.13
0.80	1.16
0.90	1.22
0.95	1.26

e. RBD Fragment Impulse Summary

Two important uncertainties were identified above. The first is the uncertainty in predicting the fragment spray pattern, and the second is the uncertainty in the mean impact velocity of the bomb fragments. The uncertainty in fragment spray pattern is a key uncertainty; however, we have not developed design factors to account for spray pattern uncertainty at this time. Improved spray pattern models are an important area for further research. The uncertainty in the mean impact velocity includes both prediction uncertainty and bomb-to-bomb variability, and is treated by applying the reliability-based design factors given in Table IV-5.

That is, the mean fragment velocity is evaluated using *PCDM* Equation (VI-20) (*i.e.*, the Gurney formula) and then multiplied by a factor selected from Table IV-5.

The recommended procedure for computing the reliability-based total fragment impulse is:

1. Multiply the fragment velocity given in the *PCDM* by the velocity load factor from Table IV-5 that corresponds to the desired reliability level.
2. Compute the mass of impacting fragments using the procedure given in Section IV.B.2.g.1 or *PCDM* Section VI.C.4.
3. Compute the total fragment impulse using the factored velocity from Step 1 and the fragment mass from Step 2.

3. Fragment Impulse Example

As an example of the reliability-based design procedure for fragmentation impulse, we analyze the same 12-*foot* by 12-*foot* door panel considered in Section IV.B.4. The threat is a Mk-82 500-*pound* GP bomb and we consider standoffs of 10, 20, 50, and 100 *feet*. We wish to estimate the 10 *percent*, 50 *percent*, and 90 *percent* reliability-based peak unit fragment impulse and total normal fragment impulse.

We assume that the weapon is H-6 loaded and has an approximately cylindrical shape. The explosive weight and casing weight are 192 *pounds* and 311 *pounds*, respectively. From *PCDM* Table IV-1, the Gurney constant is 8600 *feet/s*, and from Equation (IV-3), the average initial fragment velocity is

$$v_{0N} = \frac{8600}{\sqrt{311/192 + 2/4}} = 5910\ ft/s \qquad \text{(IV-24)}$$

where the subscript N is used to denote nominal initial velocity (*i.e.*, unfactored).

Consider the particular case of a 10-*foot* standoff and a 90 *percent* reliability requirement. The design factor on fragment velocity is obtained from Table IV-5 as 1.22. Therefore, the 90 *percent* reliability-based velocity is

$$v_{0N} = 1.22 \times 5910 = 7210\ ft/s \qquad \text{(IV-25)}$$

The casing mass is 9.658 slugs. Therefore, the 90 *percent* reliability total fragment momentum is obtained from *PCDM* Equation (VI-26) as

$$M_{I_{0.9}} = 9.658 \times 7210 = 69600\ slug\text{-}ft/s \qquad \text{(IV-26)}$$

The weapon length is 7.5 *feet*. Therefore, if we neglect reductions in fragment striking velocity due to drag, the 90 *percent* reliability peak unit impulse on the panel given by *PCDM* Equation (VI-29) as

$$M_{u,\,pk_{0.9}} = \frac{69600}{(2\pi)(10)(7.5)} = 148\ slug\text{-}ft/s \qquad \text{(IV-27)}$$

Finally, the 90 *percent* reliability total normal impulse delivered to the door panel is obtained from *PCDM* Equation (VI-32) as

$$M_{n_{0.9}} = \frac{69600}{(2\pi)}\left[\frac{1}{\sqrt{(10/12)^2 + 1/4}}\right] = 11{,}400\ slug\text{-}ft/s \qquad \text{(IV-28)}$$

Results for the additional standoffs and reliability levels are summarized in Figure IV-11. The total normal fragment impulses have been averaged over the 144 $feet^2$ panel to obtain average unit impulses for easier comparison to the peak unit impulses. The relatively narrow spread of the peak unit impulse and average unit impulse for reliabilities ranging from 10 *percent* to 90 *percent* reflects the low degree of uncertainty in predicting the mean fragment velocity. As additional prediction error models for fragment impulse (*i.e.*, spray pattern, velocity dependence on polar zone, drag, mass/velocity correlation, ricochet, scabbing, and spall) are developed, additional spread and/or shifts in the reliability-based design curves will be introduced.

4. Research Requirements

The RBD fragment impulse procedure is valid only for structures for which the equivalent uniform load method given in *PCDM* Section X.B is valid. For structures that are more sensitive to fluctuations of impulse on the structure surface, more detailed probabilistic and structure response computations may be necessary.

Research is needed to better define the fragment velocities. The Gurney formula given in the *PCDM* was not found to be conservative as previously expected. This unconservatism was evidsqent from comparison with measured mean fragment velocities. Although the reliability-based design factors account for this unconservatism (*e.g.*, for 50 *percent* reliability the *PCDM* predicted velocity is increased by 7 *percent*), we caution that these velocities may require an additional systematic increase. In particular, the fragment impact velocity may need to be increased further when the structure response is primarily influenced by fragments that emanate from the central portion of the bomb, since these fragments will have higher than average velocity. Also, the reliability-based factors presented in Table IV-5 are based on data from two types of explosive, H-6 and Tritonal. Clearly other types of explosive are of interest. Additional test data should be reviewed and/or additional tests should be performed to provide fragment velocity design values for these explosives.

An important area for further research is the deterministic and probabilistic modeling of fragment spray patterns. The assumed spray pattern can significantly affect the computed mass of fragments that impact the structure and, hence, the computed impulse. Improved models based on polar zone data from arena tests are needed. Easy-to-use, computer-based design tools will be needed to implement refined spray pattern models in protective construction.

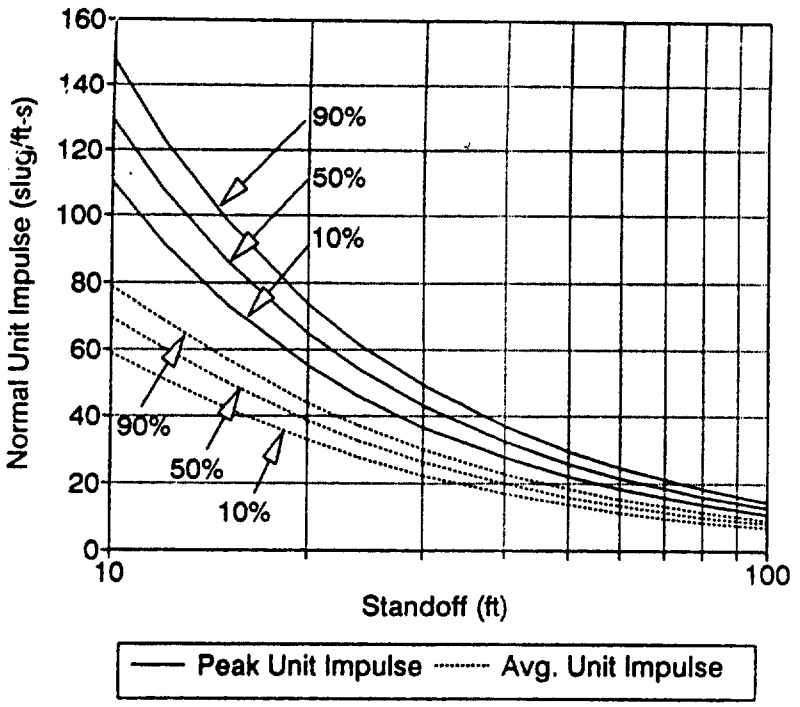

Figure IV-11. Example Peak Unit Fragment Impulse and Average Normal Fragment Impulse for Reliability Levels of 10 *percent*, 50 *percent*, and 90 *percent*.

Finally, the reliability-based procedure assumes that fragment mass and velocity are independent. This assumption was necessary because of the way in which arena test data are collected. The assumption can be conservative if large fragments contribute significantly to the total impulse imparted to the structure and velocity is actually negatively correlated with fragment mass. Treating the correlation between fragment mass and velocity is an area that requires further research. By performing reliability-based calculations with assumed mass and velocity correlation functions, it is possible to assess the need for additional data collection and modification to the recommended methodology. Hence, we recommend that this be conducted as a first step toward defining the need for improved data collection procedures.

(The reverse of this page is blank.)

V. PENETRATION

A. INTRODUCTION

When a projectile impacts a reinforced concrete structure, it may produce damage through perforation of the wall or through back-face spall. While perforation and spall damage may not necessarily degrade the overall structural integrity, these effects may cause severe damage to the structure contents and affect the functional performance of the facility.

The objective of this section is to develop reliability-based design factors through analysis of the *PCDM* prediction equations and comparison to reinforced concrete penetration data. Four penetration phenomena that are relevant to protective construction are examined:

1. Depth of penetration into a semi-infinite concrete target.
2. Spalling of a finite-thickness concrete target.
3. Perforation through a finite-thickness concrete target.
4. Residual velocity after penetrating a finite-thickness concrete target.

In Section V.B, we describe the reinforced concrete penetration database used for this research. Section V.C treats depth of penetration into massive concrete, Section V.D presents the analysis for spall and perforation, and Section V.E treats projectile residual velocity.

B. DATA SOURCES

Two penetration databases served as data sources. Both databases provide data on penetrator characteristics, target characteristics, and penetration performance.

The first information source for this study is a database that was developed for the Air Force Armament Laboratory (AFATL) [Weeks and Raspberry, 1987]. The Air Force database was taken primarily from a compilation of test results by Beth and Stipe [1943]. These results were predominantly for small projectiles impacting massive concrete targets. 712 data records were compiled by the Air Force, containing projectile characteristics, target characteristics, and test results.

A second data source used was the database created by Sandia National Laboratories [Christensen, 1988], which catalogs over 900 penetration field tests. The database encompasses data from soil, rock, ice, ocean sediments, permafrost, and concrete penetration tests. Of these tests, 147 are concrete penetration tests, some of which are also in the AFATL database.

All of the data items from both databases were reviewed and selectively reduced to eliminate obvious errors, unclear results, and duplications. This process is summarized in Figure V-1. Finally, 710 data records were selected. Of the selected 710 records, 539 records were semi-infinite targets and 171 records were targets of finite thickness. Note that, not all of these records contain sufficient information or are relevant to all four phenomena of interest. For analysis of

depth of penetration 534 records were selected; for analysis of spall and perforation 703 records were selected; and for analysis of residual velocity 45 records were selected.

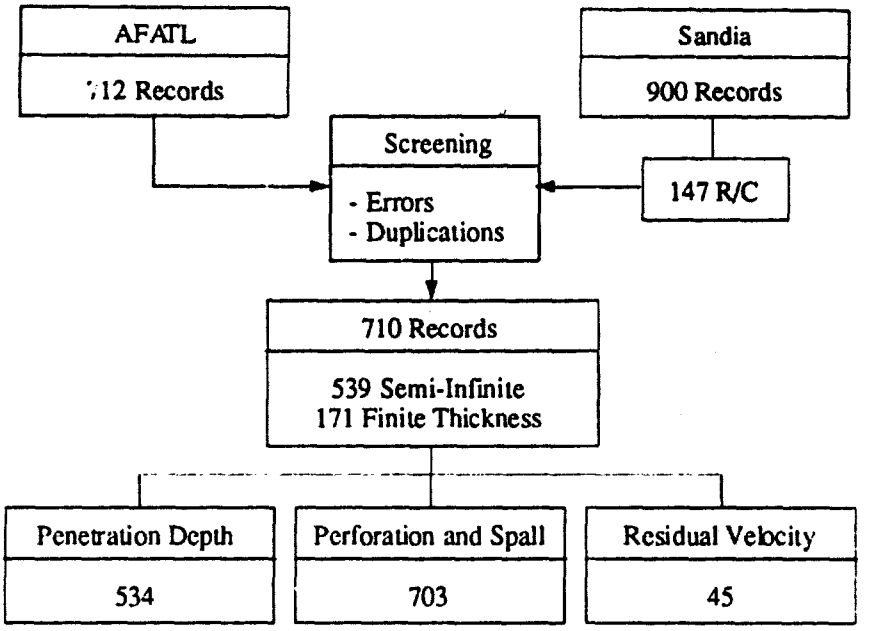

Figure V-1. Data Sources for Penetration Effects.

A detailed statistical analysis of all input and output variables for all records was performed using the SAS UNIVARIATE procedure [SAS, 1988] in order to qualify the range of applicability of the analysis and the reliability-based design factors developed herein. Summaries of these results are presented in the following sections.

C. PENETRATION DEPTH IN MASSIVE CONCRETE

1. *PCDM* Model

The penetration depth model given in the *PCDM* (*PCDM* Equation (VII-6)) is a modified version of the NDRC equations [White, 1946]. These equations assume normal, collinear impact and are given as:

$$x = \frac{26.8\sqrt{NW}\,v_s^{0.9}}{f_c'^{\,0.25}\,d^{0.4}} \qquad x \le 2d \tag{V-1a}$$

$$x = \frac{180\,NW\,(v_s/d)^{1.8}}{f_c'^{\,0.5}} + d \qquad x > 2d \tag{V-1b}$$

in which W, d, N, v_s, and f_c' are respectively: penetrator weight (*pounds*), penetrator diameter (*inches*), penetrator nose shape factor, striking velocity (*kilo-feet/second*), and concrete unconfined compressive strength (*pounds per square inch*). The factor for penetrator nose shape, N, is defined as

$$N = 0.72 + 0.25\sqrt{n - 0.25} \qquad \text{(V-2)}$$

where the quantity n is called the caliber radius head, CRH = $n = r_o/d$, and r_o is the ogive nose radius and d is the projectile diameter (see Figure V-2). The NDRC equations are empirically based, and the *PCDM* recommends their use for ordnance class penetration effects. The formulas are based largely on penetration data for projectiles with diameters less than 1 3/4 *inches* and striking velocities less than 2000 *feet/second.*

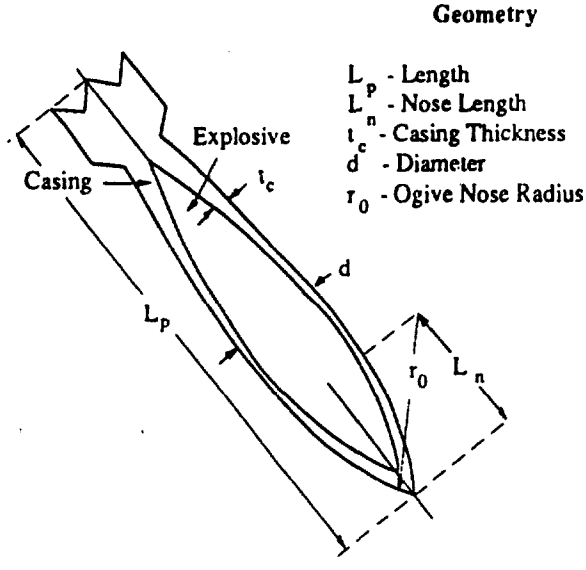

Figure V-2. Projectile Characteristics.

2. Analysis of Penetration Depth Model Prediction Error

For this analysis, 534 data records are selected from the database where projectiles are fired against semi-infinite concrete targets. Figure V-3 summarizes the distribution of all the input variables used for depth of penetration prediction — that is, W, d, N, v_s, and f'_c. Also shown in the figure is the range of output results as a function of the penetration depth to projectile diameter ratio. Note that most of the data come from small projectile testing (*i.e.*, small d) with nose shape factors of approximately 1.0 ($r_o/d \approx 1.5$). The impact velocities of the test data are distributed over a range from 400 to 3300 *feet/second*, with approximately 70 *percent* of the impact velocities in the 700 to 2000 *feet/second* range. This is a limitation of the current data set, since modern weapons (*e.g.*, 30 *millimeter* aircraft cannon) often exceed 3300 *feet/second.*[1] The depths of penetration of the test projectiles cover a wide range of x/d values, but are concentrated around the shallower depths. Approximately 20 *percent* of the data have $x/d \leq 2$. Hence, the majority of the data will be tested against Equation (V-1b).

[1]To limit the scope of this task we confined our analysis to the aforementioned data set. Preliminary analysis of 30 *mm* aircraft cannon penetration data indicate that the *PCDM* equations are conservative for modern high-speed projectiles. We strongly recommend that additional research be conducted to analyze these data and develop RBDFs for high-speed projectiles.

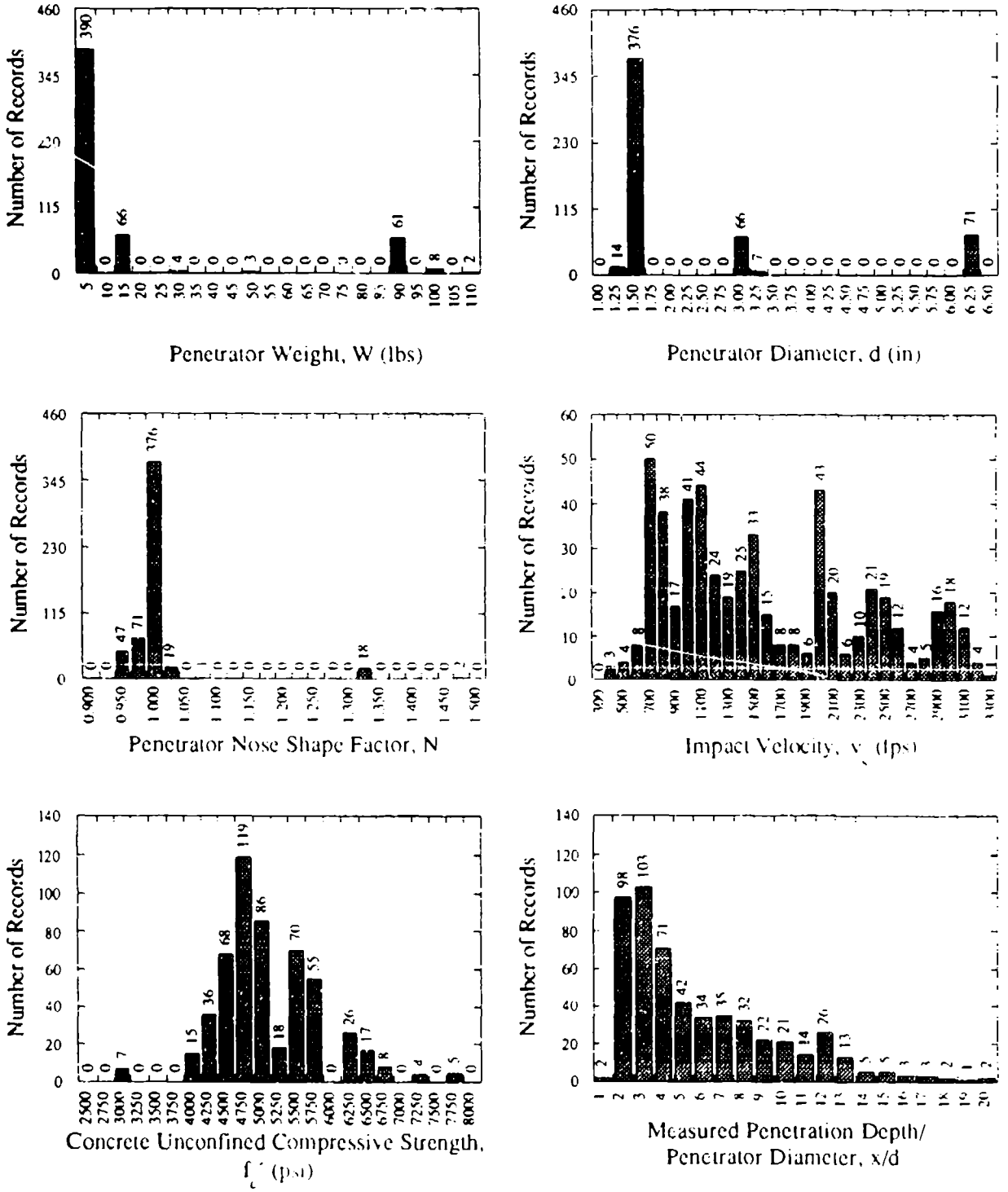

Figure V-3. Distributions of Input and Output Variables in the Data Records Selected for Depth of Penetration Analysis.

The prediction error formulation is used to evaluate the NDRC formulas against the penetration data base. The prediction error, ξ, is the ratio of observed (measured) to predicted (calculated) penetration depth,

$$\xi = \frac{x(measured)}{x(calculated)} = \frac{x_m}{x_c} . \tag{V-3}$$

Hence, for the i^{th} penetration test, the nondimensional statistic ξ_i is computed from Equation (V-3), in which the x_c penetration depth is calculated deterministically using the exact values of W, D, N, ν_s, and f'_c for that test. If $(x_c)_i = (x_m)_i$, then $\xi_i = 1.0$ and the model perfectly predicts that particular test. If $\xi_i > 1$, the NDRC equation has underpredicted depth of penetration. $\xi_i < 1$ indicates an overprediction. By evaluating the statistics of the random variable ξ, we can quantitatively assess the reliability of the prediction model, *i.e.*, the NDRC formulas. If the mean of $\xi = 1.0$, the model is said to be unbiased. The variance of ξ provides a measure of the dispersion.

A scattergram of x(measured) versus x(calculated) is given in Figure V-4. Also shown in the figure is the line for $x_m = x_c$ and the linear regression for x_m versus x_c. As can be seen, the model underpredicts, on average, and the underprediction is slightly greater at the higher penetration depths. The coefficient of variation on penetration depth is approximately 25 *percent*. Table V-1 presents summary statistics of ξ and ln (ξ). These statistics confirm that the model is slightly biased (mean = 1.06) and underpredicts penetration depth. The coefficient of variation on penetration depth is approximately 25 *percent*. This coefficient of variation is approximately the same as that given in Section II of the *PCDM* for the Sandia penetration equation, which was derived from the relative error statistics given in Nash, *et al.* [1986].

As observed earlier, Equation (V-1) has two regions corresponding to $x/d \leq 2.0$ and $x/d > 2.0$. While it would be straightforward to separately analyze these two equations, this level of refinement was not deemed necessary, and the average value obtained above will be used in the reliability-based prediction model.

Since Equation (V-1) is for penetration into massive concrete, it neglects rear boundary effects (*i.e.*, spalling or formation of a movable conical plug). Therefore, Equation (V-1) predictions should only be compared to penetration data wherein rear boundary effects are negligible. However, for some of the depth of penetration data, rear face spall occurred. Hence, we examined the effect of spall on the penetration results to determine if these data need to be removed from the data set. We found that when spalling occurs, the mean and standard deviation of ξ are, respectively 1.03 and 0.24. Thus, for the cases examined here, spall does not significantly affect ξ, and the spall data can be included in the data set.

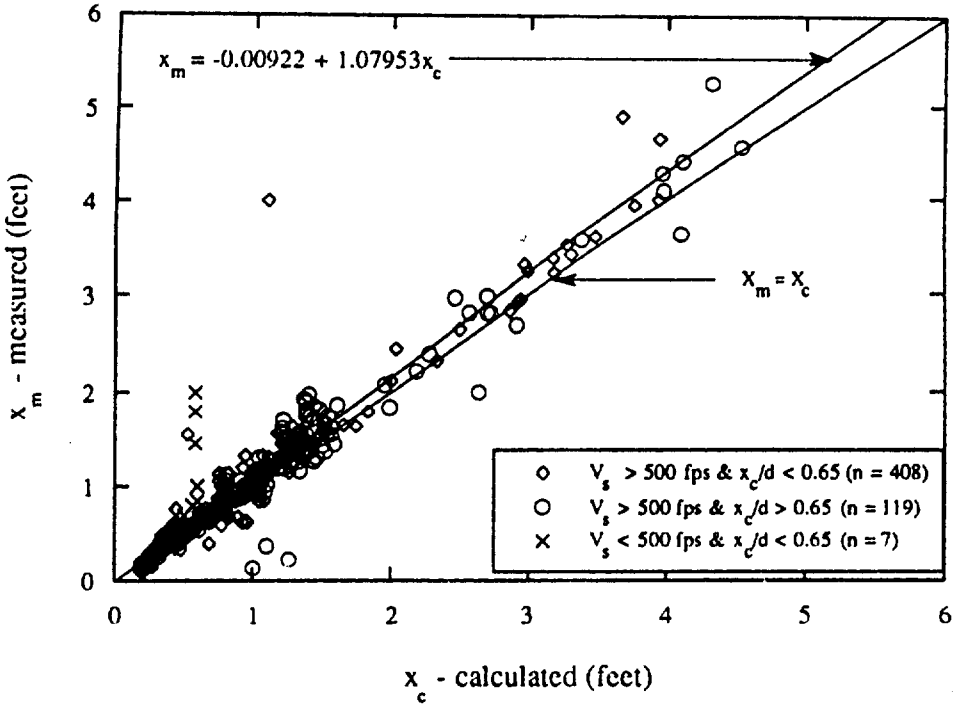

Figure V-4. Comparison of Measured Projectile Penetration Depth in Massive Concrete (x_m) *vs.* Calculated Penetration Depth (x_c).

TABLE V-1. STATISTICS OF MODEL ERROR ξ AND LN (ξ).

	ξ	ln (ξ)
Mean	1.06	0.032
Std. Dev.	0.26	0.22
W:Normal[a]	0.63	0.76
Prob < *W*	0.01	0.00

[a]Shapiro-Wilk statistic for testing of normality.

3. RBDFs for Depth of Penetration

a. No Uncertainty in W, d, N, v_s, f_c'

We first consider the case when all of the problem parameters are specified so that the only uncertainty is in the model prediction error. The probability that the actual projectile penetration depth is less than the predicted depth can be written as

$$P_s = P(x_m < x_c) \tag{V-4}$$

where x_m is the actual penetration depth and x_c is the calculated penetration depth — that is, the penetration depth predicted by the deterministic *PCDM* procedure. For design to reliability R, the

nominal penetration depth is multiplied by a reliability-based load factor, λ_d, and from Equation (V-3), the actual penetration depth is $\xi\, x_n$; therefore,

$$R = P(x_m < \lambda_d \cdot x_c) = P(\xi < \lambda_d) \qquad (V\text{-}5)$$

and the reliability-based design factors, λ_d, are obtained from the probability distribution for ξ.

Table V-1 shows that ξ fails the Shapiro-Wilk statistic (W statistic) tests for normality and lognormality. Hence, for the reliability model, we will use an empirical distribution from the actual data, rather than attempt to fit a simplified normal or lognormal model.

Table V-2 shows the resulting values of ξ, and, therefore, λ_d for several probability levels obtained from the analyses. If there is no uncertainty in the problem inputs (*i.e.*, W, d, N, v_s, and f_c'), the reliability-based prediction is made by multiplying the deterministic penetration depth by a value of λ_d selected from the table. For example, if we predict a penetration depth of 3 *inches* using Equation (V-1), and a 90 *percent* confidence value is required, then from Table V-2, the 3 *inches* prediction is multiplied by 1.23, giving 3.69 *inches*. Thus, if all of the problem inputs are known, there is a 90 *percent* probability that the penetration depth will be less than 3.69 *inches*.

TABLE V-2. RBDFS FOR DEPTH OF PENETRATION — NO UNCERTAINTIES IN W, d, N, v_s, f_c'.

Reliability, $P(\xi < \lambda_d)$	RBDF, λ_d
0.01	0.59
0.05	0.79
0.10	0.88
0.25	0.97
0.50	1.03
0.75	1.11
0.90	1.23
0.95	1.36
0.99	1.73

b. Incorporating Parameter Uncertainty

Uncertainty in the penetration equation parameters, W, d, N, v_s, and f_c' can also contribute to the prediction error for depth of penetration. Uncertainty in these parameters can be the result of both prediction error and randomness.

We first consider concrete compressive strength, f_c'. The depth of penetration predicted by Equation (V-1) is not very sensitive to the concrete compressive strength and, in light

of the model error already evaluated, it can be shown that the random uncertainty in concrete compressive strength will not contribute significantly to the prediction uncertainty.[1]

The remaining variables, W, d, N, and v_s, are weapon descriptors. Again, these parameters can have both prediction error and randomness; however, we assume that for protective design the weapon threat is specified so that there is no prediction error. Also, for a specified weapon threat, the random uncertainty in W, N, and d will be the result of manufacturing tolerances and will be small with respect to the model prediction error evaluated previously. Hence, W, N, and d are treated deterministically. However, striking velocity uncertainty may be significant. A parametric analysis has been performed to evaluate the effect of striking velocity uncertainty and to develop velocity load factors as a function of the striking velocity coefficient of variation. The resulting factors in Table V-3 were obtained via a Monte-Carlo simulation analysis and are applied to the best estimate of striking velocity for the threat weapon.[2] For example, if the mean striking velocity (μ) is 1000 *feet/second* and the standard deviation (σ) is estimated as 300 *feet/second*, the striking velocity coefficient of variation is $\delta = \sigma/\mu = 0.30$. For a desired design reliability of 90 *percent*, the mean striking velocity is multiplied by 1.27, as given in Table V-3. This factored value is used in the penetration formulas as described in the following example.

4. RBD Example

To summarize, there are two parts to the reliability-based depth of penetration prediction procedure. First the best estimate striking velocity is multiplied by the load factor given in Table V-3. This factored load is then used in Equation (V-1) with best estimates for all of the other parameters to obtain an estimate of penetration depth. This penetration depth is then multiplied by the model error factor given in Table V-2.

TABLE V-3. STRIKING VELOCITY LOAD FACTORS FOR PREDICTION OF DEPTH OF PENETRATION IN MASSIVE CONCRETE.

	Velocity Factors, λ_{dv} (for different cov of v_s)				
Reliability	0.1	0.2	0.3	0.4	0.5
0.01	0.90	0.75	0.44	0.24	0.14
0.05	0.91	0.78	0.60	0.43	0.34
0.10	0.92	0.80	0.67	0.56	0.47
0.25	0.95	0.89	0.83	0.76	0.72
0.50	1.00	1.00	1.00	1.00	1.00
0.75	1.05	1.10	1.16	1.22	1.30
0.90	1.07	1.16	1.27	1.38	1.51
0.95	1.09	1.17	1.30	1.42	1.59
0.99	1.10	1.18	1.32	1.52	1.71

[1]For a targeting study, prediction uncertainty in concrete strength will be large and could be treated by assigning probability estimates to assumed values of the concrete strength and performing the penetration analysis for the distribution of values.

[2]The load factor should be applied to the mean-centered best estimate striking velocity for the specified threat. They should not be applied to conservative upper bound estimates of v_s.

For example, consider the case of a buried bunker that is to be designed with a concrete roof that is flush with the ground surface. The roof slab must be thick enough so that a delay-fuzed concrete penetrating artillery shell detonates at least 3 *feet* from the bottom of the slab with 90 *percent* reliability. The problem parameters are $W = 90$ *pounds*, $d = 6$ *inches*, $N = 1.1$, $v_s = 1000$ *feet/second*, and $f_c' = 5000$ *per square inch*. All parameters can be taken as deterministic except striking velocity, v_s, which has a coefficient of variation (cov) of 20 *percent*. Following the design procedure, we first factor the striking velocity by the load factor from Table V-3. For 90 *percent* reliability and cov of 20 *percent*, the load factor is 1.16. Thus, the factored striking velocity is 1160 *feet/second* or 1.16 *kilo-feet/second*. We now use the factored striking velocity in Equation (V-1) to compute the depth of penetration as 19 *inches* or 1.6 *feet* (note that we used Equation (V-1b) since penetration depth is greater than twice the projectile diameter). To obtain 90 *percent* reliability, this penetration depth is multiplied by the RBDF given in Table V-2 — that is, 1.23. Therefore to have 90 *percent* reliability that the shell will explode at least 3 *feet* from the bottom of the slab, we design the slab to be $1.23 \times 1.6 + 3 = 5$ *feet*.

The reliability-based design can now be compared with the deterministic *PCDM*-based design. Applying Equation (V-1b) with the nominal striking velocity of 1000 *feet/second*, we obtain a depth of penetration of 16 *inches* or 1.33 *feet*. Thus, without applying any safety factors, the *PCDM* would give a design depth for the slab of $1.33 + 3 = 4.33$ *feet*. This design corresponds to roughly a 50 *percent* reliability level since the *PCDM* method was found to be unbiased.

It is also useful to examine the effect of velocity uncertainty on the reliability-based design. If the velocity is taken to be deterministic — that is, the velocity uncertainty is neglected, then no load factor is applied, the computed depth of penetration is 1.33 *feet* and the reliability-based design for 90 *percent* reliability is $1.23 \times 1.33 + 3 = 4.6$ *feet*. Thus, velocity uncertainty increases the computed depth of penetration by 20 *percent* and the final slab design thickness by approximately 8 *percent*. The importance of considering striking velocity uncertainty is seen if we consider that the 4.6 *feet* thick design corresponds to a reliability level of only 75 *percent* (versus the desired 90 *percent*) for striking velocity cov of 20 *percent*.

We emphasize that the *PCDM* concrete penetration formulas are for massive concrete and should not be used to design protective walls against perforation and spalling.

D. SPALL AND PERFORATION

1. *PCDM* Model

For finite-thickness slabs and walls, the thicknesses required to prevent spalling (ejection of concrete fragments from the inside face of the wall) and projectile perforation are greater than the penetration depth in massive concrete, given by Equation (V-1).

In the *PCDM*, the minimum thickness of a concrete wall required to prevent spalling, t_s, and perforation, t_p, due to projectile impact are given (*PCDM* Equations (VII-8) and (VII-9), respectively) as

$$t_s = \begin{cases} 7.91x - 5.06x^2/d & x < 0.65d \\ 1.36x + 2.12d & 0.65d \le x \le 11.75d \end{cases} \quad \text{(V-6)}$$

$$t_p = \begin{cases} 3.19x - 0.718x^2/d & x < 1.35d \\ 1.24x + 1.32d & 1.35d \le x \le 13.5d \end{cases} \quad \text{(V-7)}$$

where t_s and t_p are in *inches*, d is the projectile diameter (*inches*) and x is the depth of penetration in massive concrete (*inches*) given by Equation (V-1).

The *PCDM* prediction models are empirically based and there are both systematic and random uncertainties associated with the equations. The reliability-based design method presented here quantifies and accounts for the uncertainty associated with the spall and perforation test data, and provides factors to be applied to the nominal wall thicknesses obtained using the *PCDM* empirically based equations.

2. Dichotomous Regression Formulation for Analysis of Spall and Perforation Prediction Error

The reliability-based design procedure for spall and perforation is developed using the dichotomous regression technique [Cox and Snell, 1989; Hosmer and Lemeshow, 1989; Veneziano and Liao, 1984]. The dichotomous regression technique was presented earlier for analysis of breach and spall of aboveground walls (Section II.E). Here we apply the dichotomous regression technique to penetration testing data to find the probability of spall or perforation as a function of penetrator and target characteristics.

The dichotomous regression fits a probability distribution to a data set using the method of maximum likelihood. The term dichotomous refers to the fact that the observed data are categorized as either "fail" or "no-fail." For example, the spall data are categorized as either "spall" or "no-spall." A logistic form for the probability distribution was found to fit the spall and perforation data exceptionally well. The logistic form

$$P_d(\underline{x}) = \frac{exp\,[G\,(\underline{x})]}{1 + exp\,[G\,(\underline{x})]} \quad \text{(V-8)}$$

is the same as used in Section II.E. For this case, $\underline{x}$ are the penetrator and target characteristics, and the function $G(\underline{x})$ is a linear combination of $\underline{x}$, *i.e.*

$$G\,(\underline{x}) = A_o + \sum_{i=1}^{n} A_i\, g_i\,(\underline{x}) \quad \text{(V-9)}$$

where A_i, are determined from analyses of the data.

For this analysis, 703 records were selected from the database (see Figure V-1). The distribution of each input and output variable is shown in Figure V-5. This data set incorporates most of the tests used in the previous analysis of depth of penetration prediction. Hence, most of the data are from small projectile testing as seen in the figure. However, this data set does include a number of large projectiles. The impact velocities are similarly distributed as for the depth of penetration analysis, again with approximately 70 *percent* of the impact velocities in the 700 to 2000 *feet/second* range. The concrete compressive strengths used in the tests are centered around 5000 *per square inch*, and the data set encompasses a range of values that are representative of compressive strengths used in protective construction.[1]

a. Generalized $G(\underline{x})$ Model

For spall and perforation, the $\underline{x}$ can be any physical or mechanical properties of the penetrator and target, *e.g.*, wall size, concrete strength, penetrator size, and impact velocity, *etc.* To select parameters and a general form for the G function, we first consider the deterministic equation for the penetration depth into concrete given in the *PCDM*. This equation has a form similar to

$$G(\underline{x}) = \alpha\, W^{\beta_1} d^{\beta_2} N^{\beta_3} v_s^{\beta_4} f_c^{\prime\,\beta_5} \tag{V-10}$$

in which W, d, N, v_s, and $f_c^{\prime}$ are respectively: penetrator weight, penetrator diameter, penetrator nose shape factor, striking velocity, and concrete unconfined compressive strength.

The general form of the G function selected for modeling perforation and spall is written, using Equation (V-9), as

$$G = A_0 + A_1 \ln W + A_2 \ln d + A_3 \ln N + A_4 \ln v_s + A_5 \ln t + A_6 \ln f_c^{\prime} \tag{V-11}$$

The constants, A_0, A_1, A_2, A_3, A_4, A_5, and A_6 are fit to the data by the dichotomous regression procedure using the maximum likelihood method. Note that since the G function is an indicator of the likelihood of spall or perforation, it also includes the wall thickness, t, as a resistance variable.

Not all of the target and penetrator variables in Equation (V-11) may be statistically significant in the prediction of perforation or spall. Hence, before proceeding with the dichotomous regression, a stepwise selection of the significant quantitative variables is first performed. For this, the SAS procedure STEPDISC is used, which selects the significant

[1]We could not determine on a test-by-test basis whether the concrete strengths are actual tested values or nominal design values. No attempt was made to assess the affect of this uncertainty in development of the reliability model because concrete strength was not found (for the range of values considered here) to be a highly significant variable in the probability of spall or perforation analysis.

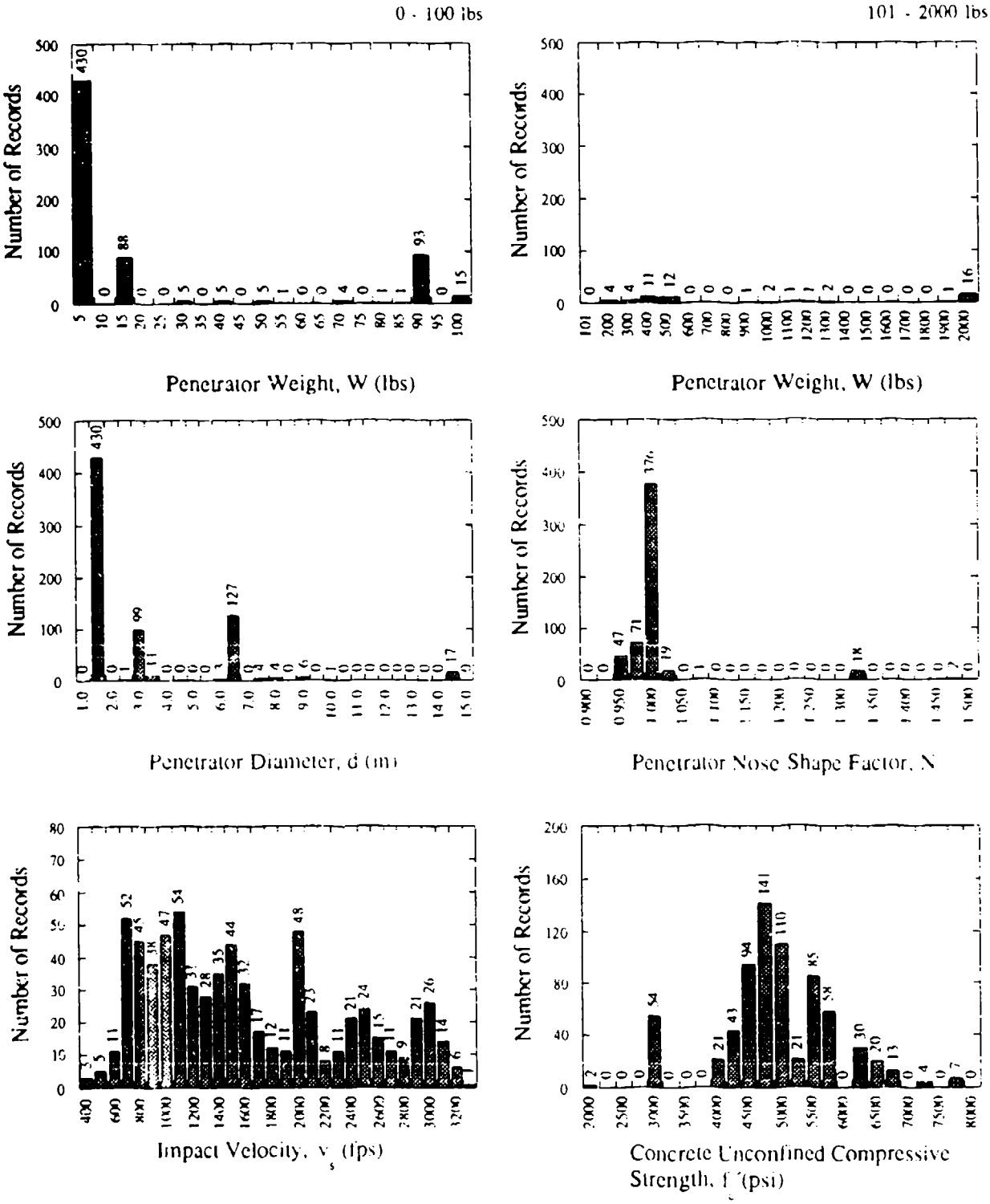

Figure V-5. Distributions of Input and Output Variables in the Data Records Selected for Spall and Perforation Analysis.

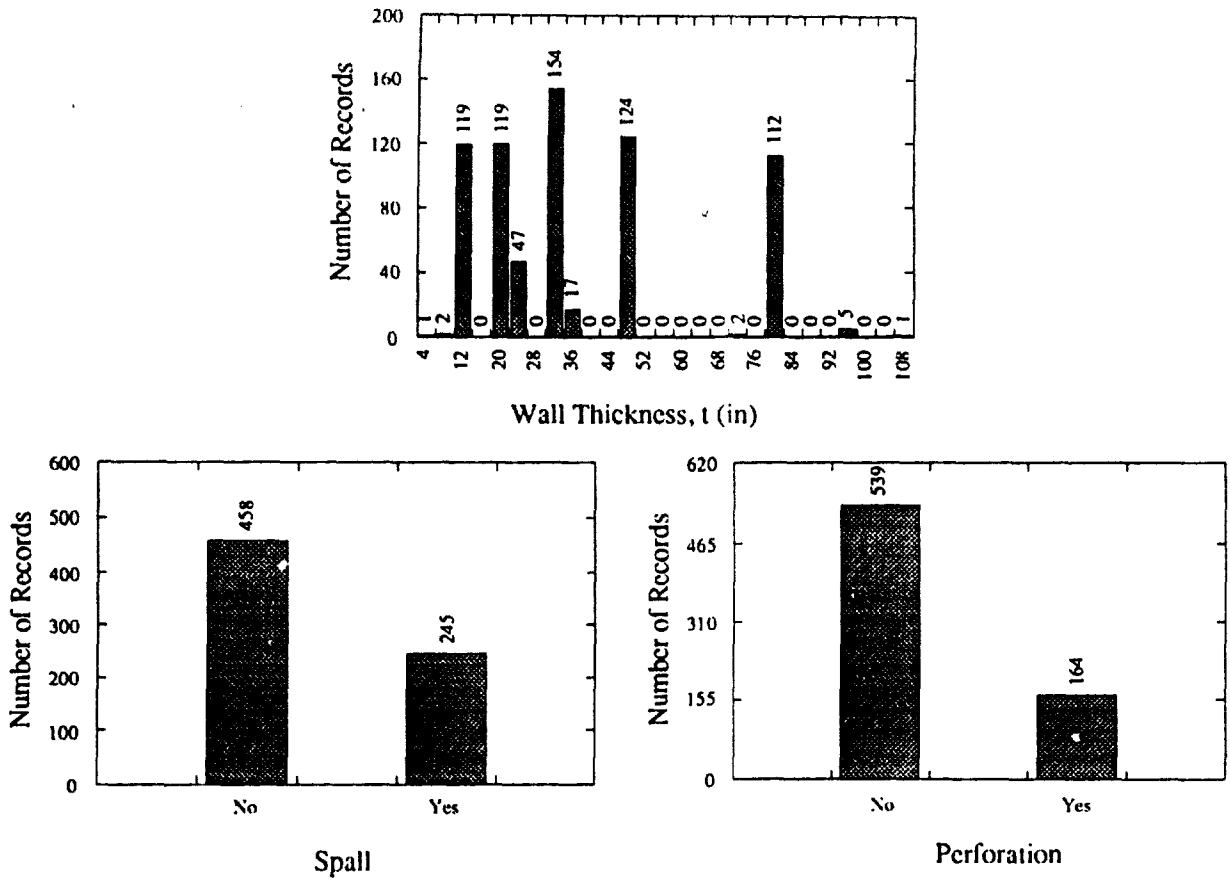

Figure V-5. Distributions of Input and Output Variables in the Data Records Selected for Spall and Perforation Analysis (Continued).

variables from among W, d, N, v_s, t, and f'_c. Using engineering judgment and the results of the STEPDISC procedure, four different models for spall and two different models for perforation were investigated. The SAS procedure LOGISTIC is used to perform the maximum likelihood estimation of the parameters for the dichotomous regression. Once the generalized $G(x)$ model parameters are estimated, statistical measures are presented to quantify goodness-of-fit and to compare the different models. Explanation of the goodness-of-fit measures is given in Section II.E.

(1) Spall

Table V-4 contains the four estimated G functions for modeling spall and the goodness-of-fit statistics. The table shows that all models fit almost equally as well and that the models are all statistically significant (since the probability of exceeding the chi-square is almost zero). Figure V-6 shows the plot of the logistic probability distribution of spall based on Model 4, which has the best fit in terms of the Akaike and Schwartz Criterion. The plot abscissa is the value of the G function and the ordinate is the probability of spall based on Model 4. Also

TABLE V-4. GENERALIZED G FUNCTIONS FOR MODELING CONCRETE SPALL AND GOODNESS-OF-FIT STATISTICS.

Candidate Spall G Function Models				
Model 1. $G(x) = 2.0493 \ln f_c' + 5.5088 \ln W + 7.5941 \ln v_s - 6.4086 \ln t - 7.8687 \ln d - 3.3370 \ln N - 21.2150$				
Model 2. $G(x) = 1.6652 \ln f_c' + 2.7674 \ln W + 7.5991 \ln v_s + 4.4874 \ln N - 6.4506 \ln t - 19.3648$				
Model 3. $G(x) = 2.6811 \ln W + 2.0378 \ln N + 7.5279 \ln v_s - 0.5850 \ln f_c' - 6.5290 \ln t$				
Model 4. $G(x) = 1.9841 \ln f_c' + 4.5765 \ln W + 7.6016 \ln v_s - 6.4248 \ln t - 5.1735 \ln d - 21.1503$				
Goodness-of-Fit Statistics				
Model	1	2	3	4
Variables	f'_c, W, v_s, t, d, N	f'_c, W, v_s, N, t	f'_c, W, v_s, N, t	f'_c, W, v_s, t, d
Intercept	Yes	Yes	No	Yes
Data Points	703	703	703	703
Percent Correctly Predicted	93.3	93.3	93.5	93.6
Likelihood Ratio	601.8	600.2	595.0	601.6
Akaike Information Criterion	321.2	320.8	324.0	319.4
Schwartz Criterion	353.1	348.2	346.8	346.7
Chi-Square	601.8	600.2	660.5	601.6
Pr > Chi-Square	0.0001	0.0001	0.0001	0.0001

[a] Shading indicates best fit.

shown in the figure are the actual data points where observations of spall are plotted as 1.0 and observations of no-spall are plotted as 0.0.

(2) Perforation

Based on the stepwise analysis, two candidate generalized G functions for modeling perforation were analyzed. Table V-5 presents each model and the goodness-of-fit statistics. The first model uses the variables selected by the STEPDISC procedure, and the second model adds concrete compression strength, f'_c while removing the intercept (constant term). The table shows that both models fit equally as well, and that all the variables in each model are found to be statistically significant. Because there is relatively little variation in perforation results over the range of f'_c values in the input data, the first model is significant without including concrete compressive strength, f'_c. As seen from Figure V-5, this range is not large, with almost 75 *percent* of the f'_c values in the range of 4000 *per square inch* to 5500 *per*

square inch. Hence, it is not possible to evaluate the effect of larger variations of f'_c on perforation, from the data. However, the model developed from these data should provide good accuracy for f'_c values in the range typically used in protective construction. In Model 2, the f'_c is significant because it effectively serves as the intercept. Figure V-7 shows the plot of the logistic probability distribution of perforation for Model 2.

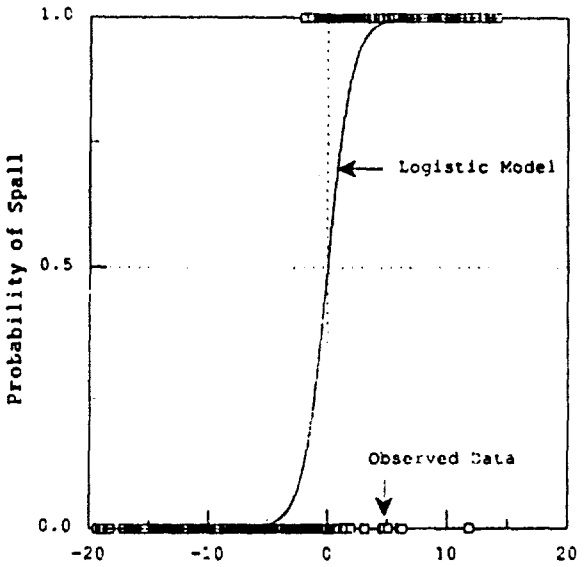

Figure V-6. Logistic Probability Model for Spall.

b. *PCDM* $G(\underline{x})$ Model

The spall and perforation models just presented can be used for reliability-based design. However, an alternative simplified approach is to base the G function directly on the deterministic equations given in the *PCDM*. In this way the reliability-based design factors can be used with the existing methodology. For these simplified models, the dichotomous regression procedure is not free to select independent coefficients for each of the parameters in the prediction equation. Hence, the simplified models will only work well if the *PCDM* method can accurately discriminate between survival and failure (spall or perforation). The simplified *PCDM* models are shown to be accurate for prediction of spall and perforation probability.

The *PCDM* prediction equations for spall and perforation were given earlier in Equations (V-6) and (V-7). If these models were exact predictors, then spall would occur whenever $t_s > t$, and perforation would occur whenever $t_p > t$. Hence, we can define G functions in terms of t_s/t and t_p/t in the dichotomous regression, and the G function for spall is

$$G(x) = A_0 + A_1 \ln (t_s/t) \tag{V-12}$$

TABLE V-5. GENERALIZED G FUNCTIONS FOR MODELING CONCRETE PERFORATION AND GOODNESS-OF-FIT STATISTICS.

Candidate Perforation G Function Models		
Model 1. $G(x) = 2.7530 \ln W + 7.2710 \ln N + 7.9832 \ln v_s - 6.5766 \ln t - 6.9491$		
Model 2. $G(x) = 2.7144 \ln W + 6.4166 \ln N + 7.9288 \ln v_s - 6.5679 \ln t - 0.8061 \ln f_c'$		
Goodness-of-Fit Statistics		
Model	1	2
Variables	t, W, N, vs	f'_c, t, W, N, v_s
Intercept	Yes	No
Data Points	703	703
Percent Correctly Predicted	92.0	92.7
Likelihood Ratio	490.7	490.5
Akaike Information Criterion	283.1	283.2
Schwartz Criterion	305.8	306.0
Chi-Square	490.7	701.3
Pr > Chi-Square	0.0001	0.0001

[a] Shading indicates best fit.

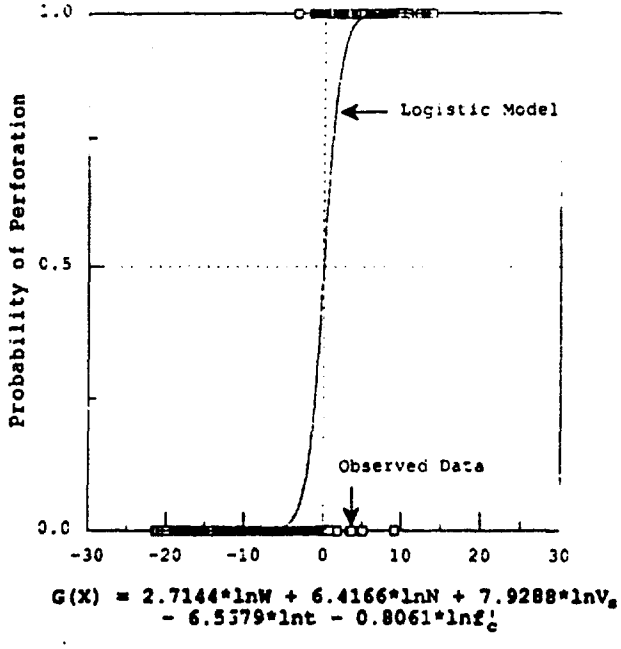

Figure V-7. Logistic Probability Model for Concrete Perforation.

while for perforation

$$G(x) = A_0 + A_1 \ln (t_p/t). \tag{V-13}$$

The estimated G functions and their goodness-of-fit statistics for spall and perforation are shown in Tables V-6 and V-7, respectively. For both cases, models in which the A_0 are set to 0 were also fit. Tables V-6 and V-7 show that all models fit equally well and are statistically significant. These results indicate that the *PCDM* prediction methods are essentially median-centered and unbiased. The plots of the logistic probability distribution for both spall and perforation are shown in Figures V-8 and V-9.

TABLE V-6. G FUNCTIONS FOR MODELING CONCRETE SPALL (t_s/t) AND GOODNESS-OF-FIT STATISTICS.

Candidate Spall G Function Models		
Model 1. $G(x) = 0.00688 + 6.2682 \ln\left(\frac{t_s}{t}\right)$		
Model 2. $G(x) = 6.2695 \ln\left(\frac{t_s}{t}\right)$		
Goodness-of-Fit Statistics		
Model	1	2
Data Points	703	703
Percent Correctly Predicted	92.7	92.7
Likelihood Ratio	541.7	541.7
Akaike Information Criterion	371.3	369.3
Schwartz Criterion	380.4	373.8
Chi-Square	541.7	607.3
Pr > Chi-Square	0.0001	0.0001

The model selected using a *PCDM* $G(x)$ is a more restricted version of the generalized $G(x)$ functions (*i.e.*, Tables V-4 and V-5). Although t_s and t_p in Equations (V-12) and (V-13) are functions of W, d, N, v_s, and f'_c, so that both models contain the same parameters, the regression procedure is not free to select coefficients for each of these variables. However, the goodness-of-fit measures for these models compare favorably with the earlier models of Tables V-4 and V-5. Hence, we can use the simplified models for the RBD approach.

3. RBDFs for Spall and Perforation

a. No Uncertainty in W, d, N, v_s, f'_c

Using the simplified model, we can develop the RBDFs for spall and perforation based on the design manual equations (Equations (V-6) and (V-7)). Given that all the

TABLE V-7. G FUNCTIONS FOR MODELING CONCRETE PERFORATION (t_p/t) AND GOODNESS-OF-FIT STATISTICS.

Candidate Perforation G Function Models		
Model 1. $G(x) = -0.3359 + 6.2740 \ln\left(\frac{t_p}{t}\right)$		
Model 2. $G(x) = 6.7784 \ln\left(\frac{t_p}{t}\right)$		
Goodness-of-Fit Statistics		
Model	1	2
Data Points	703	703
Percent Correctly Predicted	0.898	0.929
Likelihood Ratio	462.0	457.0
Akaike Information Criterion	305.8	308.8
Schwartz Criterion	314.9	313.3
Chi-Square	462.0	667.8
Pr > Chi-Square	0.0001	0.0001

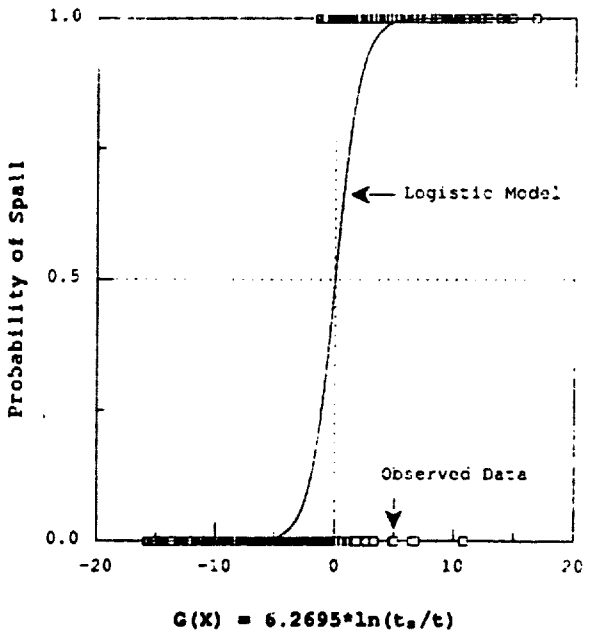

Figure V-8. Logistic Probability Model for Spall.

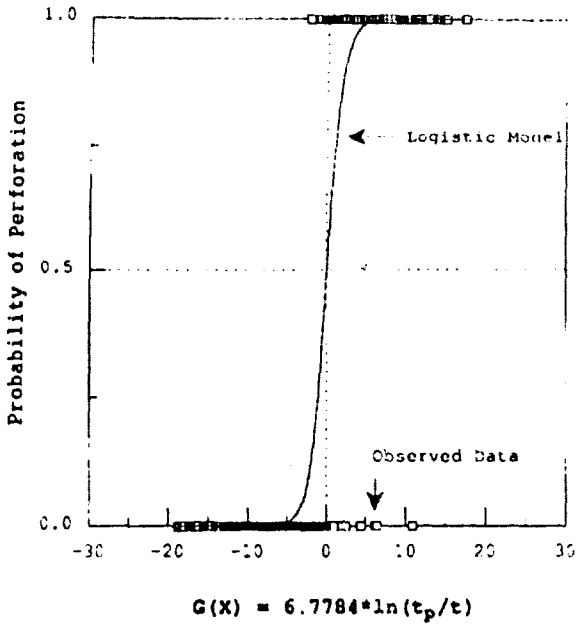

Figure V-9. Logistic Probability Model for Concrete Perforation.

design inputs are known, the reliability of a wall of thickness t to resist spall can be determined from

$$R(t/t_s) = 1 - P_F(t/t_s) = 1 - \frac{\exp[G(x)]}{1 + \exp[G(x)]} = \frac{1}{1 + \exp[G(x)]} \quad \text{(V-14)}$$

where t is the wall thickness and t_s is the spall thickness given by Equation (V-6). By substituting Model 2 of Table V-6 into the above equation, we obtain

$$R(t/t_s) = \frac{1}{1 + \exp[-6.27 \ln(t/t_s)]} = \frac{1}{1 + (t/t_s)^{-6.27}} \quad \text{(V-15)}$$

Similarly, for perforation (using Model 2 of Table V-7),

$$R(t/t_p) = \frac{1}{1 + (t/t_p)^{-6.78}} \quad \text{(V-16)}$$

b. Incorporating Parameter Uncertainty

Using Equations (V-15) and (V-16), Table V-8 lists the reliability-based design factors, t/t_s and t/t_p, and their associated reliabilities that account for the spall and perforation model error. Note that the factors are slightly greater for spall, reflecting the slightly greater uncertainty in predicting spall. To complete the reliability analysis, it is necessary to consider

TABLE V-8. RELIABILITY OF WALL THICKNESS TO PREVENT SPALL AND PERFORATION.[a]

Reliability[b]	$P_F(x)$	$G(x)$	RBDF	
			Spall	Perforation
			t/t_s	t/t_p
0.01	0.99	4.60	0.48	0.51
0.05	0.95	2.94	0.63	0.65
0.10	0.90	2.20	0.70	0.72
0.25	0.75	1.10	0.84	0.85
0.50	0.50	0.00	1.00	1.00
0.75	0.25	-1.10	1.19	1.17
0.90	0.10	-2.20	1.42	1.38
0.95	0.05	-2.94	1.60	1.54
0.99	0.01	-4.60	2.08	1.97

[a] t_s, t_p as defined by Equations (V-6) and (V-7), respectively.
[b] Assumes all inputs to Equations (V-6) and (V-7) are deterministic.

uncertainty in the problem inputs — that is, W, d, N, v_s, and f'_c. As discussed earlier for the case of depth of penetration in massive concrete, it is only necessary to consider the uncertainty in striking velocity. Tables V-9 and V-10 contain the load factors to be applied to the striking velocity for the reliability-based design procedure as a function of striking velocity coefficient of variation. These load factors were obtained from Monte-Carlo simulation analyses.

c. Reliability-Based Design Spall and Perforation Examples

The reliability-based design procedure for spall and perforation is:

1. Establish reliability goal based on structure mission.
2. Multiply best estimate striking velocity by the load factor from Table V-9 for spall and Table V-10 for perforation.
3. Compute t_s and/or t_p using design manual equations (Equations (V-6) and (V-7)) with the factored striking velocity from Step 2.
4. Select RBDF (t/t_s and/or t/t_p) values from Table V-8.
5. Obtain design wall thickness by multiplying result of Step 3 by the RBDF from Step 4.

To illustrate the procedure, consider the design of a reinforced concrete aircraft shelter. We wish to determine how thick the shelter arch wall must be to resist spall and perforation due to impact by a 90 *mm* tank round. The problem parameters are W = 23.4 *pounds*, d = 3.54 *inches*, N = 1.1, v_s = 1200 *feet/second*, and f'_c = 5000 *per square inch*. Due to uncertainty in the tank standoff and variability in the muzzle velocity, the striking velocity is uncertain with a coefficient of variation of 20 *percent*.

Following the procedure outlined above, we evaluated the required wall thicknesses to defeat spall and perforation for several reliability levels. The results are shown in

TABLE V-9. STRIKING VELOCITY LOAD FACTORS FOR PREDICTION OF CONCRETE SPALL.

Reliability	Velocity Factors, λ (for different cov of v_s)				
	0.1	0.2	0.3	0.4	0.5
0.01	0.95	0.86	0.66	0.36	0.24
0.05	0.96	0.90	0.77	0.63	0.51
0.10	0.97	0.91	0.81	0.72	0.64
0.25	0.98	0.95	0.90	0.84	0.81
0.50	1.00	1.00	1.00	1.00	1.00
0.75	1.02	1.05	1.08	1.12	1.19
0.90	1.04	1.09	1.16	1.24	1.33
0.95	1.05	1.10	1.18	1.28	1.42
0.99	1.06	1.13	1.27	1.38	1.60

TABLE V-10. STRIKING VELOCITY LOAD FACTORS FOR PREDICTION OF CONCRETE PERFORATION.

Reliability	Velocity Factors, λ (for different cov of v_s)				
	0.1	0.2	0.3	0.4	0.5
0.01	0.95	0.81	0.55	0.28	0.16
0.05	0.96	0.87	0.70	0.55	0.42
0.10	0.97	0.89	0.77	0.66	0.57
0.25	0.98	0.94	0.87	0.81	0.78
0.50	1.00	1.00	1.00	1.00	1.00
0.75	1.03	1.06	1.08	1.12	1.20
0.90	1.04	1.10	1.16	1.24	1.35
0.95	1.06	1.12	1.19	1.29	1.46
0.99	1.09	1.18	1.31	1.43	1.65

Table V-11 below and are also plotted in Figure V-10. The figure is useful in determining the increase in design reliability achieved by increasing the design wall thickness. This information can be used in mission planning and determining optimal design reliability levels (*i.e.*, trade studies between increasing construction costs due to increasing design thickness *vs.* reducing expected damage probabilities and damage costs due to increasing design thickness). The table and figure also demonstrate the effect of striking velocity uncertainty on required design thickness.

E. RESIDUAL VELOCITY

1. Residual Velocity Model

The residual velocity, v_r, of a projectile that passes through a concrete element backed by air can be related to the velocity at which a penetrator will just perforate the slab, v_p. The expression given in the *PCDM* (*PCDM* Equation (VII-10)) for computing v_r in concrete is

$$v_r^{1.8} = v_s^{1.8} - v_p^{1.8} \qquad \text{(V-17)}$$

TABLE V-11. REQUIRED WALL THICKNESS TO DEFEAT SPALL AND PERFORATION DUE TO IMPACT OF A 90 *MILLIMETER* TANK ROUND.

Reliability	Required Wall Thickness (*inches*)[a]			
	Spall		Perforation	
	No v_s Uncertainty	v_s cov = 0.20	No v_s Uncertainty	v_s cov = 0.20
0.50	25	25	21	21
0.75	30	31	24	26
0.90	36	39	29	31
0.95	40	44	32	36
0.99	52	59	41	49

[a] Problem parameters: W = 23.4 *pounds*, d = 3.54 *inches*, N = 1.1, v_s = 1200 *feet/second*, f'_c = 5000 *psi*.

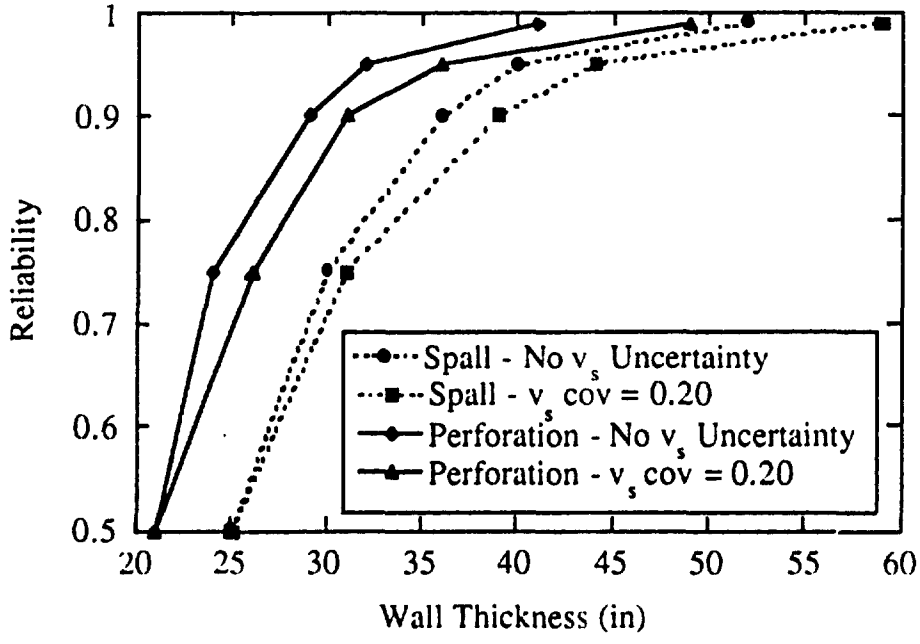

Figure V-10. Required Wall Thickness to Defeat Spall and Perforation due to Impact of a 90 *mm* Tank Round.

where v_s is striking velocity. In the *PCDM*, perforation velocity, v_p, for a given slab-projectile combination is found by solving the perforation thickness formula (Equation (V-7)) for x, and then using the massive concrete penetration formula (Equation (V-1)) to solve for v_s. Thus (*PCDM* Equation (VII-12)),

$$v_p = \left(\frac{x_p f'_c{}^{0.25} d^{0.4}}{26.8\sqrt{NW}} \right)^{1.11} \qquad x_p \le 2d \tag{V-18}$$

$$v_p = d\left(\frac{(x_p - d)\sqrt{f'_c}}{180\,NW} \right)^{0.556} \qquad x_p > 2d$$

where

$$x_p = \begin{cases} d\,(2.22 - \sqrt{4.93 - 1.39\,t/d}) & x_p < 1.35\,d \\ 0.806\,t - 1.07\,d & 1.35\,d \le x_p \le 13.5\,d \end{cases} \qquad \text{(V-19)}$$

and all other variables are as defined for Equations (V-1) and (V-7).

This set of equations leads to three possible expressions for residual velocity, depending on the ratio x_p/d ($x_p < 1.35d$; $1.35d < x_p < 2d$; $2d < x_p < 13.5d$).

2. Prediction Error Analysis

Forty-five test records (see Figure V-1)were available from the databases for analysis of residual velocity prediction. Figure V-11 shows the distributions of all input and output variables. We note that some of the residual velocities given in the database are actually determined by back calculation based on the depth of penetration into soil behind the targets; these will be identified on the model comparison plot later.

The residual velocity prediction error is analyzed using the same procedure that was used for analyzing the prediction error for depth of penetration in massive concrete (Section V.C.2). The ratio of observed (measured) velocity, v_{rm}, to predicted (calculated) velocity, v_{rc}, is

$$\xi = \frac{v_{rm}}{v_{rc}} \qquad \text{(V-20)}$$

where $\xi > 1$ indicates an underprediction, and $\xi < 1$ indicates an overprediction.

Figure V-12 is the plot of v_{rm} versus v_{rc} and Table V-12 shows the statistics of ξ and ln (ξ). These statistics indicate that, on average, the model overpredicts residual velocity. Also shown in the figure is the line for $v_{rm} = v_{rc}$ and the linear regression for v_{rm} versus v_{rc}. As can be seen, the overprediction is greater at the lower residual velocities. The W statistic and P value in the table also show that both ξ and ln ξ fail the test of normality.

Due to the apparent systematic bias in the *PCDM* model, additional residual velocity models were examined. In a study by Nash, *et al.* [1986], four techniques were used to compute projectile residual velocity. They are:

1. S-S: Sandia depth of penetration method [Nash, 1986]
   Sandia residual velocity method [Nash, 1986]
2. A-A: British A depth of penetration method [Nash, 1986]
   AFATL residual velocity method (disclosure limit)
3. A-S: British A depth of penetration method;
   Sandia residual velocity method
4. S-A: Sandia depth of penetration method
   AFATL residual velocity method

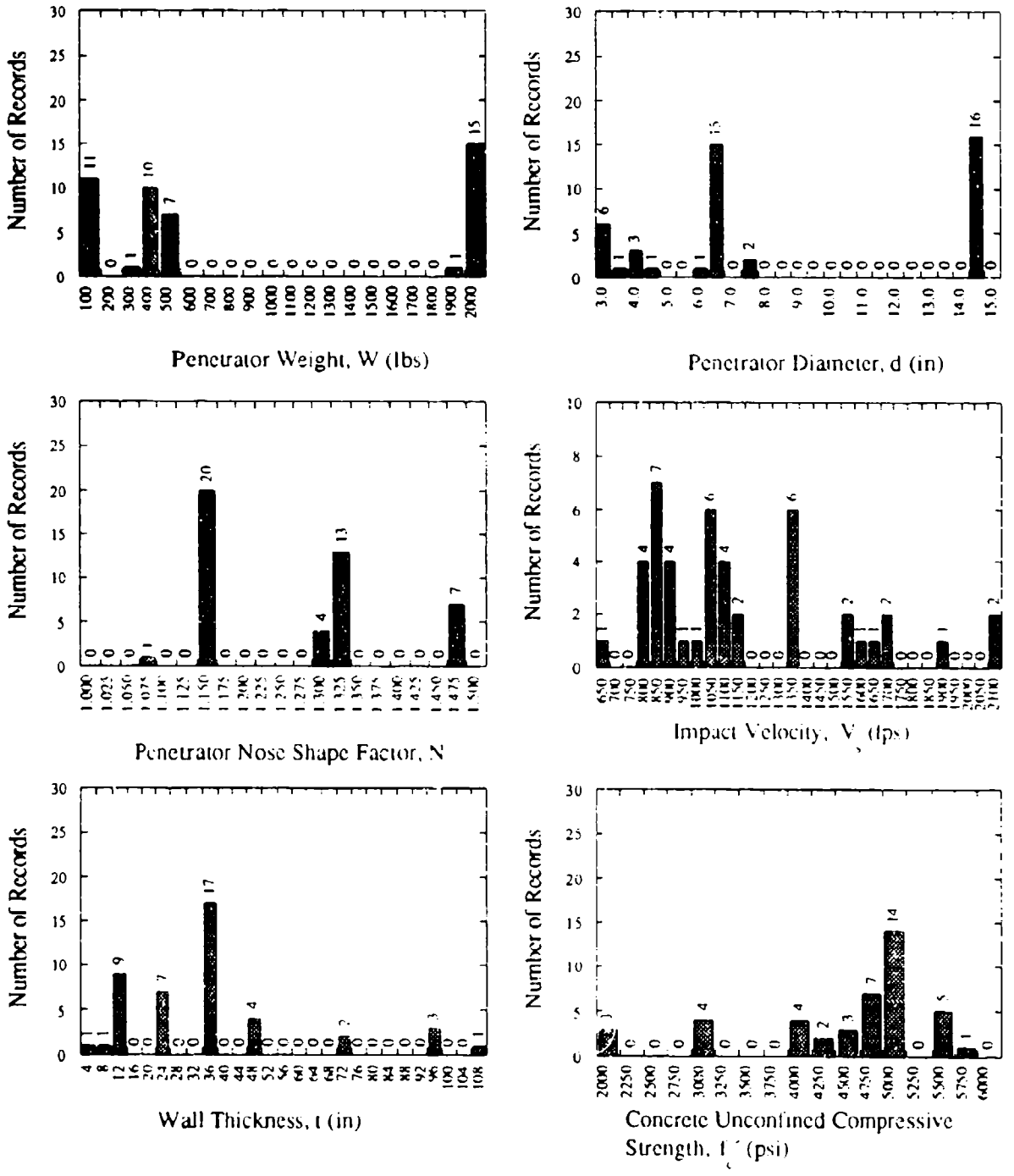

Figure V-11. Distributions of Input and Output Variables in the Data Records Selected for Residual Velocity Analysis.

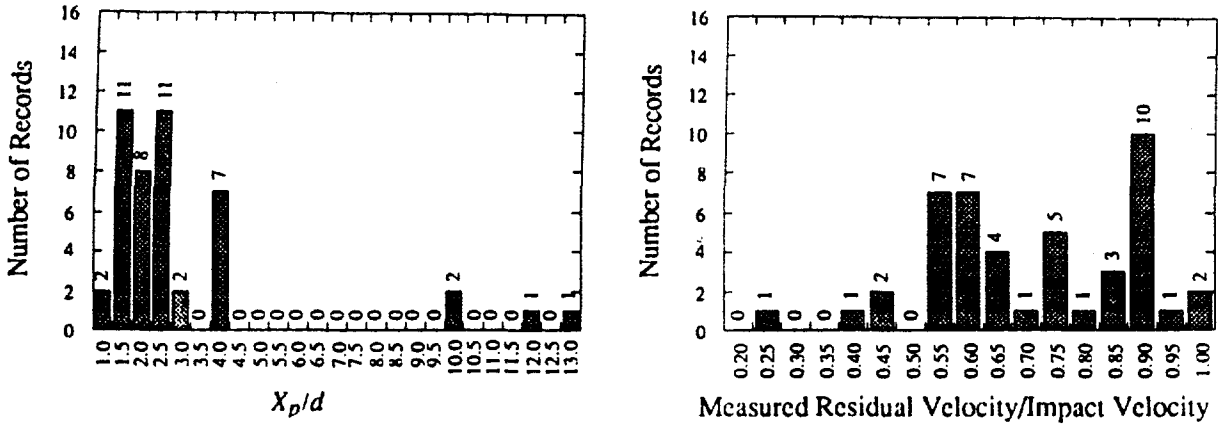

Figure V-11. Distributions of Input and Output Variables in the Data Records Selected for Residual Velocity Analysis (Continued).

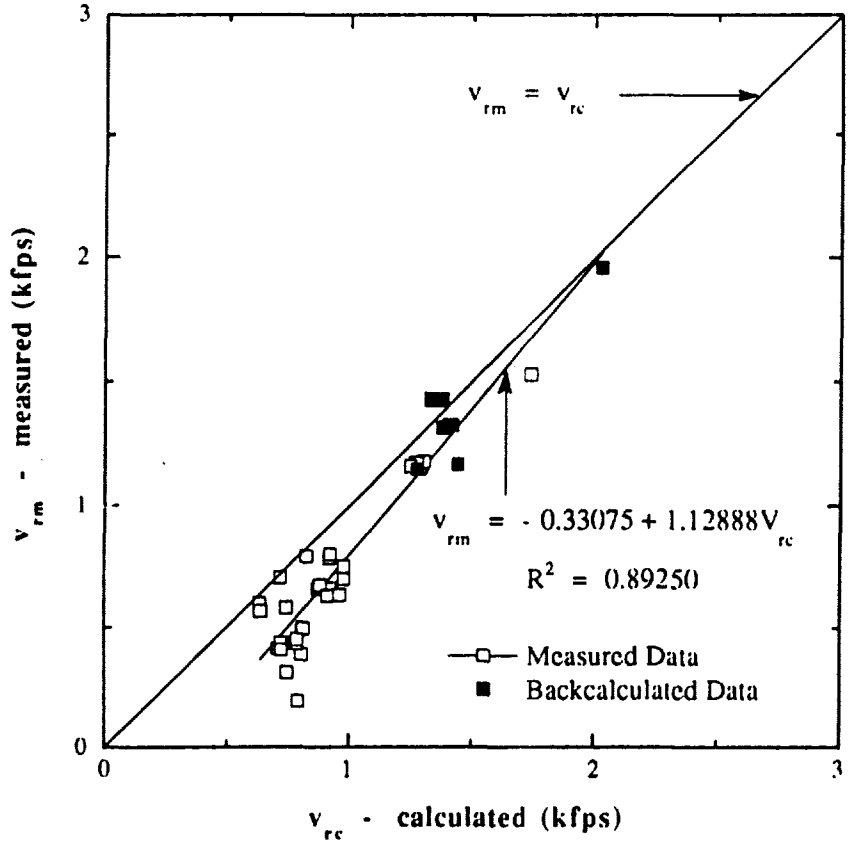

Figure V-12. Comparison of Measured and Calculated Projectile Residual Velocity after Concrete Perforation.

TABLE V-12. STATISTICS OF MODEL ERROR ξ_V AND ln (ξ_V).

	ξ_v	ln (ξ_v)
Mean	0.7719	-0.2928
Std. Dev.	0.1828	0.2819
W:Normal[a]	0.9417	0.8671
Prob < W	0.0363	0.0001

[a]Shapiro-Wilk statistic for testing of normality

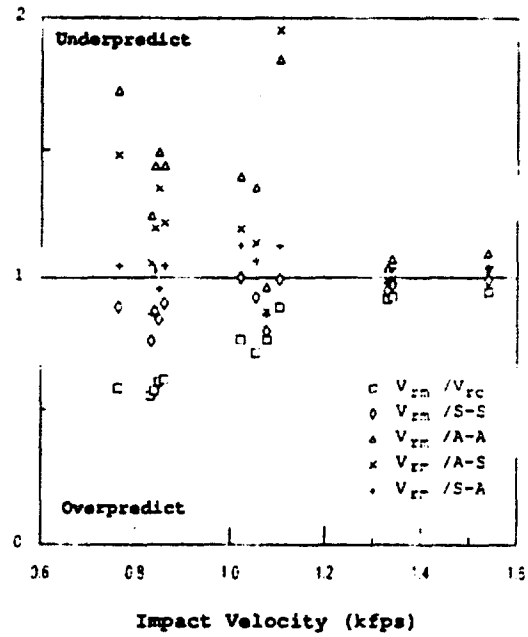

Figure V-13. Comparison of the Residual Velocity Ratio between Measured and Calculated Data for Four Different Prediction Equations.

Nash compared these prediction methods against 12 test results. In Figure V-13, the ratio of measured residual velocity to calculated residual velocity is plotted as a function of impact velocity for the model given in the design manual, and the four techniques investigated by Nash. The figure illustrates that overall the S-A technique is the best, and that the *PCDM* method is the most design conservative. However, when $v_s > 1200$ *feet/second*, all of the model predictions are approximately the same. Additional work is needed to improve residual velocity prediction methods.

3. Reliability-Based Prediction Model for Residual Velocity

The ratio ξ is a random variable that models the residual velocity model prediction error. The statistics of ξ and ln (ξ) fail the test of normality. An examination of the data reveals that ξ fails the test of normality because of a lack of fit at the extremes. At extreme confidence values, the normal distribution is slightly design conservative. The recommended reliability-based design factors, given in Table V-13, are conservative values based on both the empirical

distribution and the normal distribution. Due to the limited amount of data, the RBDFs are given only for confidence values from 0.25 to 0.90. Table V-14 shows recommended reliability-based load factors for the striking velocity obtained by Monte Carlo simulation analyses.

TABLE V-13. RBDFS FOR RESIDUAL VELOCITY GIVEN THAT PERFORATION OCCURS — NO UNCERTAINTIES IN W, d, N, v_s, f'_c.

Reliability, $P(\xi < \lambda_v)$	RBDF
0.25	0.65
0.50	0.78
0.75	0.92
0.90	1.00

TABLE V-14. STRIKING VELOCITY LOAD FACTORS FOR PREDICTION OF RESIDUAL VELOCITY THROUGH CONCRETE.

	Velocity Factors, λ_v (for different cov of v_s)				
Reliability	0.1	0.2	0.3	0.4	0.5
0.25	0.97	0.95	0.90	0.85	0.80
0.50	1.00	1.00	1.00	1.00	1.00
0.75	1.03	1.05	1.10	1.15	1.25
0.90	1.05	1.15	1.20	1.30	1.45

The reliability-based prediction of residual velocity is made by first multiplying the striking velocity by a load factor from Table V-14, evaluating the residual velocity using Equations (V-17) through (V-19), and then multiplying the computed residual velocity by an RBDF obtained from Table V-13. For example, for a 75 *percent* confidence prediction when the striking velocity has a coefficient of 0.3, the striking velocity is first multiplied by 1.10 (Table V-13). Using the factored striking velocity, use Equations (V-17) through (V-19) to predict a residual velocity, say 1200 *feet/second*. Then from Table V-13 for 75 *percent* reliability, the 1200 *feet/second* prediction is multiplied by 0.92, giving 1104 *feet/second*. Thus, there is a 75 *percent* probability that the residual velocity will be less than 1104 *feet/second* given that perforation occurs.[1] Note that the RBD factor is less than 1 because of the conservative bias in the *PCDM* method.

[1]The reliability levels given here are actually conditional reliabilities since the database are all occurrences of perforation. If the deterministic analysis procedure predicts that no perforation will occur, there is still some probability that perforation will occur and that the residual velocity will be nonzero. Hence, the procedure given here is strictly only applicable under the assumption that perforation has occurred.

(The reverse of this page is blank.)

VI. PROTECTIVE STRUCTURE SYSTEMS ANALYSIS

A. INTRODUCTION

Protective structures generally must be designed to defeat multiple weapon effects from a wide range of threats. In addition, because the loading, structural response analysis, and failure analysis will be subject to uncertainty it is often not possible to identify a single critical failure mode. For example, it may not be possible to establish, with certainty, whether a flexural failure from a standoff burst or fragment penetration will dominate. Hence, designers should consider all relevant failure modes that affect the performance of the mission. The RBDFs presented in the preceding sections provide design reliabilities for individual modes of failure. The reliability levels for the RBDFs must be selected so that when the individual failure mode reliabilities are combined, the system reliability meets the structure or facility design criteria.

To ensure that all important weapon effects and failure modes are properly considered in the reliability evaluation of a protective structure, event trees and fault trees are useful tools to identify the damage sequences and contributors. Probability theory and analytical techniques are used to combine the failure modes to quantify the reliability of the facility or system. By performing a systems reliability analysis, reliable and balanced overall designs can be achieved. A balanced design is one in which the design resources are allocated among the failure modes to provide maximum protection with available resources.

Background information on protective structures system reliability analysis is contained in the Phase I RBD report [Twisdale, Sues, and Murphy, 1988] and in the *PCDM*. The Phase I RBD report gives background information on combining failure modes for facility and structure systems reliability. Lower and upper bound equations on system reliability are given with a simple method for grouping and combining failure modes. In Section II of the *PCDM*, optimal reliability-based protective design is discussed in terms of maximizing facility mission objectives. The reliability of the system is treated as a constraint that the designer must satisfy, or as part of the design objective function. In each case, implementation requires a system reliability analysis and, generally, reliability allocation among multiple failure modes and subsystems.

In this section, we present the RBD approach for structure/facility systems analysis. In Subsection VI.B a procedure is presented for performing RBD for structural systems and facilities with multiple components and failure modes. Generic fault trees are presented in Section VI.C for an aboveground structure and a buried structure. These detailed fault trees can be easily simplified and pruned by the analyst for particular protective systems design problems. System reliability equations are summarized in Section VI.D.

B. RBD PROCEDURE FOR PROTECTIVE SYSTEMS

A simplified procedure for performing RBD for a protective system or facility is given in Figure VI-1. A brief explanation is given in the following paragraphs for each step.

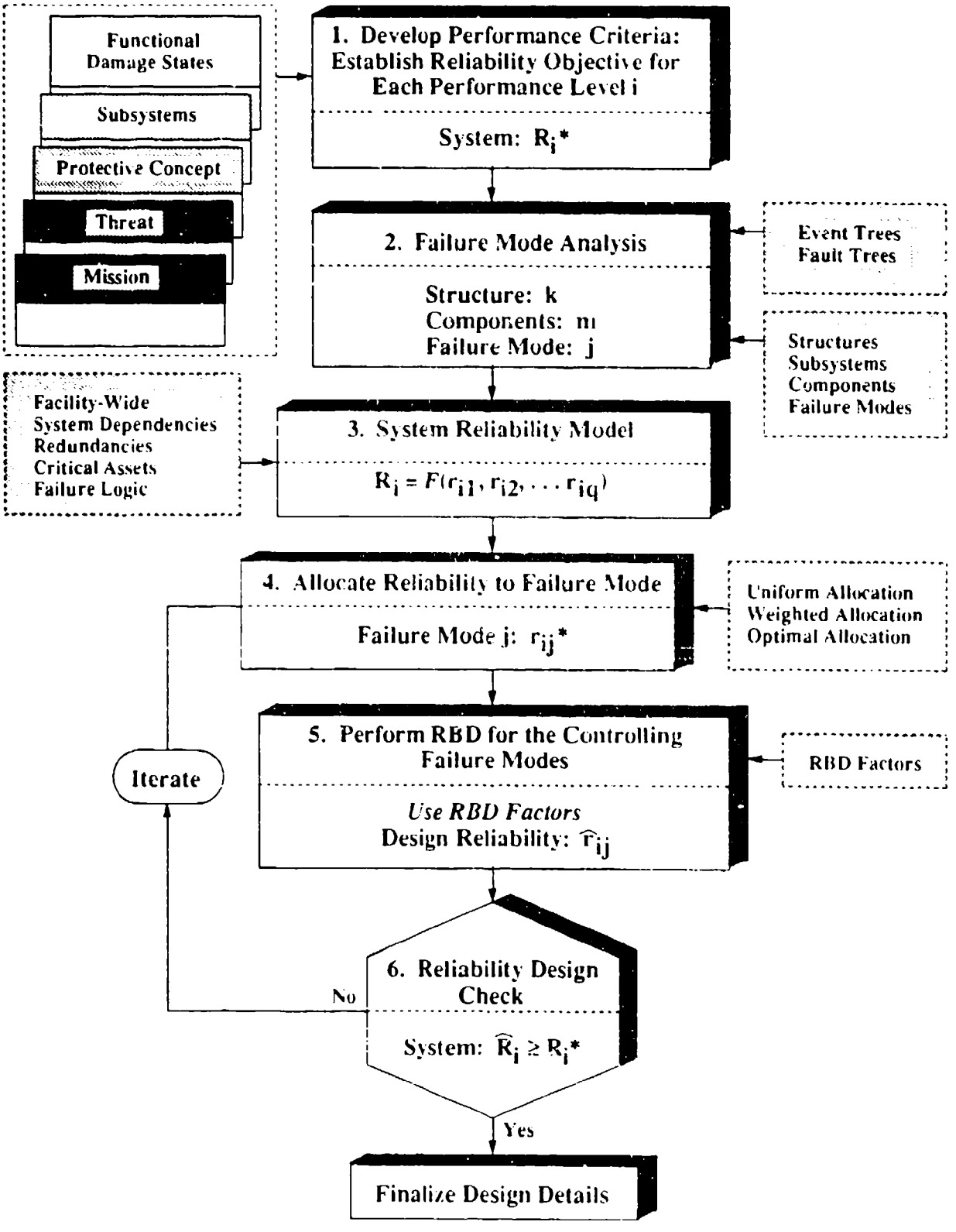

Figure VI-1. Systems RBD Procedure.

1. System Reliability Objective

The first step is to evaluate the mission objectives and threats and to develop the performance criteria for the proposed protective concept. For complex facilities or systems, there may be several levels of performance in the criteria statement. Given the performance criteria, the reliability objective of the system must either be specified at this stage or quantified through an optimization analysis, as described in Section II.B of the *PCDM*. In the absence of a facility-wide systems level optimization study, system reliability objectives (R_i*) in the range 0.90 to 0.95 may be reasonable goals for protective designs. Reliability objectives of 0.99 or higher may be appropriate for theater-level command and control facilities.

In developing system reliability objectives, consider each functional performance level in the criteria statements. For example, for an airbase facility, a *requirement* for generating 50 sorties during the first 6 hours after attack may correspond to Performance Level 1. If this level of sortie production is required for mission performance, a system of R* of 0.95 might be a reasonable design objective (in the absence of a detailed study). On the other hand, the mission requirement might also include a *goal* to produce one hundred sorties during the same period with at least 75 *percent* reliability. In this case, the system reliability objectives for these two performance levels are R_1* = 0.95 and R_2* = 0.75. Note that at this time we do not know which one of these objective will govern the design of individual structures and components at the facility. The design of some structures or systems may be dominated by R_1* and the remaining by R_2*.

2. Failure Mode Analysis

The second step involves the identification of all possible failure modes of the system. This analysis considers how structural response affects the performance of subsystems, components, and personnel. In general, the failure mode analysis must be performed for each performance level. It may be possible to identify the potential controlling failure modes at this stage. Otherwise, the analyst should carry forward all the potential modes that could contribute to the design failure. A summary table of weapon effects, protective structural elements, failure modes, and protective components is given in Figure VI-2. This figure provides a starting point for protective structure failure mode analyses. System and structure-specific fault trees can be developed, if needed, to ensure that all failure modes have been addressed in the design. Detailed generic fault trees are given in Section VI.C for use in identifying relevant failure modes for protective structures.

3. System Reliability Model

Once the failure modes are identified, a reliability model of the system is developed for each performance level. Depending on the design situation and failure mode results, the model can often be reduced to a Boolean expression of AND and OR operators that reflect the failure logic. In some cases a straightforward serial system will be adequate for a single protective

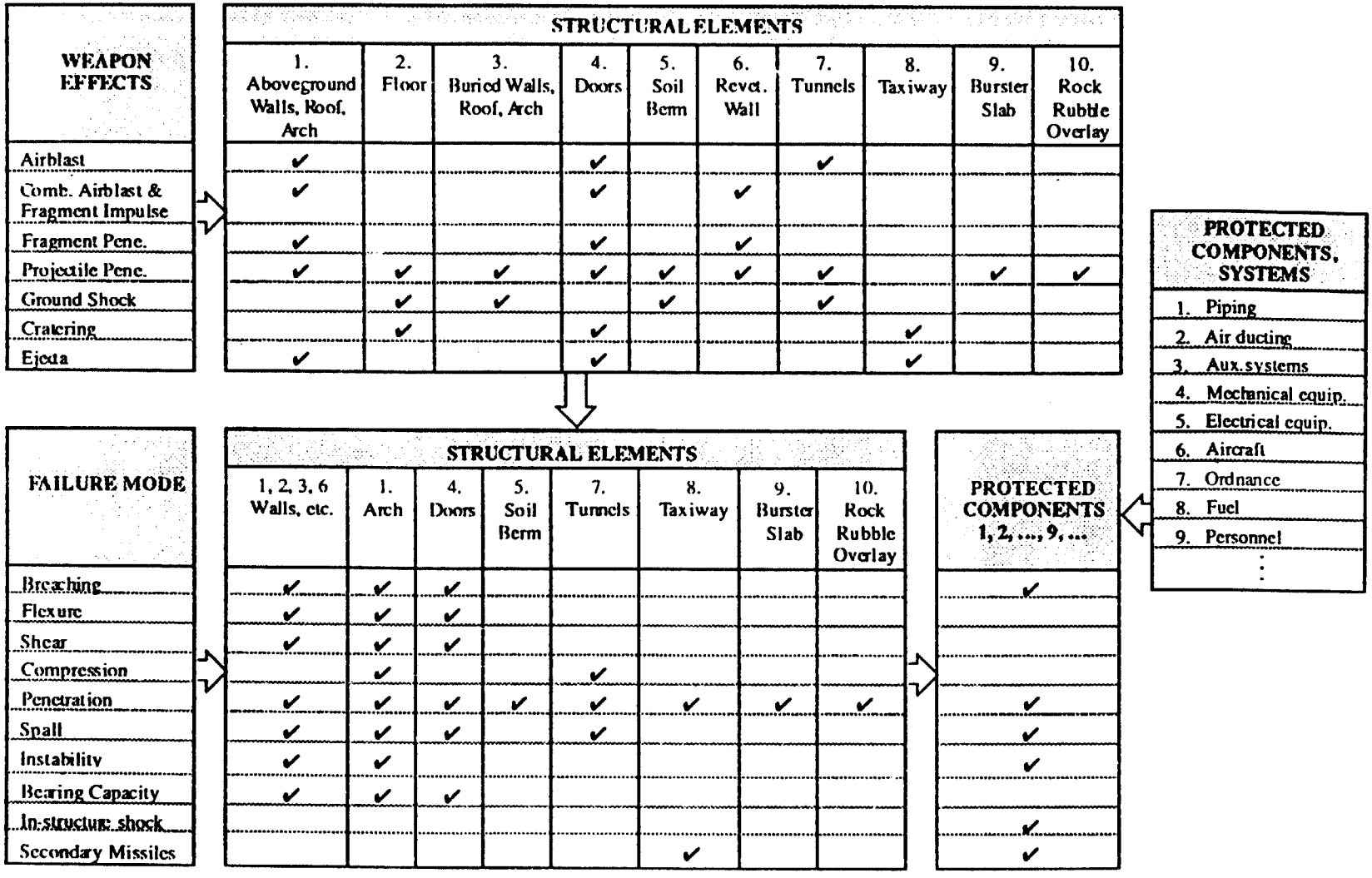

Figure VI-2. Interaction Between Weapon Effects, Structural Elements, Failure Modes, and Protected Systems.

structure, particularly for the more severe damage levels where it is clear that internal components will not survive. For example, if performance level i requires no perforation of structure k for a given weapon, perforation of any exterior surface of the structure would allow the bomb to detonate within the structure, which would lead to unity conditional failure probabilities. Thus, if there are five exterior structural components (door, floor, arch, and two end walls), then failure of any one to prevent weapon perforation would constitute the failure logic, represented by

$$F_{ik} = (f_{ik1} \cup f_{ik2} \cup f_{ik3} \cup f_{ik4} \cup f_{ik5}) \tag{VI-3}$$

where F_{ik} = failure of structure k for perforation level i; f_{ikm} = failure of component m of structure k for performance level i; and $\cup$ = union (OR) operator. Moreover, if the facility has three such structures, and only one is needed to perform the mission at performance level i, then the system reliability equation is

$$R_i = 1 - P(F_i) = 1 - P(F_{i1} \cap F_{i2} \cap F_{i3}) \tag{VI-4}$$

where F_i = facility-wide failure to perform at level i and $\cap$ = intersection (AND) operator. The value of this step is to develop a fundamental understanding of the system. Modeling at the individual component level is often not needed. What is important is to understand dependencies among failure modes, systems redundancies, and system sensitivities. Additional discussion on system reliability evaluation is given in Section VI.D.

4. Reliability Allocation

The fourth step involves the allocation of reliability to the various failure modes, including structures, subsystems, and components. The goal of this allocation process is to satisfy the reliability objective for the system (R_i*) and to maximize the cost-effectiveness of the facility design. The reliability allocation is achieved through a formal optimization procedure or by using simple rules or heuristic procedures. The dynamic programming method is often used to perform formal optimal reliability allocation (*e.g.*, see Kapur and Lamberson [1977]). The approach taken should match the level of detail in the reliability model, the performance criteria, and the cost information available. High-level allocations to entire subsystems and structures will generally be adequate.

In many cases, near optimal reliability allocations can be made based on judgment and a basic understanding of the system. For example, if the system is serial and damage to the components are independent, the system reliability for performance level i is

$$R_i = \prod_{j=1}^{q} r_{ij} \tag{VI-5}$$

where r_{ij} = predicted reliability for performance level i and failure mode j, and q = total number of failure modes across all structures and elements. If the cost sensitivity for hardening protection is

approximately the same across the q failure modes, an equal reliability allocation for Equation (VI-5) produces

$$r_{ij}^{*} = \left(R_i^{*}\right)^{1/q} \tag{VI-6}$$

for all q failure modes. Other reliability model formulations for serial-independent systems are noted by Twisdale [1986].

For a simple independent parallel system

$$R_i = 1 - \prod_{j=1}^{q} (1 - r_{ij}) \tag{VI-7}$$

and an equal reliability allocation similarly yields

$$r_{ij}^{*} = 1 - \left(1 - R_i^{*}\right)^{1/q}. \tag{VI-8}$$

Equations (VI-5) through (VI-8) are illustrative only for independent failure modes and are not necessarily the optimal allocation strategy. For complicated system models or if the failure modes are correlated, numerical reliability optimization procedures, such as dynamic programming, may be needed. A simple grouping technique according to assumptions of perfect independence and perfect correlation is given in Section VI.D.

5. RBD for Controlling Failure Modes

Once the initial reliability allocation for each failure mode is complete, the next step is to design each structural component using the RBD procedure. As described in the preceding sections, this step simply involves applying an RBD factor to the nominal design to achieve the desired reliability for that failure mode. For example, if the allocated reliability to prevent breach for an aboveground wall is 0.95, the designer would use the RBD factor of 1.29 (Table II-23) times the nominal *PCDM* thickness to achieve the 95 *percent* reliability in that failure mode. This initial design reliability from the RBD procedure is denoted $\hat{r}_{ij}$. As part of this design process, many failure modes will be found to be non-contributing and their design reliabilities $\hat{r}_{ij}$ may approach unity due to the design proportioning required for the controlling modes of failure.

6. Reliability Design Check

The final step involves a design check to recompute the system reliability, using the model developed in Step 3. This checking step is achieved by substituting the design reliability $\hat{r}_{ij}$ for each failure mode j into the system reliability model and solving for $\hat{R}_i$. If $\hat{R}_i$ exceeds, but is reasonably close to, R_i*, the designer can proceed to finalize the design details. Otherwise, as shown in Figure VI-1, some iteration is required to ensure that R_i* is achieved or, alternatively, to further balance the design reliabilities if $\hat{R}_i >> R_i$*.

C. GENERIC FAULT TREES

Step 2 of the RBD procedure for protective systems involves the identification of all relevant failure modes. Fault trees provide for the systematic identification of failure modes and graphic visualization of failure events and logic. In fault-tree analysis, an undesired state of the system, referred to as the top event, is first specified. This state of the system should correspond to each performance level identified in the criteria statement, as illustrated in Figure VI-1. For example, the top event could be that the structure sustains moderate damage and can be repaired and functionally restored within 24 hours. The system is then analyzed to find all the credible ways in which the undesired event can occur. The top event is graphically portrayed as the union and intersection of subevents. A single fault tree does not necessarily contain all possible system failure modes, however, since each fault tree is specific to the top event. For example, when the top event is major structural damage, functional failures may not appear in the fault tree.

The basic concepts of fault tree construction and analysis are well documented [NRC, 1980; Hickman, *et al.*, 1981]. The two basic types of fault tree logic gates are the OR (⌓) and the AND (⌒) gate. Together with the NOT operator (commonly shown as a dot above the gate), these gates can be used to define any other specialized fault tree gate.

For protective structures, fault trees for common structure types with common missions will be similar. Thus, detailed generic fault trees for structures such as aircraft shelters, and command and control centers can be developed as a template for review and modification for specific applications. These fault trees have been derived such that they contain a wide range of possible failure modes and consider damage ≥ light physical damage coupled with function disruption on the order of hours. Therefore, for many cases, it may require only a simple pruning process to develop the fault tree for a specific structure, for a specific damage state. Two general fault trees, one for an aboveground aircraft shelter and one for a buried command and control center, are presented in this section for this purpose. The starting points for the development of these fault trees and the failure modes developed herein correspond to those given in Figure VI-2.

1. Aircraft Shelter

Figure VI-3 shows the generic aircraft shelter fault tree. The top event is defined as damage to internal components, systems, aircraft, or personnel, resulting in significant down time. Thus, this fault tree includes damage modes ranging from spall to partial collapse. The fault trees for more severe damage states are obtained by pruning the branches of the generic tree associated with lesser damage.

At the top level of the fault tree, two threat conditions are considered: a projectile direct hit and a standoff surface or buried burst. Failure by any of these two threats will result in the top event; hence, they are connected to the top event through an OR gate. The trees for the first two weapon effects are further developed in Subtrees A and B, as noted by the transfer symbols (capital letter inside the triangle).

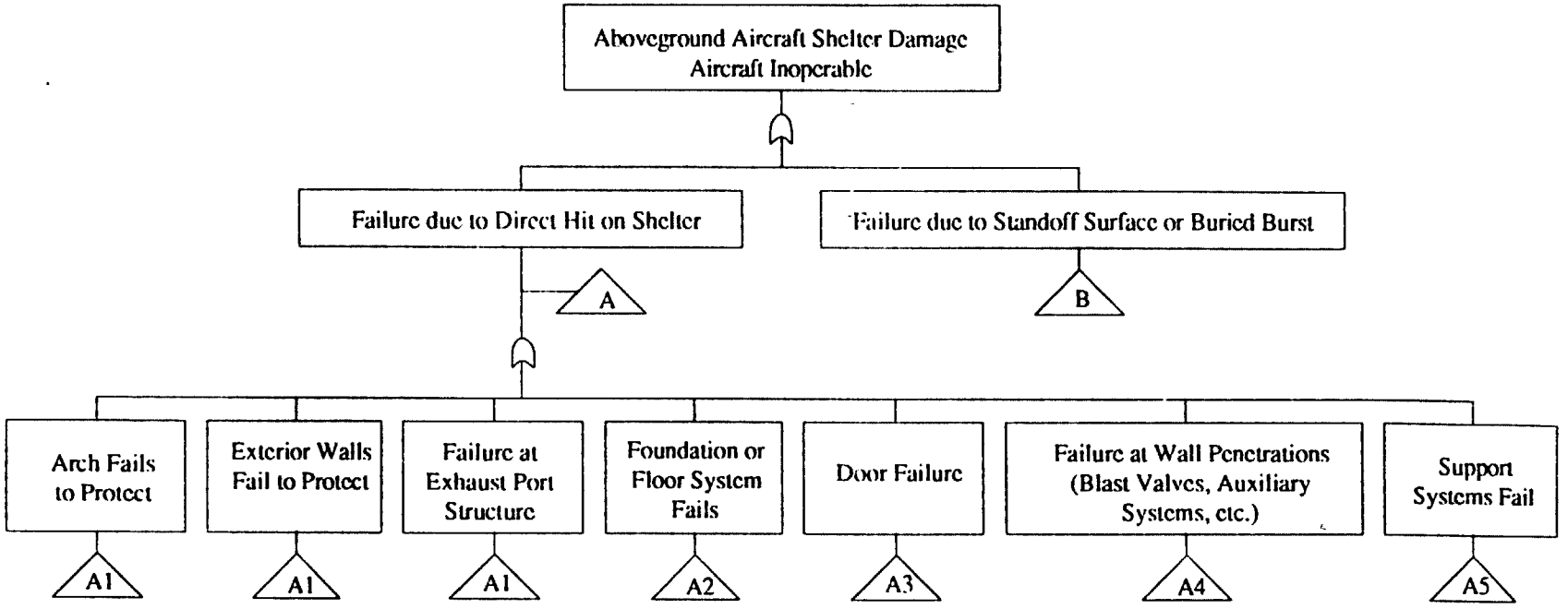

Figure VI-3. Generic Fault Tree for Aboveground Aircraft Shelter

a. Direct Hit Subtrees

Subtree A portrays all possible ways in which the structure can fail due to a direct hit. The second level of Subtree A (*i.e.*, the first level below the Subtree A top event) enumerates components of the shelter that can be damaged by a direct hit and whose failure will result in failure of the structure (since we are interested in light damage, all structure elements are included).

Subtree A1 in Figure VI-4 develops the failure paths for the main exterior structures subjected to a direct hit. The second level in Subtree A1 delineates failure according to whether or not the weapon perforates the shelter (Subtrees A1-1 and A1-2). If the weapon does not perforate the shelter (Subtree A1-1), damage can result from exterior explosive effects and/or impact loading effects. These failure modes range from local damage (breaching and spall), to in-structure shock, to structural failure with damage from secondary missiles resulting from large deformations or partial collapse. If the weapon perforates the shelter, the damage mechanisms include internal explosive effects and impact/impulsive loadings and damage mechanisms.

From a survivability standpoint, it is obvious that, unless the weapon is prevented from penetrating into the structure, design to prevent less than light damage is totally impractical. Hence, for this performance level damage state, the designer should focus on a highly reliable design to prevent penetrating effects, in-structure shock, breaching, and structural damage from impact loads.

Subtree A2 considers failure of the floor system, based on whether or not perforation occurs. For the impact or exterior explosion branch, an OR gate is used to connect foundation/bearing capacity failures with the other damage modes from the direct hit subtrees in Figure VI-4.

Door failure, considering both physical and functional damage, is given in Subtree A3 (Figure VI-5). The functional damage (doors rendered inoperable) is an example of a fault tree branch that could be pruned for more severe damage state fault trees. The door functional failure branch considers ways in which the doors can be rendered inoperable and stuck in a closed position. Structural support, hardware, and control systems damage are considered, including the possibility of random electrical and mechanical failures. Whether or not random failures contribute significantly to the probability of failure will depend on the particular threat being considered. Generally, random failures will be small contributors; however, the fault tree highlights the need for frequent testing and maintenance of these systems, to ensure that random failure is an acceptably small probability.[1]

Aircraft shelters can have penetrations through the shelter walls for electrical conduit and auxiliary systems (*e.g.*, blast valves). Subtree A4 in Figure VI-6 considers the possibility that the protective systems at these penetrations will be defeated.

---

[1]The RBD approach can be used to help determine optimal testing and maintenance intervals for these systems.

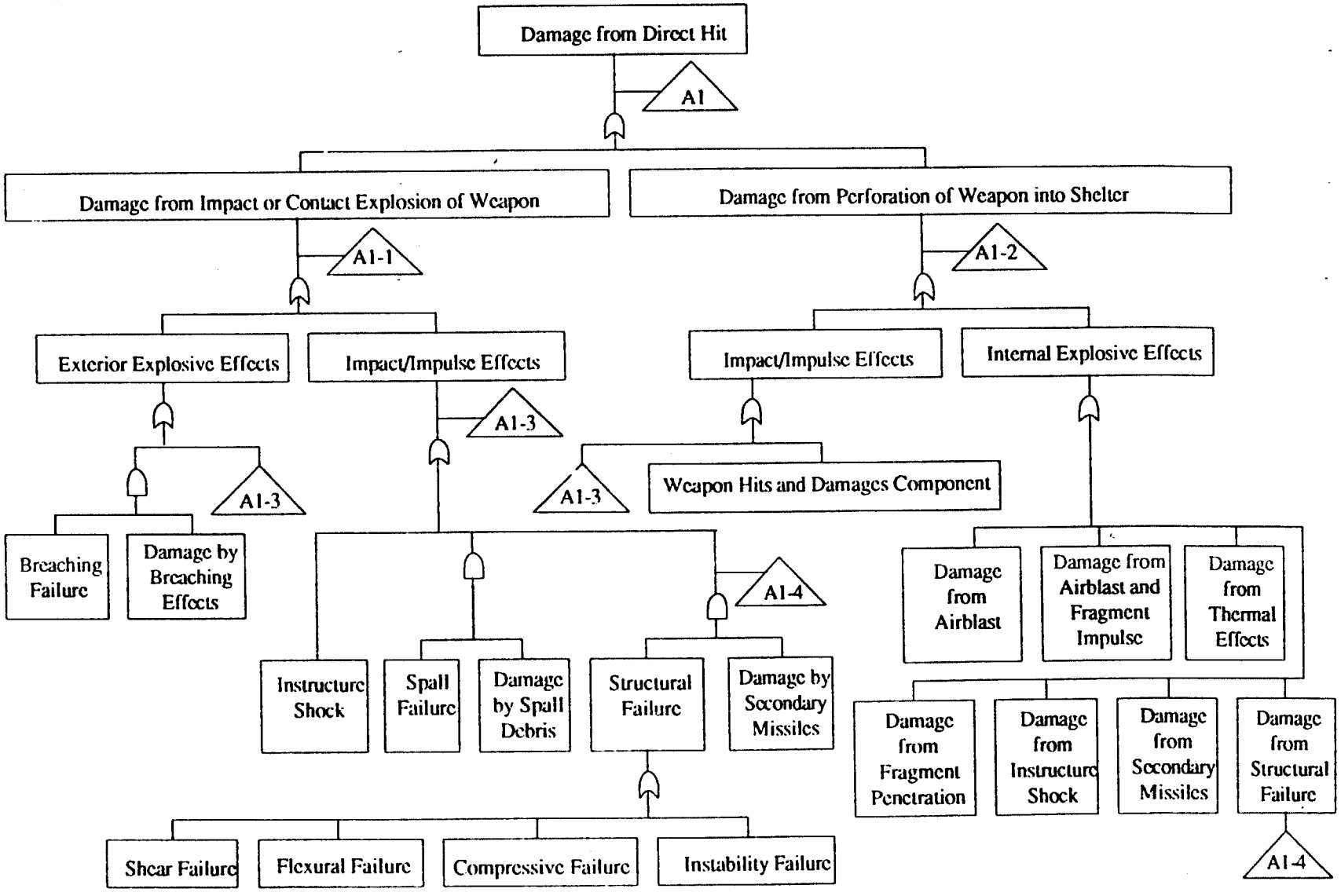

Figure VI-4. Subtree A1 — Damage from Direct Hit on Arch or Exterior Wall.

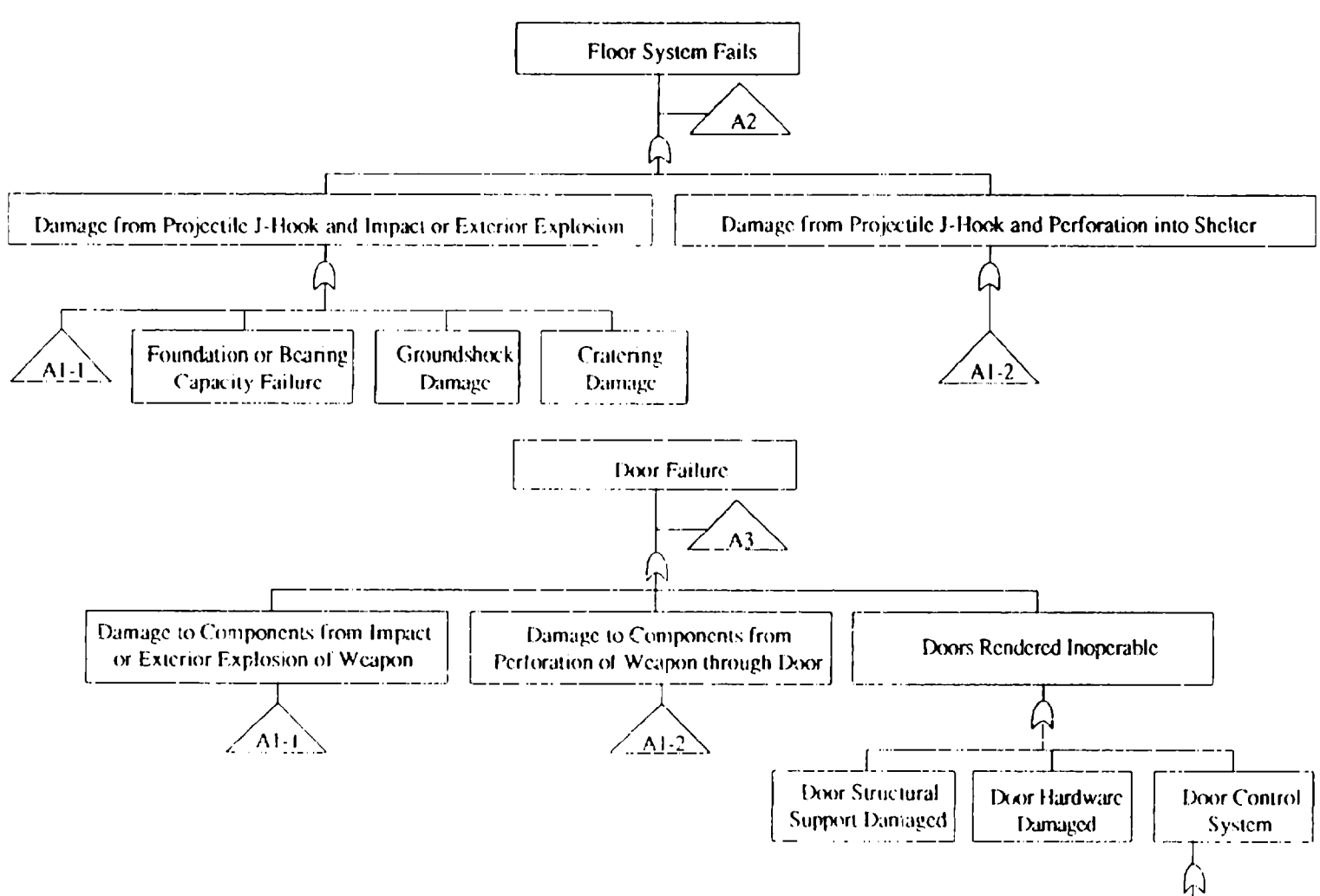

Figure VI-5. Subtrees A2 (Floor Failure) and A3 (Door Failure).

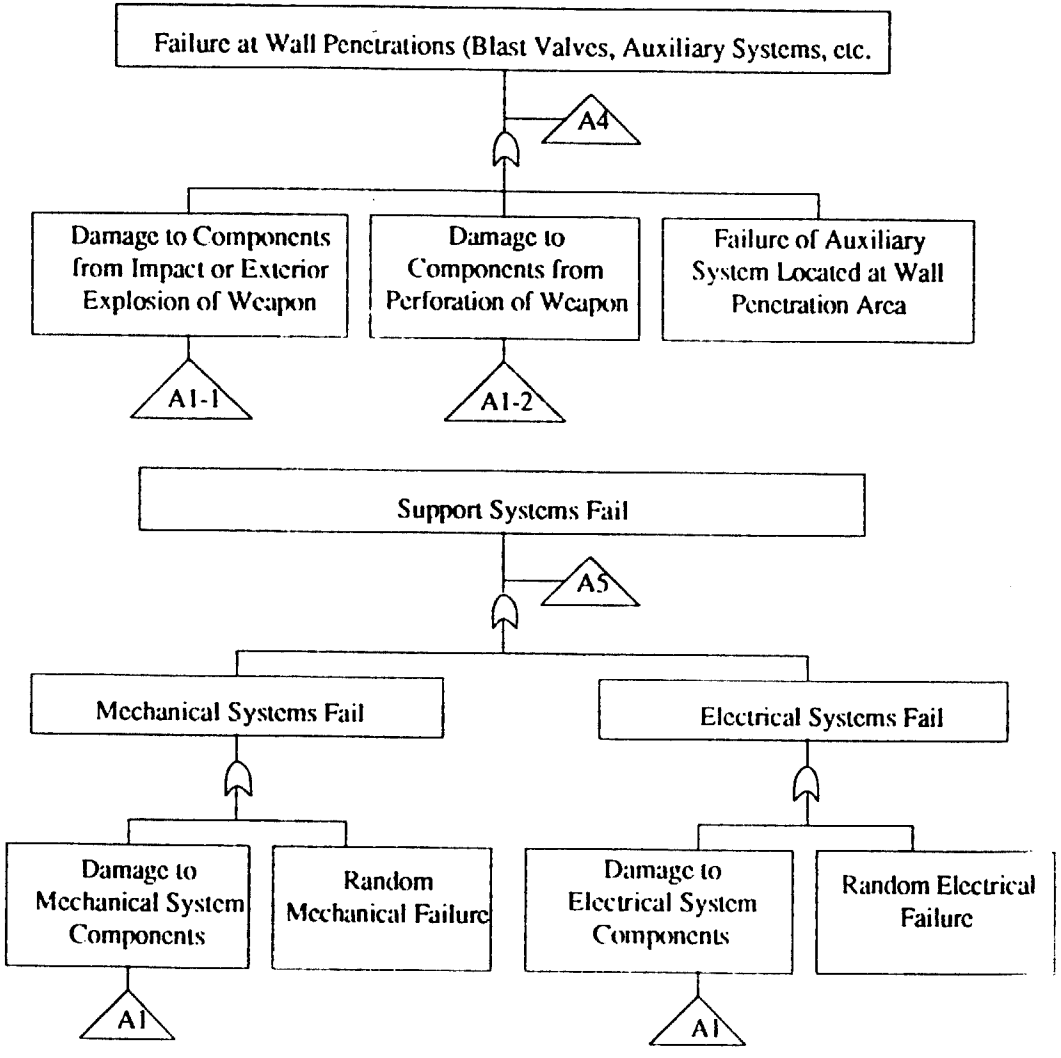

Figure VI-6. Subtrees A4 (Failure at Wall Penetration) and A5 (Support Systems Fail).

The final subtree for projectile direct hit, A5 in Figure VI-6, considers the shelter support systems. Electrical and mechanical support equipment will be needed for a variety of functions, such as communications, ventilation, maintenance and repair, etc. Failure of any of these functions can render the aircraft inoperable. The fault tree includes random failure modes and damage from direct hit effects (Subtree A1).

b. Standoff Burst Subtrees

Figure VI-7 shows the subtrees associated with damage from a standoff surface or buried burst. We have combined the surface and buried bursts, noting that some failure modes will not apply (*e.g.*, airblast and fragment damage) and can be pruned as needed. The second level of Subtree B is similar to that of Subtree A and enumerates components of the shelter system that can be damaged by a standoff burst. Subtree B1 in Figure VI-8 considers four ways in which a standoff burst can result in failure: (1) the shelter contents (aircraft or critical components) are damaged due to structural failure; (2) the contents are damaged due to spall; (3) the contents are damaged due to fragment penetration; and (4) the contents are damaged due to in-structure shock. In these failure scenarios, the damaging effects of airblast, fragment impact impulse, spall, and fragment penetration are identified. For structural failure of the arch/wall by combined airblast and fragment impulse, four possible failure modes breach, flexure, shear, and instability are considered. Also, the fault tree requires that these structural failures lead to damage of contents via structural debris impacting and damaging the shelter contents. Thus, the tree logic recognizes that certain localized failures may not result in failure of the shelter to perform its protective function. For spall damage, the failure logic requires both spall and impact/damage by the spall debris. Thus, the occurrence of spall by itself does not necessarily indicate failure.

Fragment penetration damage occurs when fragments perforate and impact critical contents or when the fragments impact with sufficient velocity to cause back face spall debris that can hit critical contents.

Subtree B2 in Figure VI-9 considers failure of the foundation or floor system due to ground shock from a surface or buried burst. Possible failure modes that have been observed in aircraft shelter tests are floor system upheaval and failure of the foundation. The fault tree logic also requires consideration as to whether or not these damage modes lead to contents damage via the AND gate. For example, foundation failure alone may not necessarily lead to structural collapse.

Standoff burst can also lead to door failure as shown in Subtree B3 in Figure VI-10. As for the case of Subtree A-3, this tree considers both defeat of the doors' protective function and functional failure. The failure modes are similar to those described previously.

Failure at the penetrations for electrical conduit and HVAC (*e.g.*, blast valves) are treated in Subtree B4 in Figure VI-11. The logic of this subtree consists of an OR gate connected to Subtree B1 and a local failure at the wall penetration area.

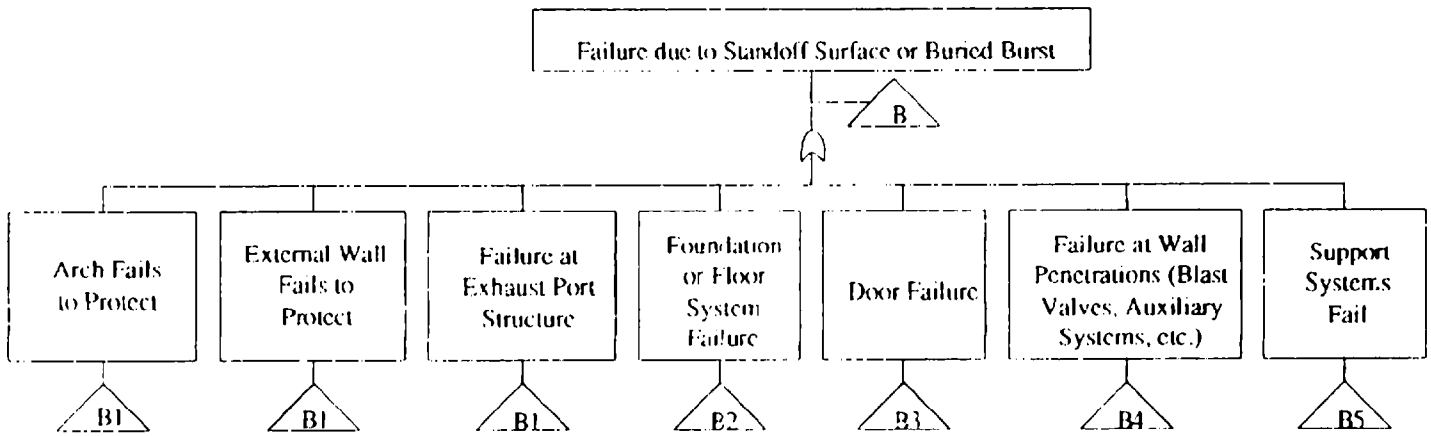

Figure VI-7. Subtree B — Failure due to Standoff Surface or Buried Burst.

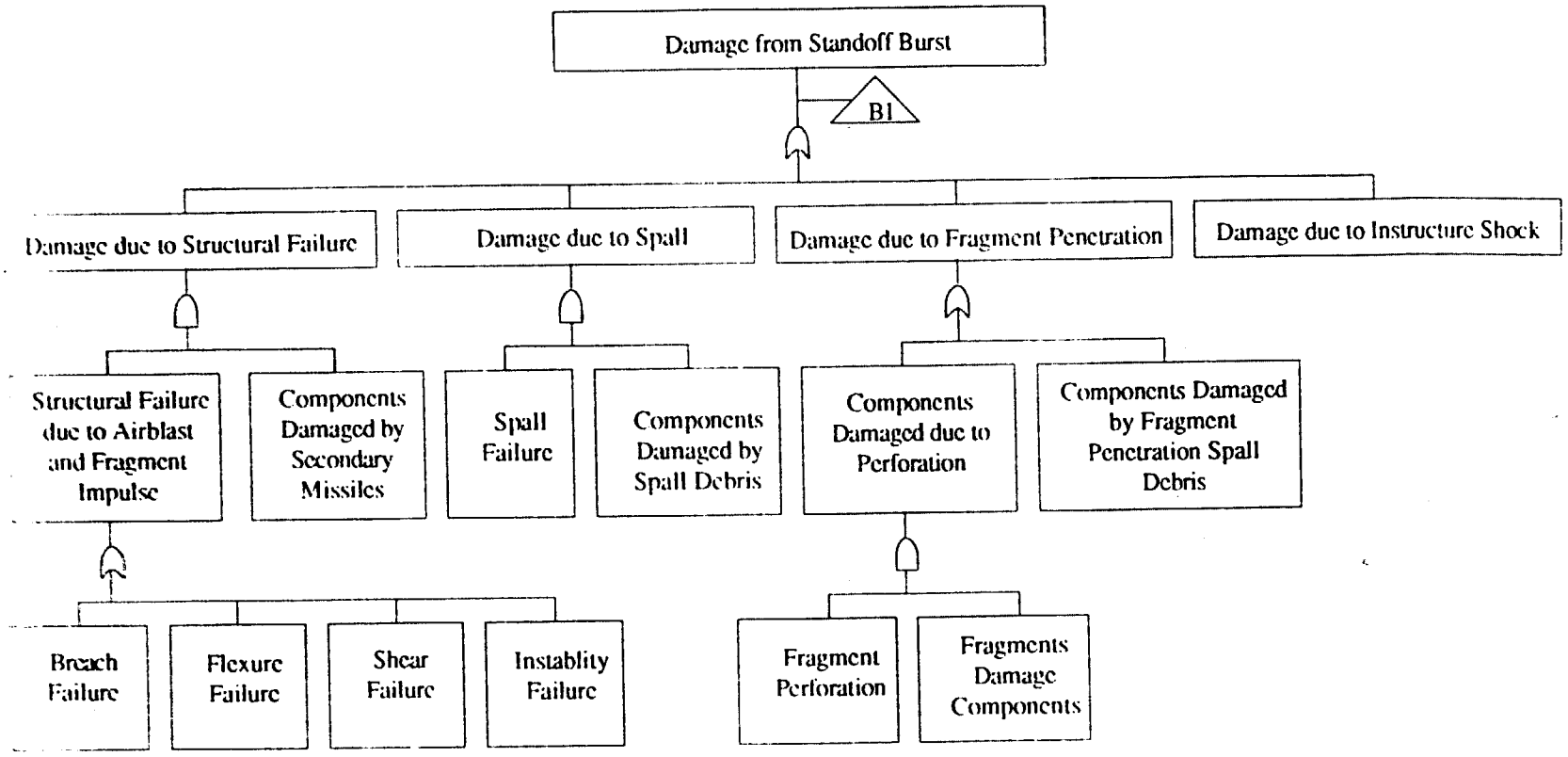

Figure VI-8. Subtree B1 — Damage from Standoff Burst.

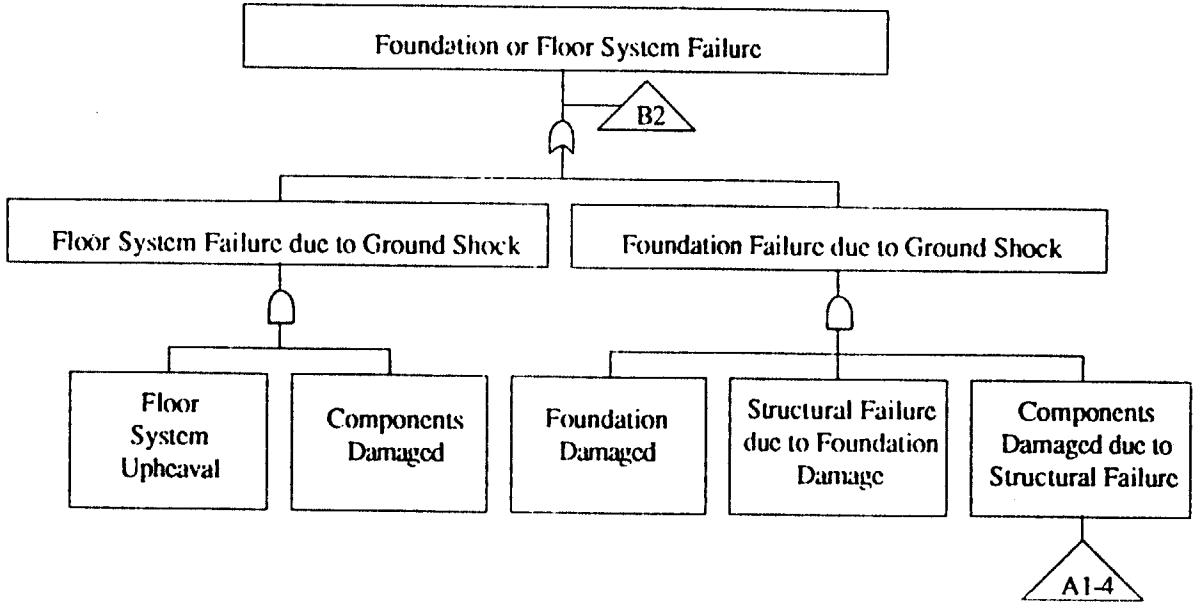

Figure VI-9. Subtree B2 — Foundation or Floor System Failure from Standoff Burst.

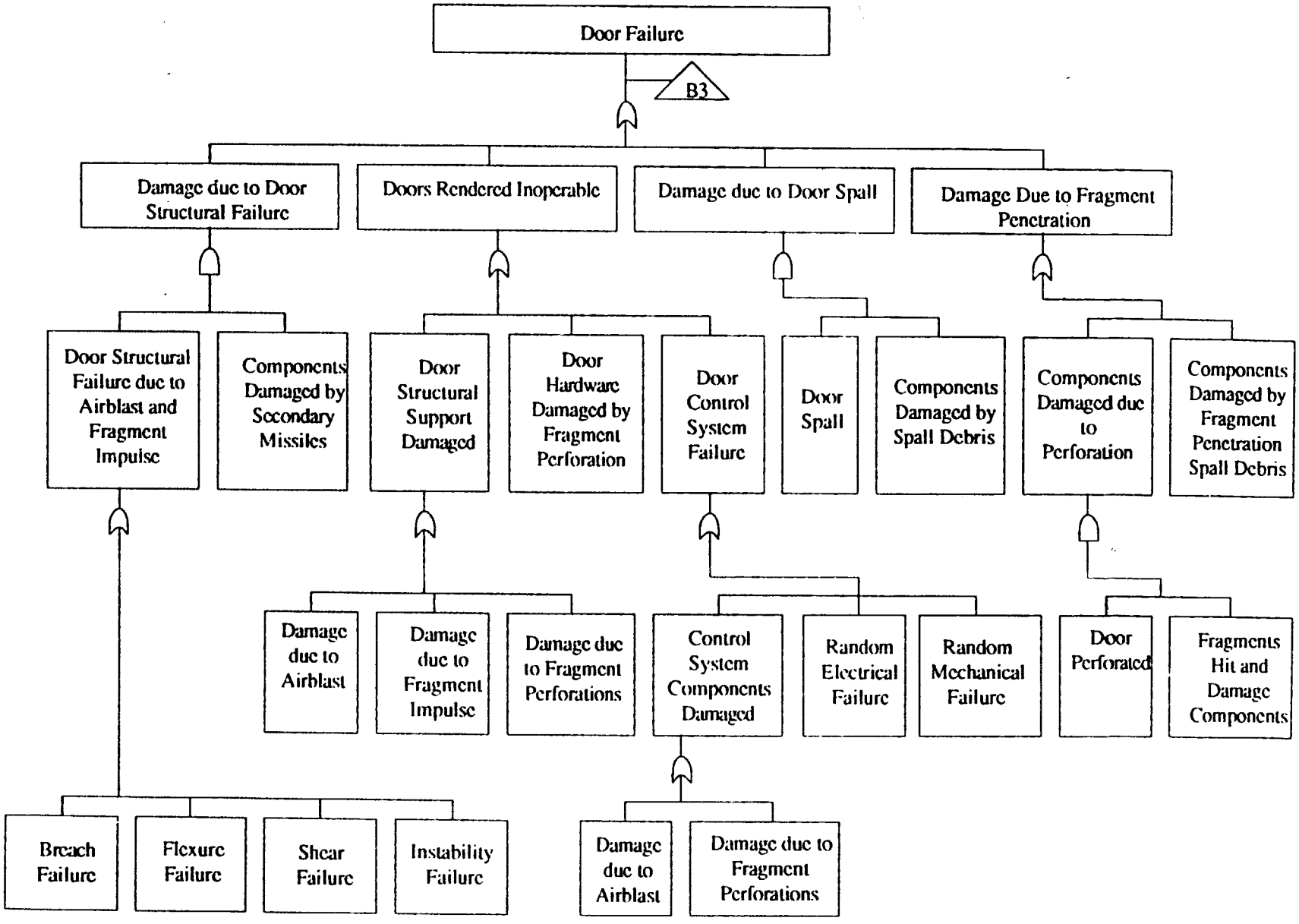

Figure VI-10. Subtree B3 — Door Failure from Standoff Burst.

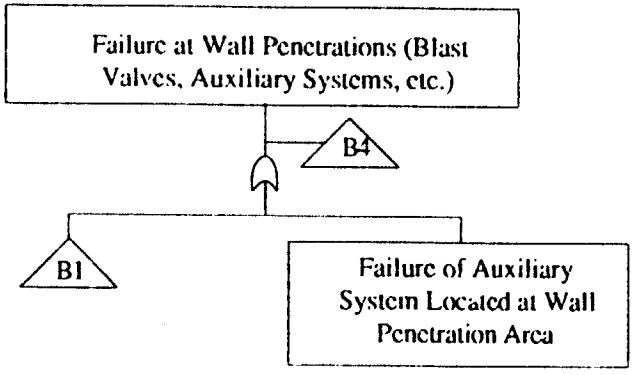

Figure VI-11. Subtree B4 — Failure at Wall Penetration from Standoff Burst.

Subtree B5 in Figure VI-12 considers electrical and mechanical support equipment that may be needed for a variety of functions (communications, ventilation, maintenance and repair, etc.). Loss of these functions could render the aircraft unusable. The fault tree includes both random failure modes and weapon effects. For support equipment, damage due to in-structure shock must be considered in addition to airblast and fragment hits.

2. Buried Command and Control Center

The fault tree for the buried command and control center is similar in many respects to the aircraft shelter fault tree. Thus, we describe here only the unique aspects of the buried structure, shown in Figure VI-13. Figure VI-14 contains the top event, damage to internal equipment, corresponding to light damage sufficient to affect functional performance for a period of several hours.

a. Direct Hit Subtree

As for the arch, the main structural elements are considered, the front wall, roof, side walls, and floor system. Since the structure is buried, the fault tree shows that for direct hit it is necessary to analyze the resistance of the structure cover (see Subtree C1 in Figure VI-15). Floor system failure is given in Subtree A2 in Figure VI-5.

Failure at the door (Subtree C2 in Figure VI-16) is also a concern for the command and control center, as it was for the arch; however, functional failure is not considered because it is assumed that operation of the doors immediately after an attack is not critical to operation of the center. Wall penetration failure is given in Subtree A4 and support system failure is given in Figure VI-17 (Subtree C3).

b. Standoff Burst Subtree

Figure VI-18 shows the subtrees for the standoff buried burst failures (Subtree D). Subtree D1 in Figure VI-19 identifies failures from groundshock to the exterior walls and roof of the command and control center. For a failure due to groundshock, Subtree D1 shows that the structure contents must be damaged by debris from the failed structural element, structural collapse, imploding geologic debris, or spall.

Door failure is considered in Figure VI-20. Typically, the buried center will have an accessway as shown in Figure VI-13; hence, Subtree D2 considers both the case of blast in the access tunnel, and blast external to the access tunnel. For blast in the access tunnel, the primary load effects become airblast and fragment impulse, and fragment penetration, rather than groundshock.

For the center to continue to function during and after an attack, all critical equipment must remain operational. Thus, equipment failure due to in-structure shock must be considered as shown in Subtree D3 in Figure VI-21. Also, the tree includes the possibility that equipment can fail by interaction with other equipment, in addition to direct shock induced damage.

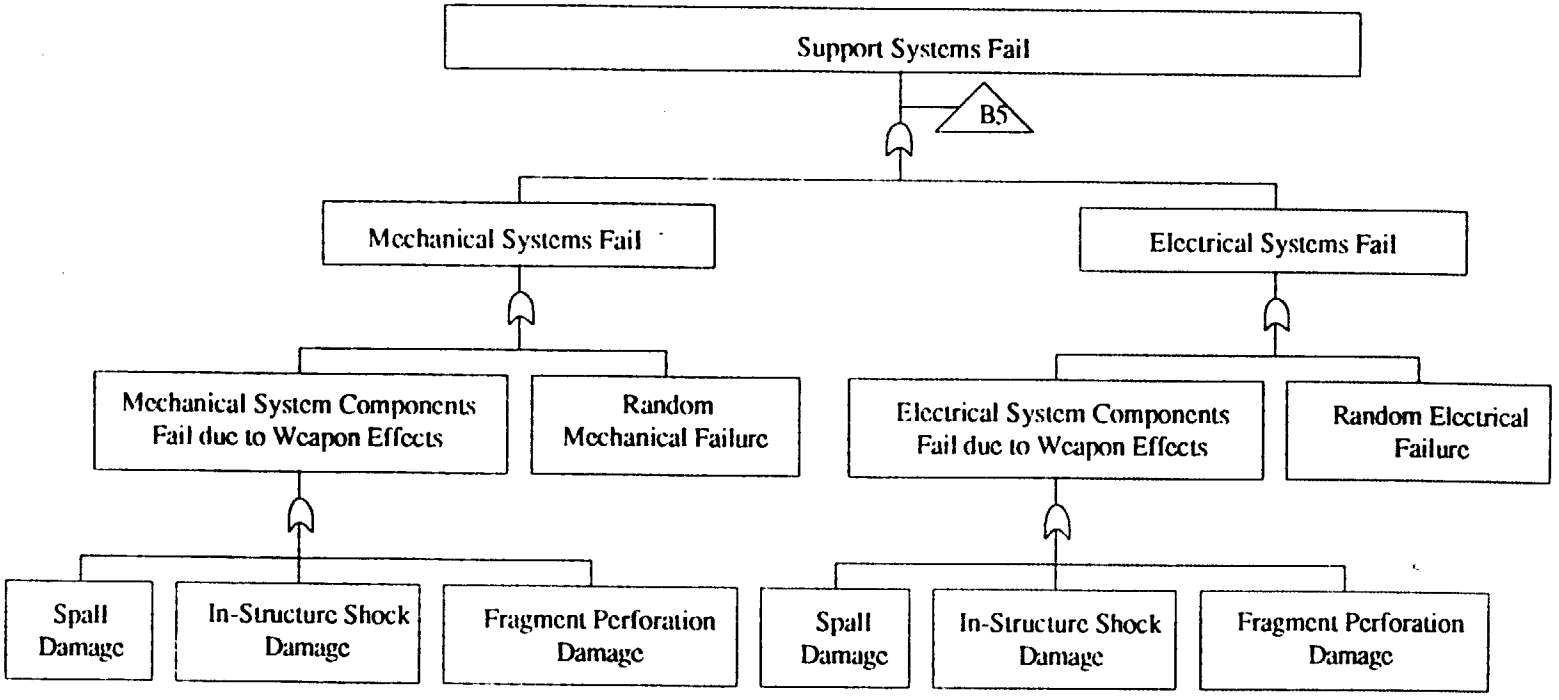

Figuer VI-12. Subtree B5 — Support Systems Fail from Standoff Burst.

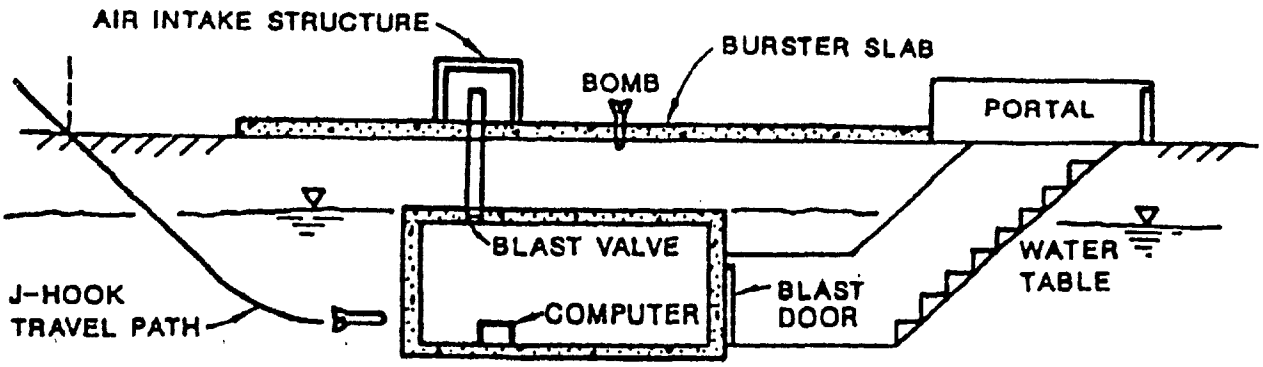

Figure VI-13. Buried Command and Control Center.

Support system failure due to standoff bursts are analyzed as shown in Subtree D4 in Figure VI-22. Support systems are necessary to run the center equipment and sustain life. Failure of the air intake structure as well as buried lifelines (electric, plumbing, HVAC) must be considered. In addition, failure of the active components (switches, vents, valves) of the system would render the center inoperable. Active component failures are further developed in Figure VI-23.

D. SYSTEM RELIABILITY

System reliability evaluation is involved in Steps 3, 4, and 6 of the RBD procedure given in Subsection VI.B. Solutions of general system reliability equations generally require computer implementation and are not discussed herein. Hence, this subsection is limited to several basic system reliability concepts. One is the distinction between the reliability of serial and parallel structural systems and how brittle/ductile elements affect the system survivability. The second concept deals with correlation among failure modes and the use of bounding assumptions to estimate system reliability.

1. Series and Parallel Systems

In protective structure reliability analysis, it is important to note the degree of ductility of the element with respect to the failure state or failure mode considered. An element is brittle if it loses its load-bearing capacity completely at failure. A ductile element maintains its load level after failure. Ductility is important in redundant structures since there is a possibility of load redistribution after element failure, which may prevent structural collapse.

A series structure is one in which failure of any element results in failure of the system. The classical example of a series system is a statically determinate structure. Clearly, if any one member fails, the structure becomes unstable and collapses. The probability of system failure is given by

$$\tilde{P}_f = P\left(F_1 \cup F_2 \cup \cdots \cup F_n\right) \qquad \text{(VI-9)}$$

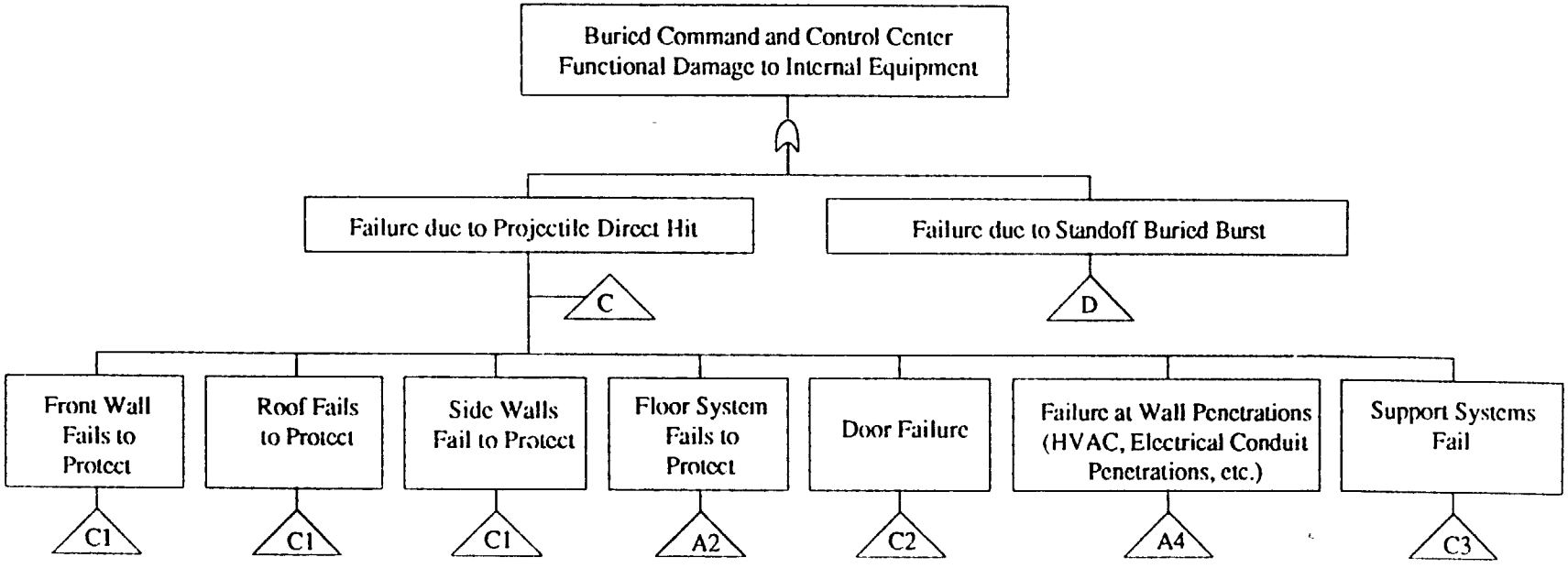

Figure VI-14. Generic Fault Tree for Buried Command and Control Center.

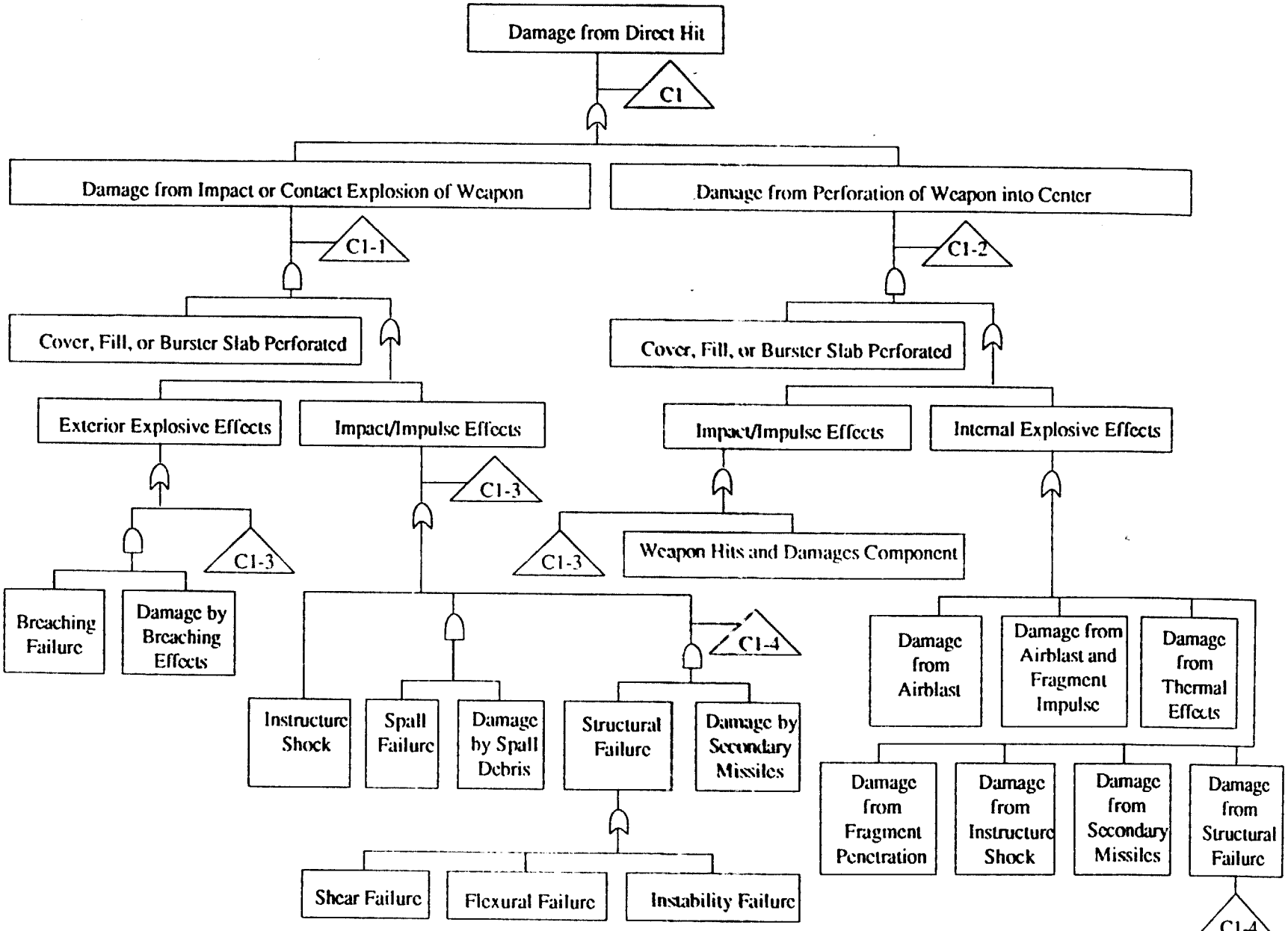

Figure VI-15. Subtree C1 — Damage from Direct Hit on Walls or Roof.

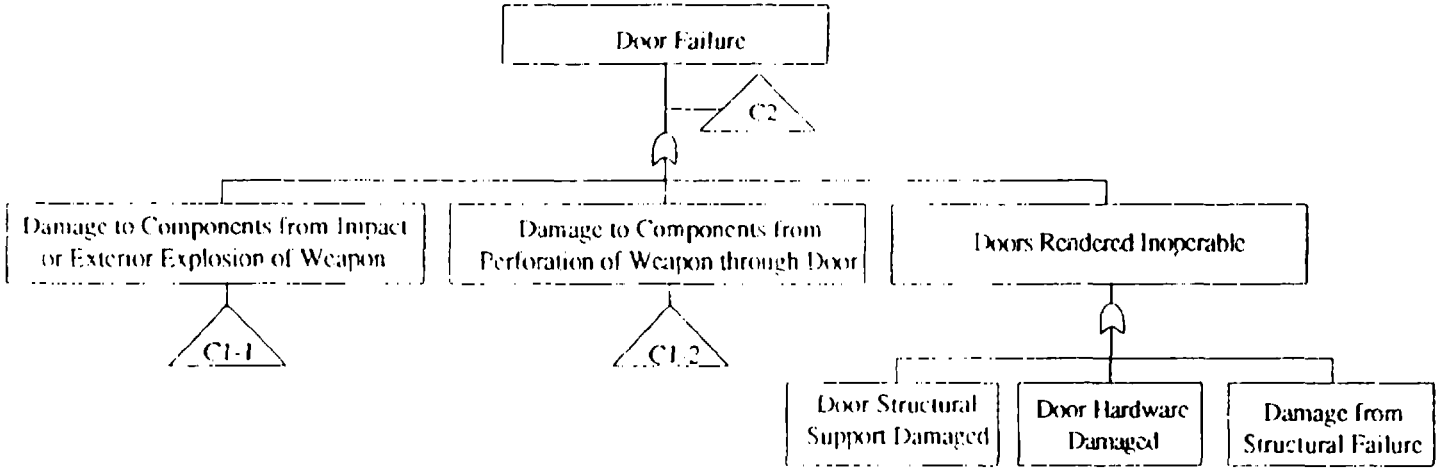

Figure VI-16. Subtree C2 (Door Failure).

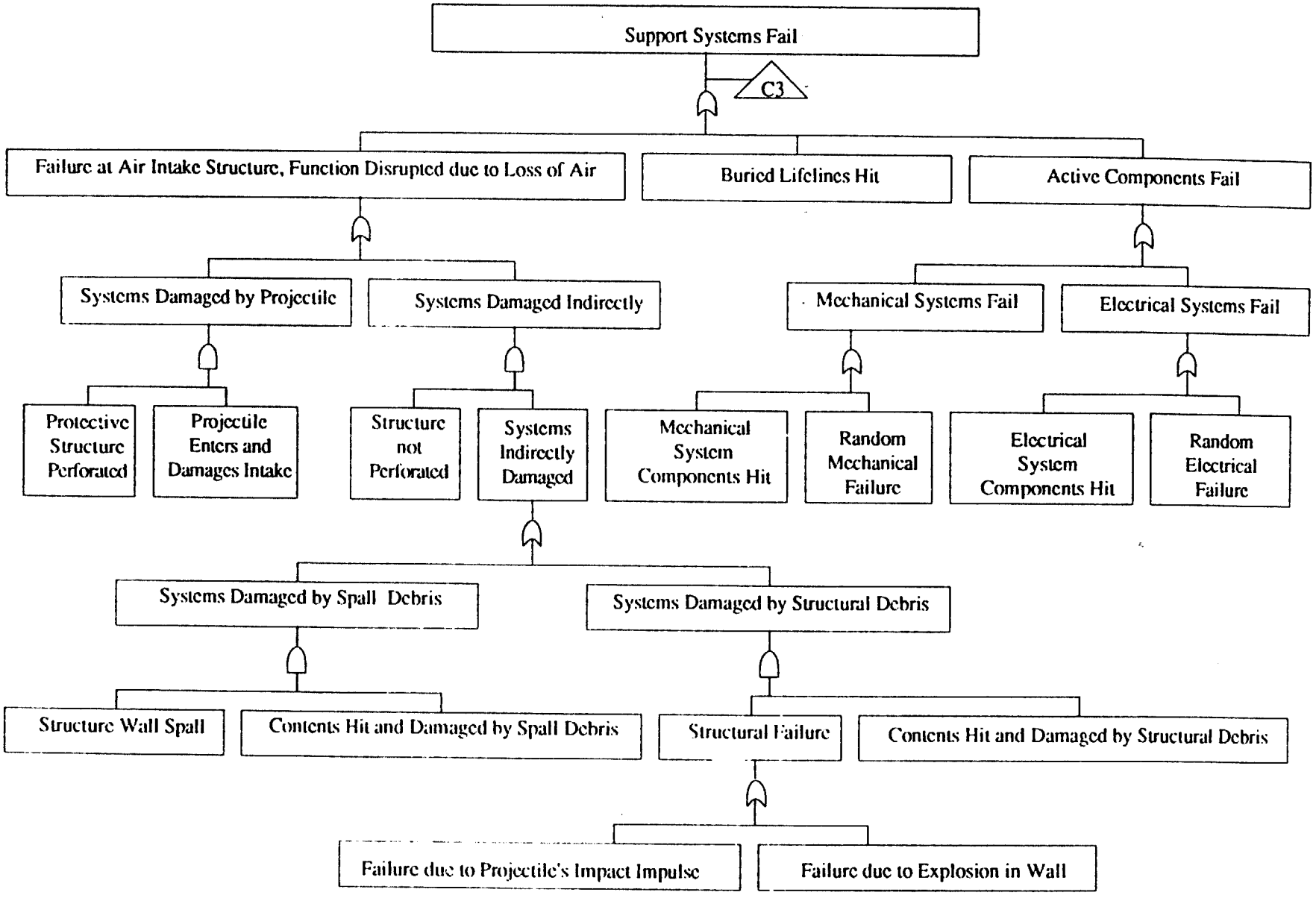

Figure VI-17. Subtree C3 — Support Systems Fail.

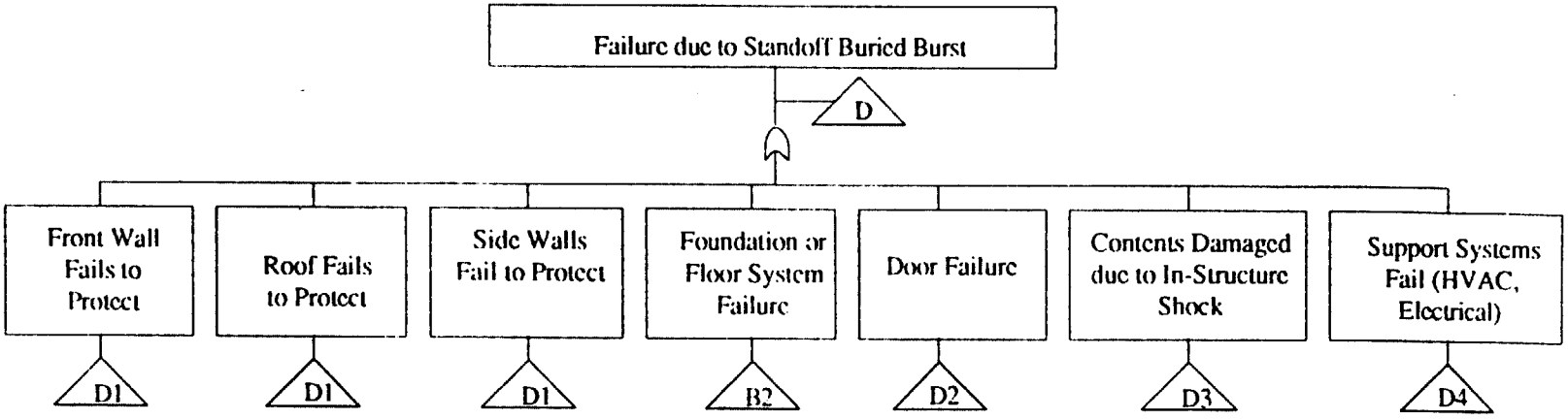

Figure VI-18. Subtree D — Failure due to Standoff Buried Burst.

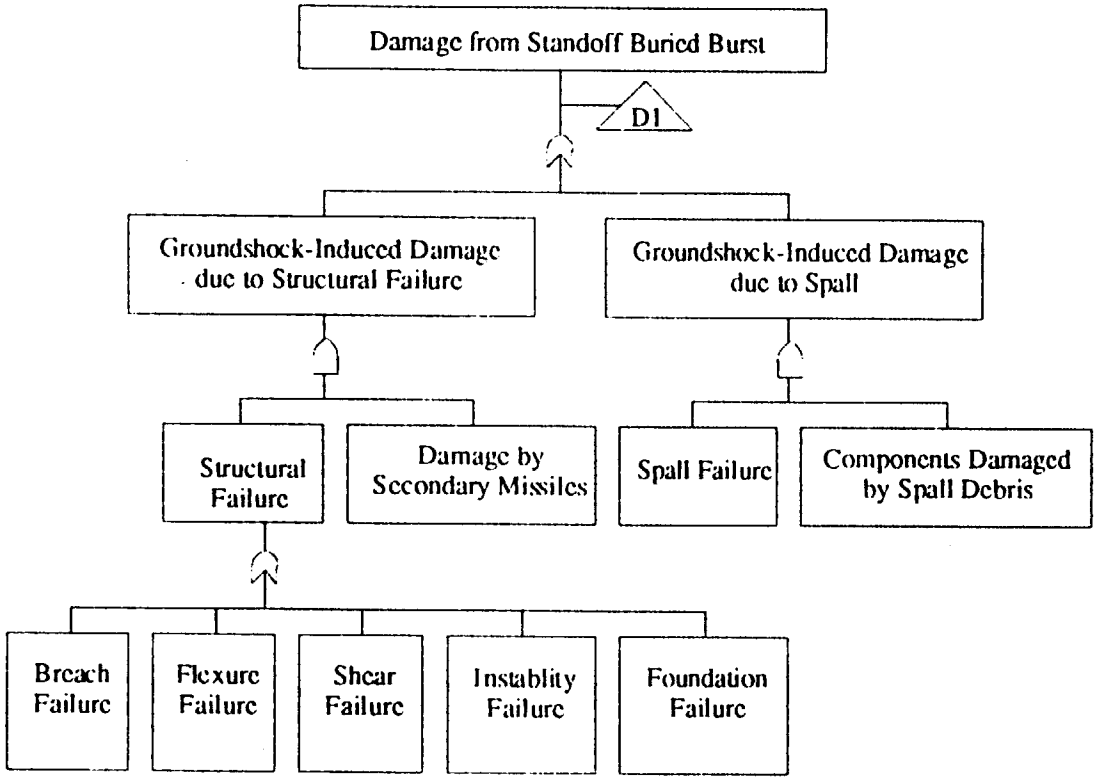

Figure VI-19. Subtree D1 — Damage from Standoff Burst.

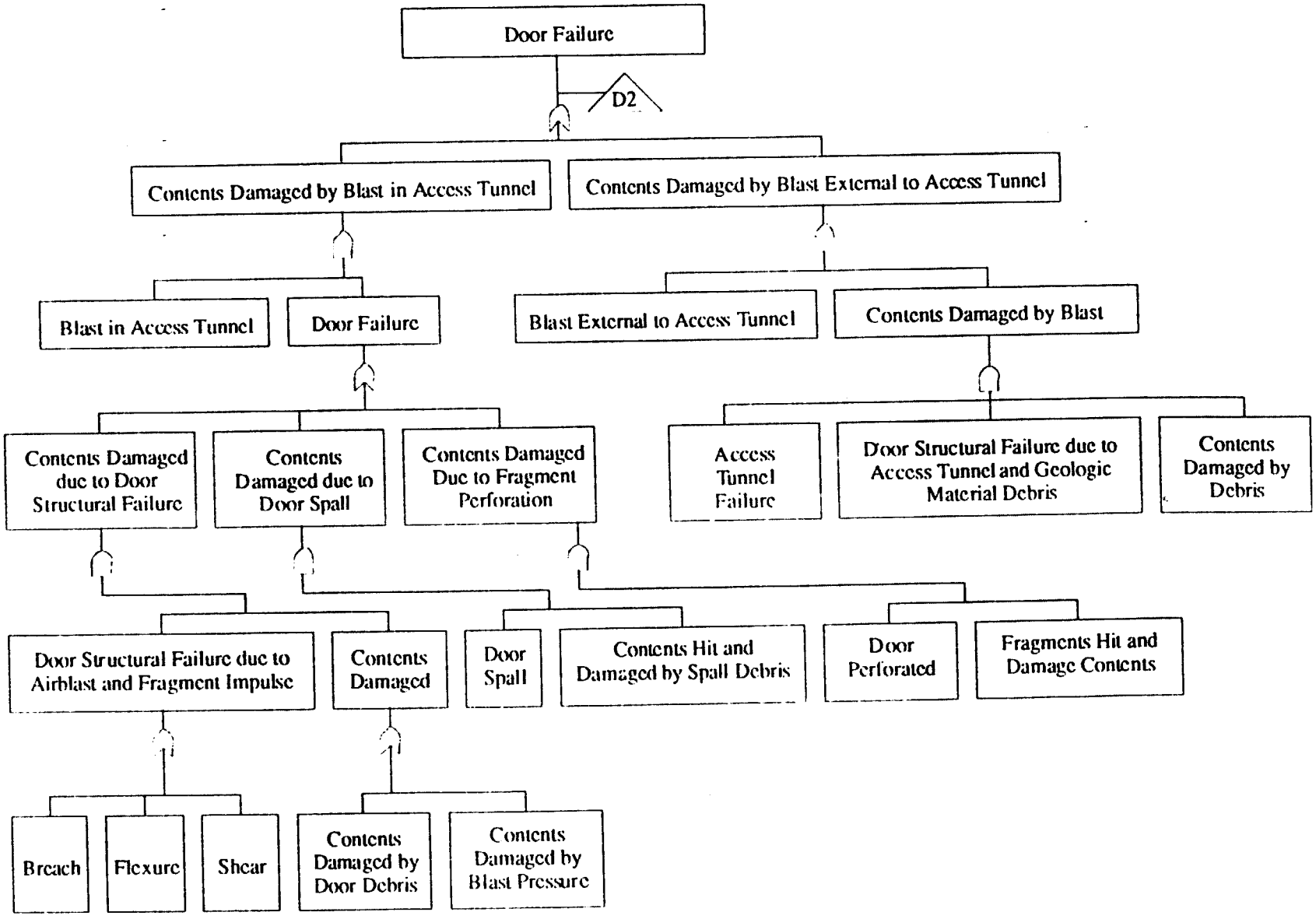

Figure VI-20. Subtree D2 — Door Failure.

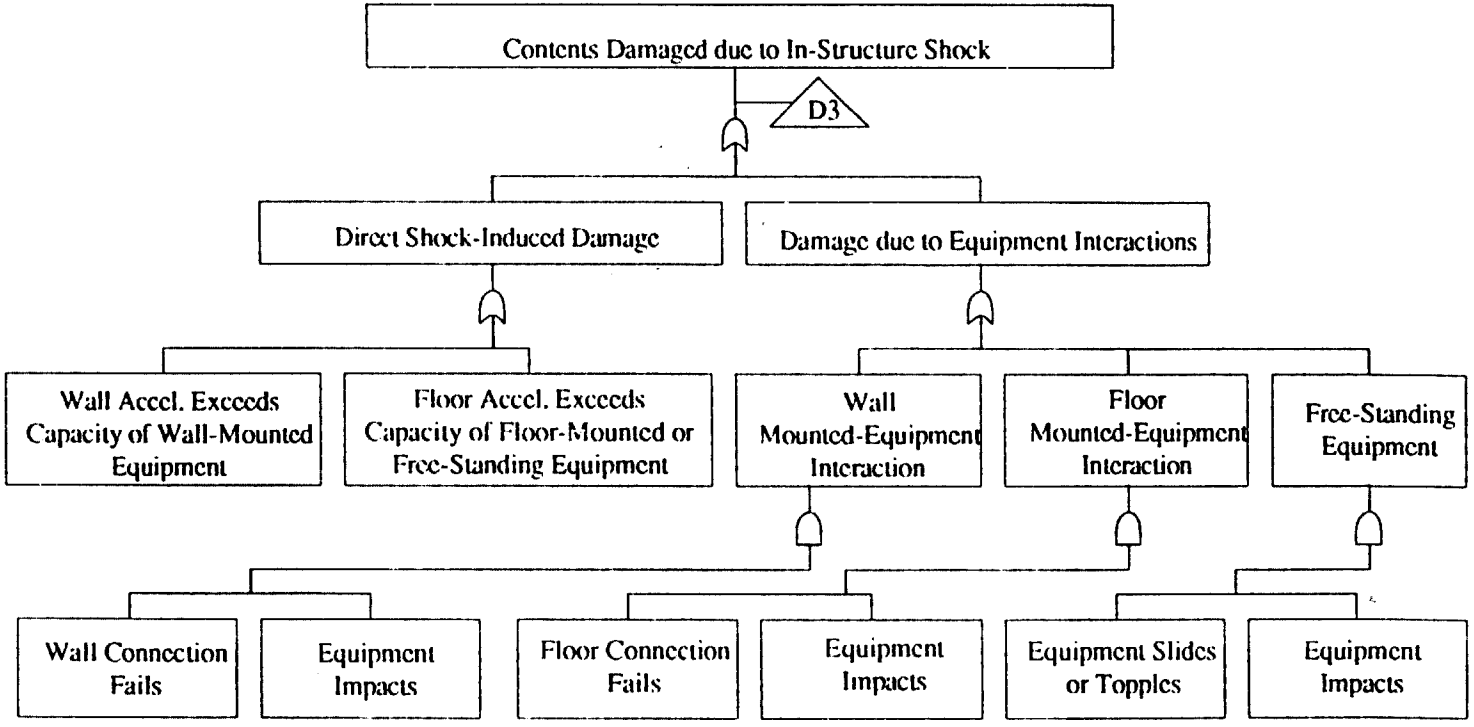

Figure VI-21. Subtree D3 — In-Structure Shock Failure.

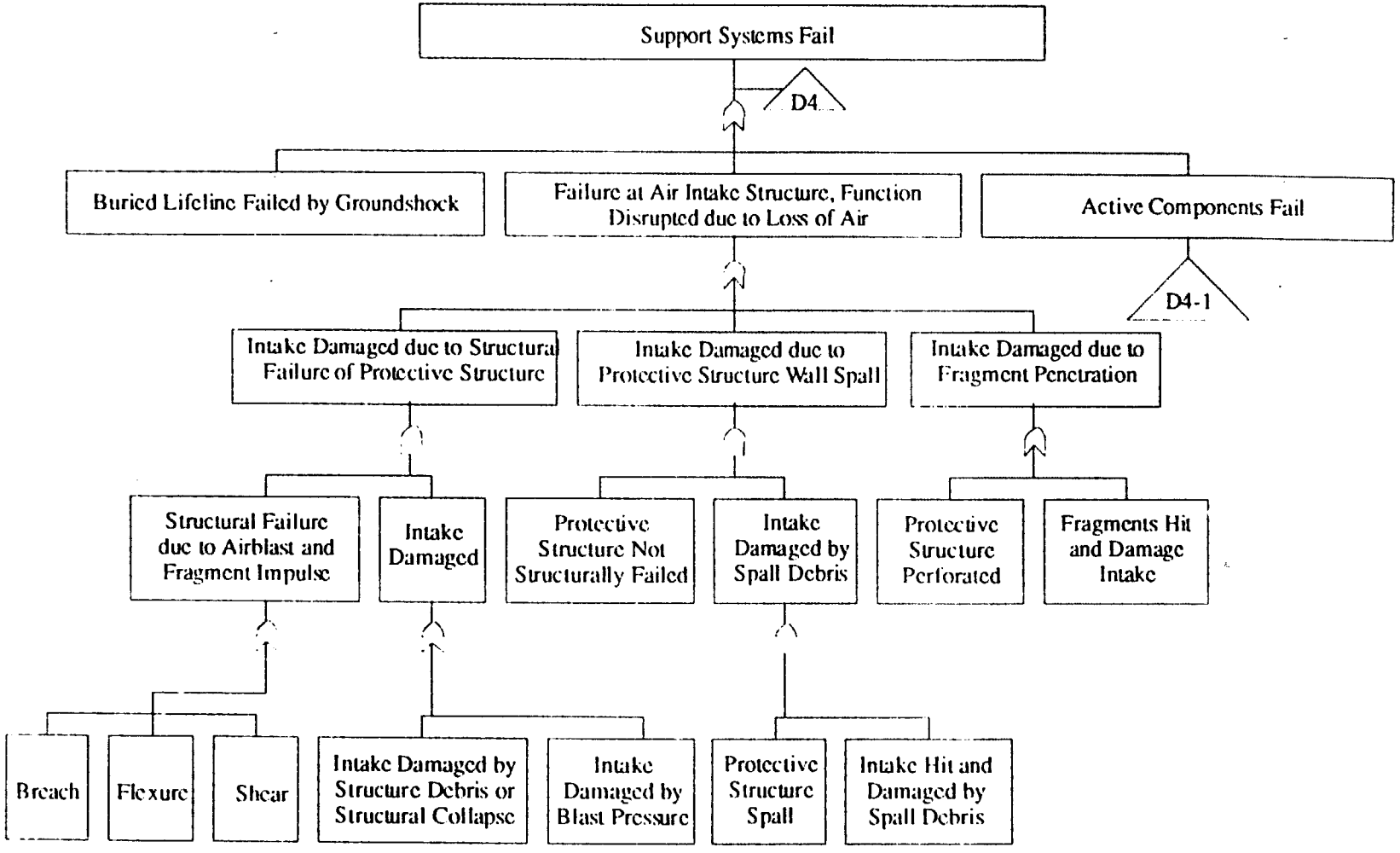

Figure VI-22. Subtree D4 — Support System Failure.

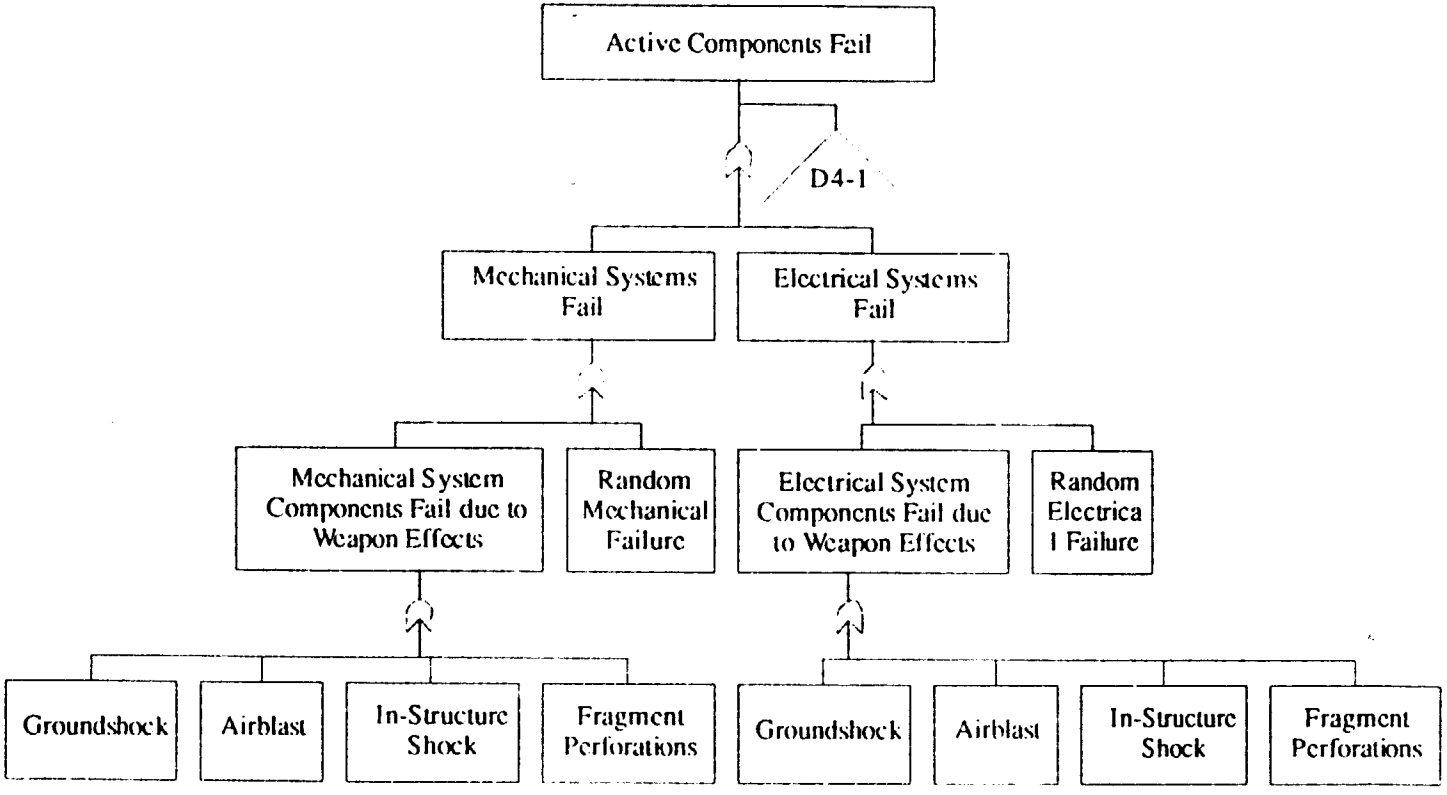

Figure VI-23. Subtree D4-1 — Active Component Failure.

where F_i denotes failure for mode i, and $\cup$ is the union operator (these failure modes would correspond to modes connected by "OR" gates in the system fault tree). System failure occurs if failure occurs in any of the F_i modes, $i = 1, 2, \cdots, n$.

In a parallel system, the failure of a single element will not always result in failure of the total system. Depending on the failure state definition, this situation can arise in redundant structures, because the remaining elements may be able to sustain the redistribution of load. Hence, the behavior of parallel systems, or subsystems, depends to a high degree on whether or not the elements are brittle or ductile with respect to the failure mode definition. The probability of system failure of a parallel system is

$$\tilde{P}_f = P\left(F_1 \cap F_2 \cap \cdots \cap F_n\right) \tag{VI-10}$$

where $\cap$ denotes the intersection operation (the failure modes would correspond to modes connected by "AND" gates in the system fault tree). Hence, a parallel system fails only if all parallel elements fail.

Exact evaluation of Equations (VI-9) and (VI-10) for correlated failure modes generally requires numerical solutions, such as Monte Carlo procedures. However, simple bounds on $\tilde{P}_f$ based on the limiting assumption of independence and perfect correlation, can be established.

2. Reliability Bounds

Since the exact determination of $\tilde{P}_f$ is not always practical for design, the development of bounds on $\tilde{P}_f$ are often useful. For the case of series systems, lower and upper bounds on $\tilde{P}_f$ are

$$\max_i P(F_i) \le \tilde{P}_f \le 1 - \prod_{i=1}^{n} [1 - P(F_i)]. \tag{VI-11}$$

For parallel ductile systems, lower and upper bounds on $\tilde{P}_f$ are

$$\prod_{i=1}^{n} P(F_i) \le \tilde{P}_f \le \min_i P(F_i) \tag{VI-12}$$

These lower and upper bound expressions correspond, respectively, to perfect dependence between modes and no dependence between modes. They provide a rapid-means to bound $\tilde{P}_f$ since only a few algebraic manipulations are performed on $P(F_i)$ for each mode. Also note that the calculations only require that we compute failure probabilities for one mode at a time — that is, joint failure probabilities are not needed. Hence, these bounds are often referred to as uni-modal bounds.

If the above simple bounds are not sufficiently narrow for system survivability, then refined methods can be used. For a serial system, tighter upper and lower bounds can be obtained as (Kounias [1968] and Hunter [1976]):

$$\tilde{P}_f \le \sum_{i=1}^{n} P(F_i) - \sum_{i=2}^{n} \max_{j<i} P\left[F_i \cap F_j\right]$$

$$\tilde{P}_f \ge P(F_1) + \sum_{i=2}^{n} \max\left\{P(F_i) - \sum_{j=1}^{i-1} P\left[F_i \cap F_j\right], 0\right\} \qquad \text{(VI-13)}$$

These bounds require that we compute joint failure probabilities for every possible combination of two failure modes. Hence, these bounds are often referred to as bi-modal bounds. Ditlevsen [1979] presents methods for approximating the required probabilities, resulting in bounds that are somewhat looser than that given by Equation (VI-13).

A second procedure is to group the modes into sets of highly correlated modes [Ang, *et. al.*, 1975; Ma and Ang, 1981]. Within each group the modes are assumed to be perfectly correlated and the group failure probability, P_{fg}, is evaluated. The group P_{fg} are combined assuming independence, thus:

$$\tilde{P}_f \approx 1 - \prod_{i=1}^{n} \left(1 - P_{fg}\right) \qquad \text{(VI-14)}$$

Equation (VI-14) provides an analytically simple, yet robust approximation to the solution of the system reliability equation for airbase facilities. Correlation among failure modes would need to be evaluated in a research phase in order to develop guidelines for grouping failure modes for each structure type that could be implemented in base survivability assessments.

(The reverse of this page is blank.)

VII. SUMMARY AND CONCLUSIONS

This research report describes the development of reliability-based analysis and design methods for protective structure design. The methods have been developed so that they can be used without detailed knowledge of probabilistic methods. They are based on the deterministic analysis and design methods given in the Air Force Protective Construction Design Manual ESL-TR-87-57 (hereinafter referred to as the *PCDM* [Drake, *et al.*, 1989]).

The current state-of-the-art in protective construction design uses deterministic methods of analysis and does not provide systematic procedures for considering uncertainties in weapon effects, loads, or structure response. In addition, the current approach provides no guidance as to the degree of conservatism or unconservatism in the analysis methods (*e.g.*, free-field environments, penetration formulas, structure response models, etc.). Hence, the designer/analyst has very limited knowledge of the safety margins achieved when using these methods and there is no rational basis for performing cost-survivability tradeoffs. In fact, one of the findings of this research is that the current *PCDM* procedures are not risk-consistent; that is, in some instances conservative designs are obtained, whereas in others, unconservative designs result.

To systematically treat the uncertainties in protective design, this research effort focused on developing methods for analyzing the effect of these uncertainties on design confidence (reliability) and applying these methods to develop reliability-based design factors (RBDFs). The RBDFs attempt to account for the key design uncertainties. The RBDFs, which are in the form of load and resistance multipliers, are tabulated as a function of design reliability level. Generally, as higher reliability is required, load multipliers (factors that are typically greater than 1.0) increase and resistance multipliers (factors that are typically less than 1.0) decrease. Using the reliability-based design procedures, the designer can evaluate the safety margin in the design and can perform cost-survivability tradeoffs. The basic analysis methodologies considered in this research are those given in the *PCDM*. Hence, the RBDFs are used in conjunction with the *PCDM* methods.

Research was conducted in five fundamental areas: (1) airblast and aboveground structure response; (2) groundshock and belowground structure response; (3) fragmentation effects; (4) projectile penetration; and (5) protective structure systems reliability. In each of the areas, emphasis was on reinforced concrete structures; however, the load uncertainty analyses are applicable to structures of any materials. For all cases both model prediction errors and model parameter uncertainties were analyzed. To assess model prediction errors, we performed analysis using the *PCDM* methods and compared these results to experimental results. In some instances we found significant biases in the *PCDM* models. In most cases where we found significant biases that could not be corrected without changes to the fundamental approach, RBDFs were not developed. Rather, we identified the dominant sources of bias and uncertainty in the method and provide recommendations for improving the accuracy of the analysis methodology. When these models are improved and updated, it will be appropriate to develop the RBDFs.

RBDFs were developed for the following conventional weapons phenomena:

1. Free-field and reflected airblast pressures and impulses.
2. Breaching of aboveground reinforced concrete walls/slabs for close-in cased bombs.
3. Spall of aboveground reinforced concrete walls/slabs due to standoff cased bombs.
4. Free-field ground shock (velocity and stress).
5. Breaching of buried reinforced concrete walls/slabs for close in buried burst.
6. Selection of design fragments for penetration, perforation, or spall effects.
7. Fragment impulse loading on aboveground walls/slabs for cased bombs.
8. Resistance factors for projectile penetration, perforation, and spall of reinforced concrete.
9. Velocity load factors for projectile penetration, perforation, and spall of reinforced concrete.
10. Residual velocity of projectiles that perforate reinforced concrete.

For the cases listed below we found significant biases in the analysis methods that could not be corrected without changes to the fundamental approach. RBDFs were not developed for these cases; however, either specific ways to improve the model prediction accuracy were recommended or improved models were provided and demonstrated.

1. Non-normally reflected airblast pressure and impulse.
2. Flexural response of aboveground reinforced concrete walls/slabs to airblast and fragment impulse.
3. Flexural response of belowground reinforced concrete walls/slabs to groundshock.
4. Resistance of reinforced concrete elements to fragment penetration, perforation, and spall.

Table VII-1 summarizes the biases (conservatisms, unconservatisms) found in the *PCDM* methods examined in this research and some of the key methodological gaps.

Based on the identification and ranking of dominant biases and uncertainties, Table VII-2 summarizes and prioritizes the CWE research needed to improve the current *PCDM* methods for the CWE phenomenology considered herein.

Several general conclusions from the research can be summarized as follows:

1. Although additional tests (well-designed and well-instrumented) are needed, a wealth of CWE data exists; useful data are often overlooked or forgotten in the preparation of design manuals. Systematic procedures have been developed for analyzing these data (accounting for varying quality and quantity of the data) to characterize model prediction errors and model parameter uncertainties. These procedures provide valuable information on the dominant sources of bias and uncertainty in the current state-of-the-art design methodologies and form the basis for developing RBDFs and prioritizing future CWE research.

2. Reliability-based analysis provides a framework for systematic experimental design. By identifying the dominant uncertainties, the reliability-based analysis approach provides a framework for prioritizing experimental data collection (*e.g.*, number and location of gages to optimize information return -- maximum reduction in uncertainty with minimal cost).

TABLE VII-1. BIASES AND METHODOLOGY GAPS IN *PCDM* METHODOLOGY.

	Conservative	Unconservative	Gap
Airblast and Aboveground Structure Response	• Non-normal reflection factors • Structural element resistance function • One-way response model • Centerstrip analysis method • Cylindrical model for fragment impulse	• Free-field impulse • Casing factor	• Partially buried bombs • Spall equation • Scale model vs. full-scale behavior for breach and spall
Ground Shock and Belowground Structure Response	• Free-field velocity for strong and/or stiff materials close in • Structural element resistance function	• Free-field velocity for weak and/or compressible materials close in • Velocity waveform decay for weak and/or compressible materials	• Dynamic shear • Breaching model very limited • Use of same stress and velocity waveform • Bomb detonation between burster slab and structure
Fragmentation	• Fragment penetration formulas • Use of standard fragment shape, normal collinear impact, zero rotational velocity • Cylindrical spray pattern	• Mean fragment velocity	• Design fragment selection grossly incorrect • Weight distribution for large fragments • Fragment loading
Projectile Penetration	• Penetration for modern high-speed projectiles (*e.g.*, 30 *mm* A/C cannon)		• Residual velocity model very limited • Rebar size/spacing

TABLE VII-2. PROTECTIVE DESIGN RESEARCH NEEDS.[1]

Aboveground Structure Response	Buried Structure Response	Fragmentation	Projectile Penetration
1. Spall and breach prediction (close-in, contact, and partial penetration bursts). 2. Reflected airblast: a. Prediction of reflected impulse over structure. b. Prediction of free-field impulse. 3. Fragment impulse over structure. 4. Structural element resistance function. 5. Response model.	1. Breaching prediction (close-in, contact, and partial penetration bursts. 2. Free-field ground shock: a. Free-field displacement, velocity, and stress. b. Waveforms. 3. Structural element resistance function. 4. SMI/SDOF modeling.	1. Update characterization of fragment descriptor variables (weight, velocity, shape, etc.) based on new, raw arena test data. 2. Develop improved fragment penetration formulas. 3. Characterize fragment spray pattern spatial distribution. 4. Develop method for mapping fragment loading over structure surface.	1. Penetration formulas for high-speed projectiles. 2. Residual velocity prediction equations. 3. Layered systems.

[1]Research needs are with respect to the specific CWE phenomenology addressed in this project.

3. The design/analysis procedures in the current version of the Air Force *PCDM* are not risk-consistent; that is, the procedures are not always conservative to the same degree and are unconservative in some cases.

With regard to reliability-based design research we make the following recommendations:

1. The process developed and applied herein should be applied to new design methodologies being incorporated in revisions to the *PCDM*. The new RBDFs should be developed in conjunction with development of the new design methodologies, so that research is focused on the dominant uncertainties. Also, by using this approach, the end product will be more useful since the designer will be made aware of the limitations of the methodologies and can properly apply safety factors to obtain risk consistent designs.

2. Additional research should be performed in analyzing integrated facility designs using the systems reliability approaches presented. In this way optimal designs with balanced reliability in the various possible failure modes can be obtained. These approaches would also provide a systematic framework for analyzing the effect of new threats on the survivability of the facility. Additionally, the methods provide a basis for optimal siting and facility layout. The RBD methods should be applied to an actual shelter, facility, or airbase design project and the results compared and evaluated against a design produced by the *PCDM* traditional design method.

3. An integrated computing environment to aid in reliability-based protective design should be developed. Protective construction design is a complex process and requires an expert designer that is cognizant of all of the important structure failure modes and the limitations of the design methodology. An integrated computing environment (consisting of database, expert system and analysis modules) would be an invaluable aid to ensure that none of the important threats and failure modes are overlooked and that survivable designs are achieved. The database should include threat weapon characteristics, material properties, and the RBDFs used in design. The expert system should serve to aid in selecting the structural configuration, incorporate the fault trees (for identification of all relevant failure modes), and incorporate knowledge of the analysis methodologies available to treat each failure mode. Finally, the analysis module should provide a user-friendly interface to the application codes used to perform the design/analysis computations.

REFERENCES

American Institute of Steel Construction (AISC), *Manual of Steel Construction: Load and Resistance Factor Design*, New York, 1986.

Ang, A. H-S., Abdelnour, J., and Chaker, A. A., "Analysis of Activity Networks Under Uncertainty," *Journal of Engineering Mechanics Division, ASCE*, Volume 101, Number EM4, August 1975, pp. 373-387.

Basler, F. E., and Partner, "Lokal Schadenwirkungen and Betonplatten Durch Sprengladungen," B3113.10-2, E. Basler and Partner, Zurich Switzerland, 1982.

Baylot, J. T., *et al.*, *Response of Buried Structures to Earth-Penetrating Conventional Weapons*, ESL-TR-85-09, Engineering and Services Laboratory, Air Force Engineering and Services Center, Tyndall Air Force Base, Florida, November 1985.

Beth, Richard A., and Stipe, J. Gordon, *Penetration and Explosion Tests on Concrete Slabs, Report I: Data*, Interim Report to the Chief of Engineers, United States Army, by the Committee on Passive Protection Against Bombing, National Research Council, CPPAB Interim Report Number 20, Washington, D. C., January, 1943.

Carson, J. M., and Morrison, D., and Hampson, R. J., *Conventional High-Explosive Blast and Shock (CHEBS) Test Series: Mark-82 General-Purpose Bomb Tests*, Air Force Weapons Laboratory, AFWL-TR-84-27, June 1984.

Carson, J. M., and Morrison, D., *Conventional High-Explosive Blast and Shock (CHEBS) Test Series: Mark-83 General-Purpose Bomb Tests*, Air Force Weapons Laboratory, AFWL-TR-86-53, Parts 1-3, January 1987.

Christensen, B. K., *Twenty-Five Years of Penetration Records at Sandia National Laboratories, PENTDB: A Relational Database*, Sandia National Laboratories, SAND-88-1402, 1988.

Coltharp, D. R., Vitayaudom, K. P., and Kiger, S. A., *Semihardened Facility Design Criteria Improvement*, Final Report ESL-TR-86-32, U. S. Army Engineer Waterways Experiment Station, June 1985.

Cox, D. R., and Snell, E. J., *The Analysis of Binary Data*, 2nd Edition, Chapman and Hall, London, 1989.

Department of the Army, *Fundamentals of Protective Design for Conventional Weapons*, TM5-855-1, Waterways Experiment Station, Vicksburg, Mississippi, 1984.

Dass, W. C., and Twisdale, L. A., "Comparison of Design Procedures for Fragmentation Effects," *International Symposium on the Interaction of Conventional Munitions with Protective Structures*, Mannheim, FRG, March 1987.

Ditlevsen, O., "Narrow Reliability Bounds for Structural Systems," *Journal of Structural Mechanics*, Volume 7, Number 4, 1979, pp. 453-472.

Drake, J. L., *et al.*, *Protective Construction Design Manual*, ESL-TR-87-57, Air Force Engineering and Services Center, Tyndall Air Force Base, November 1989.

Drake, J. L., *et al.*, *Background of Test Data and Prediction Methods for the Analysis of Below-Grade Walls Subjected to Ground Shock Loads*, DACA 4589 M 0096, U. S. Army Engineer District, Omaha, Nebraska, July 1989.

Fuehrer, Hans R. and Keeser, John W., *Response of Buried Concrete Slabs to Underground Explosions*, AFATL-TR-77-115, Air Force Armament Laboratory, Eglin Air Force Base, Florida, August 1977.

Goodman, H. J., Compiled Free-Air Blast Data on Bare Spherical Pentolite, BRL Report 1092, February 1960.

Guice, L. K., *Behavior of Partially Restrained Reinforced Concrete Slabs*, Final Report SL-86-32, September 1986.

Gurney, R. W., *The Initial Velocities of Fragments from Bombs, Shells and Grenades*, Report Numbers 405 and 635, Ballistic Research Laboratory, Aberdeen Proving Ground, Maryland, September 1943 and June 1947.

Hader; H., "Effects of Bare and Cased Explosive Charges on Reinforced Concrete Walls," presented at the *Symposium on the Interaction of Nonnuclear Munitions with Structures*, U. S. Air Force Academy, Colorado Springs, Colorado, 10-13 May 1983.

Hamilton, III, J. C., Dove, R. C., and Coltharp, D. R., *Perimeter Blast Wall Design for Terrorist Protection* (Draft Data Report), U. S. Army Engineer Waterways Experiment Station Structures Laboratory, November 1989.

Hayes, P. G., *Backfill Effects on Response of Buried Reinforced Concrete Slabs*, Technical Report SL-89-18, Department of the Army, Waterways Experiment Station, Vicksburg, Mississippi, September 1989.

Hickman, J. W., *et al.*, *PRA Procedures Guide: A Guide to the Performance of Probabilistic Risk Assessments for Nuclear Power Plants*, NUREG/CR-2300, Nuclear Regulatory Commission, Washington, D. C., 1981.

Hosmer, D. W., and Lemeshow, S., *Applied Logistic Regression*, John Wiley & Sons, Inc., New York, 1989.

Hunter, D., "An Upper Bound for the Probability of a Union," *Journal of Applied Probability*, Vol. 3, No. 3, 1976, pp. 597-603.

Jack, Jr., W. H., and Armendt, Jr., B. F., *Measurements of Normally Reflected Shock Parameters from Explosive Charges Under Simulated High Altitude Conditions*, BRL Report 1280, April 1965.

JMEM, *Joint Munitions Effectiveness Manual, Air to Surface Weapon Characteristics* (U), USAFTH61A1-3-2, Revision 3, Chapter 3, Change 3, 1990, CONFIDENTIAL.

Kapur, K. C., and Lamberson, L. R., *Reliability in Engineering Design*, John Wiley & Sons, Inc., New York, 1977.

Kidd, J. R., *Static Fragmentation Test of Mk-84, Mod 1, 2000-Pound, Low-Drag, General Purpose Bomb (Tritonal-Filled)*, ADTC-TR-68-40, Eglin Air Force Base, Florida, October, 1968.

Kiger, S. A. and Albritton, G. E., *Response of Buried Hardened Box Structures to the Effects of Localized Explosions*, Technical Report SL-80-1, Structures Laboratory, U. S. Army Engineer Waterways Experiment Station, Vicksburg, Mississippi, March 1980.

Kingery, C. N., and Bulmash, G., *Airblast Parameters from TNT Spherical Air Burst and Hemispherical Surface Burst*, ARBRL-TR-02555, Ballistic Research Laboratory, April 1984.

Kounias, E.G., "Bounds for the Probability of a Union with Applications," *Annals of Math. Stat.*, Volume 39, Number 6, 1968, pp. 2154-2158.

Ma, H-F., and Ang, A. H-S., *Reliability Analysis of Redundant Ductile Structural Systems*, University of Illinois, Civil Engineering Studies, Str. Research Series Number 494, August 1981.

McVay, M. K., *Spall Damage of Concrete Structures*, Technical Report, SL-88-22, U. S. Army Waterways Engineering Station, Vicksburg, Mississippi, January, 1988.

Nash, P. T., Blaylock, N. W., Spires, S. M., and Westine, P. S., *Concrete Penetration Data Base and Evaluation of Predictive Equations*, Southwest Research Institute, Project Number 06-8691-001, April 1986.

NRC, *The Fault Tree Handbook*, Nuclear Regulatory Commission, Washington, D. C., 1980.

SAS, *SAS/STAT Software: CALIS and LOGISTIC Procedures*, Release 6.04, SAS Technical Report P-200, SAS Institute, Inc., Cary, North Carolina, 1990.

SAS Institute, Inc., *SAS Procedures Guide, Release 6.03 Edition*, Cary, North Carolina, SAS Institute, Inc., 1988.

Shapiro, S. S., and Wilk, M. B., "An Analysis of Variance Test for Normality (Complete Samples)," *Biometrika*, 52, 1965, 591-611.

Slawson, T. R., *et al.*, "An Improved Soil-Structure Interaction Model for the Analysis of Buried Walls," *60th Shock and Vibration Symposium*, Volume I, David Taylor Research Center, Underwater Explosions Research Division, Portsmouth, Virginia, 14-16 November 1989.

Sues, R. H., Hwang, C-W., Twisdale, L. A., and Lavelle, Francis M., "Reliability-Based Design of R/C Structures for Protection Against Projectiles and Fragments," *Proceedings of the 5th International Conference on the Interaction of Non-Nuclear Munitions with Structures*, Mannheim, Germany, 22-26 April 1991.

Sues, R. H., and Twisdale, L. A., "Probability-Based Design Factors," Chapter 8 in, *DNA Manual for the Design Underground Tunnels*, Defense Nuclear Agency, DNA-TR-88-87, July 1990.

Twisdale, L. A., Sues, R. H., Lavelle, F. M., and Miller, D. B., "Research to Develop Reliability-Based Methodology for Protective Structures," *Proceedings of the Fifth International Symposium on Interaction of Conventional Munitions with Protective Structures*, Mannheim, Germany, 22-26 April 1991.

Twisdale, L. A., and Sues, R. H., "Reliability-Based Design Methods for Protective Structures Subjected to Non-Nuclear Munitions Effects," *Proceedings of the 4th International Symposium on the Interaction of Non-Nuclear Munitions with Structures*, Panama City, Florida, April 1989.

Twisdale, L. A., Sues, R. H., and Murphy, C. E., *Assessment of Reliability-Based Design Methodology for Protective Structures*, ESL-TR-88-27, Air Force Engineering and Services Center, Tyndall Air Force Base, Florida, 1988.

Twisdale, L. A., "Reliability and Risk Models Based on Independent Trials," *Probabilistic Engineering Mechanics*, Volume 1, Number 4, 1986.

Twisdale, L. A., and Sues, R. H., "Toward Reliability-Based Design of Protective Structures," *International Symposium m on the Interaction of Conventional Munitions with Protective Structures*, Mannheim, FRG, March 1987.

Veneziano, D., and Liao, S., "Statistical Analysis of Liquefaction Data," *Proceedings of ASCE Specialty Conference on Probabilistic Mechanics and Structural Reliability*, Berkeley, California, January 1984.

Weeks, David L., and Raspberry, Everett T., *Hard Target Vulnerability Databases*, Analysis and Strategic Defense Division, Air Force Armament Laboratory, Eglin Air Force Base, Florida, AFATL-TR-87-48, December 1987.

White, M. P. (ed.), "Terminal Ballistics," Part III, Effects of Impact and Explosion, Summary Technical Report of Division 2, National Defense Research Committee, Washington, D. C., 1946, pp. 155-250.

APPENDIX A

EVALUATION OF THE HYPERGEOMETRIC FUNCTION FOR LARGE NUMBERS.

Selection of the design fragment requires evaluating Equation (IV-11):

$$F_{L_{max}}(l) = P(L_{max} < l) = \frac{(N_t - m)!\,(N_t - n)!}{N_t!\,(N_t - m - n)!} \tag{A-1}$$

where N_t is the total number of fragments generated by the weapon, m is the number of these fragments with lethality greater than the design fragment, n is the number of fragments that impact the target and do not ricochet, and $F_{L_{max}}(l)$ is the extreme value distribution for lethality.

Because a general purpose bomb can generate tens of thousands of fragments, some numerical difficulty may be encountered in evaluating the factorials in this equation. Two approaches are possible to avoid this problem. The first is an approximate close form solution based on Stirling's factorial formula and the second is a simple FORTRAN algorithm that provides an exact solution yet avoids generating very large numbers that would result in numerical overflow.

Stirling's factorial formula is given as:

$$n! \approx \sqrt{2\pi}\, n^{n + 1/2}\, e^{-n} \tag{A-2}$$

Using Stirling's formula, we can rewrite Equation (A-1) as:

$$\begin{aligned} \ln [P\,(L_{max} < l)] \approx \ln P^* = {} & (N_t - m + 1/2) \ln (N_t - m) + (N_t - n + 1/2) \ln (N_t - n) \\ & - (N_t + 1/2) \ln N_t - (N_t - m - n + 1/2) \ln (N_t - m - n) \end{aligned} \tag{A-3}$$

and finally, the probability given by the hypergeometric function (Equation (A-1)) is given as:

$$P(L_{max} < l) \approx e^{\ln P^*} \tag{A-4}$$

Stirling's formula is highly accurate for large numbers and becomes exact as n approaches infinity. Even for factorials of numbers as small as 10, the error is less than 1%.

An exact FORTRAN algorithm that avoids generating very large numbers that could result in numerical overflow is given below. It takes advantage of the fact that, after dividing out common multiples in the numerator and denominator, exactly m multiplications must be performed in both the numerator and denominator. That is, after dividing common multiples, the hypergeometric function (Equation (A-1)) becomes:

$$P(L_{max} < l) = \frac{(N_t - n)(N_t - n - 1)(N_t - n - 2) \ldots (N_t - m - n + 1)}{(N_t)(N_t - 1)(N_t - 2) \ldots (N_t - m - 1)}$$

$$= \left(\frac{N_t - n}{N_t}\right)\left(\frac{N_t - n - 1}{N_t - 1}\right)\left(\frac{N_t - n - 2}{N_t - 2}\right) \ldots \left(\frac{N_t - m - n + 1}{N_t - m + 1}\right) \quad \text{(A-5)}$$

The algorithm for evaluating Equation (A-5) is:

```
A = NT - NH
B = NT
C = 1.0
DO I = 1, M
C = C * A/B
A = A - 1.0
B = B - 1.0
END DO
```
(A-6)

where NT, NH, and M represent the variables N_t, n, and m, as defined in Equation (A-1).

APPENDIX B
PERCENTAGE OF CG-CENTERED SOLID ANGLE INTERSECTED BY A TARGET

If a uniform sphere fragment dispersion pattern is assumed, the fraction of fragments that will impact the structure and will not ricochet is equal to the percentage of the surface area of the expanding fragment-spray sphere intersected by the structure. This intersected area can be calculated by following integration,

$$A = \int_S \int R_o^2 \sin\phi \, d\phi \, d\theta \tag{B-1}$$

where R_o is the radius of sphere, ϕ is the elevation angle, and θ is the azimuth angle (often θ is referred to as the longitude and ϕ the co-latitude). By applying suitable limits, the surface area can be calculated, *e.g*, the surface area of a sphere is

$$A = \int_0^{2\pi} \int_0^{\pi} R_o^2 \sin\phi \, d\phi \, d\theta = 4\pi R_o^2 \tag{B-2}$$

and the surface area of all points of co-latitude α or less on the sphere surface is

$$A = \int_0^{2\pi} \int_0^{\alpha} R_o^2 \sin\phi \, d\phi \, d\theta = 2\pi R_o^2 (1 - \cos\alpha) \tag{B-3}$$

If the target structure is much larger than the standoff distance, all the fragments with oblique angles less than the nonricochet angle, α, will impact the structure and will not ricochet. Thus, the surface area of the fragment-spray sphere intersected by the structure in this limiting case is $2\pi R_o^2(1 - \cos\alpha)$. For most cases of interest, however, the integration of the surface area is more complex.

Herein, a simple method is developed to evaluate the fraction of fragments that strike the target structure and do not ricochet. The procedure is to locate the orthogonal projection of the bomb CG on the target structure, and divide the structure wall into four sections. The surface area of the sphere intersected by the structure can be calculated by computing the summation of the four surface areas intersected by each section.

Figure B-1 shows the structure ABCD and a contact burst at a standoff distance, R_o. Point O is the orthogonal projection of the weapon CG on the structure. By passing through Point O, the structure is divided into four substructures or sections, O4A1, O1B2, O2C3, and O3D4. Due to the different possible ratios of structure dimensions to standoff distance, five cases need to be considered. Figure B-2 sketches these five cases. In the figures, R_o is the standoff distance, and a

and b are the length and height of the substructure, respectively. We also use the normalized standoffs $s = R_o/a$ and $t = R_o/b$.

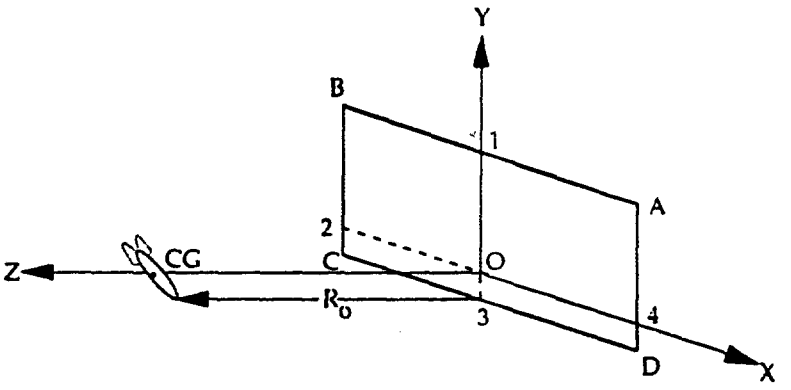

Figure B-1. Typical Weapon Structure Geometry.

1. $a \geq R_o \times \tan \alpha$ and $b \geq R_o \times \tan \alpha$ (see Figure B-2.a)

In this case, $s \leq 1/\tan \alpha$ and $t \leq 1/\tan \alpha$. All the fragments ejected from the point source with oblique angles less than α will impact the structure and will not ricochet. The intersected area of the fragment-spray sphere by the substructure is

$$A = \frac{\pi}{2} R_o^2 (1 - \cos \alpha) \tag{B-4}$$

This is a quarter of the surface area of all points of co-latitude α or less.

2. $a \geq R_o \times \tan \alpha$ and $b < R_o \times \tan \alpha$ (see Figure B-2.b)

In this case, $s \leq 1/\tan \alpha$ and $t > 1/\tan \alpha$. Some fragments even with oblique angles less than α may possibly miss the substructure. From Figure B-2.b, we can define the limits of integration as:

$$\begin{aligned} \phi_1 &= \alpha && \text{for } 0 \leq \theta \leq \theta_1 \\ \phi_2 &= \tan^{-1} \frac{b}{R_o \times \cos \theta} = \tan^{-1} \frac{1}{t \times \cos \theta} && \text{for } 0 \leq \theta \leq \theta_2 \end{aligned} \tag{B-5}$$

and

$$\begin{aligned} \theta_1 &= \sin^{-1} \frac{b}{R_o \times \tan \alpha} = \sin^{-1} \frac{1}{t \times \tan \alpha} \\ \theta_2 &= \cos^{-1} \frac{b}{R_o \times \tan \alpha} = \cos^{-1} \frac{1}{t \times \tan \alpha} \end{aligned} \tag{B-6}$$

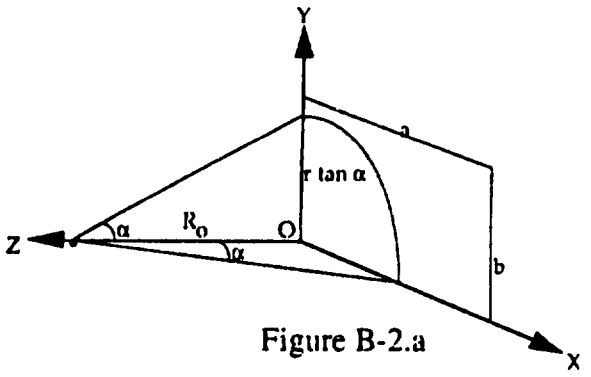

Figure B-2.a

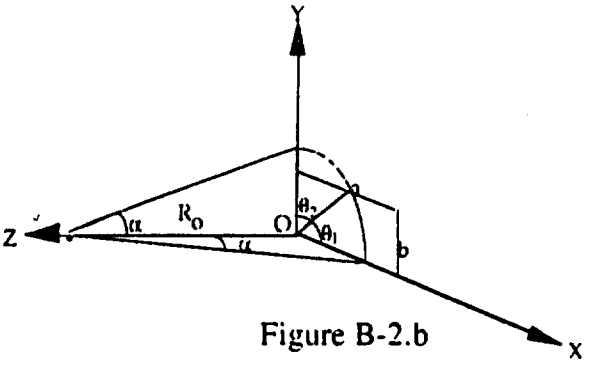

Figure B-2.b

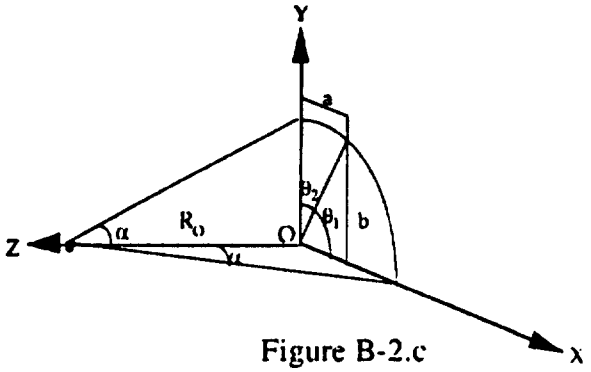

Figure B-2.c

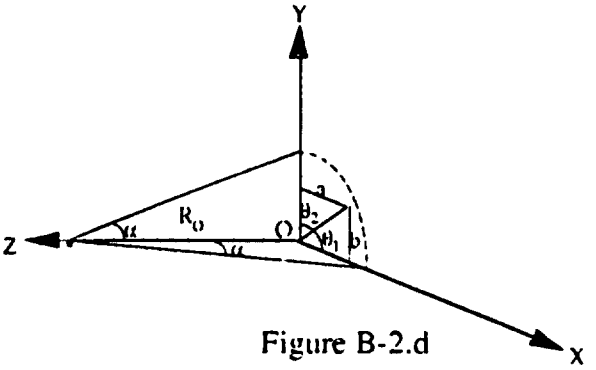

Figure B-2.d

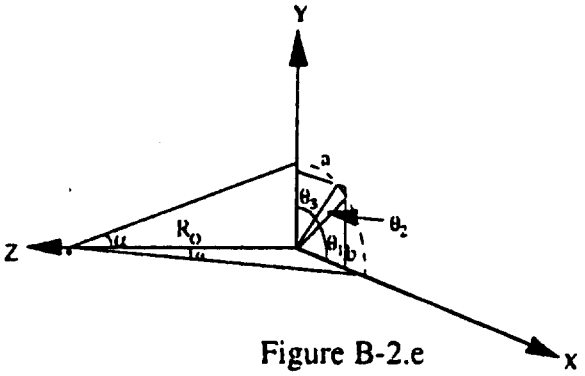

Figure B-2.e

Figure B-2. Weapon Standoff *vs* Structure Dimensions Cases for Evaluation of Number of Nonricochet Fragments.

By applying the limits, the integration formulation can be written as

$$A = \int_0^{\theta_1} \int_0^{\phi_1} R_o^2 \sin\phi \, d\phi \, d\theta + \int_0^{\theta_2} \int_0^{\phi_2} R_o^2 \sin\phi \, d\phi \, d\theta$$

$$= \int_0^{\sin^{-1}\frac{1}{t\times\tan\alpha}} \int_0^{\alpha} R_o^2 \sin\phi \, d\phi \, d\theta + \int_0^{\cos^{-1}\frac{1}{t\times\tan\alpha}} \int_0^{\tan^{-1}\frac{1}{t\cdot\cos\theta}} R_o^2 \sin\phi \, d\phi \, d\theta$$

$$= \int_0^{\sin^{-1}\frac{1}{t\times\tan\alpha}} R_o^2 (1 - \cos\alpha)\, d\theta + \int_0^{\cos^{-1}\frac{1}{t\tan\alpha}} R_o^2 \left(1 - \frac{\cos\theta}{\sqrt{\frac{1}{t^2} + \cos^2\theta}}\right) d\theta$$

$$= R_o^2\,\theta\,(1 - \cos\alpha)\Big|_0^{\sin^{-1}\frac{1}{t\tan\alpha}} + R_o^2 \left(\theta - \sin^{-1}\frac{\sin\theta}{\sqrt{1+\frac{1}{t^2}}}\right)\Big|_0^{\cos^{-1}\frac{1}{t\tan\alpha}} \qquad \text{(B-7)}$$

Finally, the intersected area of the sphere by the structure is

$$A = \frac{\pi}{2} R_o^2 - R_o^2 \cos\alpha \times \sin^{-1}\frac{1}{t\times\tan\alpha} - R_o^2 \sin^{-1}\sqrt{\frac{t^2\tan^2\alpha - 1}{(t^2+1)\tan^2\alpha}} \qquad \text{(B-8)}$$

3. $a < R_o \times \tan\alpha$ and $b \geq R_o \times \tan\alpha$ (see Figure B-2.c)

For this case, $s > 1/\tan\alpha$ and $t \leq 1/\tan\alpha$. This case is similar to Case 2. From Figure B-2.c, we can define the limits of integration as

$$\phi_1 = \tan^{-1}\frac{a}{R_o\times\cos\theta} = \tan^{-1}\frac{1}{s\times\cos\theta} \qquad 0 \leq \theta \leq \theta_1$$

$$\phi_2 = \alpha \qquad 0 \leq \theta \leq \theta_2 \qquad \text{(B-9)}$$

and

$$\theta_1 = \sin^{-1}\frac{a}{R_o\times\tan\alpha} = \sin^{-1}\frac{1}{s\times\tan\alpha}$$

$$\theta_2 = \cos^{-1}\frac{a}{R_o\times\tan\alpha} = \cos^{-1}\frac{1}{s\times\tan\alpha} \qquad \text{(B-10)}$$

The integration formulation for this case is similar to Case 2, that is

$$A = \int_0^{\theta_1}\int_0^{\phi_1} R_o^2 \sin\phi\, d\phi\, d\theta + \int_0^{\theta_2}\int_0^{\phi_2} R_o^2 \sin\phi\, d\phi\, d\theta$$

$$= \int_0^{\cos^{-1}\frac{1}{s\times\tan\alpha}}\int_0^{\tan^{-1}\frac{1}{s\times\cos\theta}} R_o^2 \sin\phi\, d\phi\, d\theta \int_0^{\sin^{-1}\frac{1}{s\times\tan\alpha}}\int_0^{\alpha} R_o^2 \sin\phi\, d\phi\, d\theta \qquad \text{(B-11)}$$

Similar to Case 2, the intersected area is

$$A = \frac{\pi}{2} R_o^2 - R_o^2 \cos\alpha \times \sin^{-1} \frac{1}{s \times \tan\alpha} - R_o^2 \sin^{-1} \sqrt{\frac{s^2 \tan^2\alpha - 1}{(s^2+1)\tan^2\alpha}} \qquad \text{(B-12)}$$

4. $a < R_o \times \tan\alpha$ and $b < R_o \times \tan\alpha$ and $(a^2 + b^2)^{1/2} < R_o \times \tan\alpha$ (see Figure B-2.d)

In this case, $s > 1/\tan\alpha$ and $t > 1/\tan\alpha$. Most of the fragments will miss the target structure. The limits of the integration are

$$\phi_1 = \tan^{-1} \frac{a}{R_o \times \cos\theta} = \tan^{-1} \frac{1}{s \times \cos\theta} \qquad 0 \le \theta \le \theta_1$$

$$\phi_2 = \tan^{-1} \frac{b}{R_o \times \cos\theta} = \tan^{-1} \frac{1}{s \times \cos\theta} \qquad 0 \le \theta \le \theta_2 \qquad \text{(B-13)}$$

and

$$\theta_1 = \tan^{-1} \frac{b}{a} = \tan^{-1} \frac{s}{t}$$

$$\theta_2 = \tan^{-1} \frac{a}{b} = \tan^{-1} \frac{t}{s} \qquad \text{(B-14)}$$

By applying the limits. the integration formulation can be written as

$$A = \int_0^{\theta_1} \int_0^{\phi_1} R_o^2 \sin\phi \, d\phi \, d\theta + \int_0^{\theta_2} \int_0^{\phi_2} R_o^2 \sin\phi \, d\phi \, d\theta$$

$$= \int_0^{\tan^{-1}\frac{s}{t}} \int_0^{\tan^{-1}\frac{1}{s \times \cos\theta}} R_o^2 \sin\phi \, d\phi \, d\theta + \int_0^{\tan^{-1}\frac{t}{s}} \int_0^{\tan^{-1}\frac{1}{t \times \cos\theta}} R_o^2 \sin\phi \, d\phi \, d\theta$$

$$= \int_0^{\tan^{-1}\frac{s}{t}} R_o^2 \left(1 - \frac{\cos\theta}{\sqrt{\frac{1}{s^2} + \cos^2\theta}}\right) d\theta + \int_0^{\tan^{-1}\frac{t}{s}} R_o^2 \left(1 - \frac{t\cos\theta}{\sqrt{\frac{1}{t^2} + \cos^2\theta}}\right) d\theta$$

$$= R_o^2 \left(\theta - \sin^{-1} \frac{\sin\theta}{\sqrt{1 + \frac{1}{s^2}}}\right) \Bigg|_0^{\tan^{-1}\frac{s}{t}} + R_o^2 \left(\theta - \sin^{-1} \frac{\sin\theta}{\sqrt{1 + \frac{1}{t^2}}}\right) \Bigg|_0^{\tan^{-1}\frac{t}{s}} \qquad \text{(B-15)}$$

The intersected area is obtained as

$$A = \frac{\pi}{2} R_o^2 - R_o^2 \left(\sin^{-1} \frac{s^2}{\sqrt{s^2 + t^2}\sqrt{s^2 + 1}} + \sin^{-1} \frac{t^2}{\sqrt{s^2 + t^2}\sqrt{t^2 + 1}} \right) \qquad \text{(B-16)}$$

5. $a < R_o \times \tan\alpha$ and $b < R_o \times \tan\alpha$ and $(a^2 + b^2)^{1/2} \geq R_o \times \tan\alpha$ (see Figure B-2.e)

This case is almost the same as Case 4. Figure B-2.e shows the limits of the integration to be

$$\phi_1 = \tan^{-1} \frac{a}{R_o \times \cos\theta} = \tan^{-1} \frac{1}{s \times \cos\theta} \qquad for\ 0 \leq \theta \leq \theta_1$$

$$\phi_2 = \alpha \qquad for\ 0 \leq \theta \leq \theta_2 \qquad \text{(B-17)}$$

$$\phi_3 = \tan^{-1} \frac{a}{R_o \times \cos\theta} = \tan^{-1} \frac{1}{t \times \cos\theta} \qquad for\ 0 \leq \theta \leq \theta_3$$

and

$$\theta_1 = \cos^{-1} \frac{a}{R_o \times \tan\alpha} = \cos^{-1} \frac{1}{s \times \tan\alpha}$$

$$\theta_2 = \frac{\pi}{2} - \theta_1 - \theta_3 \qquad \text{(B-18)}$$

$$\theta_3 = \cos^{-1} \frac{b}{R_o \times \tan\alpha} = \cos^{-1} \frac{1}{t \times \tan\alpha}$$

By applying the limits, the integration formulation is obtained as

$$A = \int_0^{\theta_1} \int_0^{\phi_1} R_o^2 \sin\phi \, d\phi \, d\theta + \int_0^{\theta_2} \int_0^{\phi_2} R_o^2 \sin\phi \, d\phi \, d\theta + \int_0^{\theta_3} \int_0^{\phi_3} R_o^2 \sin\phi \, d\phi \, d\theta$$

$$= \int_0^{\cos^{-1}\frac{1}{s \times \tan\alpha}} \int_0^{\tan^{-1}\frac{1}{s \times \cos\theta}} R_o^2 \sin\phi \, d\phi \, d\theta + \int_0^{\frac{\pi}{2} - \theta_1 - \theta_3} \int_0^{\alpha} R_o^2 \sin\phi \, d\phi \, d\theta \qquad \text{(B-19)}$$

$$+ \int_0^{\cos^{-1}\frac{1}{t \times \tan\alpha}} \int_0^{\tan^{-1}\frac{1}{t \times \cos\theta}} R_o^2 \sin\phi \, d\phi \, d\theta$$

The intersected area is then obtained as

$$A = \frac{\pi}{2} R_o^2 - R_o^2 \cos\alpha \cdot \left(\frac{\pi}{2} - \cos^{-1}\frac{1}{s \times \tan\alpha} - \cos^{-1}\frac{1}{t \times \tan\alpha}\right)$$
$$- R_o^2 \left(\sin^{-1}\frac{\sqrt{s^2\tan^2\alpha - 1}}{\sqrt{(s^2+1)\tan^2\alpha}} - \sin^{-1}\frac{\sqrt{t^2\tan^2\alpha - 1}}{\sqrt{(t^2+1)\tan^2\alpha}}\right) \quad \text{(B-20)}$$

The results for the five cases are summarized in Table B-1. The intersected area has been normalized by $1/4\pi R_o^2$. Thus, the equations in the table give the fraction of total fragments that hit the wall section and do not ricochet.

TABLE B-1. FRACTION OF TOTAL FRAGMENTS HITTING A RECTANGULAR WALL SECTION (UNIFORMLY EXPANDING SPHERE; RICOCHET ANGLE = α)

Case	Conditions	Fraction of Fragments Hitting Without Ricochet
1	$s(\tan\alpha) \le 1$ $t(\tan\alpha) \le 1$	$\frac{1}{8}(1 - \cos\alpha)$
2	$s(\tan\alpha) \le 1$ $t(\tan\alpha) > 1$	$\frac{1}{4\pi}\left(\frac{\pi}{2} - \cos\alpha \sin^{-1}\left(\frac{1}{t\tan\alpha}\right) - \sin^{-1}\left(\sqrt{\frac{t^2\tan^2\alpha - 1}{(t^2+1)\tan^2\alpha}}\right)\right)$
3	$s(\tan\alpha) > 1$ $t(\tan\alpha) \le 1$	$\frac{1}{4\pi}\left(\frac{\pi}{2} - \cos\alpha \sin^{-1}\left(\frac{1}{s\tan\alpha}\right) - \sin^{-1}\left(\sqrt{\frac{s^2\tan^2\alpha - 1}{(s^2+1)\tan^2\alpha}}\right)\right)$
4	$s(\tan\alpha) > 1$ $t(\tan\alpha) > 1$ $\tan\alpha \ge (1/s^2 + 1/t^2)^{1/2}$	$\frac{1}{4\pi}\left(\frac{\pi}{2} - \sin^{-1}\left(\frac{s^2}{\sqrt{s^2+t^2}\sqrt{s^2+1}}\right) - \sin^{-1}\left(\frac{t^2}{\sqrt{s^2+t^2}\sqrt{t^2+1}}\right)\right)$
5	$s(\tan\alpha) > 1$ $t(\tan\alpha) > 1$ $\tan\alpha < (1/s^2 + 1/t^2)^{1/2}$	$\frac{1}{4\pi}\left[\frac{\pi}{2} - \cos\alpha\left(\frac{\pi}{2} - \cos^{-1}\left(\frac{1}{s\tan\alpha}\right) - \cos^{-1}\left(\frac{1}{t\tan\alpha}\right)\right)\right.$ $\left. - \sin^{-1}\left(\sqrt{\frac{s^2\tan^2\alpha - 1}{(s^2+1)\tan^2\alpha}}\right) - \sin^{-1}\left(\sqrt{\frac{t^2\tan^2\alpha - 1}{(t^2+1)\tan^2\alpha}}\right)\right]$